

# Distortion Tolerant Fan Design



**Dušan Perović**

Department of Engineering  
University of Cambridge

This dissertation is submitted for the degree of  
*Doctor of Philosophy*

Trinity College

October 2018



# **Distortion Tolerant Fan Design**

**Dušan Perović**

## **Abstract**

Boundary Layer Ingestion (BLI) technology could achieve a fuel burn reduction of up to 15%. However, the fans need to operate in severely distorted flow, which affects the blades' mechanical integrity, aerodynamic efficiency and stability. The aim of this thesis is to understand the impact of strengthening rotor blades on aerodynamic performance, investigate how the performance can be improved by modifying the fan rotor radial work profile and explain the mechanism that allows BLI fans to operate stably even when there are regions where the fan operates beyond the clean flow stability limit.

Two test cases were used: a low speed rig fan and a representative transonic fan. The transonic fan rotor design was thickened to satisfy aeromechanical criteria and the flow field was simulated with a representative BLI inlet stagnation profile to investigate the impact of the design change. A combination of computational and experimental techniques was utilised to redesign and test a new low speed fan rotor, for a different purpose. The blade metal angles, chord and positions of maximum camber and thickness were modified to reduce the peak in loading, and hence improve the aerodynamic performance and the stability margin in the same BLI inlet flow field as for the transonic fan. Unsteady casing static pressure measurements were used to track the development of disturbances in the experimental rig at the rotor tip to analyse stall inception in distortion.

The necessary transonic blade design modification led to a loss of efficiency of 0.5% and reduction of mass flow of 2%, which were attributed to a rise in blockage due to blade thickening and an increase in profile loss in the hub region. This is a promising result, as it indicates that the necessary mechanical design changes only impacted slightly on the aerodynamic performance of the BLI fan.

The low speed fan redesign reduced the radial loading at the tip and hub and increased at the mid span to keep the same operating point. This helped alleviate the losses at the blade tip in distorted flow and improved blade performance, also increasing the stability margin. Casing static pressure measurements demonstrated that disturbances are created where the incidence is higher than the critical level at a near stall point in clean flow, but they decay as they

propagate into the region where the incidence drops below the critical level. Stall was found to occur once the disturbances were able to propagate around the entire annulus without being suppressed, which is why the loss of stability margin due to distortion is small in BLI fans.

The results are promising as they indicate that the impact of necessary mechanical design changes is not severe and that adjusting the blade design to target the regions of peak loss in distorted flow can recover some efficiency lost due to a combination of operating in distorted flow and requiring a more robust mechanical design. Moreover, the stall inception mechanism identified supports the previous findings that loss of stability margin due to distortion is minor, confirming that stability is not an issue for a fan operating in BLI.



## Preface

This work was carried out at the Whittle Laboratory, University of Cambridge, Engineering Department, between October 2014 and April 2018.

The thesis is the result of my own work and includes nothing which is the outcome of work done in collaboration except where specifically indicated in the text. No part of this thesis has been submitted to any other institution for any other degree.

The thesis does not exceed the prescribed word limit. Some of the work was published in:

Perovic D., Hall C.A., Gunn E. J., “*Stall Inception in a Boundary Layer Ingesting Fan*”. Proceedings of ASME Turbo Expo 2015, Montreal, Canada, GT2015-43025.

## Acknowledgements

I would like to thank my family for their continuous support throughout the duration of this work. None of this would have been possible without their unwavering understanding and patience. I am also deeply grateful to Tijana Janković for being immensely understanding and supportive, especially throughout the writing-up period.

I would like to thank my supervisor Chez Hall for his guidance, support, and constant availability for discussions. Completing this work would not have been possible without his supervision and numerous suggestions. Valuable suggestions and advice have come from Ewan Gunn whom I would also like to thank for establishing and sharing some of the experimental and computational methods used in this work. Timothy Williams readily shared his implementation of the method for modifying blade geometry and was always open for discussion, which I highly appreciate and for which I am most thankful.

I would also like to thank James Taylor for numerous discussions and his help with setting up the blade manufacturing process and operating the 5-axis machine, as well as Chris Clark and Nick Hooper for their assistance with 3D printing, Colin Bullman for his assistance with the experimental rig, John Saunders for continuous assistance throughout the duration of this work, and Nicola Cavaleri for comments and suggestions regarding the presentation of the work in this thesis.

This project would not have been possible without the Engineering and Physical Sciences Research Council and Rolls-Royce plc. funding. I would like to thank the team at Rolls-Royce plc. for their comments at various stages of this project, in particular Lorenzo Raffaelli, Rory Stieger, Martin Goodhand, Gabriel González-Gutiérrez, and Paul Hield.

I am grateful to Graham Pullan and Tobias Brandvik for permitting my use of the Turbostream solver. This work used the Wilkes GPU cluster at the University of Cambridge High Performance Computing Service, provided by Dell Inc., NVIDIA and Mellanox, and part funded by STFC with industrial sponsorship from Rolls-Royce and Mitsubishi Heavy Industries. I extend my thanks to Stuart Rankin for his support with using the cluster.

# Contents

Chapter 1	Introduction.....	1
1.1	Motivation .....	1
1.2	Background .....	2
1.3	Research Objectives and Thesis Structure .....	3
Chapter 2	Literature Review.....	5
2.1	BLI Systems .....	5
2.1.1	The Benefits of BLI.....	5
2.1.2	Proposed Airframe Configurations.....	6
2.1.3	BLI Propulsion Configurations .....	8
2.1.4	NASA Distortion Tolerant Fan Study .....	9
2.2	Mechanical Design for BLI.....	11
2.2.1	Mode Shapes.....	11
2.2.2	Forced Response, High Cycle Fatigue and Flutter .....	13
2.2.3	Mechanical Requirements in BLI.....	16
2.3	Fan Distortion Interaction .....	20
2.3.1	Fan Distortion Interaction Modelling .....	20
2.3.2	Flow Redistribution .....	20
2.3.3	Non-Uniform Work Input in BLI Type Flow.....	21
2.3.4	Flow Features Specific to Transonic Fans Operating in BLI .....	23
2.3.5	Distortion Tolerant Design and Impact of Severity of Inlet Distortion.....	25
2.4	Fan and Compressor Stability in Non-Uniform Flow .....	26
2.4.1	Rotating Stall .....	26
2.4.2	Stall Inception.....	27
2.4.3	Stall in Distortion.....	29
2.5	Summary .....	30
Chapter 3	Research Methods.....	31
3.1	Test Cases.....	31

3.2 Low-Speed BLI Rig Fan .....	32
3.2.1 The Rig .....	32
3.2.2 Steady Measurements .....	34
3.2.3 Unsteady Measurements .....	35
3.2.4 Blade Redesign .....	38
3.3 Transonic VITAL Fan .....	38
3.3.1 The VITAL Fan Geometry .....	38
3.3.2 Design Modifications .....	39
3.3.3 FEA Modal Analysis .....	40
3.4 Computational Fluid Dynamics Methods .....	40
3.4.1 Solver .....	40
3.4.2 Steady and Unsteady Computations .....	41
3.4.3 Domains .....	41
3.4.4 Mesh .....	43
3.4.5 Boundary Conditions and Validation .....	44
3.5 Sign Convention .....	46
3.6 Shape Space Method for Modifying Rotor Blade Design .....	47
Chapter 4 Aeromechanical Redesign of a Transonic Fan for BLI .....	50
4.1 Unsteady Forcing .....	50
4.2 Aeromechanical Requirements for Operation in BLI .....	53
4.3 Thickening the Rotor Blade .....	55
4.3.1 The FEA Model .....	55
4.3.2 Thickening Approach .....	57
4.3.3 The Final Design - Thick Blade .....	57
4.3.4 Impact on the Throat Size .....	59
4.4 Impact on Aerodynamic Performance .....	61
4.5 Clean Flow Performance .....	63
4.5.1 Reduction in Choking Mass Flow Rate .....	63

4.5.2 Rotor Flow Field.....	65
4.6 Performance in BLI Flow.....	68
4.6.1 Upstream Flow Redistribution.....	68
4.6.2 Shock Structure at the Tip .....	70
4.6.3 Flow Field in the Hub Region .....	71
4.6.4 Circumferential and Span-Wise Variation in Flow Variables.....	72
4.6.5 Rotor Losses .....	75
4.6.6 Impact on OGV and ESS Losses .....	76
4.7 Summary .....	77
Chapter 5     Aerodynamic Redesign of a Low-Speed BLI Fan.....	79
5.1 Blade Redesign.....	79
5.1.1 Redesign Target.....	79
5.1.2 Redesign Process .....	81
5.1.3 Final Redesign .....	83
5.2 Aerodynamic Performance.....	85
5.3 Clean Flow Performance.....	87
5.3.1 Upstream Flow Conditions .....	87
5.3.2 Work Input Profile and Losses .....	89
5.4 Distorted Flow Performance at Design Point.....	90
5.4.1 Impact of Work Input Profile on the Upstream Flow Redistribution.....	92
5.4.2 Rotor Flow Field.....	96
5.4.3 Loading and Pressure Rise .....	99
5.4.4 Stator Flow Field .....	102
5.4.5 Near Stall Flow Field.....	103
5.5 Summary .....	107
Chapter 6     Stall Inception in a BLI Fan.....	109
6.1 Baseline Blade Stall .....	109
6.1.1 Clean Flow Stall .....	109

6.1.2 Incidence Variation in Distorted Flow .....	114
6.1.3 Unsteady Measurements in Distorted Flow.....	115
6.1.4 Linking to the Steady Flow Field .....	118
6.1.5 Stall Inception in Distorted Flow.....	119
6.2 Redesign Blade Stall .....	124
6.2.1 Clean Flow Stall .....	124
6.2.2 Flow Field at Steady Operating Points in Distorted Flow.....	126
6.2.3 Unsteady Measurements.....	126
6.2.4 Linking with the Steady Flow Field .....	128
6.2.5 Stall Inception in Distorted Flow.....	129
6.3 Summary .....	134
Chapter 7 Conclusions and Recommendations for Future Work.....	135
7.1 Main Research Findings.....	135
7.1.1 Blade Mechanical Design Requirements.....	135
7.1.2 Impact of Mechanical Design Changes on Aerodynamic Performance.....	137
7.1.3 Impact of Modifying Rotor Work Input Profile .....	137
7.1.4 Stall Inception Mechanism in Distorted Flow .....	138
7.1.5 Fan Design for BLI.....	139
7.2 Recommendations for Future Work.....	141
7.2.1 Mechanical Design .....	141
7.2.2 Aerodynamic Design .....	142
7.2.3 Stability.....	143
7.2.4 Transonic Tests.....	143
7.2.5 Aircraft Level Analysis .....	144
References .....	145

# Nomenclature

## Symbols

$A$	Area
$C$	Class function / Force Coefficient
$c$	Chord
$c_p$	Heat capacity at constant pressure
$D$	Disturbance
$d$	Grid cell diagonal
$E$	Disturbance energy
$F$	Force
$f$	Frequency / function
$H$	Blade tip translation
$h$	Enthalpy / blade height
$h_0$	Stagnation enthalpy
$i$	Incidence
$K$	Stiffness matrix
$M$	Mach number
$M$	Mass matrix
$m$	Mass
$N$	Real number
$n$	Integer
$p_0$	Stagnation pressure
$p$	Pressure
$R$	Specific gas constant

$Re$	Reynolds number
$r$	Radial coordinate
$rev$	Time corresponding to one rotor revolution
$S$	Shape function
$s$	Specific entropy / pitch
$T_0$	Stagnation temperature
$T$	Temperature
$t$	Time
$U$	Blade speed
$U_{mid}   \bar{U}$	Blade speed at approximately 70% span
$\mathbf{u}$	Displacement vector
$V$	Velocity
$x$	x-axis (axial) coordinate
$y$	y-axis coordinate
$y_+$	Non-dimensional wall distance
$z$	z-axis coordinate
$\alpha$	Swirl angle
$\beta$	Relative swirl angle
$\delta$	Deviation
$\epsilon$	Tip gap size
$\zeta$	Radial angle
$\eta$	Efficiency
$\Theta$	Blade tip twist
$\theta$	Tangential coordinate



$\kappa$	Constant
$\mu$	Viscosity
$\rho$	Density
$\tau$	Throat size
$\chi$	Blade metal angle
$\Omega$	Blade rotational speed
$\omega$	Disturbance/stall cell speed

### **Superscripts/accents**

—	Mean / mass average / area average
·	Time derivative
^	Fourier Transform

### **Subscripts**

0	Stagnation quantity
<i>bl</i>	Baseline
<i>bp</i>	Blade passing
<i>c/clean</i>	Clean flow
<i>camb</i>	Camber
<i>d</i>	Distorted flow
<i>DP</i>	Design Point
<i>excess</i>	Above the (incidence) level in clean flow at near stall point
<i>hub</i>	Sections / part of the blade close to the hub
<i>max</i>	Maximum
<i>mid</i>	Mid-span
<i>min</i>	Minimum

$r$	Radial
$re$	Redesign
$rel$	Relative
$s$	Isentropic
$st$	Station
$TE$	Trailing edge
$th$	Thickness
$thick$	Thick VITAL blade
$tip$	Blade tip
$tt$	Total-to-total
$x$	Axial
$\theta$	Tangential
$\infty$	Far upstream

### Non-dimensional groups

$$\phi = \frac{\dot{m}}{\rho AU} \quad \text{Flow coefficient}$$

$$\psi = \frac{\Delta h_0}{U^2} \quad \text{Stage loading}$$

$$\lambda = \frac{\Delta h_{rotor}}{\Delta h_{stage}} \quad \text{Stage reaction}$$

$$\frac{\dot{m}\sqrt{c_p T_0}}{Ap_0} \quad \text{Non-dimensional mass flow}$$

### Abbreviations

ADC	Analog-to-digital converter
-----	-----------------------------

ADP	Aerodynamic Design Point
AF	Amplitude-force parameter for fatigue life assessment
AIP	Aerodynamic Interface Plane
AL	Axial location
BLI	Boundary Layer Ingestion / Boundary Layer Ingesting
BWB	Blended Wing Body
CAD	Computer Aided Design
CFD	Computational Fluid Dynamics
CPU/GPU	Central/graphics processing unit
DP	Design operating point
EO	Engine order
ESS	Engine Sector Stator
exp	Experiment
F	Flap vibration mode
FEA	Finite Element Analysis
FFT	Fast Fourier Transform
FS	Flow separation
HCF	High Cycle Fatigue
HPC	High performance computing
HWB	Hybrid Wing Body
LE	Leading edge
loc	Location
LP	Low-pass (filter)
ND	Nodal diameter

NS	Near Stall operating point
OGV	Outlet Guide Vane
PS	Pressure side
RAM	Random Access Memory
RANS	Reynolds-Averaged Navier–Stokes equations
si	Stall inception
SG	Strain gage
SS	Suction side
T	Torsional vibration mode
TE	Trailing edge
URANS	Unsteady RANS
2D	Two-dimensional
3D	Three-dimensional

# Chapter 1

## Introduction

### 1.1 Motivation

Projections indicate that air traffic will double over the next twenty years (IATA, 2017). This substantial increase in air traffic will in turn lead to a significant increase in greenhouse gas emissions. Improvements in aircraft efficiency are necessary and will assist in alleviating the environmental impact of aviation.

Boundary Layer Ingestion (BLI) is a technology that could significantly reduce fuel burn by up to 15% (Plas, et al., 2007) (Greitzer, et al., 2010). The benefits arise from fans re-energizing boundary layer fluid on novel airframe configurations, such as Silent Aircraft (Hileman, et al., 2007), achieving an improvement in the propulsive efficiency. However, BLI fans need to operate in continuously distorted flow conditions, which affects aerodynamic performance, and thus reduces the overall benefit. Moreover, the fan rotor blades' structural integrity is jeopardised, since the blades need to sustain once-per-revolution forcing due to the blades entering and exiting the distorted flow region. Stronger blades are needed, which causes additional aerodynamic performance penalties. Distortion is also found to reduce the stability margin. However, the stall inception mechanism in distortion is not well understood.

Aerodynamics of BLI fans has been extensively researched in the Whittle Laboratory using high fidelity Computational Fluid Dynamics (CFD) and detailed experimental measurements (Jerez Fidalgo, et al., 2012) (Gunn, 2015). The main finding has been that fan efficiency is reduced by 1-2% when it operates in a representative BLI flow field. The high fidelity CFD method was used in (Gunn & Hall, 2017) to design a non-axisymmetric stator. Consequent experimental tests demonstrated the benefits from tailoring each blade to local flow conditions. The research presented in this thesis further develops the work by (Gunn, 2015) in the Whittle Laboratory, investigating the impact of modifying rotor design and its work profile on the flow field in BLI, which has not been previously researched. The impact of such a design change was investigated in (Hall, et al., 2017), where non-axisymmetric throughflow analysis was developed and used to analyse differences in distortion response due to changes in a range of design parameters. The main difference between this research and Hall's work lies in the

fidelity of the method used. High fidelity CFD and detailed experimental measurements used in this research allow in-depth analysis of the flow field, which was not possible using the lower fidelity methods developed by Hall.

The NASA study described in (Arend, et al., 2017) has been, to the author's knowledge, the only study that has considered BLI fan mechanical design. The study showed that rotor blades need to be thickened up to survive in distorted flow conditions. Several other design changes were also implemented, and the final fan was tested in a transonic wind tunnel. An ambitious efficiency target initially set turned out to be hard to achieve. A detailed analysis of the flow field was not carried out to identify the reasons for losses, and neither did the study investigate to what extent different aspects of the design contributed to the distortion tolerance of the fan (Provenza, et al., 2019). The research in this thesis investigates the impact of rotor blade mechanical design changes on aerodynamic performance and was in part carried out in parallel with the NASA study. The criteria to be satisfied by the mechanical design were provided by Rolls-Royce plc, the industrial partner in this project. The main objective was different to NASA's study in that high fidelity CFD was used to understand reasons for changes in aerodynamic performance due to the thickening up of a representative transonic fan rotor to satisfy the forced response criteria set by the industrial partner.

The reduction in stability margin due to distortion is known to be small (Katz, 1958) (Longley & Greitzer, 1992). However, to the author's knowledge, the stall inception in BLI fans has not been investigated before to explain why the fan can operate stably even when some regions operate at local conditions which are beyond the clean flow stability limit. The NASA study in (Arend, et al., 2017) also found that the loss of stability margin due to distortion was small, but it remained unclear as to why exactly this was the case. This research analyses experimentally measured pressure changes at the tip of a low speed fan to track disturbances that develop during stall inception in a representative BLI flow field and explain the stall inception mechanism in a BLI fan.

## **1.2 Background**

Most of the drastic changes in tube-and-wing airframe configuration occurred when the configuration first came into use more than half a century ago. The configuration has since been perfected and further improvements will only be marginal unless there is a drastic change in airframe design. A radical new concept was proposed by NASA in the late 1980s. The idea was to remove the constraint of taking cabin pressure load in hoop tension, giving more

freedom in fuselage design. This led to the development of the Blended Wing Body (BWB) concept, which features an all lifting type airframe. In initial BWB studies (Liebeck, et al., 1998) (Liebeck, 2004), engine placement at the rear of the upper surface was a natural choice. In the early stages of research, embedded BLI and podded configurations were considered.

Significant prospective benefits associated with the upper surface embedded configuration incentivised further BLI research. Several BWB type concept aircraft studies, discussed in section 2.1.2, followed. It was repeatedly confirmed that reduction in fuel burn could be achieved both due to the novel BWB airframe and due to BLI. These concept aircraft, such as Silent Aircraft **SAX-40** (Dowling & Greitzer, 2007), MIT's **HWB** (Greitzer, et al., 2010), and NASA's **N3-X** (Felder, et al., 2011), feature a BWB type airframe with BLI propulsors mounted at the rear of the upper surface of the airframe. The airframe provides shielding that leads to a significant decrease in noise levels, which is yet another benefit of BLI. More recently, concepts featuring a conventional type of airframe with a rear fuselage mounted BLI fan, such as **DisPURSAL** (Isikveren, et al., 2014) and **STARC-ABL** (Welstead & Felder, 2016) have been studied as lower risk configurations, and are also discussed in section 2.1.2.

### 1.3 Research Objectives and Thesis Structure

The main research questions of this thesis are:

- 1) What is the aerodynamic impact of thickening up a transonic fan rotor blade to satisfy the forced response requirement of a BLI fan?
- 2) How does the radial work input profile affect the aerodynamics and performance of a BLI fan?
- 3) Can changes in the clean flow performance of a BLI fan be related to changes in the distorted flow performance?
- 4) What determines the stability boundary of a BLI fan?

**Chapter 2** discusses relevant literature. A brief overview of various future concepts utilising BLI is given to illustrate configurations in which BLI fans may be used. This is followed by a discussion on mechanical requirements. The importance of avoiding failure due to high cycle fatigue or flutter and designing for a satisfactory component life brings to light the importance of strengthening the rotor blades. Extensive progress has been made in understanding how to design a mechanically robust BLI fan rotor blade. Recent progress in understanding fan-distortion interaction is also discussed and attempts to design distortion tolerant fans and improve BLI fan performance are highlighted. Previous tests indicate that fan stability may not

be significantly affected in distortion. Literature on fan and compressor stall and impact of distortion on stability are also briefly discussed.

**Chapter 3** presents the details of the computational, experimental and design methodology. Two test cases are outlined: i) a low speed rig fan which was tested both experimentally and in CFD, and ii) a transonic low pressure ratio fan which was used for CFD simulations. The experimental and CFD setups are described, followed by a description of a method which forms the basis for design changes in both test cases. Certain post processing methods and performance calculations are also presented.

**Chapter 4** describes mechanical design modifications to the transonic test case rotor to satisfy forced response requirements for a BLI fan. Finite Element Analysis (FEA) was used to find natural modes and plot a Campbell diagram. The main emphasis was on creating a thickened up design with natural frequencies further away from the primary forcing frequencies. The criteria to be satisfied were provided by Rolls-Royce plc. CFD simulations with the final geometry were carried out to identify the impact of the design changes on the rotor performance. It was found that the required change led to a reduction of flow capacity and efficiency. Flow field analysis was carried out to explain the reasons for these changes.

In **Chapter 5** the low-speed rig rotor design was modified to reduce loading at the hub and tip while maintaining the same overall stage loading. The aim was to understand how such a work input profile affects the upstream flow field and fan performance in distortion. A new rotor blade was designed, manufactured and tested experimentally in the low-speed rig. Detailed traverse results were used to reveal the changes to the fan-distortion interaction caused by the design changes.

**Chapter 6** analyses the stall inception mechanism in the low-speed rig. Detailed measurements of the casing static pressure at the rotor tip in the low speed rig were used to understand pressure signal changes as the fan approaches stall in distortion. It was found that the fan remains stable even when there are regions of flow that are locally operating at conditions well beyond the clean flow stability limit. The correlation between pressure signal disturbance growth and incidence levels in the tip region was identified. It was shown that the stall does not occur as long as disturbances created in the region of high incidence are damped out in the region of low incidence. Measurements with both the baseline and redesign blades are used in the analysis.

Finally, **Chapter 7** presents the main conclusions and recommendations for future work.



# Chapter 2

## Literature Review

This chapter first provides an overview of the benefits of BLI and concept aircraft configurations. Subsequently, relevant literature on fan mechanical design and the specifics of designing distortion tolerant fans is discussed. The most recent findings regarding fan-distortion interaction and fan distortion tolerant design research are also presented. Finally, literature on stall inception in fans and compressors with distortion is reviewed.

### 2.1 BLI Systems

#### 2.1.1 The Benefits of BLI

Ingesting boundary layer fluid for propulsion is known to increase the propulsive efficiency, due to a more uniform downstream flow field and less wasted kinetic energy, which is why BLI technology is already in use in marine applications (Betz, 1966) and missiles (Smith Jr., 1993), where large amounts of the body's wake can be ingested by the propulsors. The idea of using BLI in aviation applications has existed for more than half a century (Smith & Roberts, 1947). However, the difficulty of ingesting a significant amount of boundary layer fluid on conventional airframes has obstructed BLI's application in aviation.

The benefit of using low momentum fluid for propulsion is that the same change in momentum is required for the same thrust but adding energy to slower moving fluid requires less energy input, as explained in (Plas, et al., 2007). Another approach is to investigate power losses on an aircraft (Drela, 2009). It can be shown that there is less power dissipation in the flow field as BLI fills in the wakes and leads to less dissipated kinetic energy, as shown in Figure 2.1. The reduction in power and the improvement in propulsive efficiency translate to a reduction in fuel burn. Various studies have shown up to 15% reduction in fuel burn (Plas, et al., 2007) (Greitzer, et al., 2010) (Uranga, et al., 2014).

The main benefit of BLI is the prospective fuel burn reduction. However, other benefits are also associated with BLI configurations. A BWB type airframe provides noise shielding, which leads to significant reductions in noise levels (Agarwal & Dowling, 2005). Another advantage

is a reduction in weight due to the elimination of pylons, as well as the elimination of nose-down thrust moment that would occur if the propulsors were podded (Liebeck, 2004).

Figure removed for copyright reasons. Copyright holder is A. Uranga.

*Figure 2.1 - Illustration of power-saving benefit of BLI (bottom) compared to a conventional aircraft (top). Reduction in axial wake velocities of combined wake and jet results in a reduction in wasted kinetic energy deposited in the flow (Uranga, et al., 2014)*

### 2.1.2 Proposed Airframe Configurations

The Blended Wing Body airframe for subsonic transport, devised by NASA in the 1990s (Liebeck, et al., 1998) and shown in Figure 2.2, makes boundary layer ingestion feasible. The project leader of the initial studies was McDonnell Douglas. Upon its merger with Boeing, a preliminary study was initiated on BWB-450, a 450 passenger concept aircraft. A demonstrator aircraft X-48, shown in Figure 2.2 in a photo taken before its maiden flight, was built and tested and the viability of BWB was demonstrated.

Following the success of the initial NASA studies, several concept aircraft studies were funded to investigate the potential of BWB and BLI for fuel burn and noise reduction. Some of the most comprehensive studies carried out are shown in the timeline in Figure 2.3. In 2006, the **Silent Aircraft Initiative** set out to design a BWB type aircraft with noise level reduction as the main target (Dowling & Greitzer, 2007). The airframe design was aided by Boeing Phantom

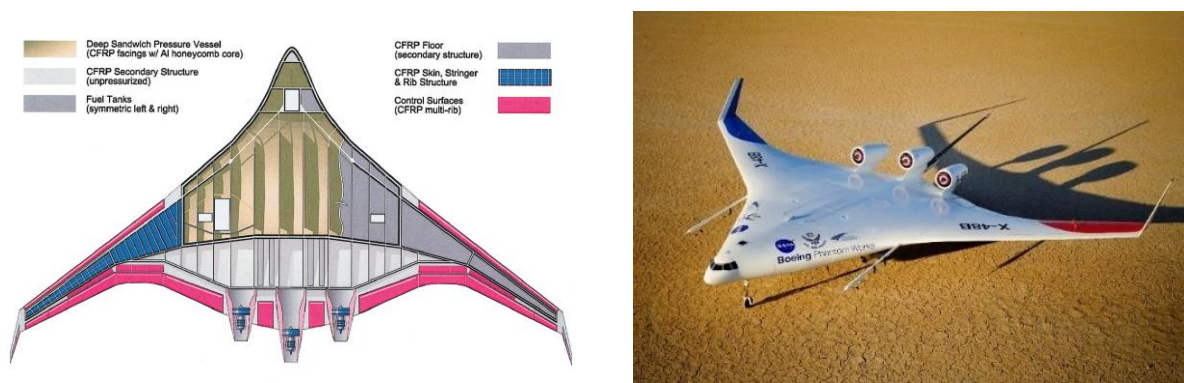


*Figure 2.2 - Structural layout of second-generation BWB (left) (Liebeck, 2004) and Boeing X-48B sub-scale technology demonstrator before beginning its flight test program (right) (Ferguson, 2012)*

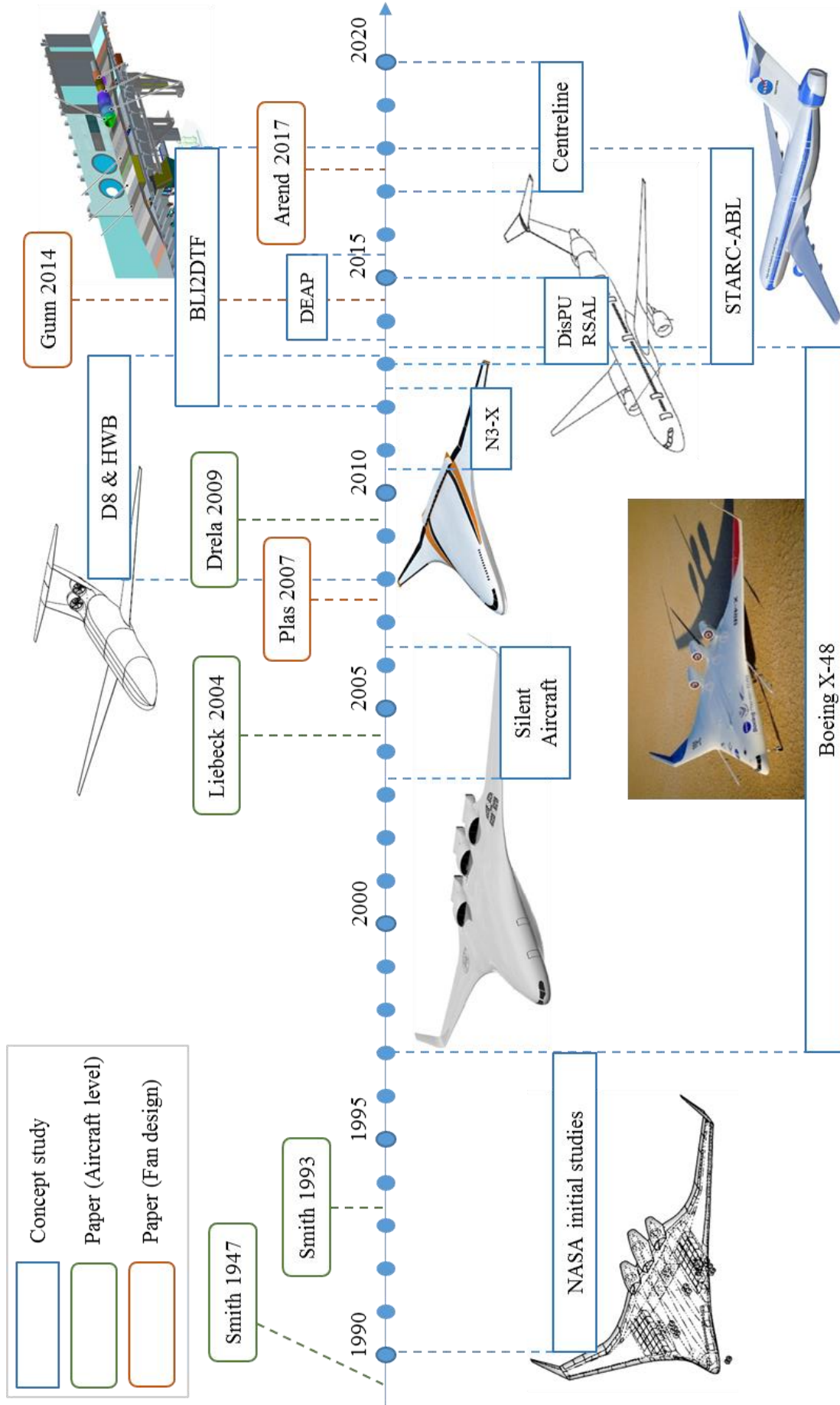


Figure 2.3 – Timeline - BWB and/or BLI concept aircraft studies and some of the main technical papers (note - some of the beginning/end dates of the projects are approximate)

Works who had experience in developing BWB airframes (Hileman, et al., 2007). An embedded engine configuration was chosen, although it was realised that this posed a major technology risk (Nickol, 2008). MIT led follow-on studies, as part of the NASA funded “N+3” program. Two aircraft were considered, the **Double Bubble D8** and the **Hybrid Wing Body HWB** concept (Greitzer, et al., 2010). **HWB** was based on the Silent Aircraft design, while the **D8** was a double circular streamlined fuselage concept which was similar to a conventional aircraft. BLI was utilized by mounting two fans between the pi-type tail fin. Another HWB type concept was NASA’s **N3-X**, an electric aircraft concept. It featured wing tip mounted engine cores that drove 15 distributed fans in a mail-slot type nacelle located at the rear of the fuselage (Felder, et al., 2011). Power was distributed electrically.

The high risk associated with BLI inevitably led to an idea to consider concepts that use BLI on a conventional type airframe, leading to several Propulsive Fuselage Concept aircraft studies, such as **DisPURSAL** (Isikveren, et al., 2014), **STARC-ABL** (Welstead & Felder, 2016), and the recently commenced **CENTRELINE** (CENTRELINE, 2017). The concepts feature a tail installed fan that re-energises the fuselage boundary layer, located either before or after the tail fin. The **DEAP** project (Pagonis, 2015), run by Airbus Group and Rolls-Royce plc, featured BLI on an airframe representing the concept called **E-Thrust**. It was a slight variation to a conventional airframe, with the engines embedded where the fuselage meets the wing suction surface.

### 2.1.3 BLI Propulsion Configurations

BLI configurations on BWB type airframes feature several fans distributed along the airframe upper surface. The propulsors are either surface mounted, as in **N3-X** or **D8**, or flush mounted with an S-duct delivering the flow to the fans, such as in **SAX-40**. Power to the fans can be transmitted either mechanically, via a gearbox that distributes power from a core to several fans, as in **SAX-40** (de la Rosa Blanco, et al., 2007), or electrically, as in **N3-X** where tip mounted cores drive a series of fans distributed within a mail slot type nacelle (Kim & Felder, 2011). Electrical transmission relies on many future technologies that are yet to be developed.

The pressure field of the surface mounted fans is strongly coupled with the airframe pressure field and is hard to separate. A coupled analysis is needed for accurate performance prediction (Felder, et al., 2009). S-duct configurations have the fan pressure field coupled with the inlet pressure field, which is coupled with the airframe pressure field. However, the coupling between the inlet and airframe is not affected by the details of the fan design. Therefore, inlet

flow field at an upstream aerodynamic interface plane (AIP) is typically imposed as a boundary condition for computational simulations and experiments.

Work in this thesis is focused on the S-duct type BLI fan system in the **SAX-40**. The **SAX-40** propulsion configuration has three nacelles, each of which delivers flow to three fans driven by a single core. The design of the S-duct for **SAX-40**, with a length-to-diameter ratio 2, is based on extensive NASA research (Berrier, et al., 2005). The development of stagnation pressure contours inside the intake of the middle engine is shown in Figure 2.4. The Mach number at the fan face is 0.67 at Mach 0.8 cruise flight condition. A vertically stratified distortion pattern with unseparated secondary flow at the fan face in the middle engine, taken from (Madani & Hynes, 2009), is the stagnation pressure profile used in the previous research carried out at the Whittle Laboratory (Gunn & Hall, 2014) (Gunn, 2015). It is also the profile used in this thesis.

Figure removed for copyright reasons. Copyright holders are A. Plas, M. Sargeant, V. Madani, D Chrichton, E. Greitzer, T. Hynes, C. Hall.

*Figure 2.4 – Stagnation pressure contours, development of the flow field in the SAX-40 intake. Axial cuts at various location along the S-duct (left) and at the AIP (right) (Plas, et al., 2007)*

#### **2.1.4 NASA Distortion Tolerant Fan Study**

NASA's Boundary Layer Ingestion/Distortion Tolerant Fan (BLI<sup>2</sup>DTF) project, described in (Arend, et al., 2017), has been, to the author's knowledge, the only study so far that has considered BLI fan mechanical design. The aim of the study was to design and test a distortion tolerant fan system for operation in representative BLI conditions on the chosen reference plane N2A-EXTE HWB (Kawai, et al., 2006). This study mainly focused on mechanical aspects of the fan rotor design, because the blades had to survive exposure to the severely distorted flow field during experimental tests.

The final fan system design is described in (Cousins, et al., 2017). The reference inlet “Inlet A” (Florea, et al., 2015) was modified to reduce the stagnation pressure loss and to minimise the incidence variation. The inlets are shown in Figure 2.5. It was believed that 24° incidence swing would cause the fan to stall. The final inlet flow field led to 17° incidence variation.

The fan was experimentally tested in a transonic section of the NASA Glenn Research Centre’s 8’x6’ Supersonic Wind Tunnel. The tests were carried out in November and December 2016. A series of papers were published in 2017 and 2018 describing the experimental setup, aeromechanical assessments, and the resulting aerodynamic performance. Aeromechanical aspects of the design process and experimental measurements are discussed in section 2.2.3.

Figure removed for copyright reasons. Copyright holder is United Technologies Corporation - United Technologies Research Center.

*Figure 2.5 – Development of the flow field in the reference “Inlet A” (left), the final inlet design and incidence variation, BLPDTF (right) (Cousins, et al., 2017), (Arend, et al., 2017)*

## 2.2 Mechanical Design for BLI

Turbomachinery blading is seen in two configurations: rooted and blisk. In a rooted configuration, each blade is inserted into a disk which is located below the annulus line in the aero path of the blade. In blisk configurations, a disk and blades are manufactured as one piece. The fan rotor blades are typically hollow Ti-alloy rooted blades (Calvert & Ginder, 1999), but use of composite materials has recently started gaining momentum due to their high strength and low weight. A typical fan rotor is shown in Figure 2.6. This section focuses on the mechanical design of rooted blades, except where a reference to blisks is made explicitly.

Fan rotor blades need to be designed to withstand high stress levels. Forced vibration excited by unsteady forces leads to dynamic stresses that may cause failure due to high cycle fatigue (El-Aini, et al., 1997). Another failure mechanism that needs to be avoided by a successful design is the self-excited vibration, called flutter. This section looks at literature concerning the blade mechanical design and aspects that are relevant to the BLI fan design.



*Figure 2.6 - Composite fan blade with Ti reinforcement at LE and TE (Sloan & Griffiths, 2012)*

### 2.2.1 Mode Shapes

Fan blade mode shape nomenclature is based on the type of deformation the blade is experiencing: flap (F), torsional (T) and edgewise. The first flap (1F) and the first torsional (1T) modes are shown in Figure 2.7. In rooted fans, the lowest frequency modes typically follow the order of 1F, 2F and 1T (Green, 2008).

In a rooted blade configuration, there is coupling between the blade modes and the disk modes. The disk modes are called nodal diameters (ND), corresponding to the number of inflexion

lines across disk diameters. Modes of an assembly comprise various combinations of blade and disk modes. An example is the 1F/2ND mode shown in Figure 2.7.

Figure removed for copyright reasons. Copyright holder is ASME.

Figure 2.7 – First flap 1F and first torsional 1T modes (left) (Butlin & Batailly, 2013) and bladed disk mode shapes (right) (Vahdati, et al., 2011)

The governing equation for undamped, unforced vibration is:

$$\mathbf{M}\ddot{\mathbf{u}} + \mathbf{K}\mathbf{u} = \mathbf{0} \quad (2.1)$$

where  $\mathbf{M}$  is the mass matrix,  $\mathbf{K}$  the stiffness matrix and  $\mathbf{u}$  is a displacement vector. It is a set of coupled equations which can be uncoupled by finding the mode shapes and natural frequencies by looking for solutions in the form of  $\mathbf{u} = \mathbf{u}_n e^{i\omega_n t}$ . Solving  $-\omega_n^2 \mathbf{M}\mathbf{u}_n + \mathbf{K}\mathbf{u}_n = \mathbf{0}$  for non-trivial  $\mathbf{u}_n$  gives the natural frequencies  $\omega_n$ . The corresponding mode shapes  $\mathbf{u}_n$  follow. An analytical approach is not possible for finding the mode shapes for complicated 3D fan rotor geometries, so a numerical approach is needed. This is typically done using Finite Element Analysis (FEA) software.

Changes in the blade shape due to centrifugal and steady pressure loads affect the blade shape and the stiffness matrix. The effect is called stress stiffening and normally has to be accounted for in structures where the bending stiffness is substantially smaller than the axial stiffness, such as fan blades (Min, et al., 2018). The mode shapes and mode frequencies change as a function of the blade rotational speed. A Campbell diagram is typically plotted to show this variation in natural frequencies, as shown in Figure 2.8. Lines of harmonic forcing are also shown as straight lines with positive slope initiating from the origin. They show how frequencies of synchronous forcing change with speed and are called engine orders, EO. The first engine order 1EO corresponds to the forcing at the shaft frequency, 2EO, to the forcing at



two times the shaft frequency, etc. The engine order lines only show the frequency, but not the amplitude of forcing.

A separate Campbell diagram needs to be created for different combinations of blade and disk modes. Depending on the respective stiffness of the blades and the disk, the natural frequencies can be blade or disk dominated. For an “infinitely” stiff disk, vibration frequencies are dominated by blade only modes as the mechanical coupling through the disk is very small (Green, 2008), i.e., the frequencies do not change with different ND such that there is little difference in the Campbell diagrams constructed for different ND patterns.

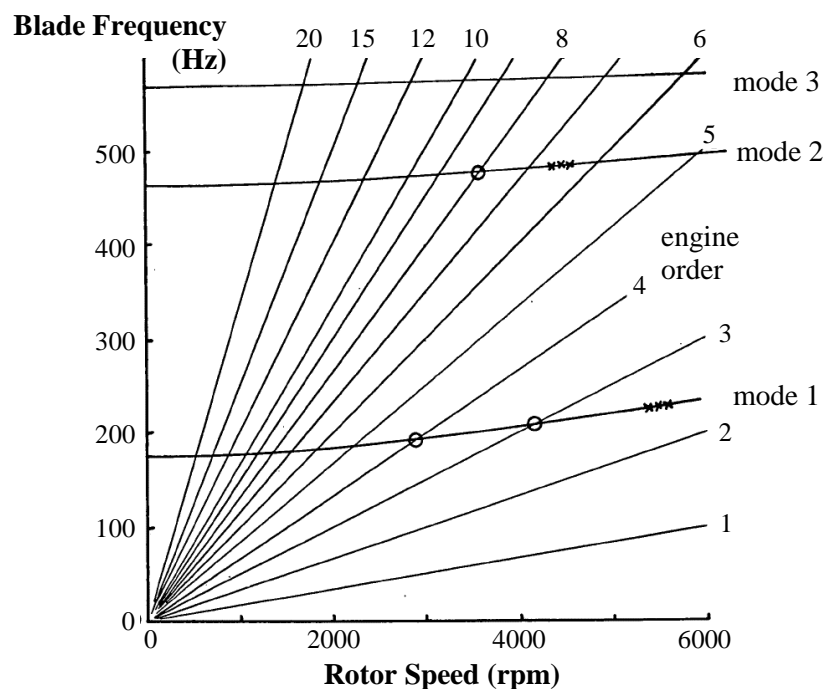


Figure 2.8 - Campbell diagram for a rotor blade (“x” stresses imply either propagating stall, flutter or other asynchronous excitation, “o” stresses indicate forced resonance) (Sisto, 1987)

## 2.2.2 Forced Response, High Cycle Fatigue and Flutter

When a rotor blade passes through wakes, the potential field of another blade-row, or through a distorted flow, it experiences a variation in loading and unsteady forcing. If the forcing frequency is close to one of the natural frequencies, resonant vibration can occur, leading to high deflections and dynamic stresses, which jeopardise structural integrity. The response amplitude depends on the magnitude of damping. If the forcing frequency is not close to any resonant frequency, the response is independent of the levels of damping (Green, 2008), as demonstrated in Figure 2.9 in which the effect of damping on the response of the first natural mode is shown. The main sources of damping are: i) material damping due to internal material

dissipation of vibration energy, ii) mechanical damping due to friction between the disk and the blade (absent in blisks), and iii) aerodynamic damping due to unsteady pressure forces that arise in response to the vibration of the blade. In Ti-alloy fans, material damping is negligible compared to mechanical and aerodynamic damping (Srinivasan, 1997).

The Campbell diagram allows graphical identification of possible crossings of the modes and EO lines at which resonance occurs. Several such crossings are labelled in Figure 2.8. It is impossible to avoid mode/EO crossings, so in general, the main design objective is to avoid any low mode and low EO crossings in the operating range, as these can lead to high deformations and high dynamic stresses. It is also impossible to avoid mode/EO crossings at part speed, so operating for prolonged periods of time at part-speed at which there is a critical crossing is undesirable.

Figure removed for copyright reasons. Copyright holder is Rolls-Royce plc.

*Figure 2.9 - Effect of damping on response (Green, 2008)*

High cycle fatigue (HCF) issues arise when alternating stress levels caused by vibration exceed the material limit. HCF assessment is made by plotting the alternating versus steady stress graph, called the Goodman diagram. A typical Goodman diagram is shown in Figure 2.10. The material limit line of maximum allowable alternating stress is based on statistical testing and is typically obtained from the material supplier (Min, et al., 2018). A successful design has alternating components of stress levels below the limit at all points, including a margin.

Another mechanism that may lead to failure is self-excited vibration, called flutter. It is a phenomenon which occurs when a dynamic response causes unsteady pressures that do positive

work in each vibration cycle, feeding energy into vibration instead of dissipating it. When flutter occurs, stress levels increase rapidly, eventually causing blade failure.

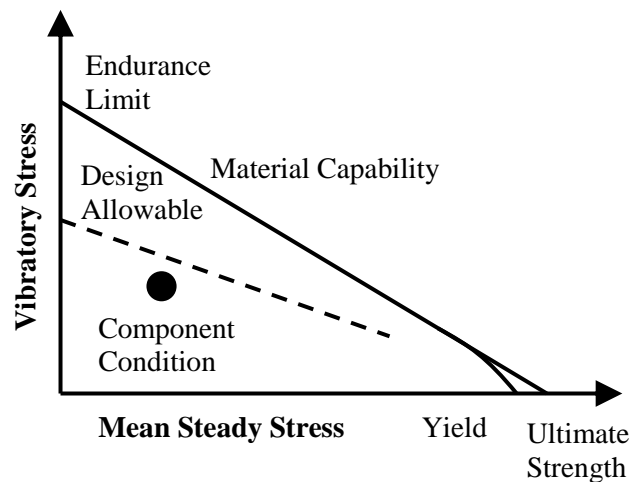


Figure 2.10 – Typical Goodman diagram, adapted from (El-Aini, et al., 1997)

A usual procedure for flutter analysis is to find aerodynamic damping by calculating work done on a vibrating blade over a vibration cycle (Vahdati & Cumpsty, 2016). Aerodynamic damping can be calculated as the negative value of the ratio of this work per cycle in relation to the average kinetic energy of the blade, i.e. aerodynamic damping =  $-1/8\pi \times \text{Work}/\text{Blade kinetic energy}$  (Bakhle, et al., 2012). Aerodynamic damping is typically calculated for different combinations of vibration modes and nodal diameter patterns, as shown in Figure 2.11. If the aerodynamic damping becomes negative for any mode/ND combination and its magnitude exceeds the magnitude of the mechanical damping, the overall damping becomes negative and flutter occurs. A parameter that governs flutter margin for the 1F mode is the ratio of twisting to plunging motion in this mode. This is because lift fluctuations due to plunge lead to positive damping and lift fluctuations due to twist always lead to negative damping (Vahdati & Cumpsty, 2016).

Figure removed for copyright reasons. Copyright holder is AIAA.

Figure 2.11 - Aerodynamic damping variation for circumferentially-averaged inflow at design rotational speed (Bakhle, et al., 2018)

### 2.2.3 Mechanical Requirements in BLI

In BLI applications, blades need to operate in heavily distorted flow without aeromechanical failure. Variation in blade surface pressures in BLI conditions causes low EO forcing, as shown in Figure 2.12. Forcing at a low EO excites low vibration modes, which can result in high deflections and high dynamic stresses (Bakhle, et al., 2014) (Min, et al., 2018) and lead to HCF. To avoid blade failure due to HCF, alternating stresses must be below the limit on the Goodman diagram. The typical limit corresponds to  $10^7$  cycles, and if it is met, the blade is considered to have an infinite life. In BLI, the limit was set to correspond to  $10^9$  cycles (Provenza, et al., 2019).

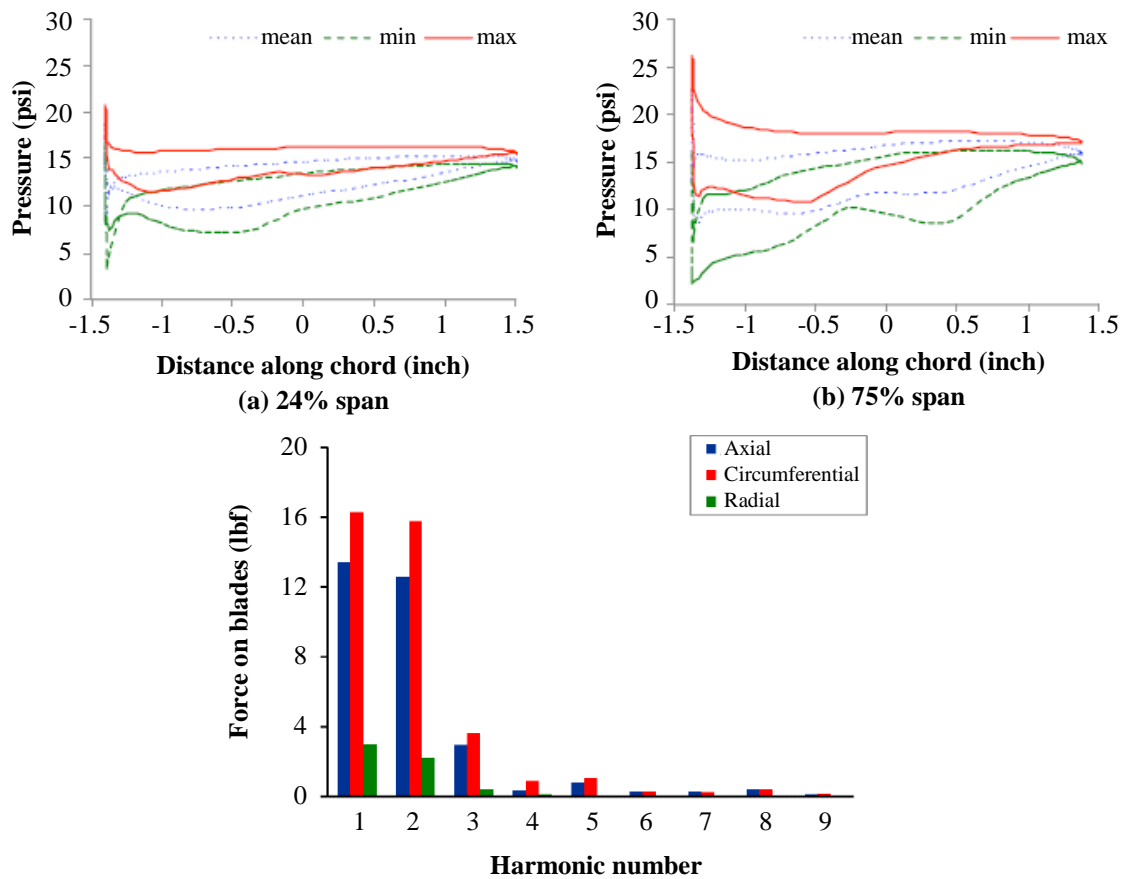


Figure 2.12 – Distortion tolerant fan (DTF) blade pressure distribution with inlet distortion, showing mean, minimum and maximum pressure (above) (Bakhle, et al., 2014), and blade unsteady pressure load in terms of EOs, harmonic numbers, at design speed (below) (Min, et al., 2018)

The Campbell diagram in Figure 2.13 shows predicted and experimentally measured mode frequencies of the BLI<sup>2</sup>DTF fan. The alternating stresses at the aerodynamic design point, ADP, arise due to an off-resonant response to EO forcing. The responses of mode 1 to 1EO forcing and mode 2 to 3EO forcing are labelled “B” and “C” in Figure 2.13.

Figure removed for copyright reasons. Copyright holder is ASME.

*Figure 2.13 – BLI<sup>2</sup>DTF fan Campbell diagram (above) and Typical response during test rig startup at blade root (below)  
(Provenza, et al., 2019)*

The fatigue life is affected by resonant responses that occur as the blade is sped up to ADP. The experimentally measured responses, also shown in Figure 2.13, indicate that there is a strong response of mode 1 when it crosses the 3EO line, labelled “1” in the Campbell diagram, and a strong response at approximately 6000rpm, due to M1/2EO resonance, labelled “2”. These resonant responses are considered safe if the resulting alternating stress amplitude is below the critical value on the Goodman diagram, which was the case in the BLI<sup>2</sup>DTF project. However, the dynamic stress amplitude at resonance strongly depends on the value of damping. The total damping for the critical crossing “2”, M1/2EO, obtained from the experimental test data was 2.9%. Structural damping comprising the material and root friction damping was measured in a vacuum and was found to be 0.2%. The total damping was unusually high. With this level of damping, the dynamic stress did not exceed the limit. Had it been lower and closer

to the typical values in the order of 0.5-1% expected for this mode (Provenza, et al., 2019), the Goodman limit would have been exceeded. It is unclear as to why such a high damping occurred. While damping is important for resonant response, it does not affect the off-resonant response at ADP.

The baseline blade used in the BLI<sup>2</sup>DTF project would not have survived in the BLI conditions, as is apparent from Figure 2.14. The plot shows that dynamic stresses due to M2/3EO interaction at ADP, measured by the strain gage 1 (SG1), exceed the limit. The main design changes that made the final blade survivable were a thicker blade root, a shorter tip chord, a restacking to balance moments around the blade's centre of gravity and modifications to accommodate surface shot peening. Although it is uncertain as to which extent these modifications contributed to achieving the required task (Provenza, et al., 2019), blade root thickening undeniably led to a reduction in both steady and dynamic stresses, improving the blade fatigue life.

Figure removed for copyright reasons. Copyright holder is ASME.

*Figure 2.14 – BLI<sup>2</sup>DTF: Strain gage location on the final blade (left) and effects of inlet shape tailoring and final blade design changes on M2/3EO vibration component amplitude at SG1 root gage location at ADP (right) (Provenza, et al., 2019)*

The approach for calculating the work per cycle for the flutter analysis in BLI in the BLI<sup>2</sup>DTF project resulted in a range of values for different cycles, depending on which part of the annulus the vibration cycle occurred in (Bakhle, et al., 2012) (Bakhle, et al., 2018). Unlike the clean flow case where convergence to a single value occurs after approximately three vibration cycles for the mode 1/0ND vibration (Figure 2.15a), enabling a plot of aerodynamic damping versus nodal diameter pattern for mode 1 (Figure 2.15b), in distorted flow there is a higher degree of variation in damping in each vibration cycle. Nevertheless, averages were calculated showing that the average damping is virtually constant for different cycles (Figure 2.15c,d). In the

BLI<sup>2</sup>DTF fan design, the aim was to avoid negative aerodynamic damping at all times. Distortion was found to have an insignificant impact on aeroelastic stability (Herrick, 2011) (Bakhle, et al., 2012), i.e., no features specific to distortion were identified which would affect flutter stability differently compared to operation in clean flow. While the approach for determining flutter stability in distorted flow was not ideal and was only one of several options considered (Bakhle, et al., 2012), it was sufficient to create a design that did not flutter in the operating range of interest. It was reported that flutter occurred only at 100% speed at an operating point which was far up on the characteristic and could not be simulated in CFD, as it was beyond the numerical limit, disabling flutter analysis.

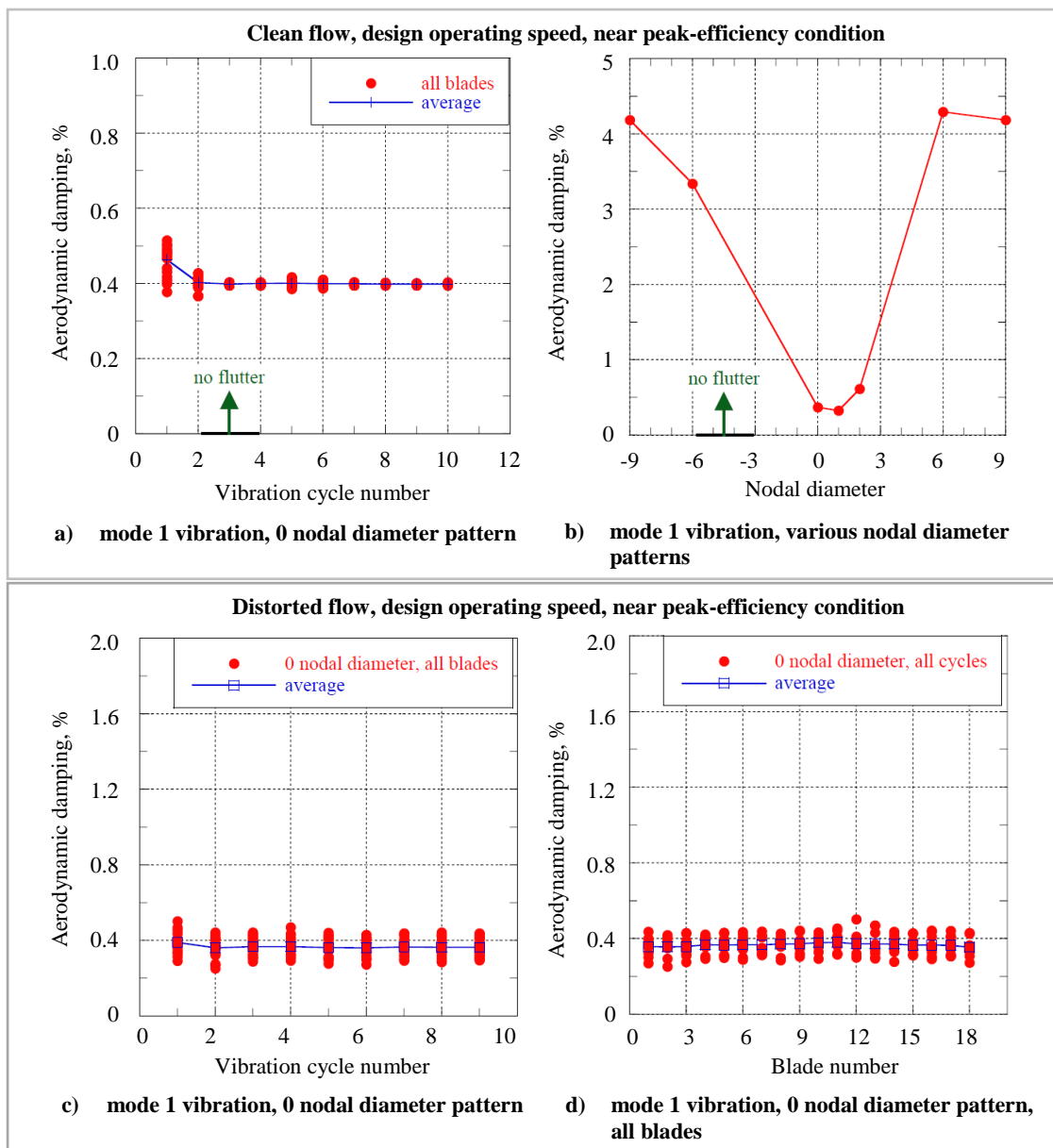


Figure 2.15 - Aerodynamic damping in clean and distorted flows, adapted from (Bakhle, et al., 2012)

## **2.3 Fan Distortion Interaction**

In the past, the main concern was the impact of distortion on stability, as the distortions were mostly of a transient nature. Many studies were carried out to understand the impact of various square wave circumferential stagnation pressure distortions on the performance of high hub-to-tip ratio compressors. The main topic of interest in BLI applications has been performance. Since distortion is present throughout the entire flight, the impact of distortion on efficiency is important as it affects the overall fuel burn benefit.

### **2.3.1 Fan Distortion Interaction Modelling**

Early use of high fidelity Unsteady Reynolds-Averaged Navier–Stokes equations (URANS) CFD method for modelling fan distortion interaction showed high flow complexity in distortion compared to clean flow (Hah, et al., 1998). URANS modelling of fan distortion interaction in military fans (Yao, et al., 2007) (Gorrell, et al., 2008) (Yao, et al., 2010) demonstrated how local operating conditions vary circumferentially. Jerez Fidalgo (Jerez Fidalgo, et al., 2012) used URANS to simulate the NASA stage 67 response to a 120° circumferential square wave distortion, providing detailed insight into the flow field of a transonic fan operating in distortion. Gunn (Gunn & Hall, 2014) used URANS to model the flow field in a low speed and transonic fan in representative BLI conditions.

Before URANS became available, lower fidelity methods were used for modelling flows in distortion. These methods included the parallel compressor model (Mazzawy, 1977), actuator disks (Hawthorne, et al., 1978) and body force models (Xu, 2002). Distributed source term throughflow methods are still used for analyses that require many runs, due to their substantially lower computational cost compared to URANS. Examples include studies of impact of different inlet distortion profiles (Defoe, et al., 2018), or fan parameter studies (Hall, et al., 2017).

### **2.3.2 Flow Redistribution**

Upstream flow is affected by the presence of the fan. As the fan sucks harder in the region of low momentum, the pressure field becomes distorted and a region of low pressure is induced in the low momentum region. This pressure field acts on the fluid particles which move towards the low momentum region, as shown schematically in Figure 2.16, reducing the mass flux distortion as the flow approaches the fan face, which is why this effect is extremely important. Regions of co-swirl and counter-swirl are created as the flow migrates around the spinner towards the low momentum region. The effect was observed in both subsonic and transonic



machines with either a large or small hub-to-tip ratio (Longley & Greitzer, 1992) (Jerez Fidalgo, et al., 2012) (Gunn & Hall, 2014). One of the key findings in (Jerez Fidalgo, et al., 2012) was that rotor redistribution upstream of the fan reduces mass flux distortion making it easier for the fan to accommodate the high level of upstream distortion.

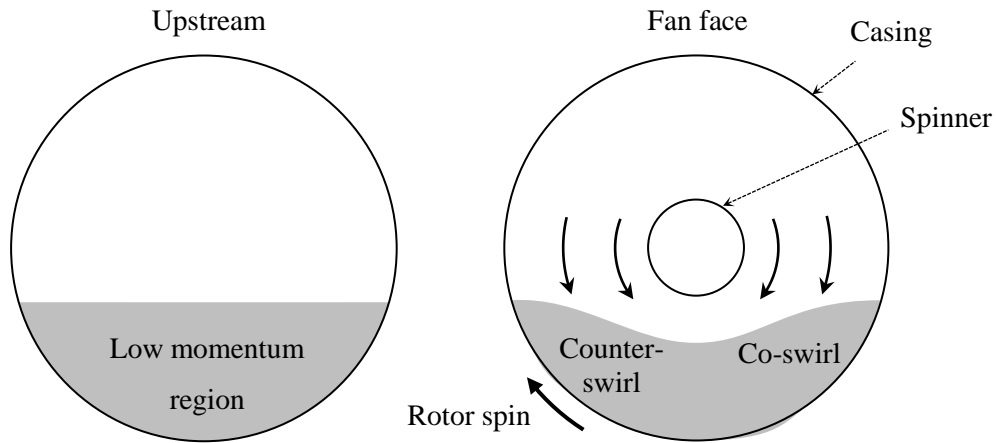


Figure 2.16 - Upstream flow redistribution schematic

Flow redistribution continues inside the rotor blade-row. While upstream redistribution in distorted flows is both radial and circumferential, redistribution within a blade row is mostly radial due to blades constraining circumferential mass flux redistribution. The driving force for redistribution disappears downstream of the rotor row, so little redistribution is seen through the stator row and in the exhaust (Gunn & Hall, 2014).

Pressure field coupling may occur depending on the proximity of the downstream nozzle. Previous studies show that upstream influence on flow depends on whether there is a diffuser or a nozzle at the outlet. Nozzles tend to reduce the circumferential flow distortion, while diffusers increase it (Greitzer, et al., 1978).

### 2.3.3 Non-Uniform Work Input in BLI Type Flow

(Jerez Fidalgo, et al., 2012) showed that the upstream redistribution introduces swirl and variation in incidence. The upstream domain was separated into several circumferential sectors and streamline tracking was used in the averaged flow field to determine the performance of each sector. The method was used to plot orbits that depict a locus of local operating points on a compressor map. It was found that variation in the upstream flow field leads to variation in local work input.

The main contribution to understanding the work and loss distribution in a BLI fan was made by (Gunn, 2015), who carried out high-fidelity, full annulus CFD simulations on a low-speed BLI rig fan and used streamline tracking adapted from (Jerez Fidalgo, et al., 2012) to determine rotor performance. Work input for a streamtube was shown to depend on the inlet conditions, radial flow migration and the extent of streamtube contraction. Euler's work equation was broken down into different physically meaningful terms, as shown in equation (2.2):

$$\frac{\Delta h_0}{U_3^2} = \underbrace{\frac{U_4^2}{U_3^2}}_{\text{Change in blade speed}} + \underbrace{\frac{V_{x3}}{U_3} \frac{V_{x4}}{V_{x3}} \frac{U_4}{U_3} \tan(\beta_4)}_{\text{Relative exit swirl}} - \underbrace{\frac{V_{x3}}{U_3} \tan(\alpha_3)}_{\text{Inlet swirl}} \quad (2.2)$$

Indices 3 and 4 denote axial locations just upstream and downstream of the rotor. The second term is affected by the conditions at the inlet, streamtube contraction, radius change and relative turning. Increased work input occurs when:

- There is counter-swirl at inlet - the third term becomes negative, due to the negative swirl angle  $\alpha_3$
- Streamtube is being displaced to a higher radius – increases the centrifugal work component, making the first term larger
- Streamtube is contracting – makes the second term higher due to an increased axial velocity ratio  $V_{x4}/V_{x3}$

Calculated isentropic and lost work are shown in Figure 2.17. Most of the losses occur at the casing in the counter-swirl region. Similarly, the loss at the casing is slightly reduced in the co-swirl region. These variations are caused by the variation in incidence levels. At other span fractions, there is little variation in lost work. There is slightly more lost work in the counter swirl region, but the magnitude of this difference is very small.

A striking fact is that efficiency is the highest in the low momentum region. The reason behind the high efficiency in the low momentum region where incidence is high is that a large proportion of high work input stems from the non-diffusive centrifugal effects, due to strong radial flows found in this region, while work input from diffusive mechanisms is lowered. Consequently, high work is imparted with low losses.

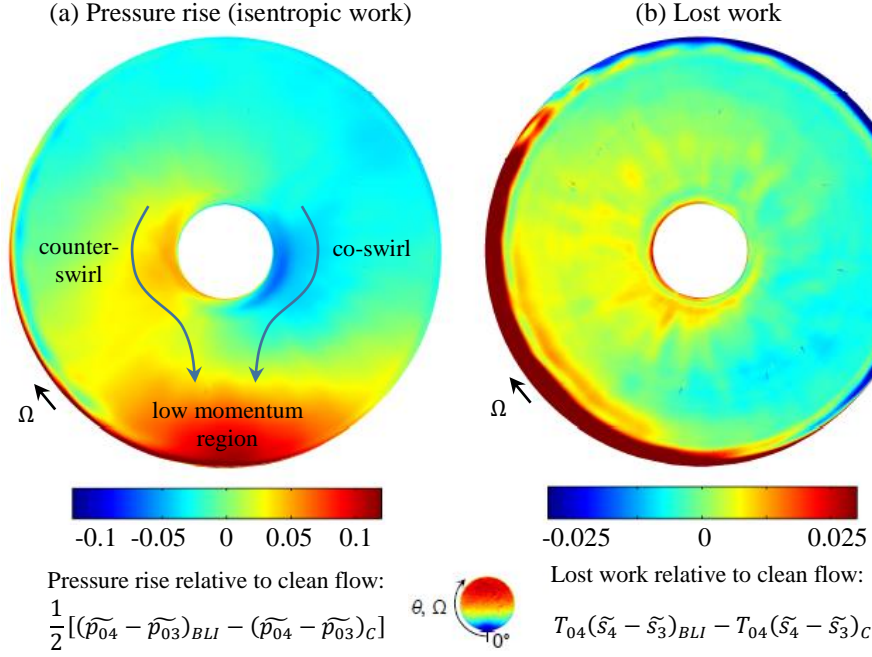


Figure 2.17 - Computed effect of simulated BLI inlet flow on the rotor stagnation pressure rise and lost work along streamlines, plotted against streamline locations at rotor inlet (Gunn, 2015)

High loss in the counter-swirl region was also observed in (Wartzek, et al., 2015), who carried out experimental investigation of the impact of a casing separation due to  $120^\circ$ , 10% span distortion beam placed upstream of the rotor. The circumferential extent of the distortion was motivated by findings from an earlier experimental campaign (Wartzek, et al., 2012) which used  $60^\circ$  distorted sector. A stronger effect was desired, so  $120^\circ$  distortion was used to exceed the  $90^\circ$  level which was found to be critical for single distortion sectors (Longley & Greitzer, 1992). The tests were carried out in a transonic tunnel at TU Darmstadt. They showed that regions of counter and co-swirl formed downstream of the distortion beam, leading to a variation in incidence. Loss core was identified as the rotor blades left the affected region of the flow, i.e., in the counter-swirl region where the incidence and work input were high.

### 2.3.4 Flow Features Specific to Transonic Fans Operating in BLI

The details of the BLI flow field in a transonic fan differ from the low speed case. However, most of the findings from the low speed case translate to the transonic case, as shown in (Gunn, 2015). For example, bulk flow redistribution is the same in both cases, with regions of co- and counter-swirl present ahead of the fan. Another aspect that is similar in both cases is the location of the regions of high loss, although the loss mechanisms responsible are different. The loss generation in a transonic fan occurs due to shock loss and shock boundary layer interaction.

The main feature of the BLI flow in a transonic fan is the variable shock structure, shown in Figure 2.18 (Gunn & Hall, 2014). Shock structure at the tip at 90% span shows a full range of shock structures observed across a range of operating points in clean flow, due to varying shock strength and flow angles. The relative Mach number ahead of the LE shocks varies from 1.15 in the co-swirl region,  $-180^\circ < \theta < 0^\circ$ , to 1.35 in the counter-swirl region,  $0^\circ < \theta < 180^\circ$ , as shown in Figure 2.19. Shock structure in the counter-swirling region is similar to that observed at a near stall operating point in clean flow, with a single expelled bow shock ahead of the LE. The shock structure at  $(-40^\circ < \theta < 0^\circ)$  is similar to the design operation in clean flow. The rest of the annulus, i.e., the co-swirling region  $(-180^\circ < \theta < -40^\circ)$ , operates under choked conditions, with LE and passage shocks.

Figure removed for copyright reasons. Copyright holder is ASME.

*Figure 2.18 – Relative Mach number distribution in the VITAL (see section 3.1) fan at 90% span with BLI inlet flow (Gunn & Hall, 2014)*

Flow conditions vary not just at the tip, but across the entire span. This is shown in Figure 2.19 (Gunn & Hall, 2014). Instantaneous static pressure distribution on two blades is shown, one in the counter-swirl region,  $\theta = 90^\circ$ , and the other in the co-swirl region,  $\theta = -90^\circ$ . The fraction of the blade span that is transonic is depicted as a function of circumferential location. The shock is shown to extend down to the hub in the counter-swirl region of the flow, as is apparent in the surface contour plot. On the other hand, the shock structure in the co-swirl region extends only down to mid-span. This leads to non-uniform variation in loss, work input, and loading. The variation in loading is responsible for unsteady mechanical forcing.

Figure removed for copyright reasons. Copyright holder is ASME.

*Figure 2.19 - Variation of shock strength, location and spanwise extent in the VITAL (see section 3.1 ) fan with BLI inlet flow (left), pressure distribution on the suction surfaces of two rotor blades at different circumferential locations (right) (Gunn & Hall, 2014)*

Losses in the transonic fan caused by BLI are in the order of 1-2% (Gunn & Hall, 2014). Even though the shock structure varies around the annulus, the inlet relative Mach numbers are below 1.5. No significant increase in shock loss is expected under such conditions. Most of the additional loss comes from the interaction of the shocks with the boundary layers. In the counter-swirling region, strong shocks that interact with the SS boundary layer cause boundary layer thickening and increase in wake size. In the co-swirl region, additional boundary layer thickening originates from shock boundary layer interaction on the pressure surface.

### **2.3.5 Distortion Tolerant Design and Impact of Severity of Inlet Distortion**

The non-uniformity at the inlet to the stator can be managed by adjusting each blade to local operating conditions. An attempt to do this is presented in (Gunn & Hall, 2017). The aim was to control diffusion by varying chord and incidence by in turn varying the inlet angle. This method was successful in eliminating casing corner separations and reducing profile loss. It was less effective in the hub region where the flow is predominantly three-dimensional. Compound lean was applied in this region in order to reduce hub corner separations. It was found that reduction in hub losses was offset by increase in profile loss further up the span. Overall, it was demonstrated that significant improvement in stator performance can be achieved by employing non-axisymmetric stator design. (Hall, et al., 2017) investigated a series of stage design parameters and found that non-axisymmetric stator design had the strongest impact on stage performance in BLI.

(Defoe, et al., 2018) investigated the impact of a range of inlet distortions on performance. The distributed source term approach, developed in (Hall, et al., 2017), has been used to model rotor and stator in a low-speed fan, eliminating the need to run computationally expensive unsteady simulations with 3D blade geometry. Viscous effects are not modelled. A metric based on diffusion factor is defined to assess expected change in efficiency, since the fidelity of the model does not allow direct calculation of the efficiency. The increase in distortion intensity is found to affect the diffusion factor metric linearly, but the change in location of the distortion has a non-linear effect on the metric.

The recent NASA BLI<sup>2</sup>DTF study took a different approach. The aim was to design a mechanically robust blade that could survive in the distorted flow environment. The stage efficiency was 87.9% (Arend, et al., 2017), which was lower than the baseline blade, but it was unclear what contribution each of the many design changes had on either aerodynamic performance or aeromechanical stability (Provenza, et al., 2019).

## **2.4 Fan and Compressor Stability in Non-Uniform Flow**

### **2.4.1 Rotating Stall**

Rotating stall is characterised by cells of low flow and a sudden loss of pressure rise. Stall cells either occupy a part of the blade span or extend along the entire span. Part span stall usually occurs on long aspect ratio blades. The size of the stall cell varies, as does the speed. In the rotating frame of reference, a stall cell moves when a new separation is triggered at the end of the stall cell, and the separation at the front clears, hence moving backwards. In the absolute frame of reference, the stall moves forward with a speed of between 20% and 80% of the rotor speed. The speed depends on the size of the stall cell. Large stall cells usually move slower.

Rotating stall research has been underway since the mid-20<sup>th</sup> century. There has been significant progress in understanding rotating stall. However, research has mostly been of a descriptive nature, and has not contributed much to explaining how to design a more stable machine. It has rather focused on explaining how stall occurs after it has already happened (Day, 2016).

The development of stall can be tracked by following disturbance development in the casing static pressure field. Possible causes range from boundary layer blockage (McDougall, et al., 1990), to critical incidence (Camp & Day, 1998), tip leakage flow (Hoying, et al., 1999) (Day, 1991) (McDougall, et al., 1990), and trailing edge backflow (Vo, et al., 2008).

### 2.4.2 Stall Inception

Two routes into rotating stall are known: spike type and modal stall inception (Moore & Greitzer, 1986) (Camp & Day, 1998). Spike type stall is caused by localised, small length-scale disturbances in the order of a blade pitch, that trigger separation on one of the blades (Day, 1991), as shown in Figure 2.20. As flow in the neighbouring passages is affected by the newly formed blockage, more blades stall and a stall cell forms. This type of stall inception is commonly found in aero engines (Weichert & Day, 2014). Modal stall inception is characterised by large length-scale disturbances, in the order of blade circumference, that affect many blades simultaneously (McDougall, et al., 1990). Modal stall inception is less common since the development of modes is dependent on the stages being perfectly matched.

Figure removed for copyright reasons. Copyright holder is ASME.

*Figure 2.20 - Spike type stall (left) and modal type stall (right) (Day, 1991)*

Work by (Pullan, et al., 2015) showed that even though there are many possible ways for a blade to stall, the spike-type stall inception process is characterised by leading edge separation at high incidence during which a radial vortex is shed, as shown in Figure 2.21. One end of this vortex is on the casing and the other on the blade suction side. The vortex, if strong enough, is then convected and it hits the next blade, triggering a new separation. The process repeats itself until a stall cell forms. This is backed up by experimental and computational work and was observed in other experimental studies (Weichert & Day, 2014).

Many stall inception mechanisms have been reported in research papers, due to the great variety of machines being tested. The process described in (Pullan, et al., 2015) is unique in the sense that it does not depend on the specific event that caused the initial increase in incidence and separation. Once it has occurred, the process always proceeds in the same way. It is also noted that it happens irrespective of whether there is tip leakage flow or not, i.e. regardless of whether there is a tip gap or a shroud.

Figure removed for copyright reasons. Copyright holder is ASME.

*Figure 2.21 - The vortical structure and propagation of the spike (Pullan, et al., 2015)*

The cause of the initial separation can vary from tip leakage flow spillage, where the tip leakage flow hits the leading edge of the neighbouring blade, to blockage due to casing corner separation (Hewkin-Smith, et al., 2017). In transonic machines this is further complicated due to the presence of shocks.

Stall in transonic fans is known to occur when the shocks move away from the leading edge as the mass flow coefficient reduces, as shown in Figure 2.22. (Strazisar, 1985) observed that the shock is not stationary in the relative frame and that it oscillates, but the link between this observation and the stall inception is not clear. (Suder & Celestina, 1994) found that tip leakage flow-shock interaction may play an important role in stall inception. (Adamczyk, et al., 1991) showed that the forward part of the tip leakage flow interacts with the shock and that interaction is thought to reduce the flow range. Closing the front 50% chord length of the tip gap is shown to lead to an increase in flow range.

Figure removed for copyright reasons. Copyright holder is ASME.

*Figure 2.22 - Intersection of rotor passage shock with the mid gap hub-to-shroud streamsurface (left), rotor shock structure at design speed for various operating conditions (right) (Strazisar, 1985)*



Recent computational studies in (Kim, et al., 2018) have investigated stall inception in two low pressure ratio engine fans. The computations were validated against experimental measurements. The two fans had different radial loading profiles: one had uniform loading up the entire span and the other had reduced loading at the tip. Stall inception was found to be caused by casing corner separation blockage in the fan with uniform loading, while the fan with low loading at the tip experienced stall due to tip leakage flow spillage ahead of the fan leading edge. The loading profile affected the stall cell size. Stall in the fan with uniform loading experienced part span stall, while the fan with lower tip loading experienced full span stall. This was because the flow was already separated at lower span fractions prior to stall.

### **2.4.3 Stall in Distortion**

Some early attempts to model the impact of distortion on stability margin used the parallel compressor model, analytical methods and CFD. In general, these methods over-predicted the reduction in stability margin. Methods such as parallel compressor model predicted that stall would occur once the local flow conditions were beyond the stall point in clean flow. However, this is not sufficient, as demonstrated in (Katz, 1958), where it was observed that disturbances would appear in the region of low momentum, but steady operation would be restored once the affected blades entered the high momentum flow region. Stall was found to occur at a flow coefficient which is only around 1% higher, compared to the clean flow. This was confirmed in experimentally measured characteristics in (Longley, 1990) and (Shaw, et al., 2013). More recently, experimental measurements in (Wartzek, et al., 2015) verified that distortion affects stability, since the fan was stalling at an earlier point than in clean flow, due to the tip flow not being able to recover from distortion initiated disturbances.

Recent experimental tests carried out at NASA have demonstrated a similar behaviour in relation to the transonic blade (Arend, et al., 2017). As the blade moves in and out of distortion, flow disturbances occur locally, but the flow recovers as the blade leaves the counter-swirl region and enters the high momentum flow (Cousins, et al., 2017). The measured fan map in Figure 2.23 shows that there is significant stability margin. At design speed, the fan experiences flutter before stall, which was not predicted in CFD because of the numerical method failing before the point at which flutter occurred (Bakhle, et al., 2018).

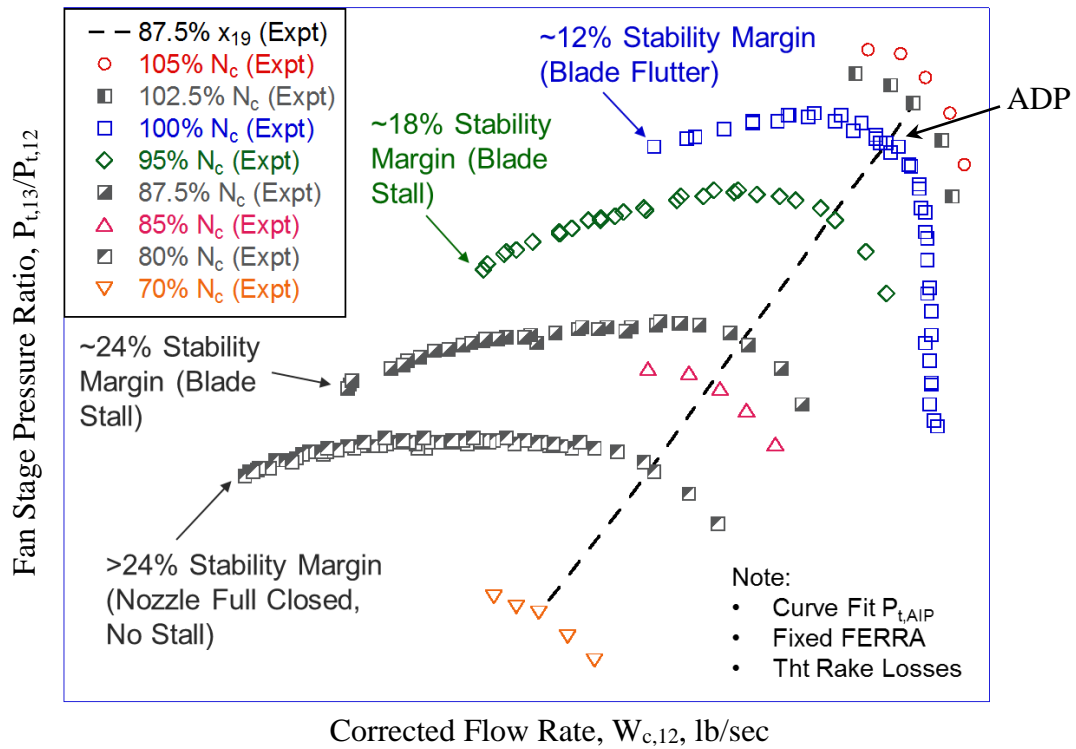


Figure 2.23 – BLI²DTF propulsor preliminary nominal operating map (Arend, et al., 2017)

## 2.5 Summary

High cycle fatigue is a key concern for BLI fans. Previous work has shown that distortion causes significant forcing at low EOs. Excessive dynamic stresses due to forced response have been successfully reduced by applying several design modifications including blade thickening at the root, but the resulting impact of a robust blade on the aerodynamic performance is unknown.

The work and loss in a BLI fan depend on 3D flows including radius changes in the rotor. The tip flow is also shown to be critical and experiences circumferential variations in loss that are too large. Further research is needed to understand the impact of radial work distribution on performance in distortion combined with reduced tip loading.

Previous work has shown that the stability margin is not affected significantly in BLI flows, even when there are regions of flow that locally operate beyond the clean flow stability limit. The mechanism is not yet well understood, and further research is needed to explain the reasons why the impact on stability is small.

# Chapter 3

## Research Methods

This chapter describes the fan test cases used for the research: a low-speed rig fan and a transonic fan. The steady and unsteady experimental methods are presented, as well as the design methods employed for modifying fan geometry and the CFD techniques.

### 3.1 Test Cases

The two test cases are a low speed fan rig, called the BLI rig (Gunn & Hall, 2014), and a transonic fan, called VITAL (Kyprianidis, et al., 2009). The two designs are similar in the sense that they are both low hub-to-tip ratio fans with comparable design parameters. The major difference is the Mach number, since the BLI rig fan is low speed. Another difference is an order of magnitude lower Reynolds number in the BLI rig. The main parameters are given in Table 3.1.

	BLI rig	VITAL
Tip relative Mach number, $M_{rel}$	0.13	1.25
Reynolds number, $Re = \rho V_{3,rel} c / \mu$	$2 \times 10^5$	$2.3 \times 10^6$
Hub-to-tip ratio	0.30	0.33
Design flow coefficient, $\phi = V_x / U_{mid}$	0.50	0.65
Stage loading, $\psi$	0.47	0.48
Reaction, $\lambda$	0.78	0.74
Running tip clearance (% span)	0.50	0.20

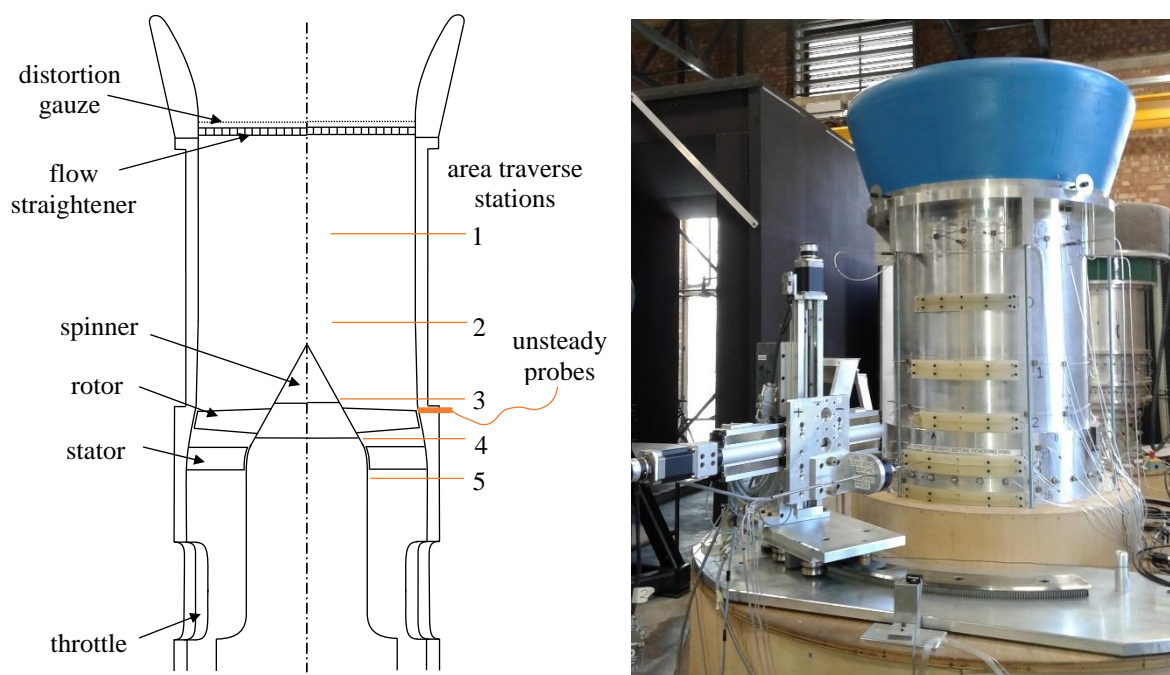
*Table 3.1 - BLI rig fan and VITAL fan design parameters*

The BLI rig allowed experiments and CFD to be carried out to find how a low speed fan responds to a representative BLI inlet stagnation pressure profile. A redesign of the rotor blade was carried out and the new rotor was installed and tested. The focus of the redesign was to understand the impact of rotor design changes on aerodynamic performance and stability. On the other hand, the VITAL fan, a representative low pressure ratio transonic fan, was used to study the impact of implementing necessary mechanical design changes on aerodynamics. The VITAL fan is only used in CFD simulations.

## 3.2 Low-Speed BLI Rig Fan

### 3.2.1 The Rig

The BLI rig was purpose built to study fan-distortion interaction in a BLI type flow field. It is a low hub-to-tip ratio, low Mach number fan rig. A schematic of the BLI rig is shown in Figure 3.1. It is a vertical rig which features a flow straightener at the inlet, a non-rotating spinner ahead of the rotor bladerow, followed by a stator bladerow. A distortion gauze can be placed on top of the flow straightener to create a non-uniform stagnation pressure drop and produce the required inlet stagnation pressure profile. The operating point is set by adjusting a variable area throttle at the outlet, hence controlling the mass flow rate through the rig.



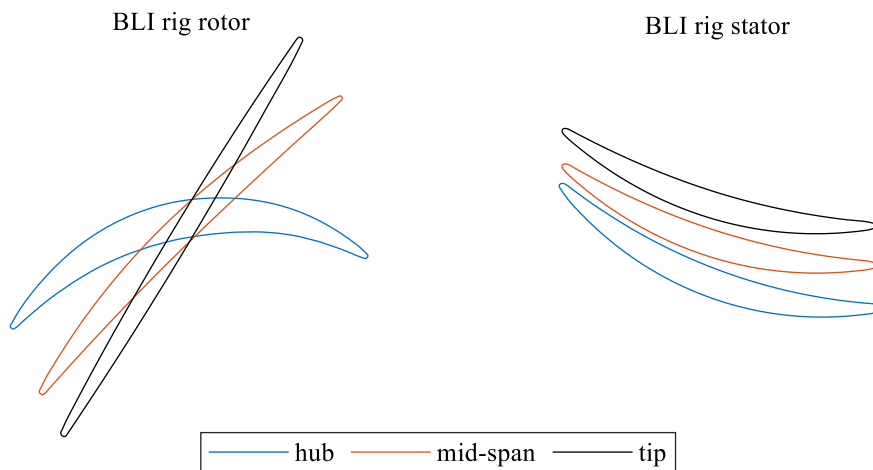
Circumferentially distributed unsteady probes



Figure 3.1 - BLI rig schematic and a photo of the rig (above), location of the unsteady probes (below)

The baseline rotor blade design is highly twisted and has sections similar to a conventional fan, varying from highly cambered hub sections to un-cambered tip sections, as shown in Figure 3.2. The section stacking is radial. Turning at the tip is achieved by running at an incidence of approximately  $5^\circ$ .

The baseline stator blades have a relatively constant cross section across their span, as shown in Figure 3.2. The sections are stacked with a  $6^\circ$  lean, pressure side facing the hub. The stator has a hub gap, which is different to actual fans in which stator blades are built in both endwalls. Both the rotor and the stator blade sections are circular arc. A new non-axisymmetric stator was designed in a previous PhD that used the same rig (Gunn & Hall, 2017). The stator blades were individually tailored to local conditions to reduce losses. The original axisymmetric stator is used in this research.



*Figure 3.2 – BLI rig rotor and stator sections*

The BLI type distortion which mimics flow conditions at the middle engine of **SAX-40** was achieved by placing a non-uniform porosity gauze at the inlet, as shown in Figure 3.3. For a given thickness, the drop in stagnation pressure was a function of the gauze solidity (fraction of the area that is blocked), which could be manipulated such that the desired stagnation pressure profile was achieved. The gauze was designed and printed on a 3D printer in the previous PhD (Gunn, 2015). The measured stagnation pressure profile at station 1 matched the target profile from (Madani & Hynes, 2009). The measured velocity distribution at the same station is shown in Figure 3.4. The measurement procedure is described in the following section.

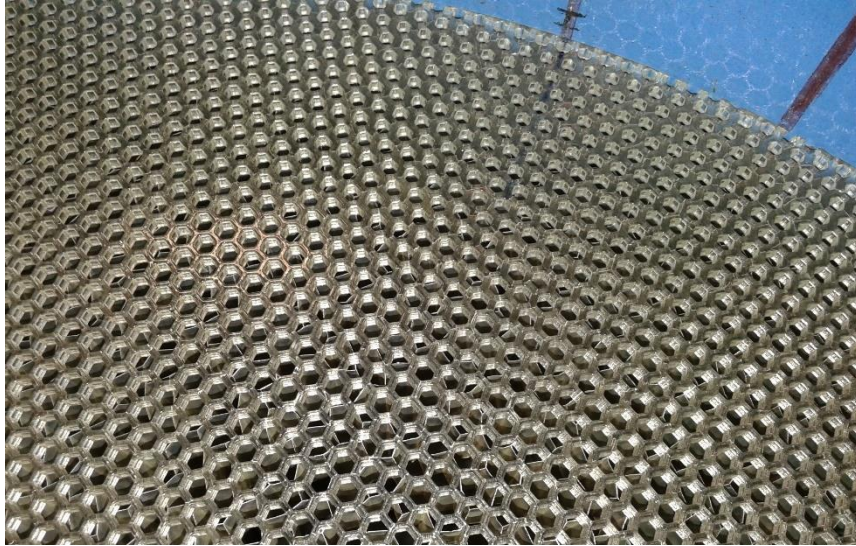


Figure 3.3 - Distortion gauze at the inlet of the BLI rig, placed on top of the flow straightener

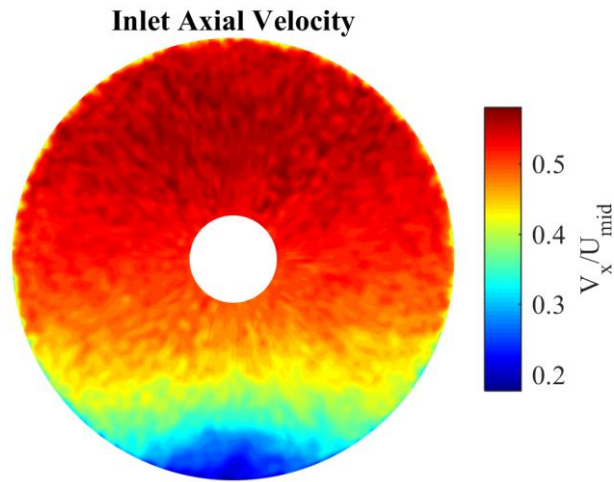


Figure 3.4 - Inlet boundary condition - measured axial velocity

### 3.2.2 Steady Measurements

Five traverse slots exist in the rig casing at different axial locations. The slots are numbered as shown in Figure 3.1. Measurements of the steady flow field in the BLI fan rig were taken using a 5-hole probe. The probe was mounted onto a stepper motor which enabled automatic traversing. While measurements were being taken at one slot, the other four were flush sealed and a plastic strip slid along with the probe to seal the currently used slot. The steady traverses of the flow field were carried out using the stepper motor which allowed traversing of  $1/10^{\text{th}}$  of the circumference, i.e. a  $36^\circ$  sector. To traverse the entire annulus in BLI flow, the distortion gauze needed to be rotated relative to the traverse area. The inner radius could not be reached by the probe at stations 1 and 2. This is not the case at stations 3-5, where the probe reached all the way to the hub.

A standard 5-hole probe was used for taking the measurements. The five holes measure pressures from which the stagnation pressure, dynamic head and flow angles were found. The atmospheric pressure and temperature were recorded simultaneously. Assuming incompressible flow, work input and efficiency could be calculated from these measurements.

Detailed flow field measurements were used to calculate one dimensional parameters in distorted flow: flow coefficient, stage loading and efficiency. These parameters could be calculated from the averaged flow variables. The variables were mass or area averaged, as appropriate. The reasoning behind opting for mass or area averaging is as described in (Cumpsty & Horlock, 2006). The flow coefficient was defined as:

$$\phi = \frac{\dot{m}}{\rho A_1 \bar{U}} \quad (3.1)$$

Stage loading was calculated from Euler's equation:

$$\psi = \frac{h_{04} - h_{03}}{\bar{U}^2} = \frac{\Omega((\overline{rV_\theta})_4 - (\overline{rV_\theta})_3)}{\bar{U}^2} \quad (3.2)$$

Isentropic total-to-total and total-to-static efficiency could be calculated from the expressions:

$$\eta_{tt} = \frac{h_{0s,st} - h_{03}}{h_{0,st} - h_{03}} = \frac{(p_{0,st} - p_{03}) / \rho}{\Omega((\overline{rV_\theta})_4 - (\overline{rV_\theta})_3)}, \quad \eta_{ts} = \frac{(p_{st} - p_{03}) / \rho}{\Omega((\overline{rV_\theta})_4 - (\overline{rV_\theta})_3)} \quad (3.3)$$

The subscript *st* is used to indicate whether the value is for the rotor or the stage. Measurements at station 4 are used to calculate the rotor performance, while *st* 5 corresponds to the stage performance.

The total-to-total and total-to-static pressure rise are calculated from the expressions:

$$\psi_{tt} = \frac{p_{0,st} - p_{03}}{\frac{1}{2} \rho \bar{U}^2}, \quad \psi_{ts} = \frac{p_{st} - p_{03}}{\frac{1}{2} \rho \bar{U}^2} \quad (3.4)$$

### 3.2.3 Unsteady Measurements

Disturbances that are created during stall inception events can be captured using high frequency response pressure probes flush mounted in the casing just upstream of the rotor leading edge. For this purpose, 18 high-frequency probes were placed around the circumference at a spacing of 20°, as shown in Figure 3.1. The baseline rotor geometry was modified during the PhD, and



stagger at the tip was reduced, as described in section 5.1.1. Consequently, the probes were located further away from the redesign rotor LE, as shown in Figure 3.5. The distance of the blade leading edge from the probes was 10% of the axial chord with the baseline blade and 17.5% with the redesigned blade.

The probes measured differential pressure, relative to the atmospheric value. The measurement apparatus is shown in Figure 3.5. The measured analogue signal is low pass filtered using the amplifier's in-built filter at the frequency of 10kHz, which is 16.7 times the blade passing frequency,  $f_{bp}$ , when the rig is running at 1800rpm in order to avoid aliasing. According to the Nyquist theorem, the signal should be sampled at least at twice the filtering frequency. Sampling was initially conducted at 30kHz, or  $50f_{bp}$ , while some later measurements were sampled at 60kHz, or  $100f_{bp}$ . The measured signals were amplified and recorded on a PC, using LabVIEW (LabVIEW, 2013). Probe calibration data was provided by the manufacturer and the appropriate sensitivity values were set on the amplifiers.

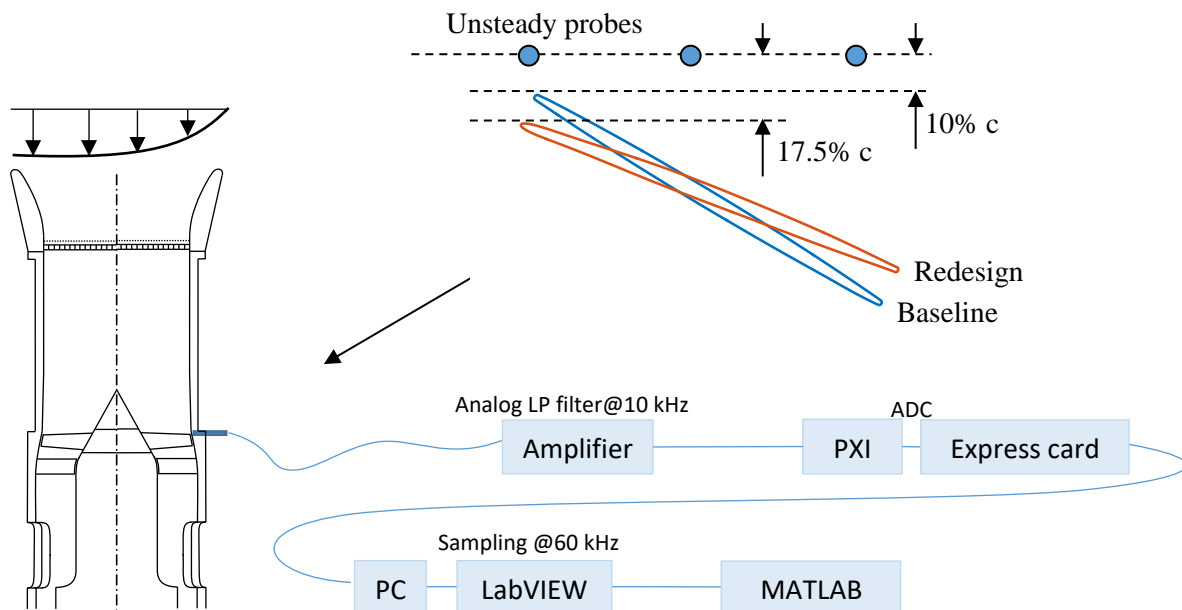


Figure 3.5 – Unsteady measurements setup

Unsteady casing static pressure measurements were taken both at steady operating points, the design point (DP) and near the stall point (NS), and during stall inception events. These operating conditions are shown in Figure 3.6. At stable operating points, the throttle was set to a desired position and the probe signals were recorded. To capture a stall event, the throttle setting had to be changed from a near stall stable operating point setting. Two approaches were used. One way, *si-I*, was to close the throttle just slightly while the signal was recorded, which



triggered stall inception. This ensures that a stall event was recorded each time. Another approach, *si-2*, was to close the throttle by a very small amount using a lever. The rig continued to run without stalling with the operating point very close to instability and eventually fell into stall on its own. The amount of time taken for the stall to initiate was unpredictable. The rate of success of capturing a stall event in this way was only around 10%. Most of the stall events were therefore recorded using approach *si-1*. The results presented in Chapter 6 showed that there was no difference between the two approaches.

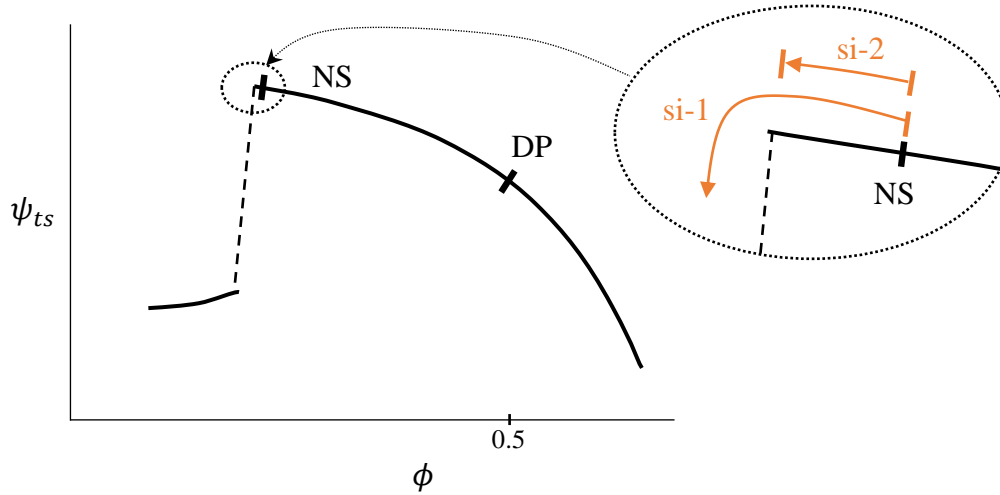


Figure 3.6 - Capturing stall inception events: by closing the throttle slightly to initiate stall (*si-1*), or by closing the throttle very little to bring it to a point which is on the very limit of stability, then waiting for stall to occur on its own (*si-2*)

One way of visualising the measured data is by plotting pressure waveforms. Signals are plotted on the same time axis and the pressure fluctuation is shown on the y-axis. There is offset between signals measured at different circumferential locations. Disturbance propagation can be tracked on such a plot by identifying features that appear in any one signal and then appear at a consecutive location at a later time.

Increased signal unsteadiness leads to frequency content at frequencies other than the harmonic frequencies. A way to quantify this level of disturbance is to calculate the power of the signal contained at these frequencies. The power of the signal in a range of frequencies  $[f_1, f_2]$  can be calculated as:

$$\Delta E(f_1, f_2) = \int_{f_1}^{f_2} |\hat{p}(f)|^2 df \quad (3.5)$$

where  $|\hat{p}(f)|^2$  is the energy spectral density, and  $\hat{p}(f)$  is the Fourier transform of pressure  $p$ :

$$\hat{p}(f) = \int_{-\infty}^{\infty} e^{-2\pi i f t} p(t) dt \quad (3.6)$$

The total power of the signal in a certain frequency range is referred to as disturbance energy,  $E$ , in this thesis.

### 3.2.4 Blade Redesign

The aim of the redesign of the low speed fan rotor was to modify the design for aerodynamic reasons, which included modification of blade angles and a change in positions of the maximum camber and thickness, as described in section 5.1.1. The section redesign was carried out using the Shape Space Method, described in section 3.6. The sections were parameterised and then modified. The original low-speed rotor sections had a circular arc design. Therefore, the thickness and camber distributions were symmetric about the mid chord. This was skewed to move the position of maximum camber and thickness. It was done in a consistent way to ensure that the shape was smooth after the sections were blended together. The required changes in blade angles were then applied.

## 3.3 Transonic VITAL Fan

### 3.3.1 The VITAL Fan Geometry

The VITAL fan was designed in the EnVIronmenTALly Friendly Aero Engine project (VITAL), a 4 year project which started in 2005 (Korsia, 2007). The project aimed at designing fan architecture for achieving ambitious fuel burn and noise reduction targets. The VITAL fan is a transonic, low pressure ratio fan, developed for use in a high bypass ratio fan system. The rig fan was built and tested at the AneCom AeroTest facility in Germany. The test fan, shown in Figure 3.7, is approximately 1/3 of the engine fan scale.

Photo of VITAL fan removed for copyright reasons.  
Copyright holder is ASME.

*Figure 3.7 - VITAL fan in the test rig (Kim, et al., 2018)*

The stage consists of spinner, followed by a rotor bladerow, after which the splitter separates the flow into the bypass and core flows, as shown in the meridional view of the computational domain in Figure 3.8. The mass flow rate through the ESS is fixed by placing a choked nozzle downstream, which mimics the steep characteristic of the core compressor. The OGV is also followed by a convergent nozzle. The details of the computational setup are discussed in section 3.4.

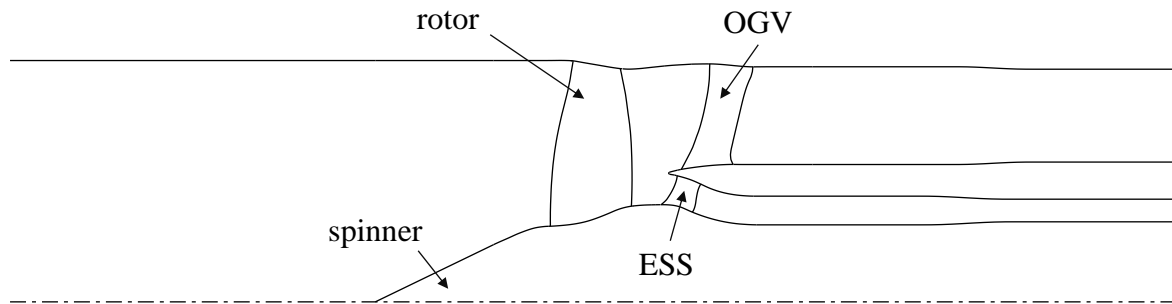


*Figure 3.8 – Meridional view of VITAL fan computational domain*

### 3.3.2 Design Modifications

A CAD model of the VITAL fan blade was provided by Rolls-Royce plc. The model contains the aero part of the blade as well as the part of the blade below the annulus line and the root, as shown in Figure 3.9. For the purposes of work presented in Chapter 4, the blade sections had to be thickened in a consistent way across the span. The Shape Space method, described in section 3.6, works with aerofoil shapes. However, the part of the blade below the annulus line is not an aerofoil.

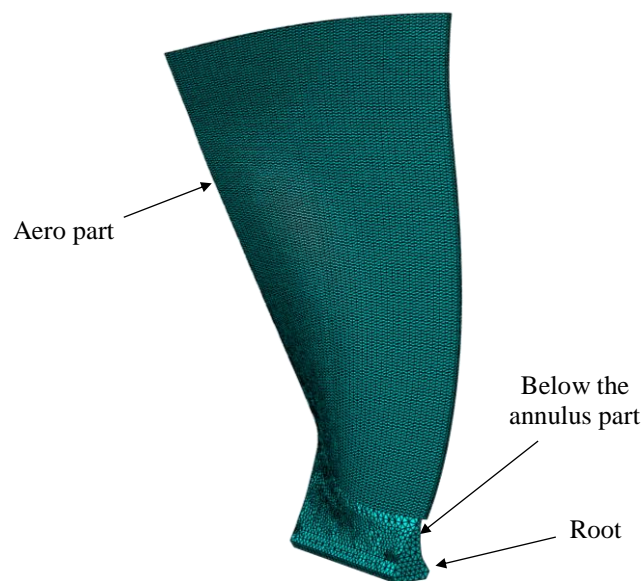


*Figure 3.9 - Meshed VITAL fan blade*

To modify the shape, several sections across the span were extracted from the CAD model. The sections below the annulus line were modified into aerofoils by adding artificial leading and trailing edges. The sections were then modified using the Shape Space method. The sections below the annulus were then cropped to their original shape and blended together in CAD to form the new blade. The root was modelled and modified in CAD.

### **3.3.3 FEA Modal Analysis**

The modal analysis was carried out in commercial software Abaqus (Abaqus, 2012). The CAD model of the blade was imported and meshed using the Abaqus automatic mesher. The resulting mesh has around  $10^4$  tetrahedral elements. The blade was modelled as the rigid solid Ti-alloy blade.

Blade only modes are found by running a modal analysis. No attempt was made to find modes with different nodal diameters. The boundary condition imposed constrained the top part of the root to move in the perpendicular direction or axially, which was the only imposed constraint.

The centrifugal load was applied and the resulting deflected shape was kept as an input for the modal analysis. No pressure loads were included in the model. The modal analysis was repeated for various rotational speeds. Natural frequencies were obtained in each case. This approach allowed for the Campbell diagram to be constructed. The modification procedure and construction of the Campbell diagrams is further discussed in section 4.3.

## **3.4 Computational Fluid Dynamics Methods**

### **3.4.1 Solver**

The solver used in this research was called Turbostream (Brandvik & Pullan, 2011) and was based on John Denton's TBLOCK code (Denton, 1983). Turbostream runs on GPU clusters and the high degree of parallelisation allows speed up by a factor of 10 compared to codes running on CPU clusters (Brandvik & Pullan, 2010). The solver works with multi-block structured meshes. It allows several turbulence models to be used. In this work Spalart-Allmaras' single equation turbulence model was used (Spalart & Allmaras, 1992). Flow is allowed to slip at solid walls so that high grid resolution is not required in the boundary layers and the non-dimensional wall distance is set to  $y_+ = 5$ . The validation was carried out in the previous PhD (Gunn, 2015). Due to similarity with the cases run in that work, it was unnecessary to repeat the validation procedure.

### 3.4.2 Steady and Unsteady Computations

Steady CFD was used to run the clean flow cases. The flow is passed between the rotating and stationary blocks through a mixing plane, i.e. the downstream stator did not see the rotor wakes, but observed an averaged-out radial profile at all circumferential locations. This meant that some aspects of the unsteady fluid mechanics were lost. However, this approach is frequently used due to its low computational cost and the short time required to run the simulation.

Steady calculations are not appropriate for BLI flow field simulation, since the distortion would be mixed out. Therefore, full annulus unsteady CFD is needed. Running a BLI case requires non-axisymmetric inlet boundary conditions to be set, and the distortion seen by the rotor is not stationary in the rotor frame of reference.

The method used for unsteady CFD is the dual-stepping technique described in (Jameson, 1991). The solution procedure consists of outer and inner time steps. The outer time steps are physical time steps. After each physical time step is made, the solver runs through inner time steps to converge the solution. The number of outer time steps used in both of the test cases is 2880 per rotor revolution. This corresponds to 144 and 160 time steps per rotor blade pitch in the BLI rig and VITAL fans respectively. This time resolution is sufficient for resolving frequencies of interest in BLI distortion-fan interaction.

The CFD runs were deemed converged once the flow coefficient, pressure rise coefficient and isentropic efficiency values averaged over one revolution did not change with time, to the fourth significant digit. The steady calculations were typically run for 200,000 steps, which was more than necessary. However, the clean flow cases were run for this number of steps for convenience since the steady runs were not computationally expensive, providing firm confirmation of whether a solution was diverging without any need for further runs.

### 3.4.3 Domains

The inlet of the BLI rig CFD domain is at the axial location of the traverse station 1 (see Figure 3.1). The domain is shown in Figure 3.10. It includes the rotor and the stator blade-rows, with the hub and casing lines matching the rig geometry. The rotor tip gap and stator hub gap are represented accurately, as well as the rotor blade fillets. One difference is the outlet where the throttle is not modelled. There is a converging nozzle instead and the operating point is set by changing the back pressure, as described in section 3.4.5.

The VITAL fan domain is also shown in Figure 3.10. The inlet is located one rotor diameter upstream of the rotor leading edge. The bypass duct and the core flow path are represented. The meridional view of the domain is shown in Figure 3.8.

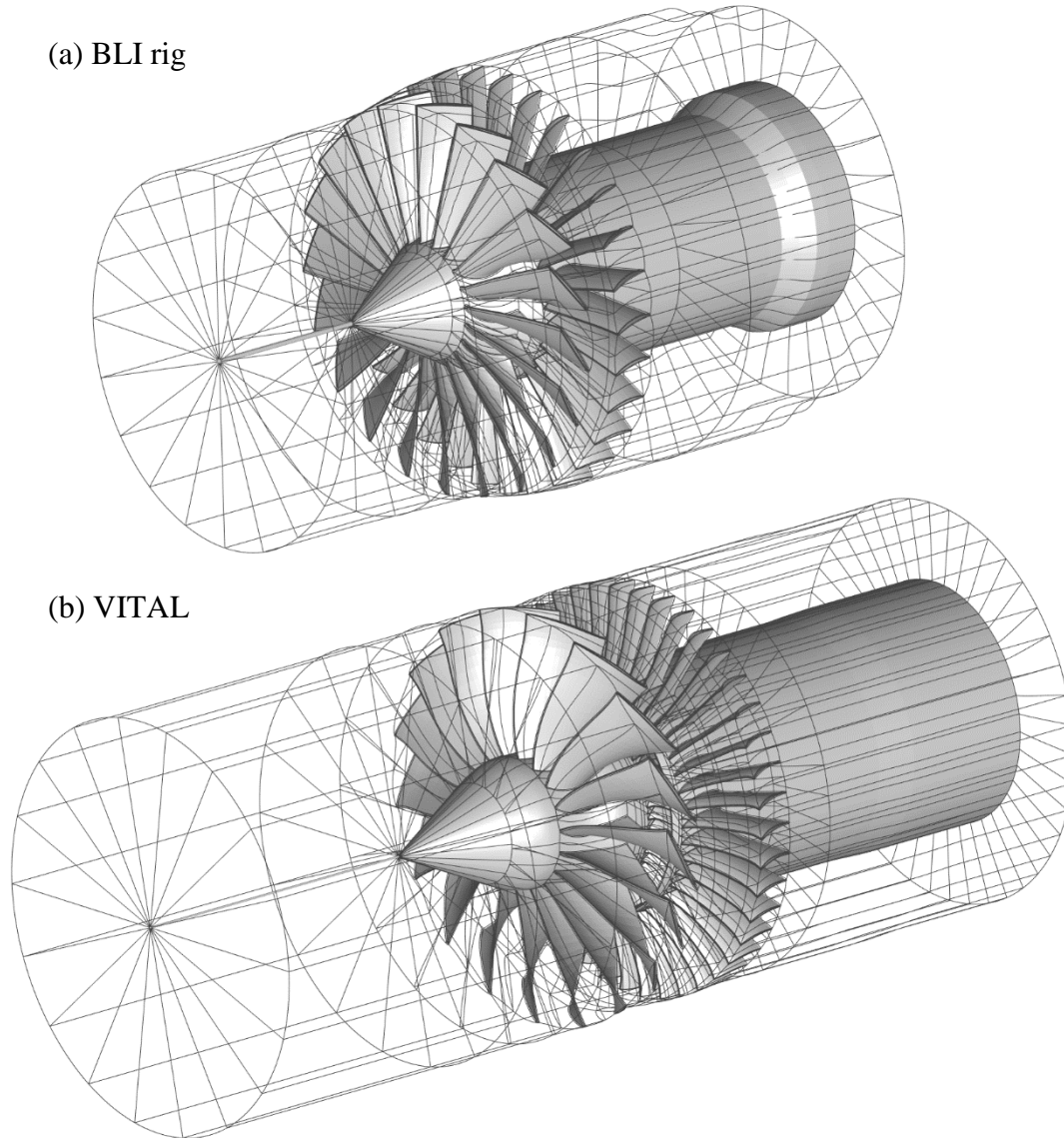


*Figure 3.10 - Computational domains: (a) BLI rig, (b) VITAL fan*

The rotor tip gap is represented, while the stator blades in the bypass and the ESS are built in the wall, as is conventional in real fans. The bypass duct outlet is a convergent nozzle, with the area ratio lower than in the BLI rig domain. This is to avoid possible choking. The core flow path ends with a choked convergent nozzle. The location of the nozzle is approximately coincident with the inlet to the intermediate pressure compressor.

### 3.4.4 Mesh

Meshing was done using PADRAM (Milli & Shahpar, 2012). An “HOH” topology was used, with O-blocks surrounding each blade. The non-dimensional wall distance was set to  $y_+ = 5$  on all solid surfaces. The rotor and the stator meshes were generated in PADRAM, while the inlet and outlet meshes were generated manually in MATLAB. The blade row mesh has larger mesh density in the circumferential direction compared to the upstream and downstream meshes.

The mesh at the tip of the BLI rig is shown in Figure 3.11. The total number of mesh points in the domain is 83.3 million. There are approximately 120 radial points in both the BLI rig and VITAL meshes, which was chosen due to the importance of resolving the radial flows. The number of points on each rotor blade section of both fans is approximately 190, while there are approximately 170 points around each section of the BLI rig stators and OGV and ESS sections in the VITAL fan. There are 11 points in all the tip gaps in both fans and also 11 points in the hub gap of the BLI rig stator. A sensitivity analysis was carried out in the early stages of this work to investigate the effect of increasing the number of points in the tip gap. No significant difference was observed between using fewer or more points in the tip gap, up to a maximum of 16 points, so the original number of 11 points was kept.

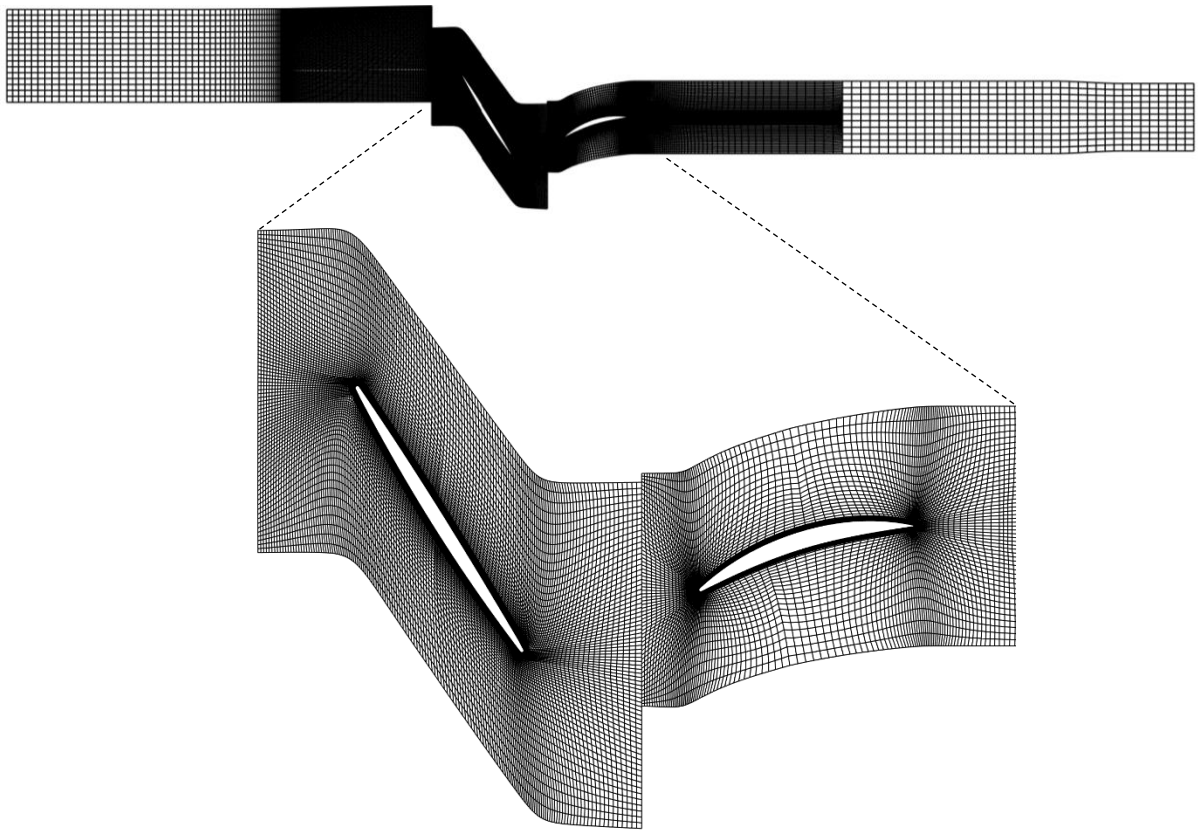


*Figure 3.11 - BLI rig mesh at a radius close to the casing*

A detailed grid dependency study was carried out by (Jerez Fidalgo, 2012) on a transonic fan geometry similar to VITAL fan. The same turbulence model and wall function approach were used. Findings from that work were used in (Gunn, 2015) to create meshes for the BLI rig and VITAL fans. The same grids were used in this work with the baseline blade geometries, while redesign blade meshes were created using the same methods and keeping the same number of grid points as in the respective baseline cases. The total number of grid points is shown in Table 3.2. The grid density was four times the size found to be necessary by Jerez Fidalgo for grid independence in clean flow. One of differences was the stator grid density which was refined compared to that used by Jerez Fidalgo. The main difference compared to typical CFD meshes was the higher number of radial grid points, which were used due to the importance of resolving radial flows away from the endwalls in BLI.

<b>Region</b>	<b>BLI rig mesh nodes (mil.)</b>		<b>VITAL mesh nodes (mil.)</b>	
	<b>Single passage</b>	<b>Full annulus</b>	<b>Single passage</b>	<b>Full annulus</b>
Inlet, spinner	0.58	11.6	0.40	7.29
Rotor	1.66	33.1	2.38	42.86
Stator/OGV	1.25	37.4	0.82	34.56
ESS			0.37	16.32
Exhaust	0.06	1.17	0.04	1.68
Exhaust ESS			0.02	16.32
<b>Total</b>		<b>83.3</b>		<b>101.03</b>

*Table 3.2 - Mesh size breakdown*

### 3.4.5 Boundary Conditions and Validation

The inlet boundary condition for simulating the BLI flow field is taken from (Madani & Hynes, 2009). The stagnation pressure profile was initially used on the BLI rig simulations and experiments. The experimentally measured stagnation pressure profile from the BLI rig was scaled to the transonic Mach numbers experienced in VITAL, as described in (Gunn, 2015). The stagnation pressure profile is shown in Figure 3.12. In the BLI rig, inlet flow angles are set to the experimentally measured values, which are almost negligible. In the VITAL fan case, the inlet flow angles are all set to zero.

The usual approach for setting the mass flow is either to change the contraction of a downstream nozzle, which is the approach typically used in research on stall (Vahdati, et al., 2005), or to set the back pressure. In this work, the back pressure approach was used. The value of the static pressure at the hub was set, and then radial equilibrium was applied by the solver



to set the radial profile. This was used in the BLI rig case and in the bypass duct of VITAL fan. The nozzle at the exhaust of the core section in VITAL fan was choked to mimic the steep characteristic of the core compressor. This was achieved by setting the back pressure to a very low value.

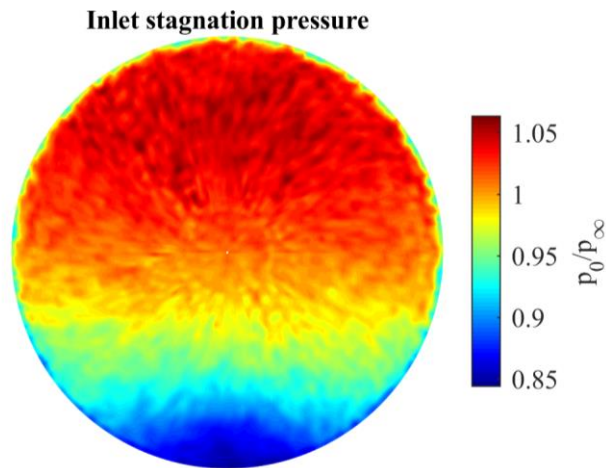


Figure 3.12 – VITAL inlet boundary condition - stagnation pressure profile

The performance parameters in the BLI rig computations were calculated in the same way as in experiment, as in equations (3.1), (3.2), (3.3), and (3.4). Discrepancy between calculating them in this way and from compressible flow relations was found to be negligible for the BLI fan rig (Gunn, 2015). Compressible flow relations were used for VITAL fan calculations.

Validation of VITAL fan CFD was carried out in the previous PhD (Gunn, 2015). A comparison of steady CFD against the unpublished measurement data at design speed in clean flow and the reference CFD case obtained from Rolls-Royce plc. is shown in Figure 3.13. The measurement data was available for the rotor only. The figure shows that the stall point was overpredicted, but this was not investigated further since the main focus was on the design operating point. Choking mass flow rate and the shape of the rotor pressure rise characteristic were both predicted well, but there was an overprediction of rotor efficiency by approximately 1%. Unsteady CFD was also run at two operating points, a choking point and a point on the working line. The estimate of rotor efficiency was slightly improved, by approximately 0.5%, while the differences in the pressure rise and choking mass flow rate were minor. The same setup was used in runs presented in this thesis.

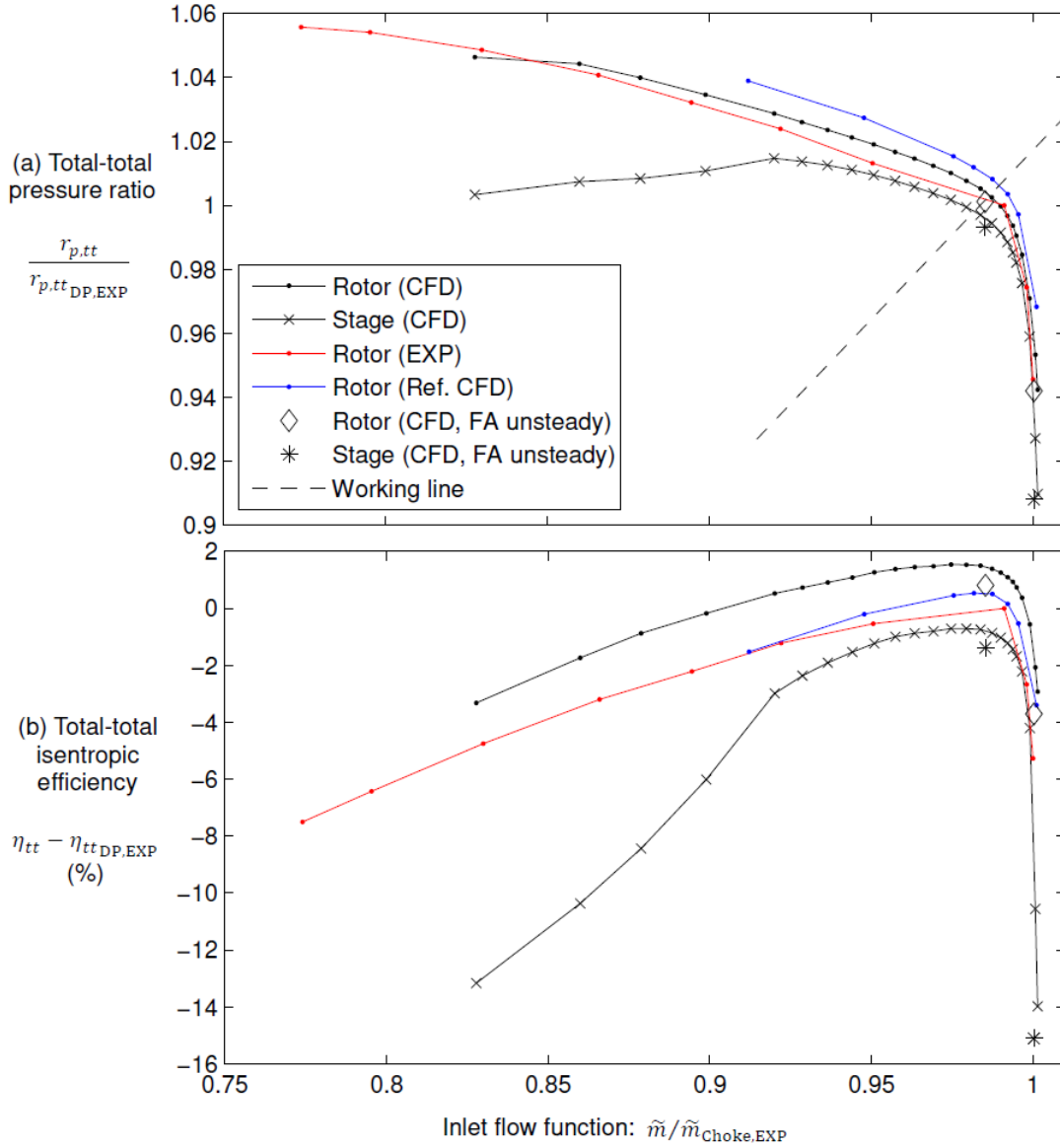


Figure 3.13 – Measured and computed clean flow characteristics for the VITAL fan at design speed (Gunn, 2015)

### 3.5 Sign Convention

The sign convention is shown in Figure 3.14. Blade rotation is clockwise, looking upstream, and the circumferential angle  $\theta$  is defined as positive in the direction of blade rotation. In clean flow, position of  $\theta = 0$  is arbitrary, so  $\theta$  is defined relative to the traverse slot, with zero being at the angular position corresponding to the centres of the traverse slots. In distortion,  $\theta$  is specified relative to distortion, with the zero being the bottom location, in the low momentum region.

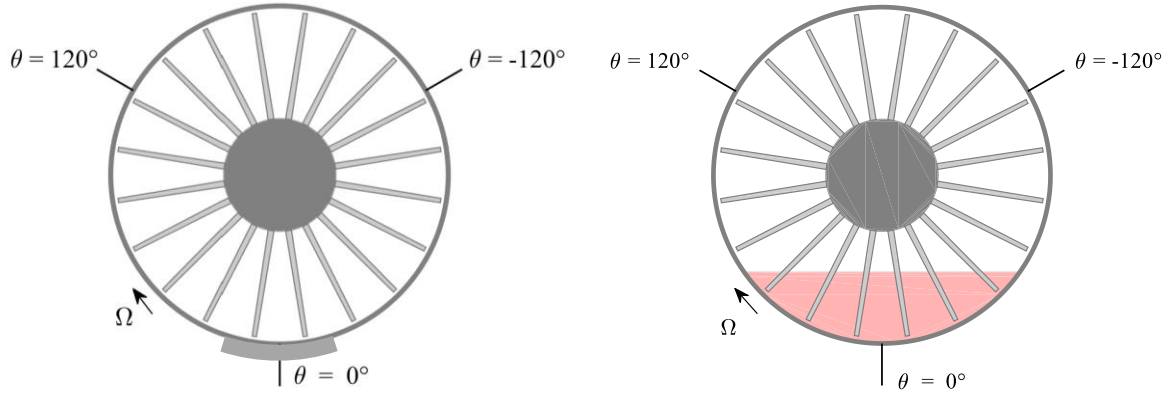


Figure 3.14 – Circumferential location sign convention in clean flow (left) and distorted flow (right). Coloured part denotes distorted flow.

### 3.6 Shape Space Method for Modifying Rotor Blade Design

A method to parameterize and modify aerofoils developed by Boeing (Kulfan, 2008), called Shape Space, was used for modifying baseline blade geometry. The method was implemented in MATLAB as described in (Lane & Marshall, 2010) by Tim Williams during his work on reversed thrust aerodynamics (Williams & Hall, 2018). This code was adapted for the purposes of altering the BLI rig rotor and VITIAL fan rotor geometries.

The method is based on representing either: i) the pressure side (PS) and the suction side (SS) curves, or ii) thickness and camber curves. In the current work, thickness and camber representation were used. Typical thickness and camber distributions of a turbomachinery blade section are shown in Figure 3.15.

The curves are represented in Shape Space by the following equation:

$$\frac{z}{c} = C\left(\frac{x}{c}\right)S\left(\frac{x}{c}\right) + \frac{x}{c}\frac{\Delta z_{TE}}{c} = f\left(\frac{x}{c}, \frac{\Delta z_{TE}}{c}\right) \quad (3.7)$$

The distribution  $z/c$  is obtained by multiplying the class function  $C$  with the shape function  $S$ , and then adding a term to account for non-zero thickness at the trailing edge. The non-zero trailing edge term is a linear function with a zero value at  $x = 0$  and a value at  $x = c$ . The class function and the shape function are then used to represent the remainder.

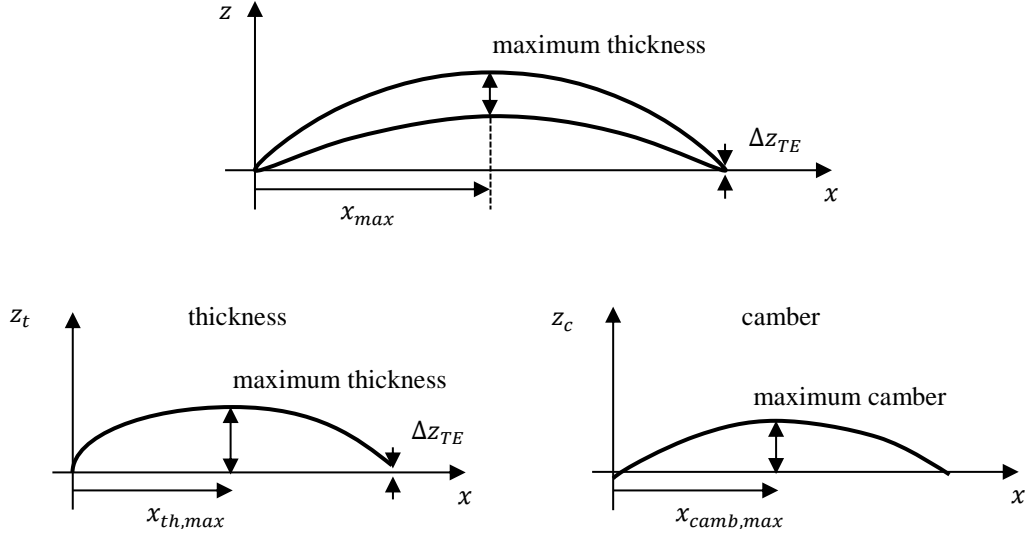


Figure 3.15 – Thickness and camber distributions for a BLI rig rotor blade section

The class function, shown in equation (3.8), ensures that the limits  $x \rightarrow 0$  and  $x \rightarrow c$  are correct. Values  $N_1$  and  $N_2$  set to control how the derivatives of the expression in eq. (3.7) behave in the vicinity of  $x = 0$  and  $x = c$ . For example, picking  $N_1 = 1/2$  for the thickness distribution curve ensures that the function behaves as a square root around  $x = 0$ . The main advantage of this representation is the derivative of the expression in equation (3.8) tends to zero as  $x$  tends to zero, for  $0 < N < 1$ . Similarly, a choice of  $N_1 = 1$  for the thickness distribution is appropriate for the linear behaviour of the camber distribution close to the LE.  $N_2$  is chosen in a similar way.

$$C\left(\frac{x}{c}\right) = \left(\frac{x}{c}\right)^{N_1} \left(1 - \frac{x}{c}\right)^{N_2} \quad (3.8)$$

The class function is multiplied by the shape function to give the overall shape of the camber and thickness distributions. It can be represented as any function. In this case, Bernstein polynomial representation in equation (3.9) is chosen for convenience, as the polynomial is very well behaved when its coefficients are changed. The order of the polynomial  $n$  can be set to any value. More details on the properties of the Bernstein polynomial are given in (Kulfan, 2008).

$$S\left(\frac{x}{c}\right) = \sum_{i=0}^n A_i \frac{n!}{i! (n-i)!} \left(\frac{x}{c}\right)^i \left(1 - \frac{x}{c}\right)^{n-i} \quad (3.9)$$

A Shape Space representation of a section is shown in Figure 3.16. The fine details of the LE and TE can be controlled, from matching the shape exactly to modifying it as desired. In this case, the LE radius was reduced and the fine details of the section geometry at the LE and TE are slightly different.

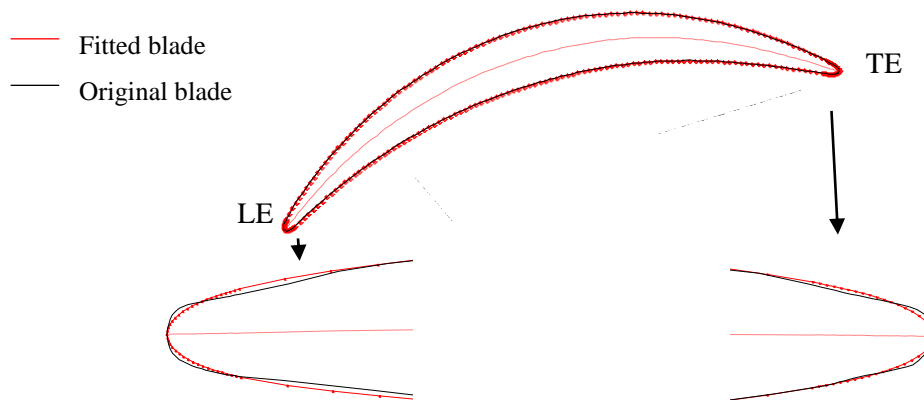


*Figure 3.16 – Shape Space representation of a blade section*

# Chapter 4

## Aeromechanical Redesign of a Transonic Fan for BLI

The aim of this chapter is to investigate the impact of blade strengthening on the aerodynamic performance of a transonic fan. The transonic, low pressure ratio VITAL fan, described in section 3.3, is used for this purpose.

The approach taken is to thicken up the blade to satisfy the frequency margin requirements between the 1F and 2F modes and low EOs, as specified by the industrial partner of the project, Rolls-Royce plc. The thickening up approach and subsequent modal analyses results are presented. The impact on aerodynamic performance of CFD simulations in clean and distorted flows carried out with baseline and redesign blades is analysed, followed by a detailed investigation of the flow field to identify which flow features are responsible for the change in performance.

### 4.1 Unsteady Forcing

Unsteady forcing arises due to non-uniformities in the flow. In transonic fans, the spacing between the OGVs and the rotor blades is relatively large for noise considerations (Calvert & Ginder, 1999), which means that the amplitude of the unsteady rotor forcing due to OGV and ESS potential fields is negligible, especially because it occurs at high EOs which correspond to the respective OGV and ESS blade counts. A major concern for fan aeromechanical stability are non-uniformities in inlets that arise due to high angle of attack or cross wind flow separations on the nacelle. The impact of this type of distortion is significant because it gives rise to low EO forcing, exciting low modes. This excitation can lead to high dynamic stresses and could potentially lead to failure due to high cycle fatigue (HCF).

The VITAL fan is mid-span loaded, as shown in Figure 4.1. In clean flow, the loading remains virtually constant as the blades move around the annulus, due to axisymmetric inlet flow conditions. Only a small variation in blade surface pressure distribution is expected due to interaction with the OGVs' potential field, leading to a small amplitude forcing at a high

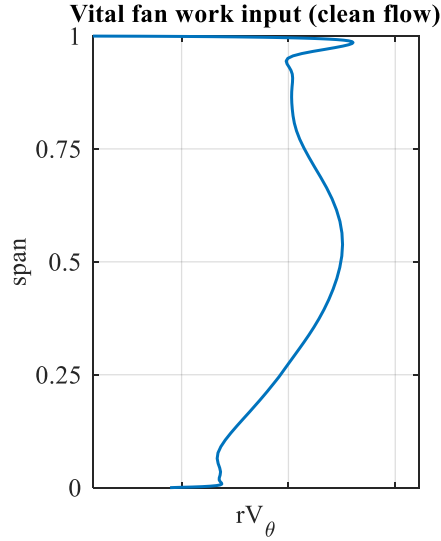


Figure 4.1 - VITAL fan radial work profile obtained from clean flow CFD at a peak efficiency point

harmonic corresponding to the number of OGVs. In BLI flow, distortion is continuously present, and it is not possible to avoid high amplitude low EO forcing.

The forcing is calculated from the unsteady blade surface pressure data extracted at each outer time-step during one rotor revolution of an unsteady CFD run at the design speed peak efficiency point (see Figure 4.13). The run was started from a fully converged case.

The pressure forces are calculated for each cell on the blade surface. For a cell shown in Figure 4.2, the pressure force is calculated as:

$$\mathbf{F} = - \sum_i \sum_j \frac{p_{i,j} + p_{i+1,j} + p_{i,j+1} + p_{i+1,j+1}}{4} \left( \frac{1}{2} \mathbf{d}_1 \times \mathbf{d}_2 \right) \quad (4.1)$$

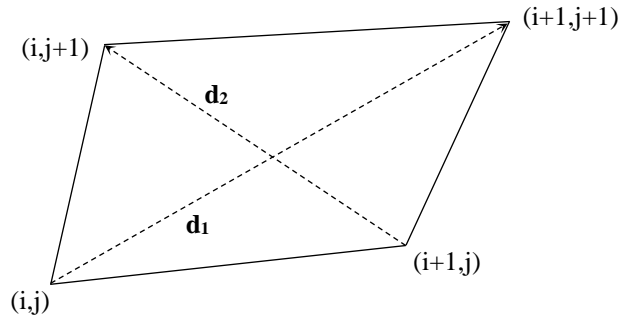


Figure 4.2 – A grid cell

The total force includes only pressure force contributions. An approximate method was developed to calculate the shear forces, but the shear force contribution to the total force was

found to be negligible. Pressure force summation is accurate since the surface pressures are not sensitive to the details of boundary layer development at design point in the computation.

The plot in Figure 4.3 shows how the forcing on a VITAL baseline rotor blade varies with time when operating in BLI flow. The axial and tangential components of the total force are shown in Figure 4.3. The mean value of axial component of the non-dimensional force coefficient is around 0.45, and the tangential component is around 20% higher. The plots show that the alternating components' peak to peak values are approximately 0.15. This is confirmed in the frequency domain, where the forcing content at the fundamental frequency is the most pronounced, with a magnitude of approximately 0.07. There is significant content at 2EO, constituting around 50% of that at 1EO. At 3EO and 4EO the magnitudes are approximately 10% of that at 1EO. Forcing is of the same order of magnitude as that experienced by the fan blades in BLI<sup>2</sup>DTF project (Bakhle, et al., 2014). An estimate of the forcing coefficient based on the data available in that and later publications (Provenza, et al., 2019) (Arend, et al., 2017), where the 22" rig fan was assumed to run at 200Hz, resulted in an estimate of the BLI<sup>2</sup>DTF fan

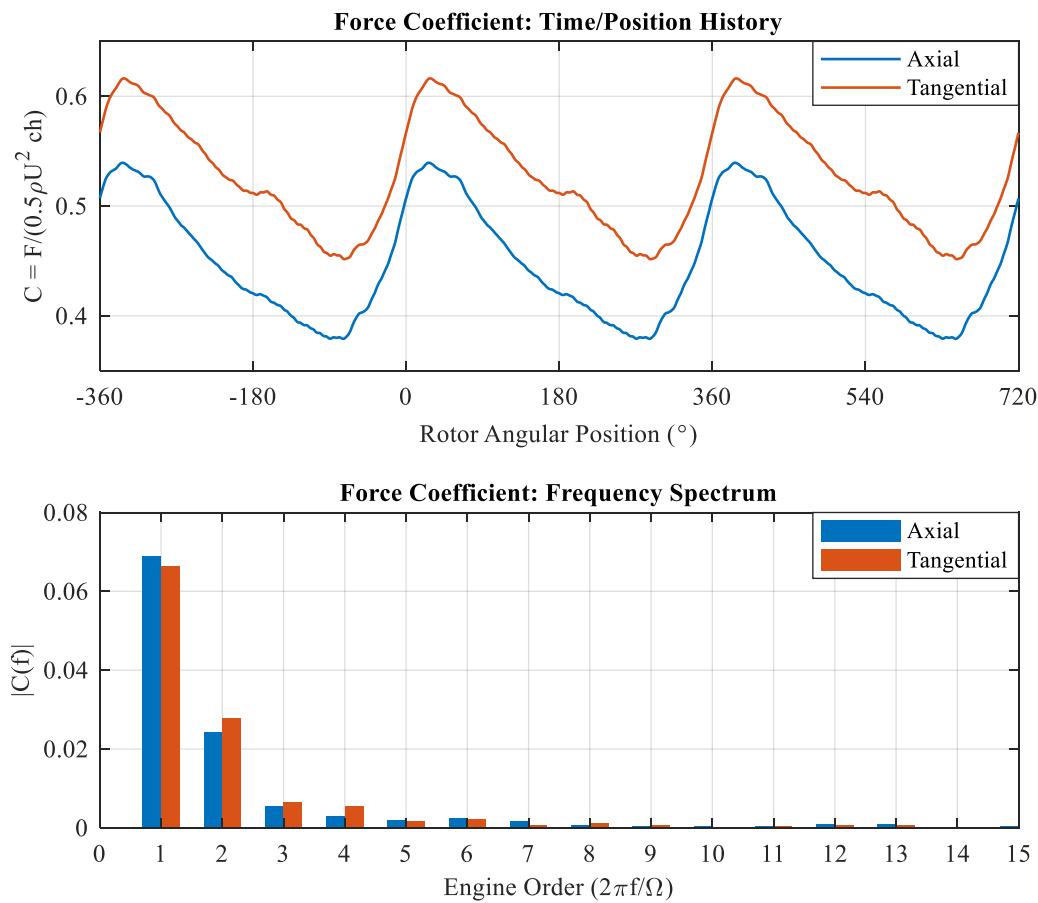


Figure 4.3 - Forcing variation on one of the blades, with baseline blade geometry. Time domain (above) and frequency spectrum (below)



1EO force coefficient of 0.02, which is of the same order of magnitude as the forcing calculated for the VITAL fan operating in the BLI flow field.

## 4.2 Aeromechanical Requirements for Operation in BLI

Requirements for the blade mechanical design for BLI were provided by the industrial partner of this project, Rolls-Royce plc. (Gonzalez-Gutierrez, 2015). The constraints that a mechanically robust blade needs to satisfy are shown in Table 4.1.

Aerodynamic design		
Blade loading	$\Delta h_0 / U_{tip}^2 < 0.3$	(criterion 1)
Mechanical design		
Forced response and HCF	1F-1EO margin 60%, i.e. $1F/1EO > 1.60$	(criterion 2)
	AF strength 1F mode – limit	(criterion 3)
Flutter	1F torsion content (see Figure 4.4) $\frac{c_{tip}\Theta}{H} / \frac{c_{tip}2\pi f_{1F}}{V_{1,rel}}$ – limit	(criterion 4)
	1F-1T frequency separation > 20%, i.e. $1T/1F > 1.20$ (at maximum mechanical speed)	(criterion 5)

Table 4.1 - Design criteria for distortion tolerant blade

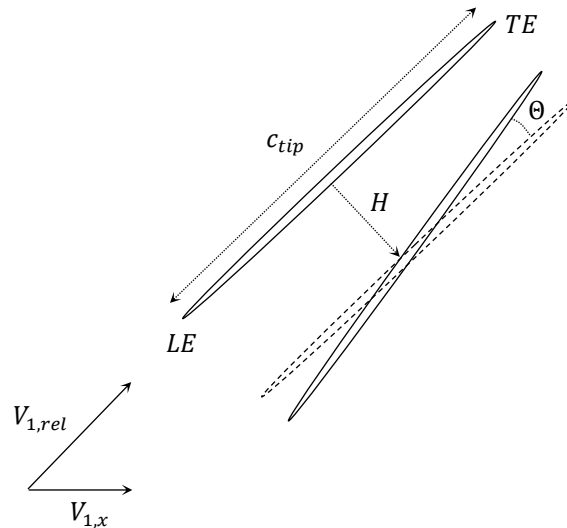


Figure 4.4 - Mode 1F tip deflection

The aerodynamic design criterion, criterion 1, is aimed at reducing the forcing amplitude. The lower the loading, the lower the dynamic stresses due to vibration. Typical loading in conventional transonic fans based on the tip rotor speed is around 0.35. In low pressure ratio fans such as VITAL, typical loading is in the order of 0.30. The VITAL fan loading is 0.31

based on the design tip speed (0.48 based on the speed at 70% span, see Table 3.1). Therefore, achieving this specification with a low pressure ratio BLI fan is not difficult.

On the mechanical side, two categories of criteria are specified: those concerned with forced response and HCF, and those concerned with flutter. The first mechanical criterion, criterion 2, specifies the required margin between the 1F mode and the 1EO. The typical 1F-1EO margin in conventional transonic fans is 10% (Provenza, et al., 2019), but high dynamic stresses in BLI due to 1F/1EO off-resonant response require a higher margin in BLI. The BLI<sup>2</sup>DTF blade has a 22.9% 1F-1EO margin, but it is unclear whether the frequency margin guideline used in conventional fan design needs to be increased for a distortion tolerant fan that operates continuously in BLI distortion (Provenza, et al., 2019). The value specified by Rolls-Royce is 60%, which is significantly higher than in conventional fans that operate in clean flow.

Increasing the 1F frequency is beneficial for two reasons. Firstly, the higher the separation, the lower the excitation due to 1EO forcing. Secondly, increasing the 1F frequency requires stiffening the blade at the root. Stiffening leads to smaller deflections and lower dynamic stresses due to 1F/1EO off-resonant response, improving fatigue life. However, this benefit can be realized up to a certain point because increasing the 1F frequency means that it approaches the 2EO, at which point there is also a high magnitude component of unsteady force. There is an optimal point in-between, at 60% as suggested by the design criterion.

The second mechanical criterion, criterion 3, is concerned with fatigue life. Limits on Rolls-Royce's Amplitude-Frequency AF level parameter, calculated by multiplying the maximum response displacement with the forcing frequency, can be set to ensure sufficient fatigue life. Calculating the AF level requires modelling blade response to forcing using an aeromechanics code, such as AU3D (Sayma, et al., 2000) as suggested by Rolls-Royce, but modelling the response was beyond the scope of the work in this thesis.

The flutter criteria, 4 and 5, set a limit on the maximum allowable torsional content in the 1F mode for a flutter free design and a limit on the 1F-1T frequency separation. When a highly twisted fan blade vibrates in the 1F mode, the tip experiences both translation and a certain degree of rotation. The larger the twist component in the 1F mode relative to the plunge component, the smaller the flutter margin. Criterion 4 sets the limit on the amount of twist content in the 1F mode. On the other hand, criterion 5 sets the limit on how close 1F and 1T come together at maximum mechanical speed. The 1T/1F ratio at the maximum mechanical

speed is of interest because it is lowest at the maximum mechanical speed due to centrifugal stiffening of the 1F mode and softening of the 1T mode.

To summarise, the main requirement to be achieved by the VITAL blade redesign is the shift in 1F flap frequency from 20% 1F-1EO margin to the desired value of 60%. This design change is conducive to improved fatigue life, but requires thickening of the blade, as described in the following section. Flutter criteria also need to be assessed during the design process, as outlined in section 4.3.3.

## 4.3 Thickening the Rotor Blade

### 4.3.1 The FEA Model

The VITAL engine blade was modelled as a solid Titanium blade. A CAD model of the baseline blade was provided by Rolls Royce. To obtain the modal frequencies and construct a Campbell diagram, the CAD model was exported to Abaqus (Dassault Systèmes, 2012) for modal analysis.

The blade root was constrained to move perpendicular to the root-disk contact surface as shown in Figure 4.5, which is the surface that comes in contact with the disk when the blade is spun. Sliding along the axial axis was also constrained. Imposing such constraints to carry out modal analysis to obtain the blade alone modes was suggested by Rolls-Royce (Taylor, 2016).

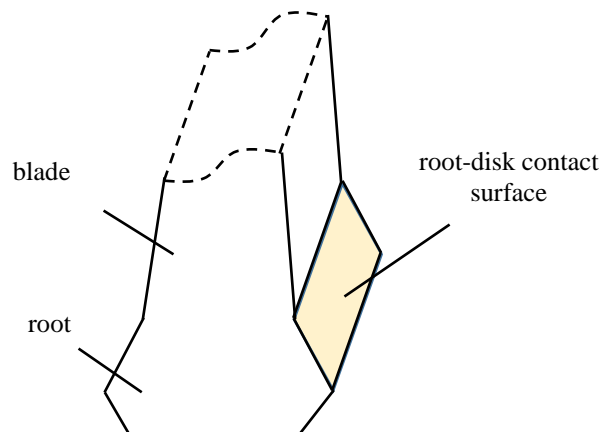


*Figure 4.5 - Rotor blade root schematic*

Centrifugal loading was applied by setting the blade to spin at various speeds. Static analysis was carried out and the resulting deformed shape kept as input for the modal analysis. In this way, the change of the blade's natural frequencies at different speeds was captured. Pressure forces were not included in the static analysis. The modal analysis was set to obtain the first

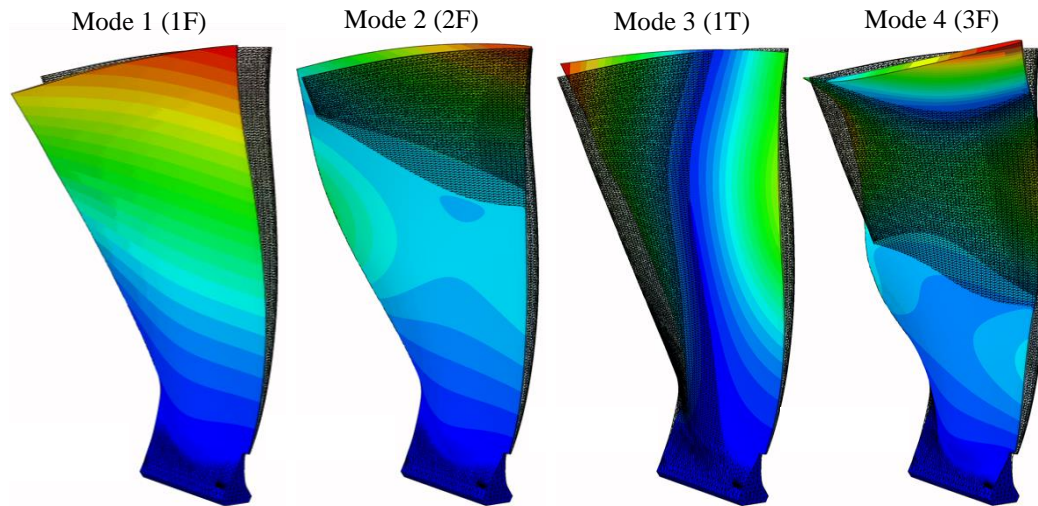


Figure 4.6 - Blade vibration modes for VITAL fan

eight modes. The deflections in the first four modes are shown in Figure 4.6 for the unmodified VITAL rotor, referred to in this section as the “baseline” blade.

The results of the simulations are shown on a Campbell diagram in Figure 4.7. Comparison with a Rolls-Royce model (Vanluggene, 2008) depicts good matching, especially in relation to the 1F predictions. It should be noted that the baseline blade has a 2F-3EO overlap. This is undesirable and means that the baseline blade would need to be further modified to avoid possible 2F/3EO resonant response.

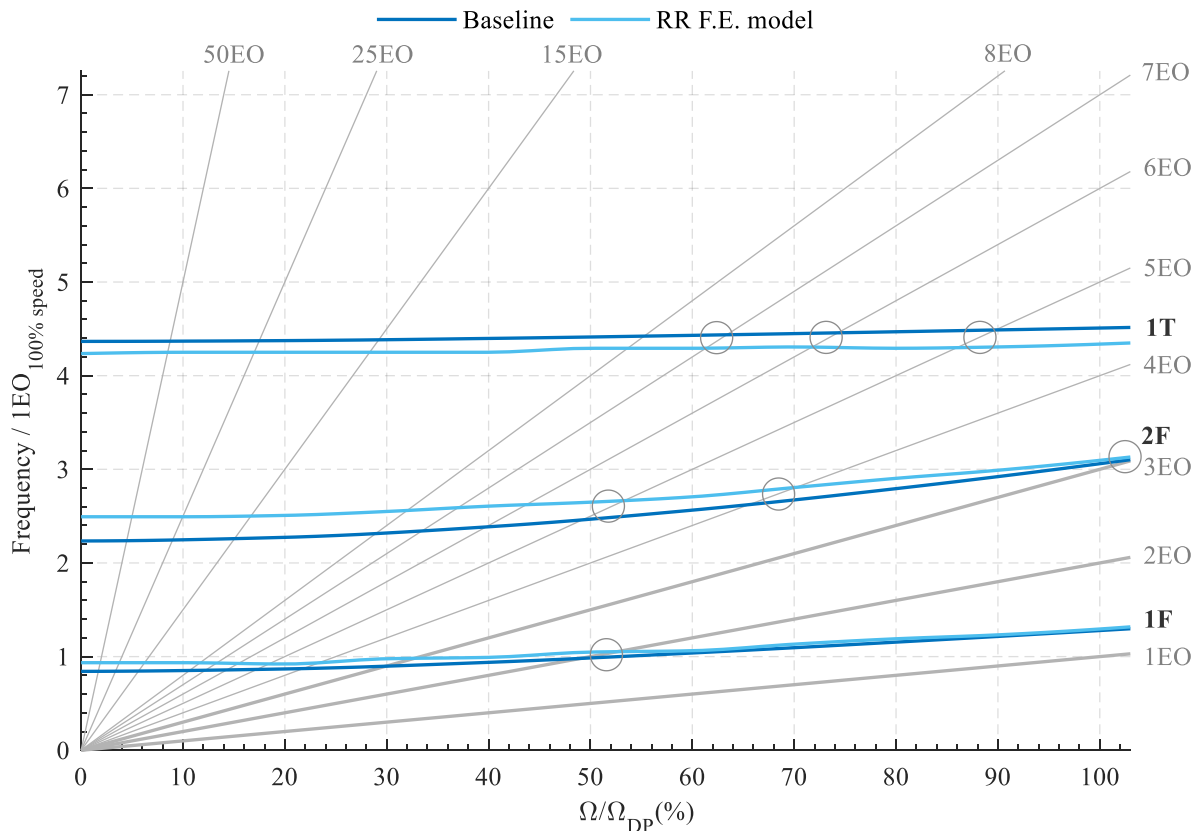


Figure 4.7 – Campbell diagram for the VITAL rotor: FEA model vs Rolls-Royce model

### 4.3.2 Thickening Approach

In order to achieve a shift in the 1F frequency, additional material was required to increase the stiffness without adding mass in the areas that experience high displacement in 1F mode. This meant adding material in regions with high strain but low amplitude of displacement in the part of the blade close to the root.

Thickening was carried out by scaling the blade section thickness distribution along the chord, as described in section 3.3.2. Thickening the blade without increasing the root size leads to high localized stresses, as indicated in Figure 4.8. Considering the geometric requirement that the root has to fit into the disk, there is a maximum of  $20^\circ$  space for each of the 18 rotor blades. Several scaling factor distributions were attempted, and the modal analyses demonstrated that adding mass at the upper part of the blade did not significantly influence the 1F frequency.

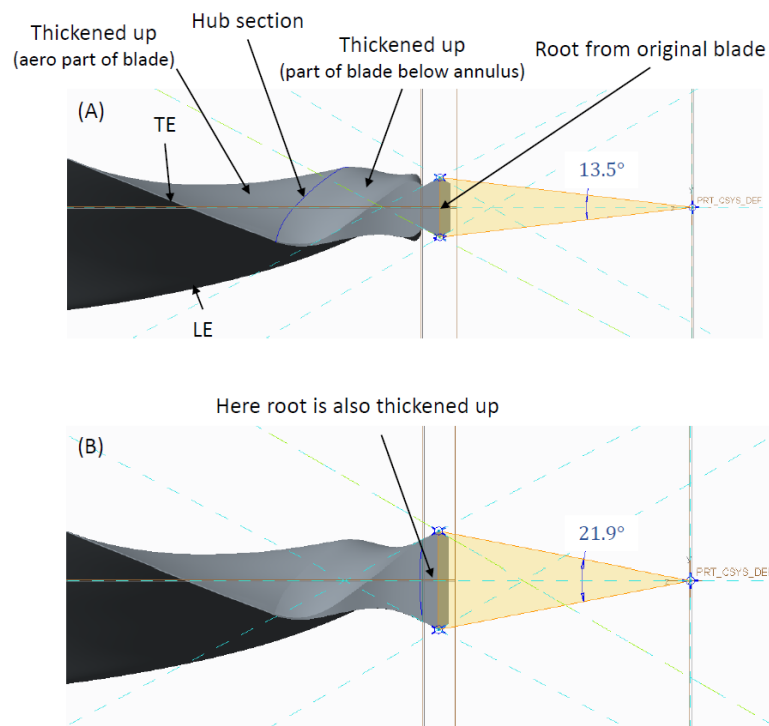


Figure 4.8 – Root thickening

### 4.3.3 The Final Design - Thick Blade

The final design was the result of several design iterations. The final root size was  $16^\circ$ , which is 20% larger than the original  $13.5^\circ$  root. A modified disk design was required to support the blade. It was assumed that this root and blade size were feasible.

The final blade design is shown in Figure 4.9. Meshed FEA models of the baseline and thick blades are shown for comparison. A graph depicting the scaling factor shows maximum scaling

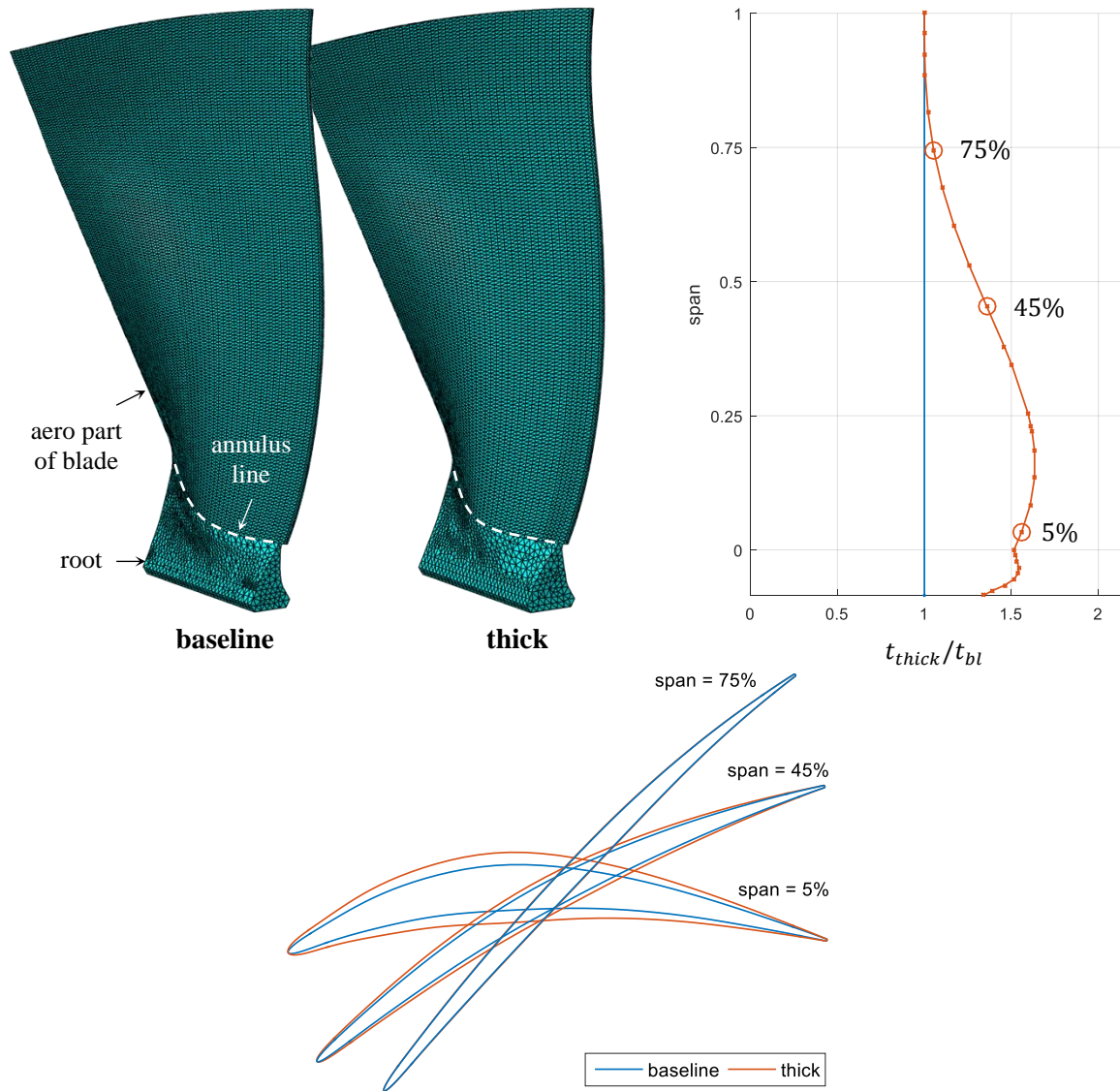


Figure 4.9 – Baseline and thick blades: blade sections (below), FEA model (left) and thickening factor (right)

percentage at around 20% span (note that the span is defined in a conventional way, i.e. the aero part of the blade ranges from 0% span at the hub to 100% span at the tip; negative span corresponds to the part of the blade below the annulus line). The sections at 5%, 45% and 75% span are also shown. The section plots reveal that there is substantial thickening at the root sections.

The results of the simulations with the thick blade, shown in Figure 4.10, indicate that the frequencies of the first three modes increase as a result of blade thickening in the lower part of the blade. The 1F frequency satisfies the imposed 60% margin requirement. It is apparent from the Campbell diagram that increasing the 1F frequency further could cause problems with the 1F/2EO interaction. Some difficulties may be experienced at the 1F-2EO crossing when accelerating to the operating speed. Other issues may be caused by the 2F-4EO and 1T-6EO

crossings. The 2F mode is significantly improved compared to the baseline blade, where the 2F-3EO crossing occurred at the maximum mechanical speed. The details of this are not further addressed here as the redesign intention was not to create an optimal mechanical design.

The Campbell diagram in Figure 4.10 shows that the 1F-1T frequency separation is much higher than required by criterion 5. The parameter in criterion 4 for flutter,  $(c_{tip}\Theta/H)/(c_{tip}2\pi f_{1F}/V_{1,rel})$ , was calculated for both blades. The term  $c_{tip}\Theta/H$  was calculated from the LE and TE displacements, using the method from (Vahdati & Cumpsty, 2016), while the  $V_{1,rel}$  was calculated assuming the design relative tip Mach number and sea level condition. The parameters for the baseline and thick blades were approximately the same, and very close to the limit specified by criterion 4. The twist component in mode 1F was found to be larger in the thick blade. However, this increase was compensated by the increase in  $f_{1F}$ , giving approximately the same parameter overall.

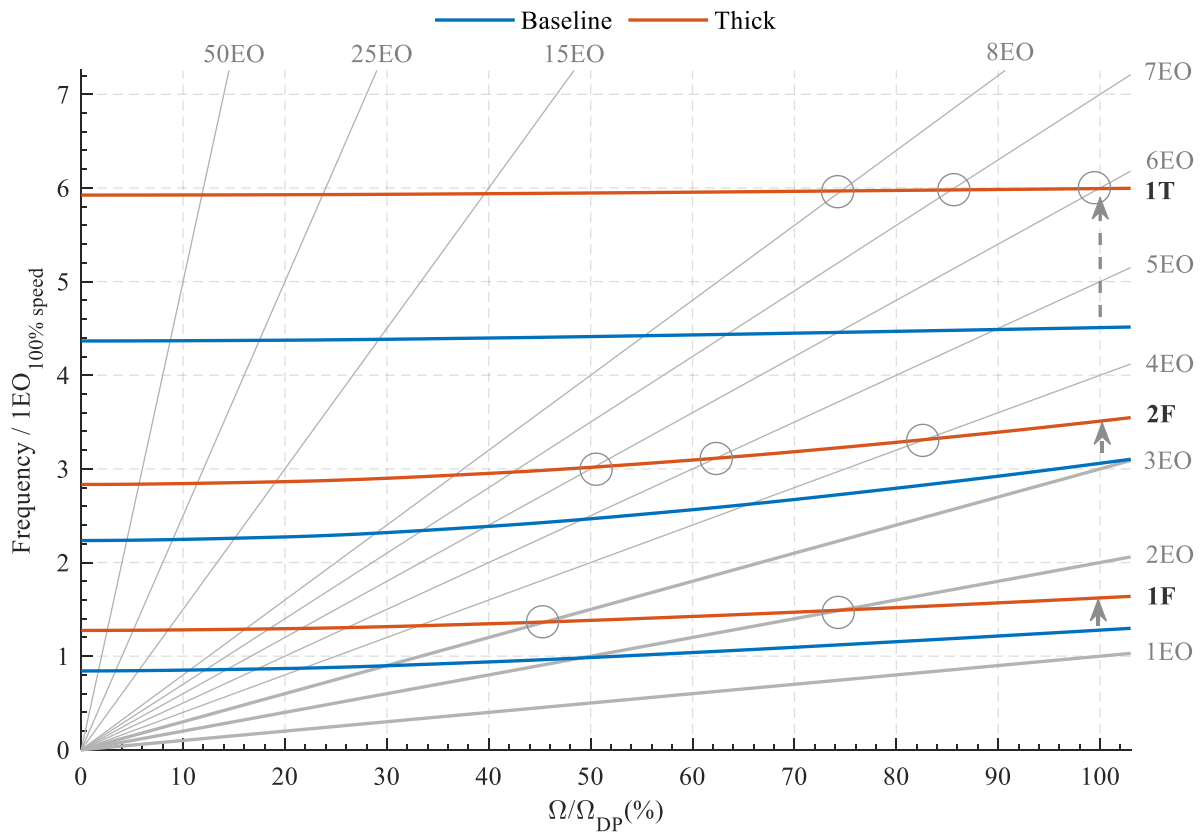
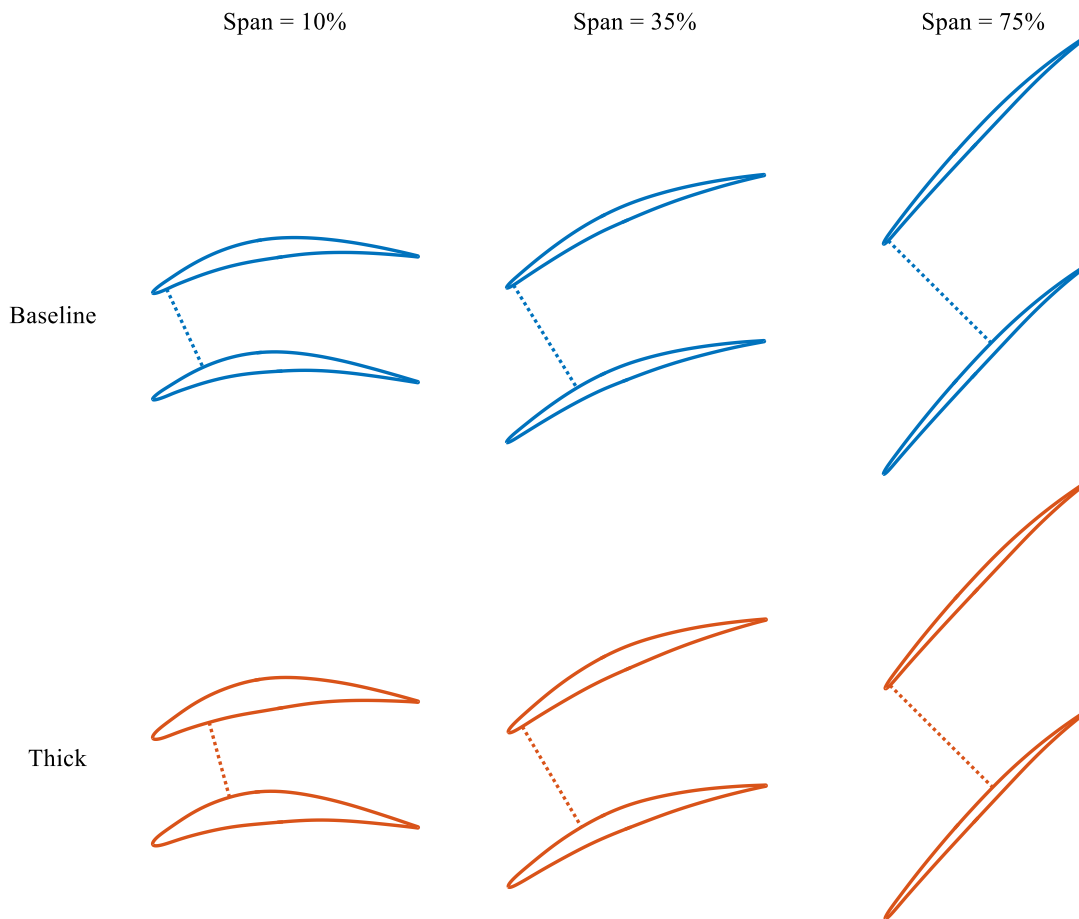


Figure 4.10 - Campbell diagram: Baseline vs thick (FEA)

#### 4.3.4 Impact on the Throat Size

Thickening the blades results in a reduction in throat size. This is apparent from Figure 4.11, in which three sections, at 10%, 35% and 75% span, of the baseline and thick blades are shown, as well as the 2D throats. Sections at 75% are very similar as there is very little

thickening at this span-wise location. The throat location and size are consequently about the same. At 35% span, the effect of blade thickening is more apparent. The throat size changes slightly, as well as its location. The throat is deeper inside the passage in the thick blade. Further down the span, this is even more pronounced. Comparison of throat location at 10% span sections shows that the throat location in the thick blade is even further inside the passage. Its size is also significantly reduced.



*Figure 4.11 - Throat locations and size for sections at 10%, 35% and 75% span*

The actual 3D throat is a highly twisted surface, as shown in Figure 4.12. The figure displays throat location on the pressure and suction sides of two neighbouring blades across different spans. The location is determined by finding the throats in a two-dimensional sense, for all sections across the span.

At the tip, the throats of the two geometries are the same, as can be seen in Figure 4.12. The throat is intercepting the pressure side of one of the blades at a location very close to the blade leading edge. The interception on the suction side of the other blade is deep inside the passage, due to the high stagger angle of the tip sections. Moving towards the mid-span, the stagger



reduces and the throat interception with the suction surface moves further up the passage. At around 50% span, the locations of the throats in the two cases remain the same, but there starts to be a difference in their sizes. Closer to the hub, the throat in the thick blade moves further inside the blade passage, relative to the baseline case. Its size reduces too, as shown in the plot of throat size in Figure 4.12.

A rough estimate of the change in throat area can be calculated by integrating the throat size as function of the radius, i.e. by calculating  $\int_{r_{hub}}^{r_{tip}} \tau dr$ , where throat size  $\tau$  is a function of radius  $r$ . The result is:

$$\frac{A_{T,thick}}{A_{T,bl}} = \int_{r_{hub}}^{r_{tip}} \tau_{thick} dr \bigg/ \int_{r_{hub}}^{r_{tip}} \tau_{bl} dr = 97.06\% \quad (4.2)$$

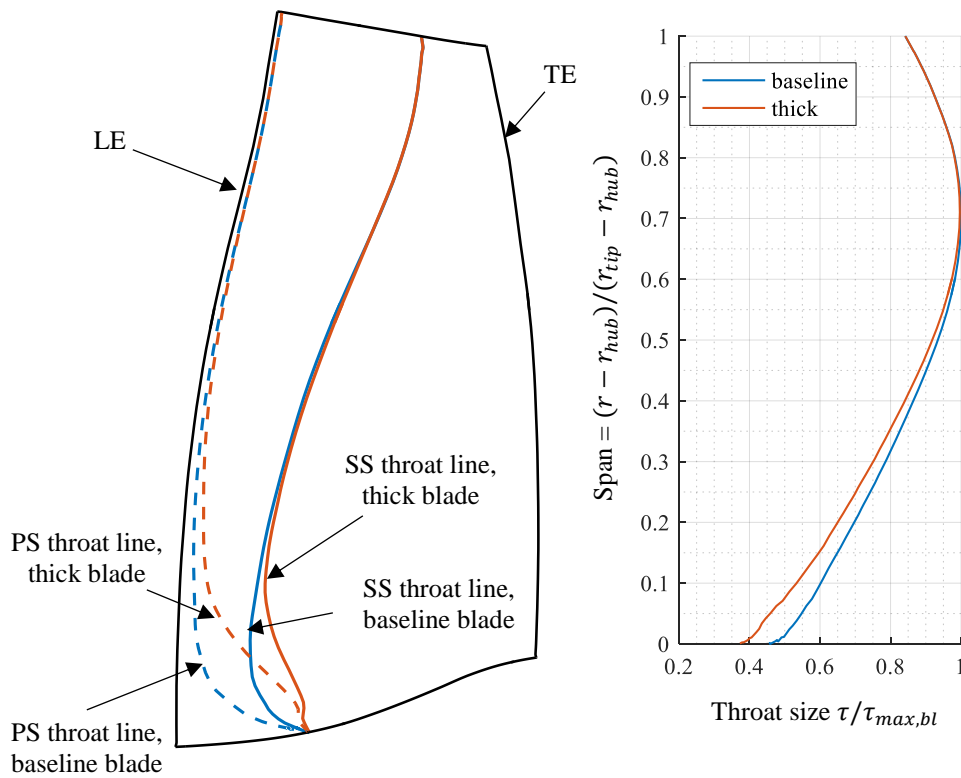


Figure 4.12 – Baseline vs thick blade: Comparison of throat location (left) and size (right)

## 4.4 Impact on Aerodynamic Performance

The impact of mechanical design changes on the aerodynamic performance was investigated by assessing the baseline and the thick blades in CFD. Steady CFD was used to find the constant speed characteristics for both blades in clean flow. This was not possible in distorted flow,

where unsteady CFD had to be used. Each operating point took around 5 rotor revolutions to converge. Each revolution required approximately 400 GPU hours, which took up to a day to run on the Cambridge HPC cluster per revolution (the exact run time depended on the number of GPUs used in parallel).

Figure 4.13 shows the resulting stage pressure rise and efficiency characteristics of the two blades in clean and distorted flow. The distorted flow operating points are shown with dots. The peak efficiency points for each flow condition for the two blades are labelled with circles. Distorted flow unsteady CFD was run at twelve operating points with the baseline blade and eleven with the thick blade, in order to show the shape of the characteristics around the peak-efficiency points and the choked parts of the characteristics. No attempt was made to model the flow at near stall conditions or predict the stall point by running CFD cases further up the characteristics. Steady CFD was run at more operating points along the characteristics, as the clean flow cases were computationally significantly less expensive compared to the distorted flow runs.

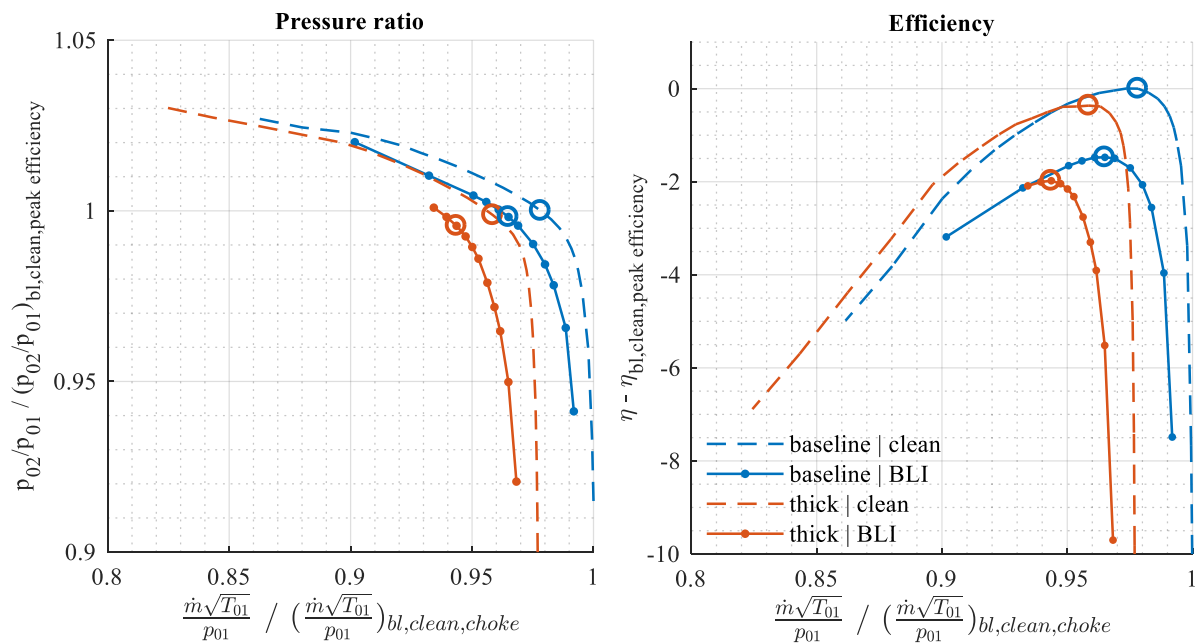


Figure 4.13 - Stage pressure ratio and efficiency: baseline vs thick blade

To quantify the impact on performance caused by the changes in blade thickness, the performances of the two blades in clean and distorted flow are compared. The changes in performance are detailed in Table 4.2.

Blade thickening is found to reduce both the efficiency and the mass flow rate. Compared with the performance of the two blades in clean flow, it was found that there is a 2% drop in the

mass flow rate and 0.4% drop in efficiency. The drop in the mass flow was expected due to the reduction in the throat area. The reduction in mass flow in distorted flow conditions was 2.1%, while the drop in efficiency was 0.5%. These results indicate that the impact of the mechanical design change is similar regardless of the flow condition, i.e., the deterioration in blade performance caused by blade thickening is the same in clean and distorted flows.

	<u>Effect of blade modification</u>		<u>Effect of Distortion</u>	
	Clean flow (baseline–thick)	BLI flow (baseline – thick)	Baseline (clean – BLI)	Thick (clean – BLI)
$\dot{m}\sqrt{T_{01}}/p_{01}$	2.0%	2.1%	1.3%	1.5%
$\eta$	0.4%	0.5%	1.5%	1.6%

Table 4.2 - Change in performance: baseline vs thick blade

Distortion on the baseline blade performance reduced both the efficiency and the mass flow rate. The reduction in the mass flow rate was 1.3% and the reduction in efficiency was 1.5%. Similar changes were found with the thickened blade, where the drop in mass flow rate was found to be 1.5% and the drop in efficiency 1.6%. The reasons behind these drops in mass flow and efficiency in distorted flow with the baseline blade are presented by (Gunn & Hall, 2014). and are briefly reviewed in the discussion on flow field presented later in this chapter.

A comparison of these results shows that the drop in efficiency due to distortion is 3 times that achieved by mechanical design changes. The mass flow reduction is roughly similar in both cases, with the reduction being slightly higher when the blade is thickened up. Overall, there is a 3.5% drop in mass flow and 2% drop in efficiency when both the mechanical design is modified and the blade is operated in BLI flow. The following sections look at the details of the flow field to explain these performance changes.

## 4.5 Clean Flow Performance

### 4.5.1 Reduction in Choking Mass Flow Rate

Reduction in choking mass flow with the baseline VITAL blade due to distortion occurs as a result of increased blockage. A method was developed in (Gunn, 2015) to calculate the reduction in effective flow area due to distortion. It was shown that the percentage reduction in mass flow is comparable to the percentage reduction in the throat area.

Blade thickening has the same effect, but the additional blockage in this case is due to added material, rather than the flow physics. The results in Figure 4.13 reveal that the drop in choking mass flow in clean flow due to blade thickening is approximately 2.2%, which is consistent

with the reduction in the throat area of 2.94% calculated in section 4.3.4. The drop in mass flow in clean flow at peak efficiency is approximately equal to the reduction in choking mass flow, as shown in Figure 4.13 and Table 4.2.

Changes in the circumferentially averaged axial mass flux upstream of the blade leading edge reveal how the flow redistributes upstream of the throat. Plots of axial and radial mass fluxes are shown in Figure 4.14. Two cuts are made, as shown in the meridional plot. One cut is further upstream where there is little difference between the fluxes for the two blades, except for the offset which exists because the two operating points are at slightly different mass flows. The other cut is made just upstream of the leading edge. In this cut, it is apparent that the flow is redistributed radially as it approaches the fan face. This is in line with the fact that coupling between the rotor and the intake occurs over a length-scale in the order of the blade pitch (Gunn, 2015). Plots of axial mass flux at this location indicate that the axial flux at the tip of the thick blade approaches the value of that in the baseline blade. Moving down the span towards the hub, the difference increases. In the case of the thick blade, this radial redistribution drives the flow away from the hub and towards the casing.

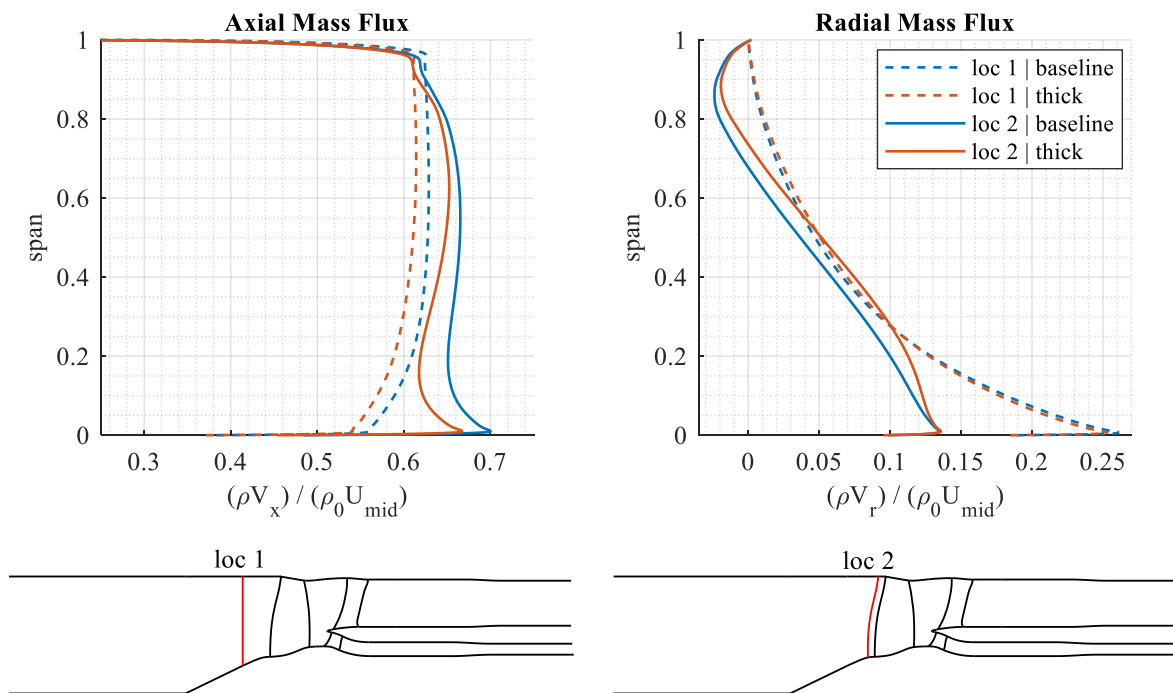


Figure 4.14 - Upstream flow clean redistribution with baseline and thick blades

Redistribution that occurs upstream of the rotor is also apparent from the radial mass flux plots. At the upstream location, there is barely any difference between the two cases. However, just ahead of the blade row there is substantially more radial flow migration in the thick blade case.

The flow is redistributed up to this point and continues to redistribute as it is pushed away from the hub. The reduction in axial mass flux in the thick blade leads to increased relative swirl angles compared to the baseline case. At the hub, the incidence is increased by  $1.5^\circ$ , but remains roughly the same at the tip.

#### 4.5.2 Rotor Flow Field

Pressure distributions at two span fractions, 20% and 80%, are shown in Figure 4.15. The plot shows that at the tip at 80% span, the surface pressure distributions are almost identical for both blades. There is a shock at around mid-chord which is expected at the tip sections. The differences are significant at the hub at 20% span. The plot shows that the pressures on both PS and SS are lower on average in the thick blade. On the SS, the diffusion does not start until approximately the mid-chord point, where it becomes more abrupt than in the baseline blade. A stronger adverse pressure gradient at the rear of the SS is apparent, which is expected to thicken up the boundary layers to a larger extent.

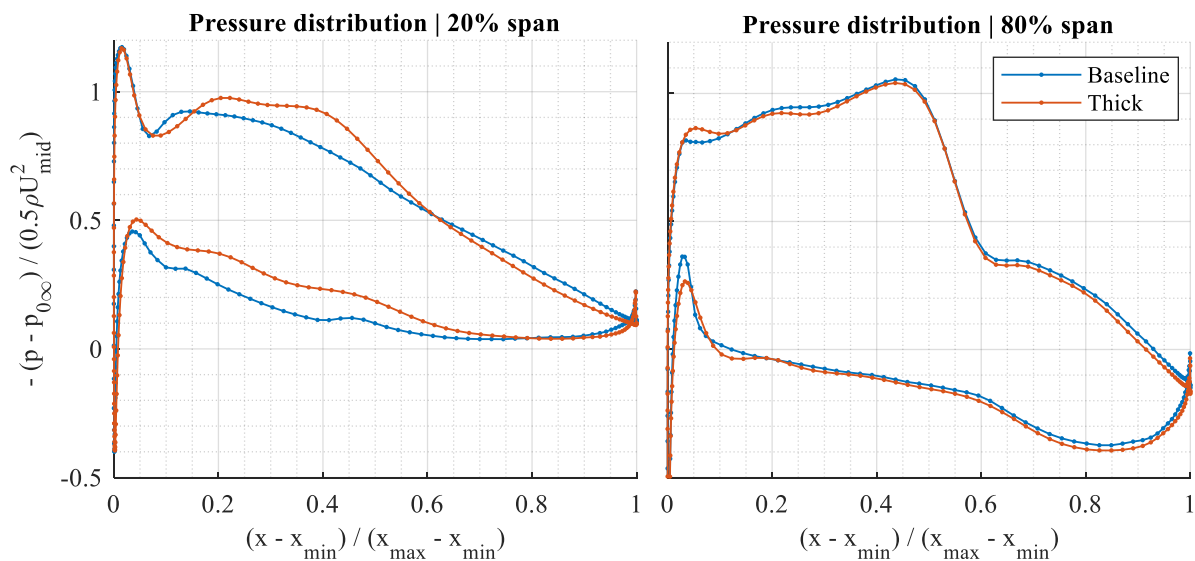


Figure 4.15 – Pressure distributions at 20% and 80% span: baseline vs thick blade

Blade-to-blade contours of the relative Mach number in Figure 4.16 reveal more details for sections near the hub. Both blades have a transonic patch at the LE, which is the cause of the initial SS bump seen in the pressure distributions in Figure 4.15. Following the LE patch, the flow accelerates over a very short distance in the baseline blade and then gradually starts decelerating. In the thick blade, the acceleration continues for longer and transonic Mach numbers are seen up to approximately mid-chord. The flow then decelerates rapidly over a shorter distance, which thickens the boundary layers and leads to larger wakes downstream of the blade.

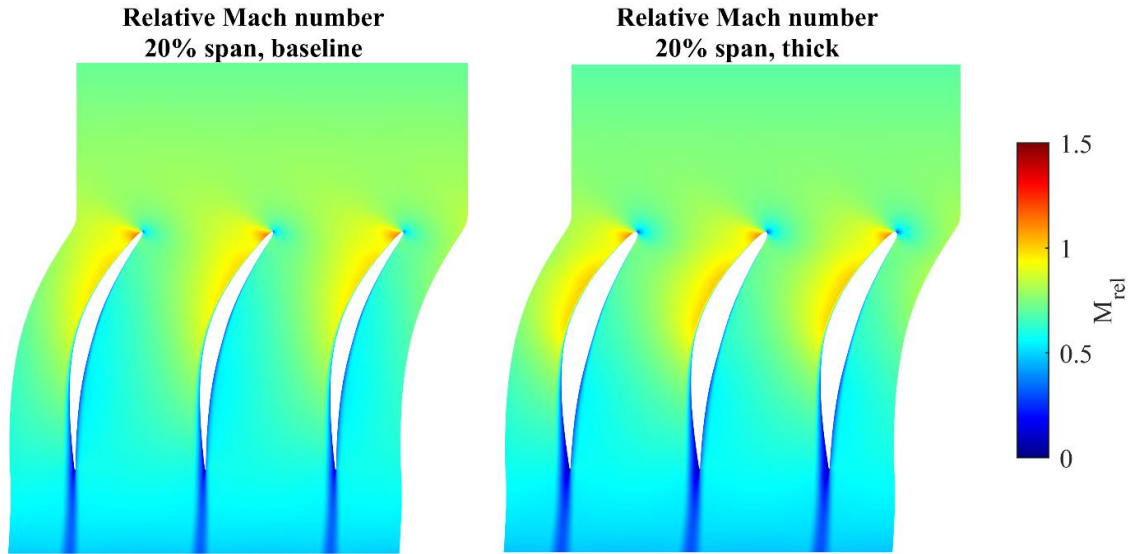


Figure 4.16 – Blade-to-blade contour of relative Mach number at 20% span: baseline vs thick blade

Figure 4.17 shows contours of the relative Mach number close to the blade surface on the SS. A plot of the difference between the two cases is also shown. The difference in the two cases is mostly in the region close to the hub where the flow is subsonic. Flow acceleration to a slightly higher Mach number in the thick blade is followed by deceleration to a slightly lower Mach number. This is consistent with the observations made in Figure 4.15, which demonstrates that this sort of pattern of late diffusion is present up to approximately mid-span, above which there is little difference between the two cases. Contours of static pressure in Figure 4.17 show that the adverse pressure gradient is higher in the hub region of the thick blade. The shock position in the tip region is slightly different, but this does not have a significant impact on the blade performance.

Entropy contours at a location just downstream of the rotor are shown in Figure 4.18. A slight increase in loss in the rotor occurs below the mid-span, where there is a higher profile loss due to thicker wakes. In addition, the hub corner separation is more pronounced. Overall, this slight increase in profile loss and the higher loss due to corner separation are responsible for the 0.4% decrease in efficiency observed for the thick blade.

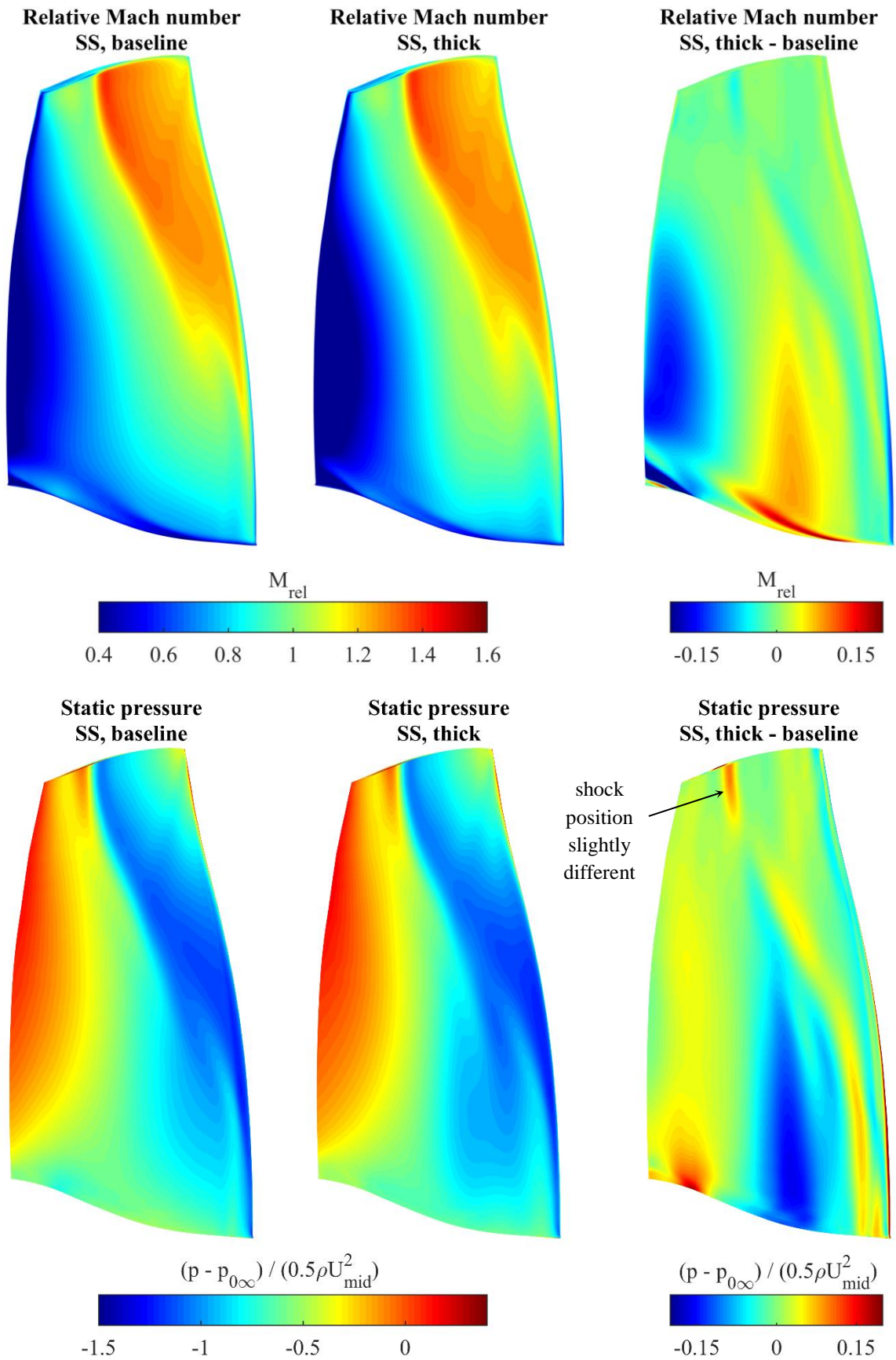


Figure 4.17 - Blade surface contour of relative Mach number (above) and static pressure (below): baseline vs thick blade



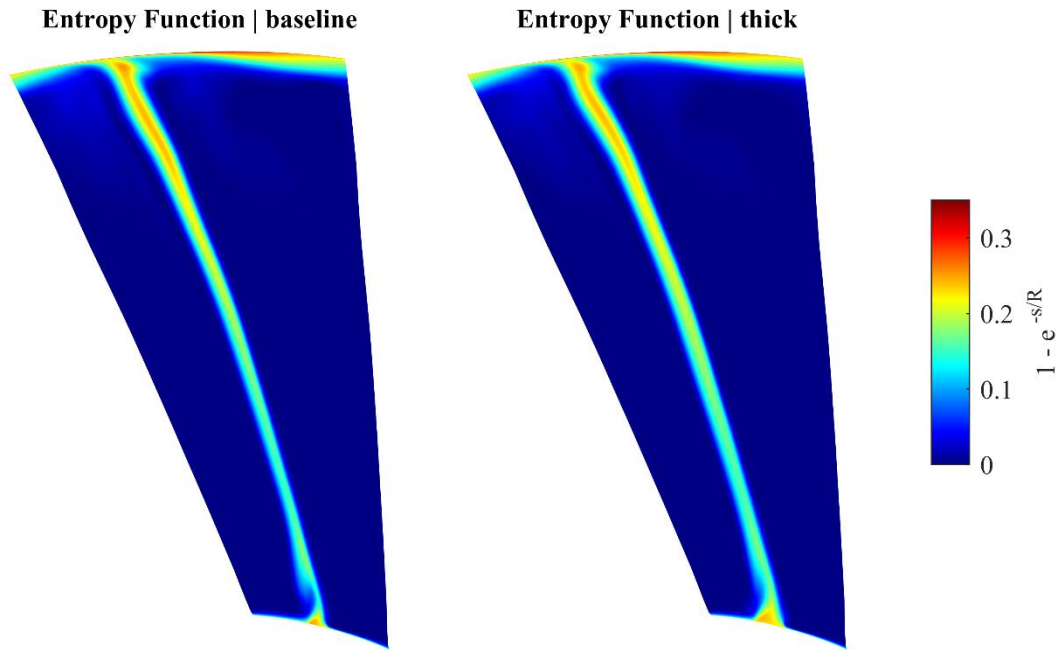


Figure 4.18 – Entropy at an axial location just downstream of rotor: baseline vs thick blade

## 4.6 Performance in BLI Flow

### 4.6.1 Upstream Flow Redistribution

Reduction in mass flow due to blade thickening can also be observed in distorted flow. Contours of axial mass flux upstream of the fan are shown in Figure 4.19 alongside a plot showing the difference between the two cases. Overall, the reduction in mass flow is in the order of 2%, due to axial mass flux deficit in the case of the redesign blade in the order of 0.01, which is 2% of the average flow coefficient. The difference plot also depicts that the level of reduction is higher in the bottom 50% of the span, but uniform around the annulus, which

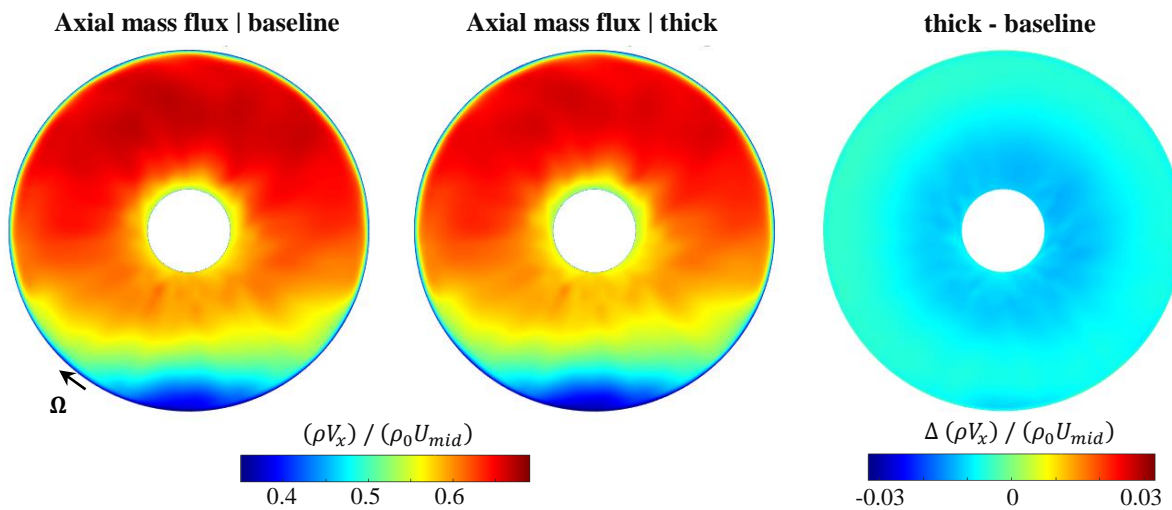


Figure 4.19 - Contours of axial mass flux upstream of the rotor: baseline vs thick blade



means that the reduction in mass flow which occurs due to reduction in the throat area is not affected by the presence of distortion.

Blade-to-blade cuts in Figure 4.20 indicate radial velocity contours at 50% span. The contours show that most of the flow redistribution occurs close to the leading edge in both cases. There is more radial flow in the thick blade, as compared to the baseline design, since the flow is pushed radially up from the hub.

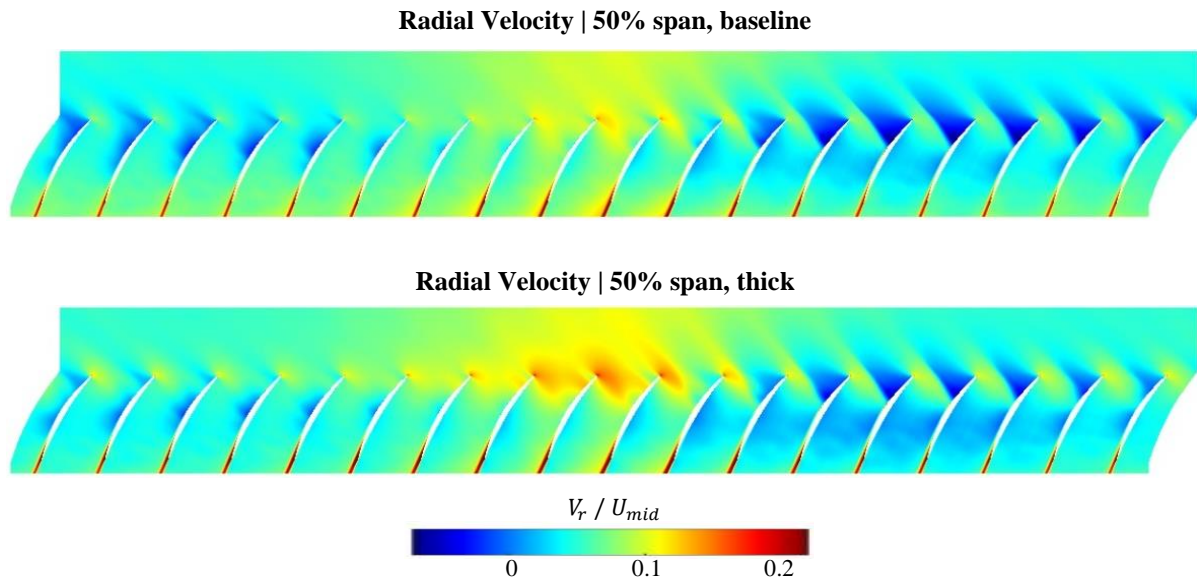


Figure 4.20 - Blade-to-blade cuts at 50% span: radial velocity, baseline vs thick

Plots of swirl angle and radial angle just upstream of the leading edge, shown in Figure 4.21, reveal that a similar level of bulk flow redistribution occurs in both the baseline and thick blade. The plot of the difference between the two cases shows just slightly higher swirl angles close to the hub of the thick blade, in the order of  $0.5^\circ$ . The radial angle plot in Figure 4.22

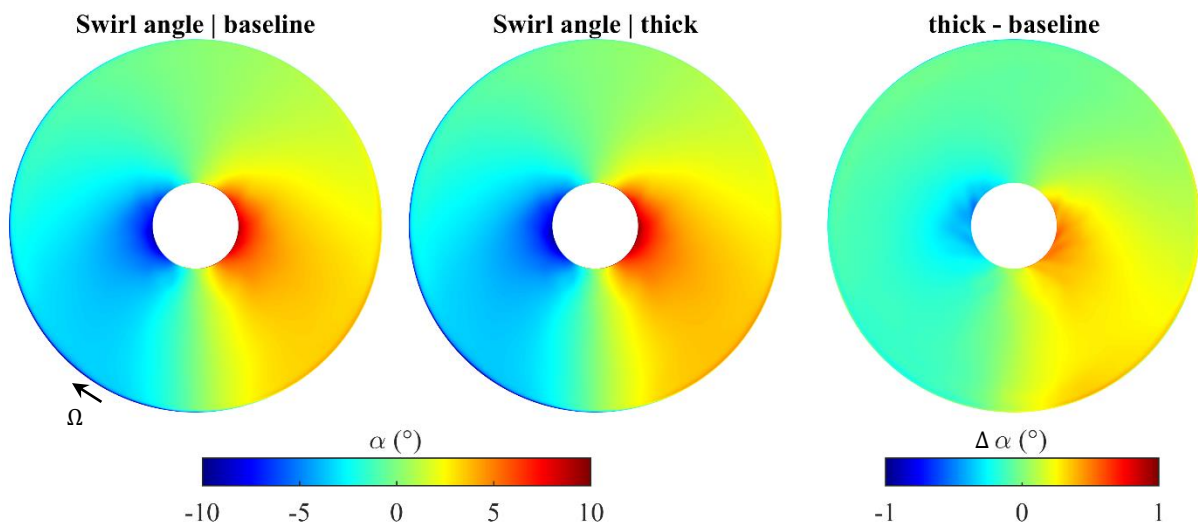


Figure 4.21 - Contours of swirl angle upstream of the rotor: baseline vs thick

demonstrates that radial angles at the bottom part of the annulus are higher, especially close to the hub. There is more radial flow with the redesigned blade.

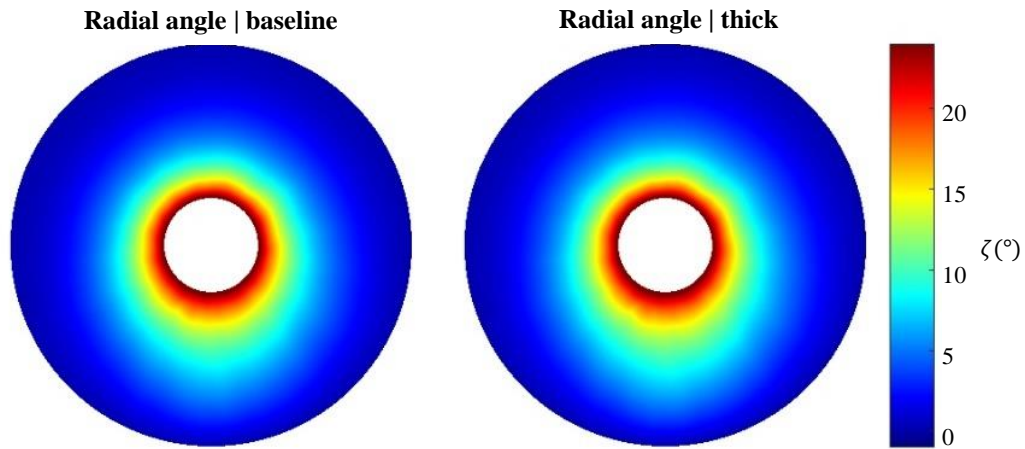


Figure 4.22 - Contours of radial angle upstream of the rotor: baseline vs thick

#### 4.6.2 Shock Structure at the Tip

Shock structure at the tip is shown in Figure 4.23. The plot reveals that there is little difference between the shock structures in the two cases. Incidence in the co-swirl region is negative and pushes the flow into a choked condition. The structure at  $-60^\circ < \theta < 0^\circ$  is similar to that of the peak efficiency point in clean flow. Further around the annulus in the counter-swirl region, the flow is similar to that observed at a near stall point in clean flow, where the shocks are expelled. Incidence is high and there are no passage shocks. The shock structure for the thick blade is very similar to the baseline case. This is expected since most of the differences occur in the region close to the hub.

In the plot of the LE shock Mach number variation in Figure 4.24, little difference is visible between the two cases. The blades experience higher than design shock Mach numbers in the counter-swirl region. The opposite is true for the co-swirl region. This modulates the shock structure, as shown in Figure 4.23.

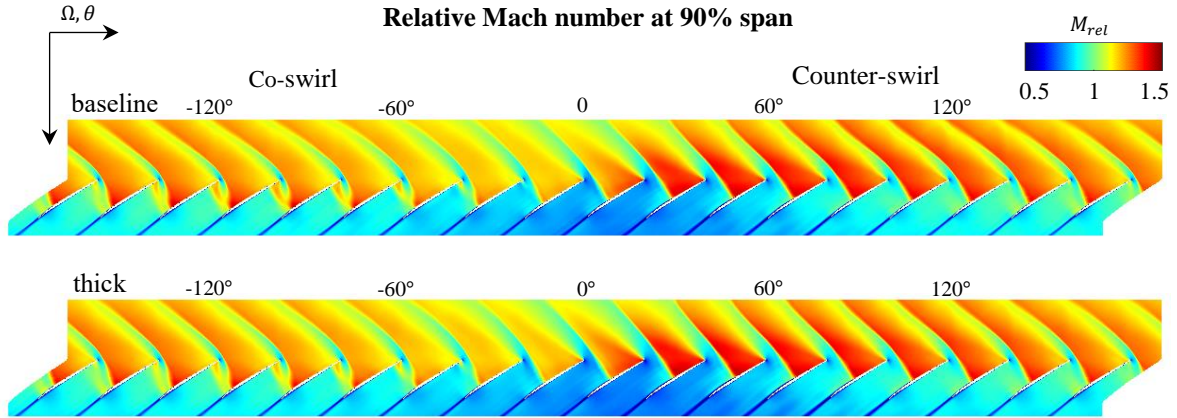


Figure 4.23 - Shock structure at the rotor tip: baseline vs thick

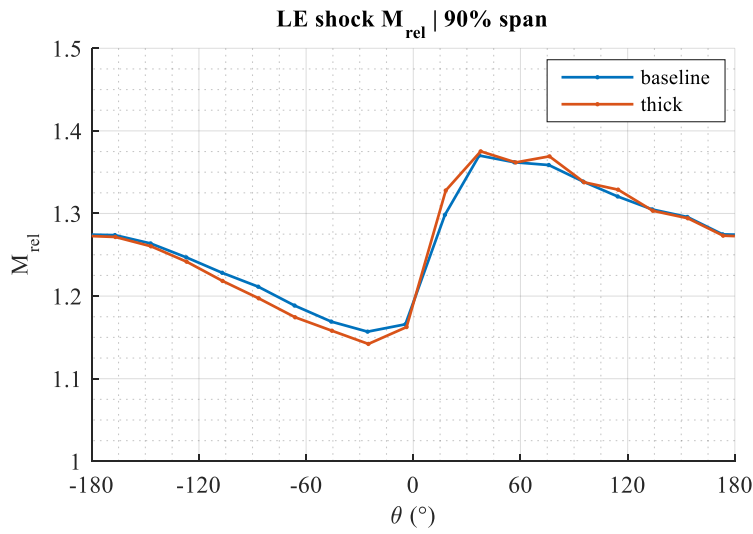


Figure 4.24 - LE shock Mach number

### 4.6.3 Flow Field in the Hub Region

Most of the additional loss seen downstream of the rotor in clean flow occurs due to worsened hub corner separations and increased profile loss. This is also the case in distorted flow. Blade-to-blade contours of relative Mach number close to the hub are shown in Figure 4.25. The plot shows that blade loading varies around the annulus. In the baseline blade, the flow in the counter-swirl region reaches speeds higher than Mach 1 at the leading edge. These supersonic patches end with shocks. Further around the annulus, the flow is subsonic at the leading edges. It accelerates but does not reach Mach 1. This is not true of the thick case. Thicker sections lead to higher accelerations, causing most of the sections in the co-swirl region to be supersonic. The flow accelerates to above Mach 1 at around mid-chord, and then decelerates without a shock. The flow is complicated in the region  $0^\circ < \theta < 60^\circ$ , where the leading edge shocks merge with the transonic patches on the SS.

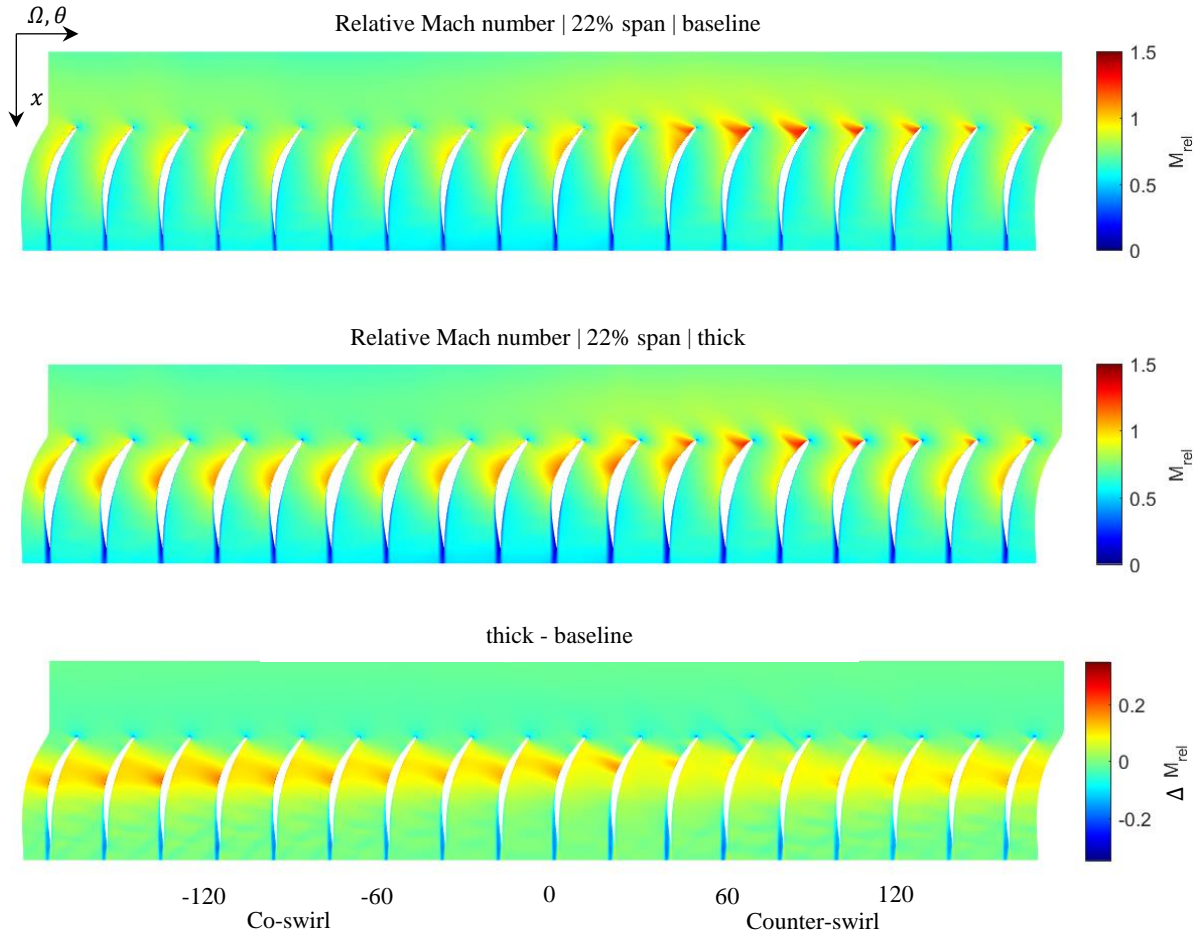


Figure 4.25 - Blade-to-blade cut at 22% span, rotor flow field, contours of relative Mach number, baseline vs thick

A consequence of this higher acceleration is diffusion on the rear of the SS that causes the boundary layer thickness to increase. The flow separates earlier, resulting in thicker wakes in the thick blades. This is also apparent from the difference plot. Thicker wakes and higher velocities on the suction surface cause an increase in profile loss.

#### 4.6.4 Circumferential and Span-Wise Variation in Flow Variables

Blade surface plots in Figure 4.26 and Figure 4.27 shows that the pattern of increased velocity on the SS of the thick blades exists at other spans. Blade surface contours of relative Mach number at two circumferential locations, one in the counter-swirl region and another in the co-swirl region, are shown. At  $\theta = -75^\circ$ , in the co-swirl region of the flow, the shock on the suction surface extends down to mid-span. In the thick blade, the shocks extend from the tip down to around 25% span. The difference plot shows that the flow accelerates more across the entire span in the thick blade. The increased acceleration and subsequent deceleration lead to thicker boundary layers and earlier flow separation on the thick blade. At  $\theta = 125^\circ$ , the shock extends to the hub in both blades. The flow is transonic across the entire span. The difference



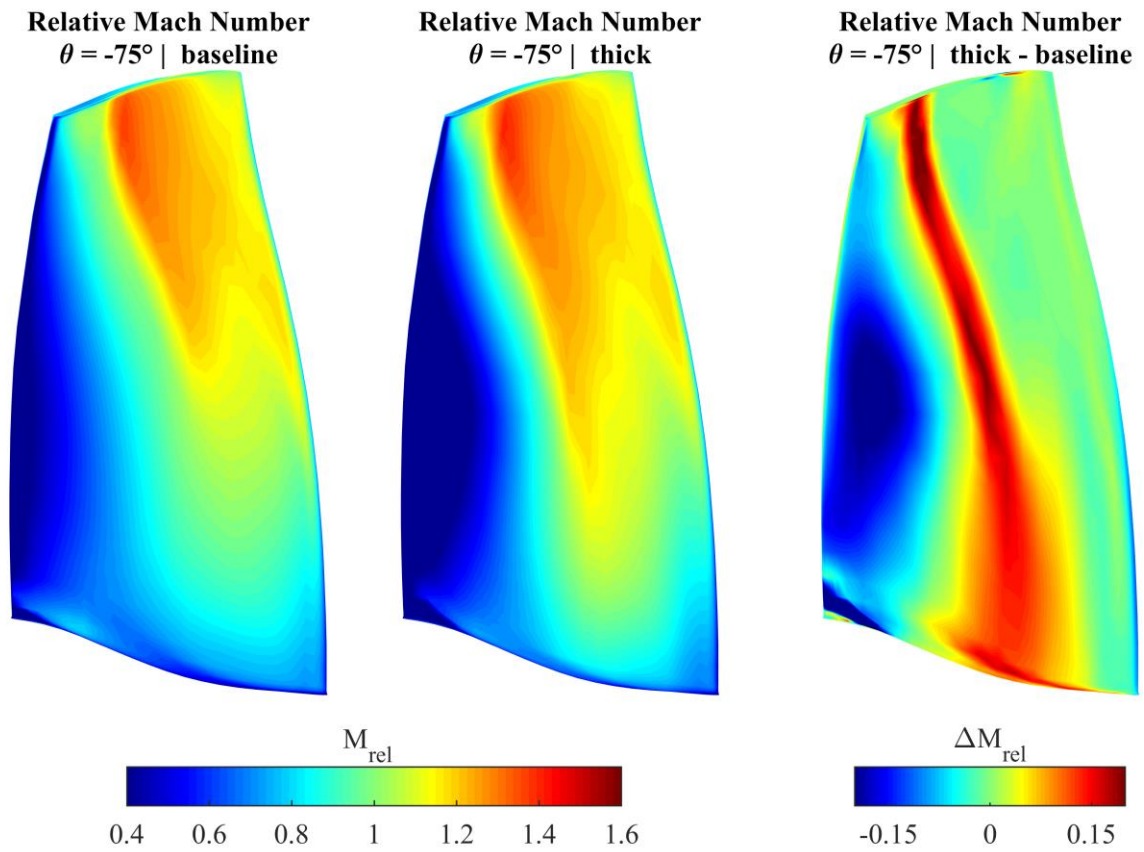


Figure 4.26 - Blade surface plot of relative Mach number, co-swirl region, suction surface: baseline vs thick

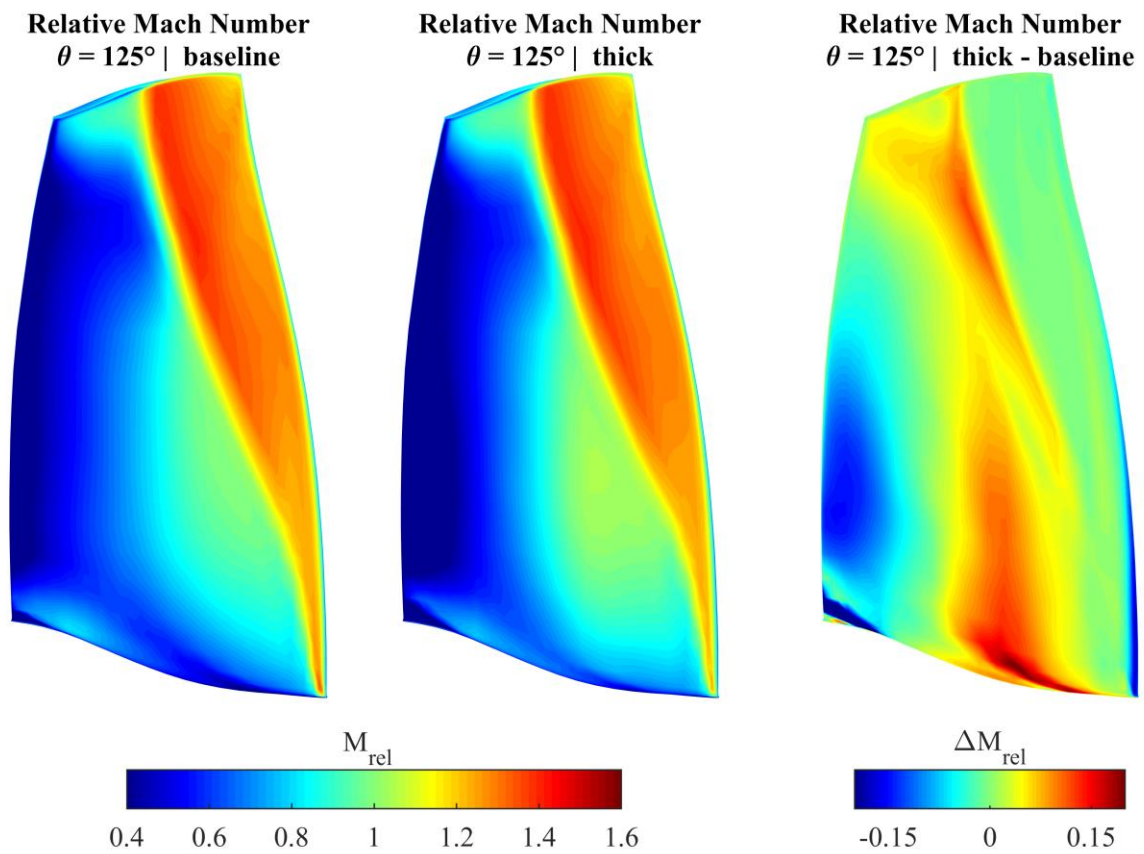


Figure 4.27 - Blade surface plot of relative Mach number, counter-swirl region, suction surface: baseline vs thick

plot reveals a similar acceleration and deceleration pattern as observed in the co-swirl region of the flow. However, the acceleration is more gradual and the peak difference in relative Mach number between the two blades is more moderate. From the hub up to the mid-span, the flow is decelerating to lower velocities. Toward the tip, there is less of a difference in deceleration in the thick blade, as compared to the baseline blade. As a result, almost no difference is expected in wake thickness and loss.

The top part of the blade is transonic in clean flow, while the hub sections remain subsonic and operate below Mach 1. In distorted flow there is a circumferential variation in flow conditions which leads to variation in the percentage of the blade span that operates in the transonic regime, as seen in Figure 4.28. Two types of transonic patches on the SS can be distinguished, one where the flow accelerates to transonic speeds at the LE, and one in which there is acceleration to transonic speeds at around mid-chord.

Increased Mach numbers across the span in the counter-swirl region (cf. Figure 4.25, Figure 4.27) push the LE Mach number to high values. Transonic patches at the leading edge are seen with all spans. In the co-swirl region, there is a relaxation due to lower Mach numbers (cf. Figure 4.25, Figure 4.26), and this moves the point of transonic LE further up the span. At  $\theta = -60^\circ$ , the line reaches nearly 40% span. The pattern is similar in both the baseline and thick cases.

Inside the passage, flow acceleration on the suction surface depends on blade geometry. In the thick blade, flow accelerates to higher speeds. Consequently, the line in Figure 4.28 showing the span at which mid-chord transonic patches first appear is lower in the thick blade. This

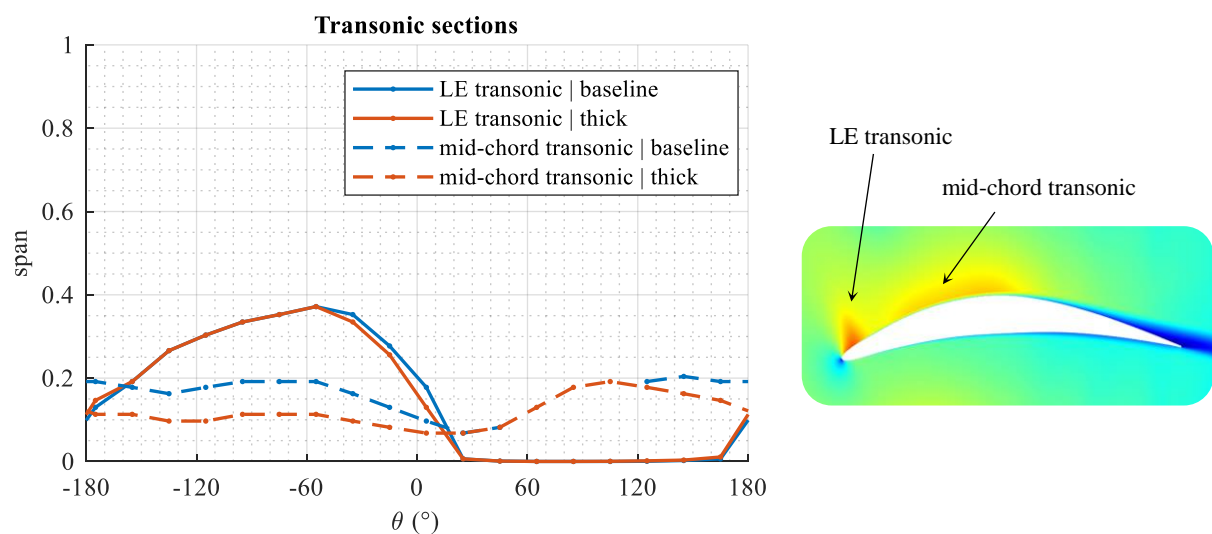


Figure 4.28 – Span at which blades become transonic, circumferential variation

confirms the finding that Mach numbers on the SS of the thick blade reach higher values compared to the baseline case.

#### 4.6.5 Rotor Losses

Entropy contours just downstream of the rotor are shown in Figure 4.29. A difference plot is also depicted, which reveals that there is little difference except in the wakes. Most of the extra loss occurs around and below the mid-span, as in the case of clean flow. At the hub, the intensity of corner separations is stronger around the annulus. Losses in the wakes up the span are higher in intensity, up to around 70% span. This coincides with the extent to which there is substantial thickening up of the blades. Further up in the tip region, there is less loss. In particular, there is almost no difference in the counter-swirl region, while there is some additional loss in the co-swirl region. The passage shocks in this region of the circumference

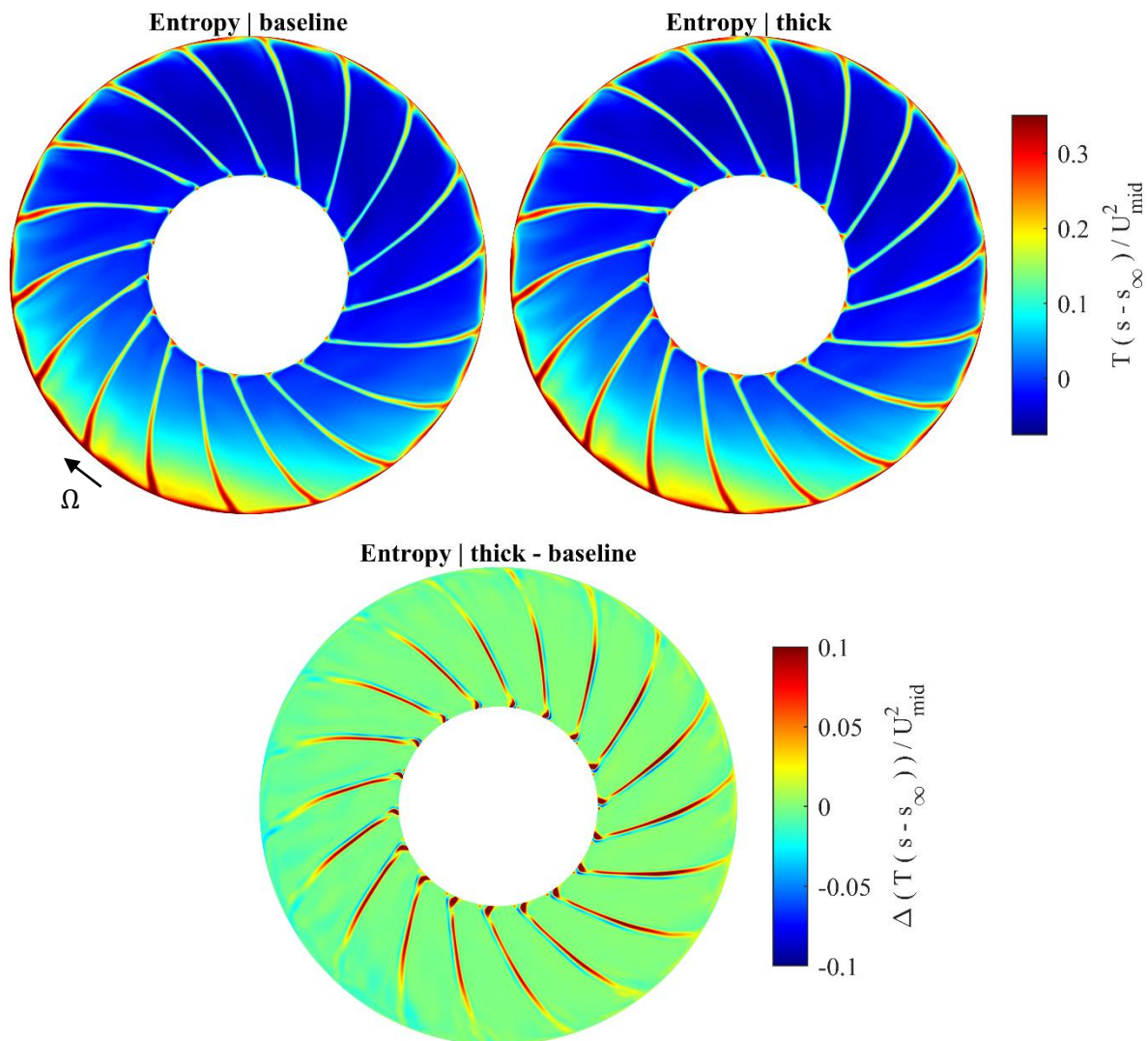


Figure 4.29 - Contours of entropy downstream of the rotor: baseline vs redesign

are slightly stronger in the thick blade (cf. Figure 4.23), causing thicker boundary layers and slightly thicker wakes.

#### 4.6.6 Impact on OGV and ESS Losses

The OGV and ESS flow fields depend on the rotor exit flow field. Variation around the circumference that occurs due to distortion dictates the angles seen by the stator blades. This causes variation in loss around the circumference.

Swirl angle and Mach number circumferential variation, upstream of the OGV, is shown in Figure 4.30. The differences are small, with the swirl angle approximately  $2^\circ$  higher for the thick blade. The Mach number is slightly reduced compared to the baseline blade. The difference is higher closer to the hub. As a result of these variations, incidence onto the OGV blades increases. However, the incidence variation is already very severe with the distortion present so the additional change of the order of  $2^\circ$  does not affect the loss distribution significantly.

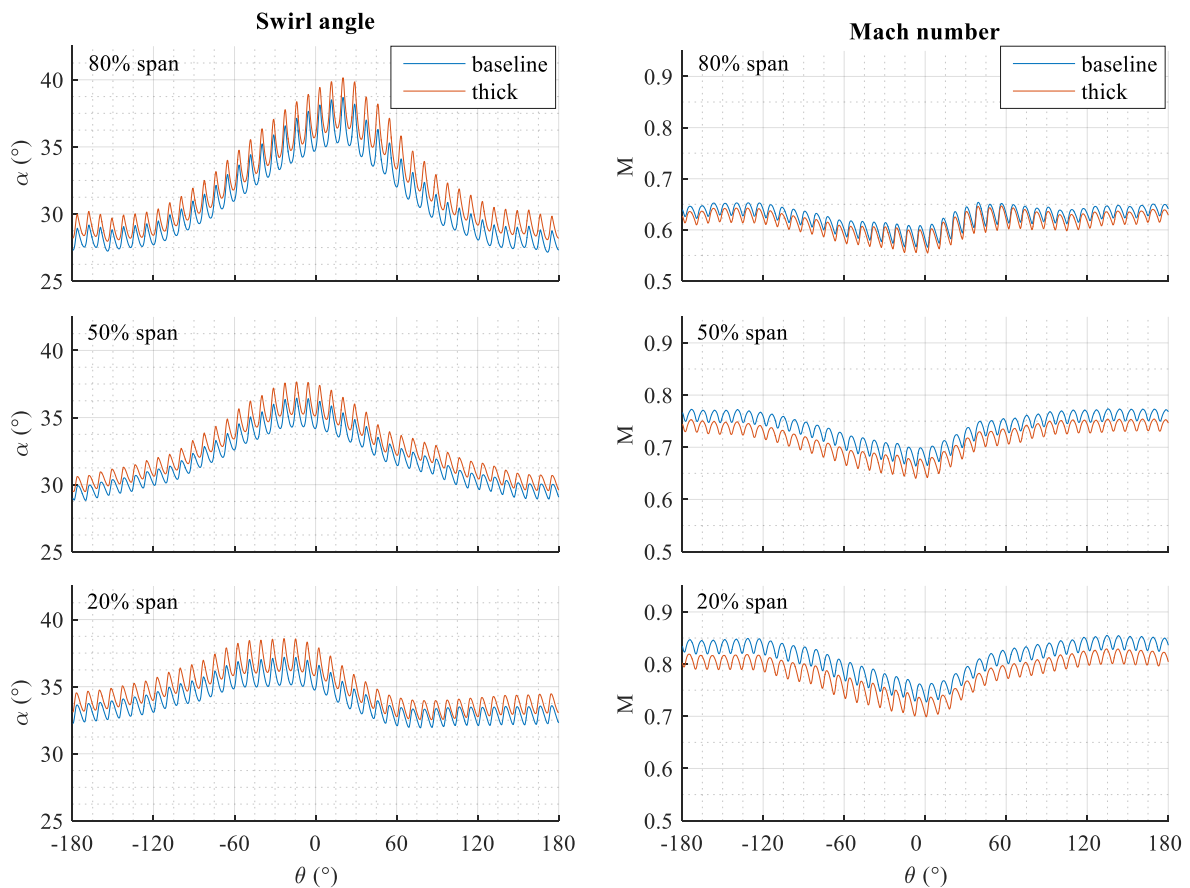


Figure 4.30 - Swirl angle and Mach number at a station just upstream of the OGV: baseline vs thick

Figure 4.31 shows contours of entropy downstream of the OGV and ESS in the two cases. The 0.1% drop in efficiency through the OGV and ESS is due to slight differences in the ESS hub



region and in the counter-swirl region at the tip of the OGV. The former is due to worsened hub region separations in the rotor. The hub separations and reduced mass flux in this region of the flow lead to off-design incidence in the ESS. Possible non-axisymmetric design, and lean and sweep could be employed to resolve the issue. The OGV wake size increase occurs at the tip in the region  $-10^\circ < \theta < 60^\circ$ . Figure 4.30 shows that this is the region where the incidence is the highest. The additional  $2^\circ$  increase in incidence is the main cause of the thicker wakes downstream of the OGV.

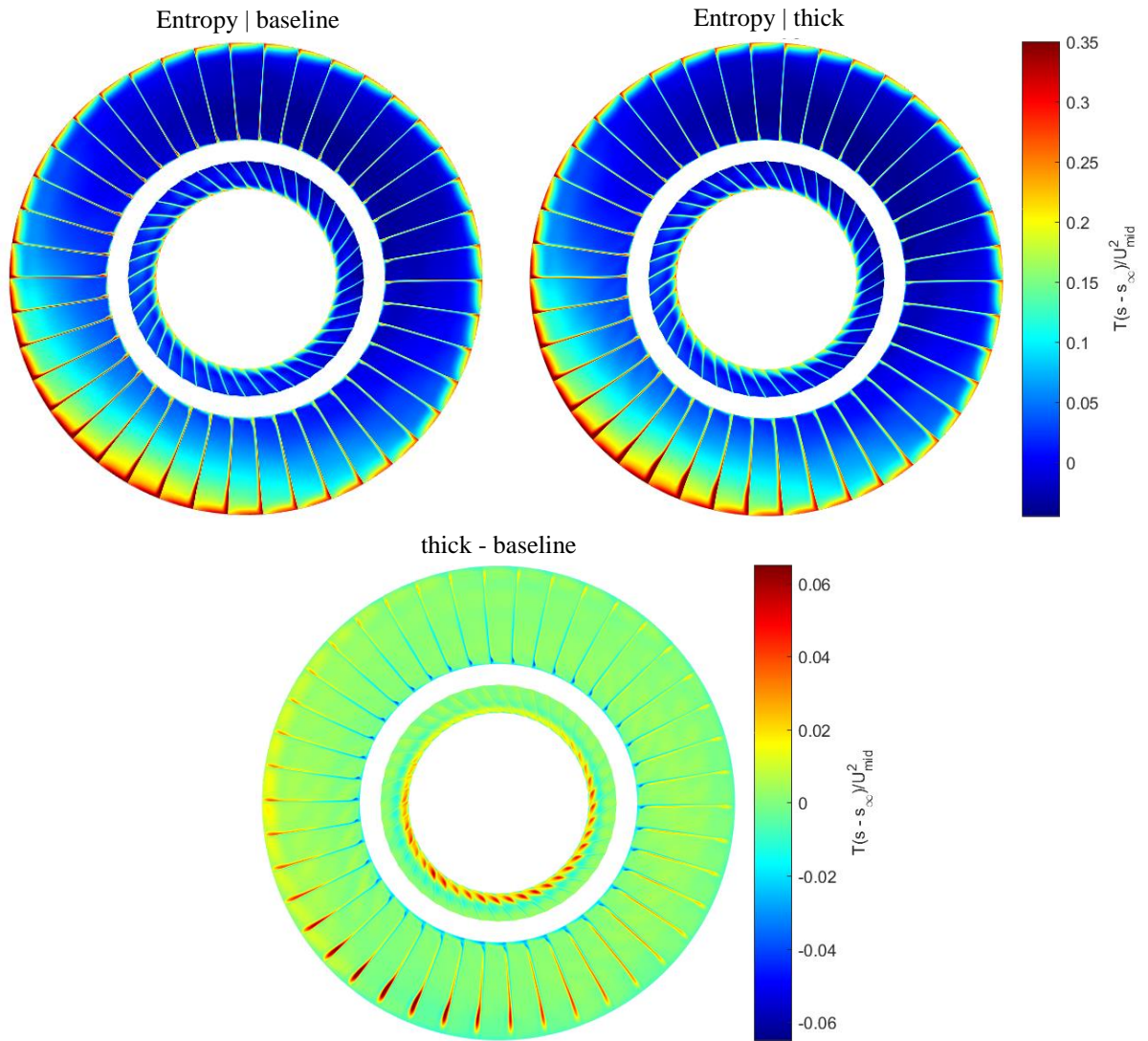


Figure 4.31 - Contours of entropy downstream of the stage: baseline vs redesign

## 4.7 Summary

A linear scaling factor, which varied radially, was applied to thickening the root and aerofoil of the VITAL rotor. This was successful in increasing the 1F-1EO margin from 20% to 60%.

The aerodynamic impact of thickening up the VITAL fan rotor blade to satisfy the 1F-1EO margin requirement set by the mechanical design considerations is investigated in this chapter. Implementation of the required thickening up of the hub sections results in a moderate impact on aerodynamic performance. Most of the differences occur in the hub region of the blade due to raised Mach numbers on the thicker blade sections and increased flow redistribution towards the tip. There is also some additional OGV loss due to increased swirl angles.

The overall effect of the blade design change can be summarised as follows:

- A drop in efficiency of 0.5% in clean flow
- A mass flow reduction of 2% in clean flow
- Similar drops in efficiency and mass flow for distorted flow

The drop in efficiency due to BLI type distortion is larger by a factor of 3, while the drop in mass flow is similar, i.e.:

- A drop in efficiency of 1.5%
- A mass flow reduction of 1.4%

The drop in mass flow is undesirable since it leads to a reduction in thrust. This research found that the drop occurred due to a reduction in the throat area. Recovery of the lost mass flow could be achieved by re-staggering the blade, running at a higher speed or increasing the fan diameter. The next chapter investigates the impact of modifying rotor radial work profile on aerodynamic performance.

# Chapter 5

## Aerodynamic Redesign of a Low-Speed BLI Fan

The aim of this chapter is to investigate the impact of work input profile on the BLI rig fan performance in the BLI flow.

The BLI rig rotor blade geometry was modified to change its work input profile in clean flow. The target was to keep the same overall loading while offloading the tip and the hub. The reduction in work at these two regions of the blade was balanced by an increase in work input at the mid-span.

CFD was used to aid the redesign process and predict the redesign blade performance. The final redesign was manufactured in-house and tested in clean and distorted flow in the BLI rig.

The redesign process is described first and the redesign blade parameters are given. Experimental measurements are used for the redesign performance analysis. The overall performance in clean and distorted flows is presented. A comparison with the baseline blade performance is made, followed by a detailed analysis of the similarities and differences of the two flows.

### 5.1 Blade Redesign

#### 5.1.1 Redesign Target

The redesign target was to modify the work input profile while keeping the same design flow coefficient and stage loading. The summary of all the design changes described in this section is given in Table 5.1 and the main overall design parameters that are maintained are given in Table 3.1.

The baseline blade has a free vortex design, with approximately constant work input at all radii, except close to the end-walls. The aim of the redesign was to modify the blade design such that the hub and tip are offloaded, while the mid-span loading is increased to balance the reduction. This is shown schematically in Figure 5.1. The intent was to reduce the loading at the tip by approximately 15-20% and increase it at mid-span by approximately 15%, with the loading

profiles crossing at around 1/3 and 2/3 of the span. Blade angles and velocity triangles are shown as well in the figure. The desired modification can be implemented by changing the exit metal angle,  $\chi_2$ , in order to increase or decrease the required flow turning. The tip-gap size was kept the same.

Region	Change	Aim
Tip	Increase $\chi_1$ and $\chi_2$	Reduce peak incidence and loading in distorted flow, hence reducing loss and improving the stability margin
Mid-span	Increase $\chi_1$	Reduce peak incidence in distorted flow
	Decrease $\chi_2$	Increase work input
	Increase chord	Lower diffusion
	Move forward positions of maximum camber and thickness	Create a front-loaded blade - better performance at low speed
Hub	Decrease $\chi_1$ and $\chi_2$	Adjust incidence and decrease work input

Table 5.1 – Redesign targets

The increase in work at the mid-span inevitably leads to an increase in diffusion. The chord length at the mid-span was adjusted accordingly to reduce the diffusion levels in this region. The chord was not modified in the tip or hub regions.

Another blade parameter modified during the redesign was the inlet metal angle,  $\chi_1$ . This was done in order to reduce peak incidence variations seen in distorted flow, with the intention of reducing the losses in distortion and improving the stability margin.

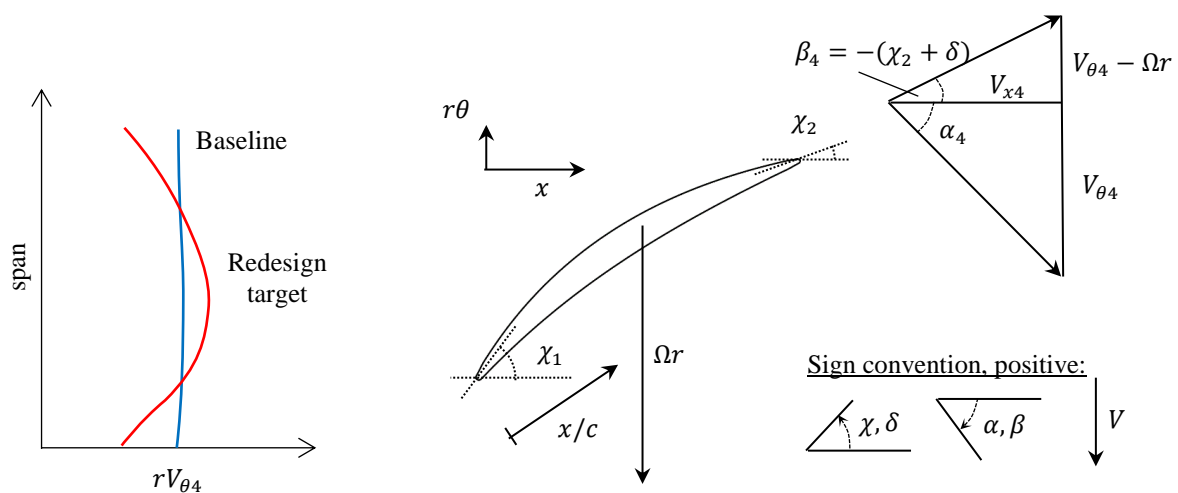


Figure 5.1 - Redesign target work input (left) and a blade section showing the inlet and exit metal angles and the coordinate system (right).

Another change in the redesign was to move the positions of maximum camber and thickness forward by approximately 10%, such a change is known to have a positive impact on a low Reynolds number section performance (Maffioli, et al., 2015). This design change is of secondary importance, but it was implemented to have a positive impact on efficiency. Note that the baseline design has double circular arc sections and peak maximum camber and thickness at half-chord.

### 5.1.2 Redesign Process

The main challenge in the redesign was to create a distribution of exit metal angles that will lead to the desired work profile while keeping the same operating point, i.e. the same stage loading at the same design flow coefficient. An iterative procedure was used until the desired work profile was matched.

The desired work distribution was created and the required exit angles  $\chi_2$  calculated. The main target was to match the stage loading at the design flow coefficient:

$$\psi = \psi_{bl} = \frac{\Omega((\overline{rV_\theta})_{4,bl} - (\overline{rV_\theta})_{3,bl})}{\bar{U}^2} = \frac{\Omega((\overline{rV_\theta})_{4,re} - (\overline{rV_\theta})_{3,re})}{\bar{U}^2} = \psi_{re} \quad (5.1)$$

Knowing the target stage loading  $\psi$ , the target mass averaged  $(\overline{rV_\theta})_{4,re}$  can be expressed as:

$$(\overline{rV_\theta})_{4,re} = \frac{\psi \bar{U}^2}{\Omega} + (\overline{rV_\theta})_{3,re} \quad (5.2)$$

Another expression for  $(\overline{rV_\theta})_{4,re}$  can be obtained by expressing it as mass averaged  $rV_{\theta 4,re}(r)$ , where the target profile  $rV_{\theta 4,re}(r)$  is:

$$rV_{\theta 4,re}(r) = f_{target}(r) + f_{endwall}(r) + \kappa \quad (5.3)$$

Where  $f_{target}(r)$  is a function that fixes the shape of the desired work profile,  $f_{endwall}(r)$  is a term that accounts for the increased work input close to the end-walls where the flow does not follow the blade metal angle, and  $\kappa$  is an arbitrary constant that allows “fine tuning” so that the required  $(\overline{rV_\theta})_{4,re}$  can be achieved.

The mass averaged  $(\overline{rV_\theta})_{4,re}$  is expressed using the terms in eq. (5.3) and an estimate of the axial velocity profile. The baseline case value of  $V_{x4}(r)$  is used in the first iteration. The term

$f_{target}(r)$  is set to the desired profile,  $f_{endwall}(r)$  is estimated from the baseline solution in the first iteration, and the constant term  $\kappa$  is initially set to zero.

$$\overline{(rV_\theta)}_{4,re} = \frac{\sum (f_{target}(r) + f_{endwall}(r) + \kappa) V_{x4}(r) r \delta r}{\sum V_{x4}(r) r \delta r} \quad (5.4)$$

The constant  $\kappa$  is found by substituting the expressions for mass averaged  $\overline{(rV_\theta)}_{4,re}$  in equation (5.4) into equation (5.2). On the right-hand side of the equation (5.2), the first term is known, while  $\overline{(rV_\theta)}_{3,re}$  is very close to zero and is negligible. It was included in the calculation nevertheless, and its value was set to  $\overline{(rV_\theta)}_{3,bl}$  in the first iteration. Once  $\kappa$  is found, an estimate of the distribution  $V_{\theta4}(r)$  is known from eq. (5.3).

From the velocity triangles in Figure 5.1:

$$\tan \beta_4(r) = \frac{V_{\theta4}(r) - \Omega r}{V_{x4}(r)} \quad (5.5)$$

Using the estimated  $V_{\theta4}(r)$  and assumed  $V_{x4}(r)$ , and noting that  $\beta_4 = -(\chi_2 + \delta)$ , the exit metal blade angle distribution  $\chi_2(r)$  can be found:

$$\chi_2(r) = -\beta_4(r) - \delta(r) = -\text{atan} \frac{V_{\theta4}(r) - \Omega r}{V_{x4}(r)} - \delta(r) \quad (5.6)$$

In the first iteration, deviation  $\delta(r)$  is set to the value from the baseline case experiment, as measured in clean flow.

An estimate of the distribution of  $\chi_2(r)$  needed for achieving the desired work profile obtained from equation (5.6) was implemented using the method described in section 3.2.4. Steady CFD was run to find the new blade performance. Estimates of  $V_{x4}(r)$ ,  $f_{endwall}(r)$ ,  $\delta(r)$ , and  $\overline{(rV_\theta)}_{3,re}$  are set to the values in the most recent CFD run and the procedure is repeated. The desired angle distribution that achieves both the set operating point and the desired work profile was obtained after several iterations.

The described process was carried out in parallel with other design changes. Inlet metal angle  $\chi_1$ , the chord extension at the mid-span and position of maximum camber and thickness modifications did not affect the previously described process in any way. These modifications were implemented manually based on outcomes of the CFD runs.

### 5.1.3 Final Redesign

CAD models of the baseline and the final redesign blade are shown in Figure 5.2. Hub, mid-span and tip sections are also shown for comparison. The sections are stacked radially, with no lean or sweep. The sections in the figure are flipped for the purpose of showing them in a conventional way with the LE on the left.

The main geometry parameters for the baseline and the final redesign blades are shown in Figure 5.3. Change in the blade angles leads to a significant change in camber. There is more camber at the tip and the mid-span and much less camber at the hub. In a transonic fan, this may be a cause for concern as this kind of modification would reduce the stiffness of the 1F mode.

The figure shows that the locations of maximum camber and thickness were successfully moved forward by approximately 10%. Thickness-to-chord distribution was kept constant, while the pitch-to-chord ratio reduced slightly at mid-span as a result of increasing the chord length to control the level of diffusion.

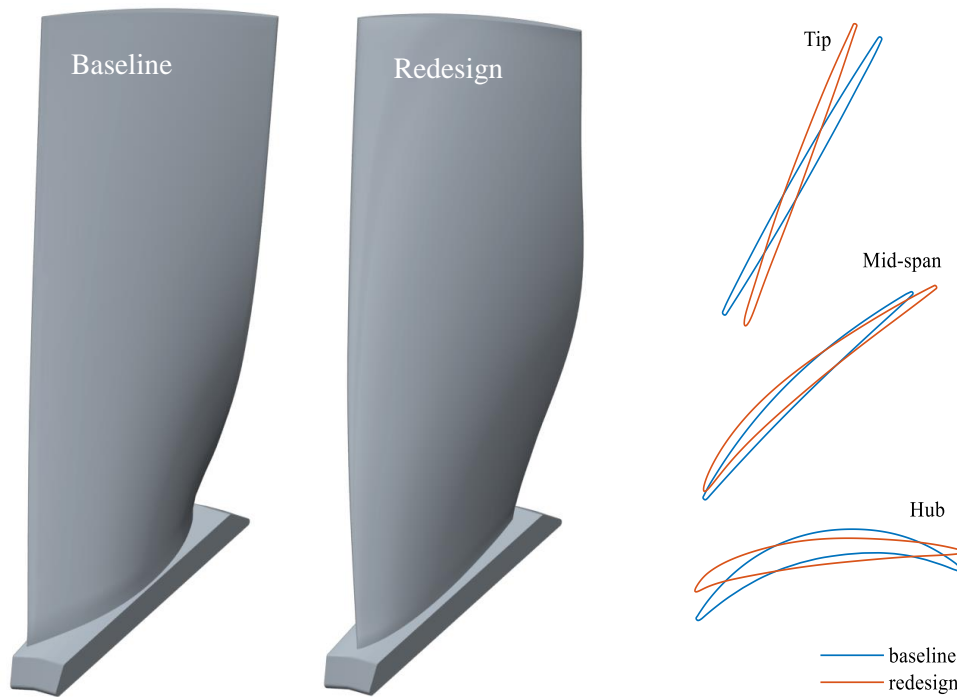


Figure 5.2 - CAD models of the baseline and redesign blades (left) and cross sections at tip, mid-span and hub (right)

The redesigned blade was manufactured in-house on a 5-axis machine, with the assistance of James Taylor (Taylor & Miller, 2017). The redesign blades were cut from solid Aluminium

blocks. Figure 5.4 shows one of the blocks in the 5-axis machine at the end of the process. The figure also shows the redesign and the baseline blades.

The redesign tip gap was the same as the baseline blade. This was confirmed by a 3D scan of the blades as well as by a feeler gauge once the blades were installed in the rig. The blade surface finish was slightly different since the material and manufacturing process for the

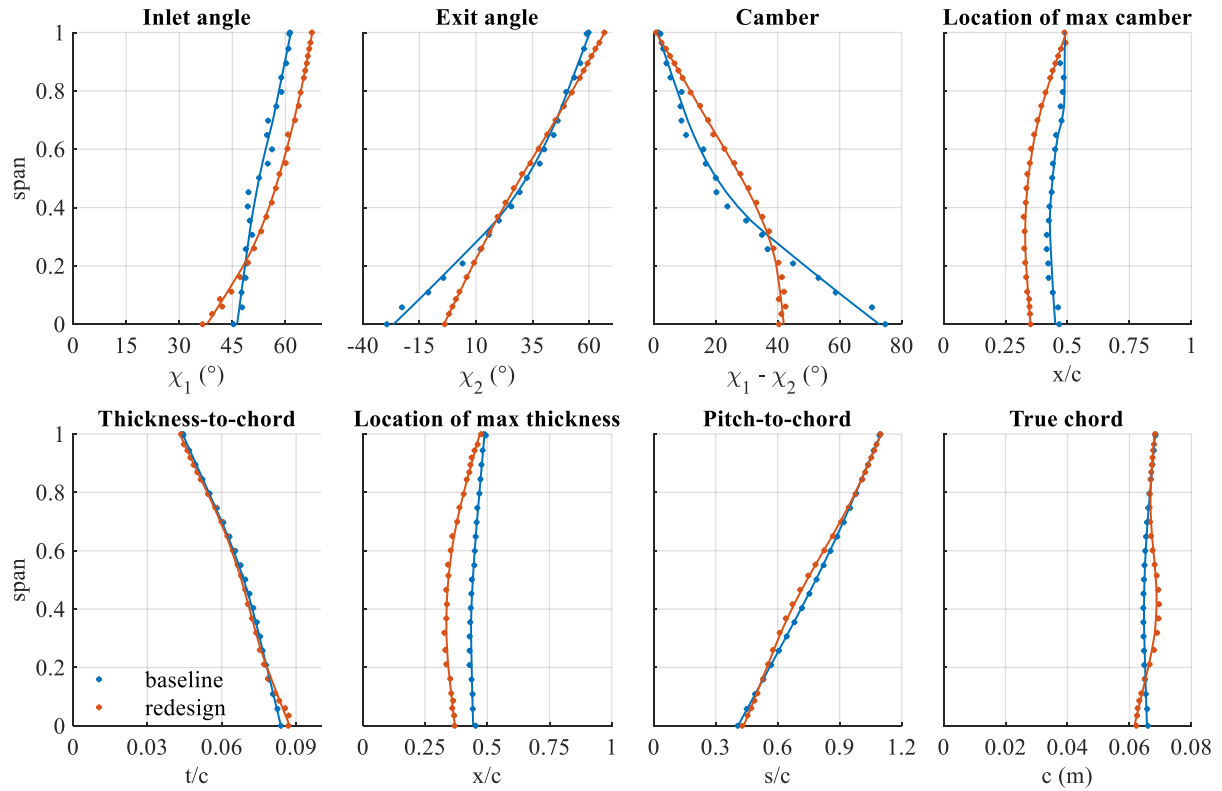


Figure 5.3 – Geometry parameters: baseline vs redesign blade

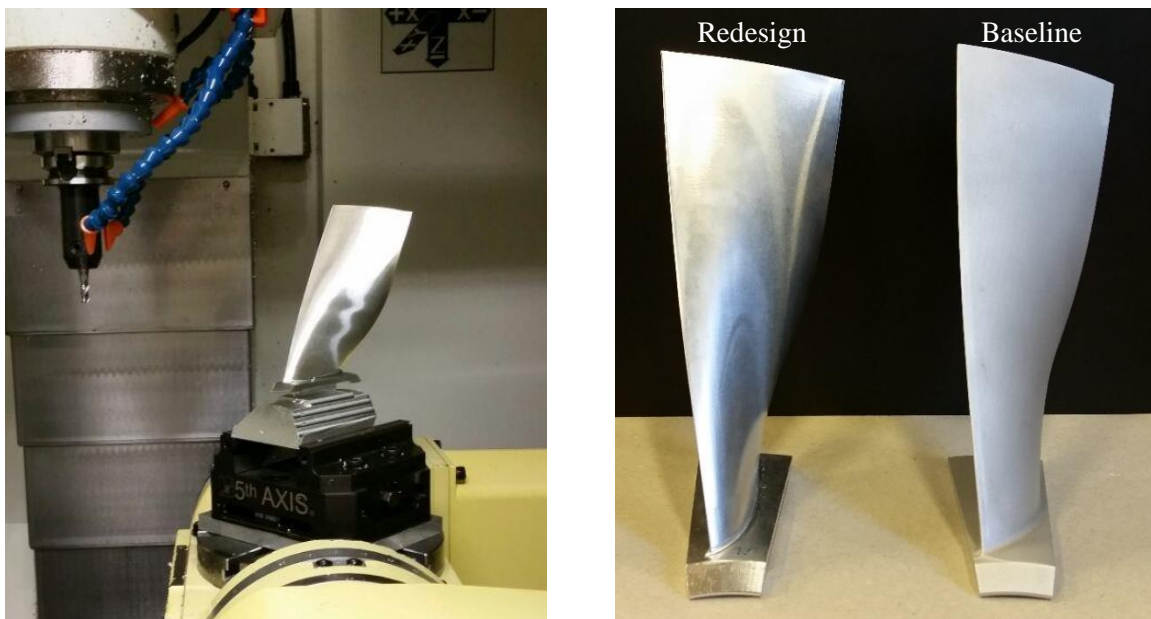


Figure 5.4 – Redesign blade manufacture in the 5-axis machine (left), and redesign and baseline blades (right)



redesign blades were new. However, the impact of the difference in surface roughness was not investigated. All the redesign blades have the same weight with a variation of less than 1%.

## 5.2 Aerodynamic Performance

Traverses in clean and distorted flows were carried out using the experimental setup described in section 3.2.2 to investigate the performance of the redesign blade. The static pressure rise and stage loading characteristics based on experimental measurements are shown in Figure 5.5. The two graphs each show two characteristics with the baseline and the redesign blade. The red line corresponding to the redesign blade extends to lower flow coefficients showing improved range with the redesign blade. This is discussed further in Chapter 6.

Two operating points in distorted flow, DP and NS, are shown for each of the two blades. Design operating points DP are the operating points at the design flow coefficient  $\phi = 0.5$ . Near stall operating points NS are the last stable operating points before the rig stalls. The characteristics show that the stage loading was matched as in clean flow, as was desired by the redesign. There is a slight drop of loading in BLI for both the baseline and redesign blades.

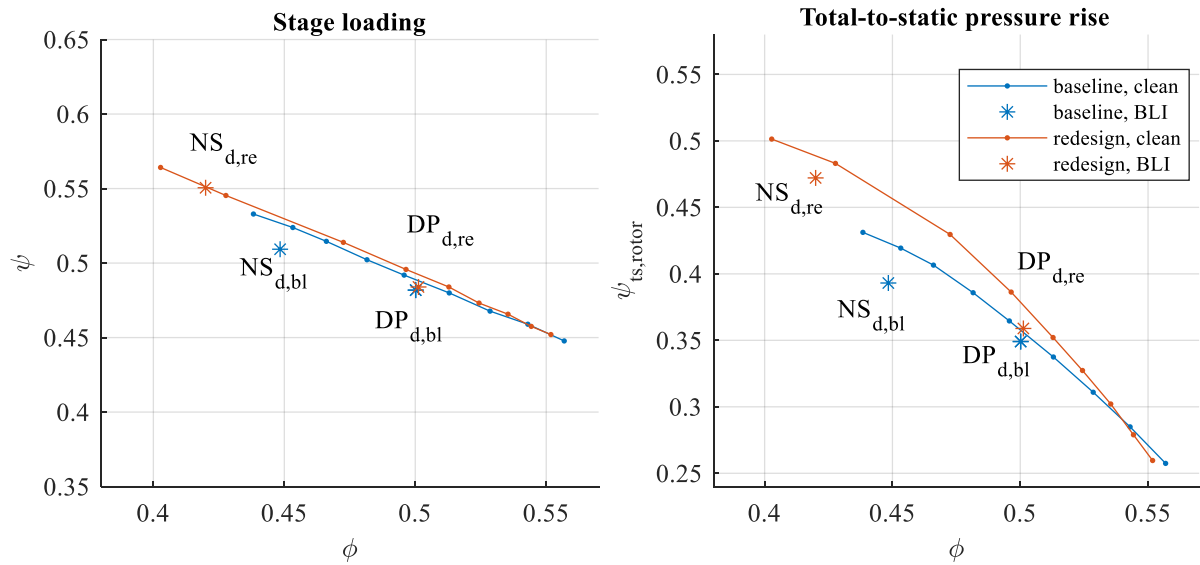


Figure 5.5 – Stage loading and rotor total-to-static pressure rise characteristics (exp)

Comparison of performances of the baseline and redesign blades at DP is summarised in Table 5.2. The performance at the design point is significantly improved. There is a 1.8% improvement in efficiency in clean flow and a 3.6% improvement in BLI flow. Moreover, for the redesign blade, the efficiency is higher in BLI flow. Table 5.2 shows that total-to-total pressure rise is increased with the redesign blade, and the value is higher in BLI flow, while Figure 5.5 shows that loading in BLI is lower. This is believed to occur due to a reduction in

losses at the tip in BLI, especially in the counter-swirl region. The following sections will explore the details of the flow field responsible for the differences measured.

	Baseline		Redesign	
	Clean	BLI	Clean	BLI
$\phi_{DP}$	0.500	0.500	0.500	0.501
$\phi_{NS}$	0.438	0.449	0.403	0.420
$\psi_{tt,rotor,DP}$	0.882	0.880	0.911	0.918
$\eta_{tt,rotor,DP}$	91.9%	91.3%	93.7%	94.9%

Table 5.2 - Performance parameters in clean and distorted flows

A sensitivity analysis was carried out to investigate how the integral flow parameters change due to variation in flow angles. Results are shown in Figure 5.6. The angles  $\alpha$  and  $\zeta$  were varied independently in steps of  $1.5^\circ$  up to  $\pm 4.5^\circ$ . The variation in flow angles did not affect stagnation pressure, as shown in Figure 5.6, since the stagnation pressure is found directly from the probe pressure measurements. The absolute velocity is also determined directly from the measurement data. However, its components in the axial and tangential directions depend on the flow angles, which affects both the flow coefficient and stage loading. Small experimental errors, due to probe head deflections of the order of  $\Delta\zeta = \pm 1.5^\circ$  can lead to a  $0.5\% - 1\%$  variation in total-to-total efficiency. In combination with  $\Delta\alpha = \pm 1.5^\circ$ , the experimental error in total-to-total efficiency can be of the order of  $1.5\%$ . Even though a consistent systematic error at all measurement points is unlikely to occur, i.e.  $\Delta\alpha$  is not expected to be  $2^\circ$  at all measurement locations, it should be noted that there is an uncertainty associated with the value of total-to-total efficiency, which is estimated to be within  $\pm 0.5\%$ .

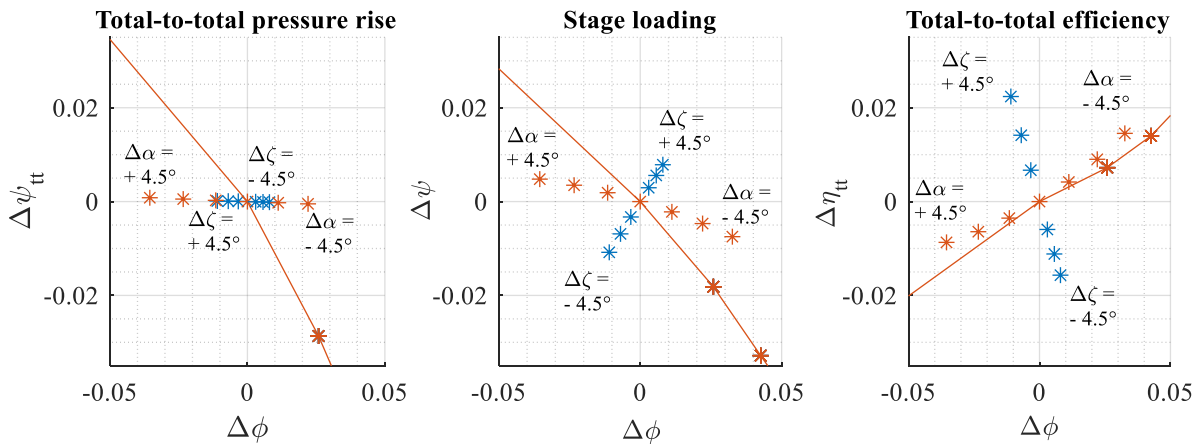


Figure 5.6 – Sensitivity analysis for a point in clean flow with redesigned blade, showing how total-to-total pressure rise, stage loading and total-to-total efficiency vary with flow angles. Swirl angle  $\alpha$  and radial angle  $\zeta$  are varied independently in steps of  $1.5^\circ$  up to  $\pm 4.5^\circ$ . The extreme points for either angle are labelled in the plots.

## 5.3 Clean Flow Performance

### 5.3.1 Upstream Flow Conditions

Flow conditions upstream of the rotor at station 3 are shown in Figure 5.7. Axial velocity, relative swirl angle and radial angle are shown. Absolute swirl angle is zero as there are no blade rows ahead of the rotor. The figure shows experimental and CFD profiles with both the baseline and the redesign blades.

The experimental axial velocity profiles show that there is little variation between the two cases, indicating that the work input profile does not have a strong impact on the upstream flow in clean flow conditions. This is expected since the coupling between the rotor pressure field and the upstream flow occurs over a length scale of the order of one blade pitch (Gunn, 2015).

There is a slight variation at the tip where the casing boundary layer is thicker in the redesign blade case. Since work input is reduced here, suction is lower, hence a tip streamtube contracts less than with the baseline blade.

The CFD runs were carried out at a slightly higher flow coefficient. In the CFD, more flow is passed at the tip, which is a sign that blockage within the blade row is not accurately predicted in CFD. Consequently, there is less flow at the hub (in this case it is the same due to the discrepancy in the mass flow).

Incidence depends on the axial velocity profile and swirl. Since there is no blade-row ahead of the fan stage, there is no swirl and the incidence depends on the axial velocity profile only.

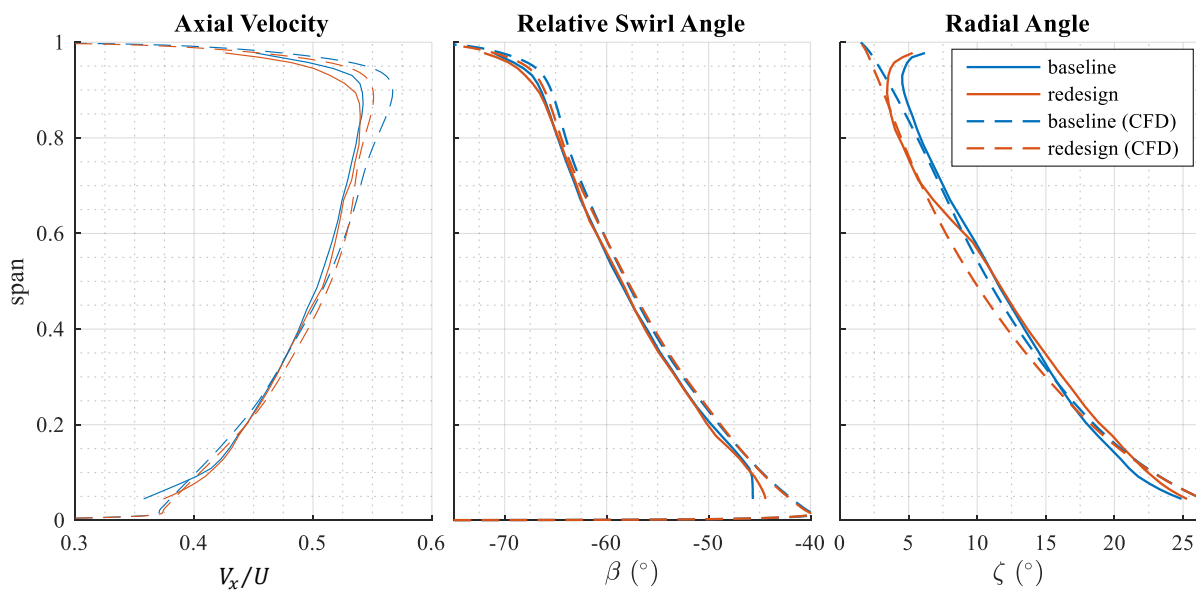


Figure 5.7 – Flow conditions at station 3

Since the axial velocity profiles are the same for the two cases, the relative swirl angles are the same as shown in Figure 5.7. Therefore, incidence variation follows the inlet metal angle variation.

The radial angle plot shows that there is more radial flow at the tip of the baseline blade. This goes in line with the finding that a tip streamtube contracts less ahead of the redesign blade. Further down the span, the situation is different and there is just slightly more radial flow in the redesign blade.

Typical surface pressure distributions in Figure 5.8 can be used to analyse pressure distributions in Figure 5.9 and see how incidence varies along the span. At high incidence, a blade section is typically front-loaded. As the incidence reduces, the loading moves rearward. At high negative incidence, there is a suction peak at the PS.

Figure 5.9 shows that loading at 10% span is low. At 30% span, there is slightly more loading at the front of the redesign blade due to maximum camber being moved forward in this section which has high camber. At 50% span, the baseline blade starts to experience increased incidence. High incidence becomes even more pronounced at 70% span. There is less incidence in the redesign blade, and front loading is mostly due to the maximum camber being forward at the front part of the section. At 90% span, there is negative incidence in both cases, with the suction peak on the PS being more pronounced in the baseline blade case. This is the region where the mass flow is increased in CFD relative to experiment, resulting in negative incidence. The flow angles are lower at this span fraction, especially in the baseline blade, as shown in Figure 5.7. Higher up at 95% span, the incidence is positive and high in both blades, due to low  $V_x$  in the boundary layers. The incidence is especially high in the baseline blade. Overall, the loading distribution plots show that the redesign is better aligned to incoming flow.

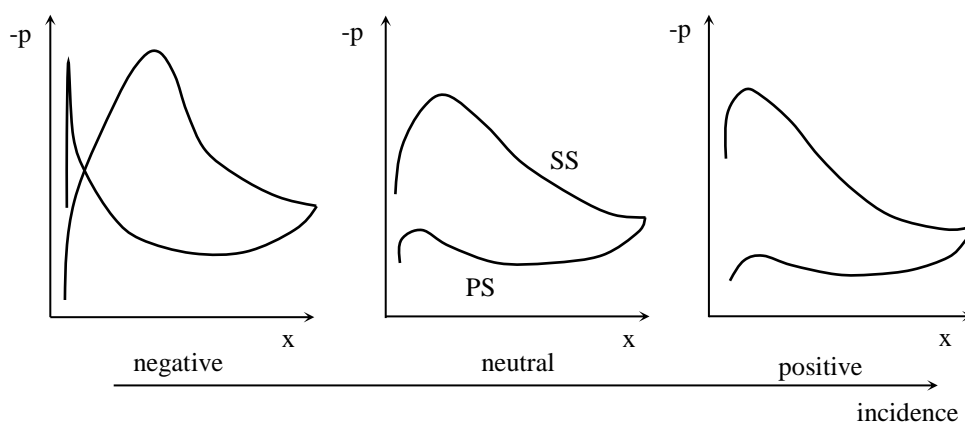


Figure 5.8 - Typical variation in pressure distributions with incidence, adapted from (Xu, 2014)

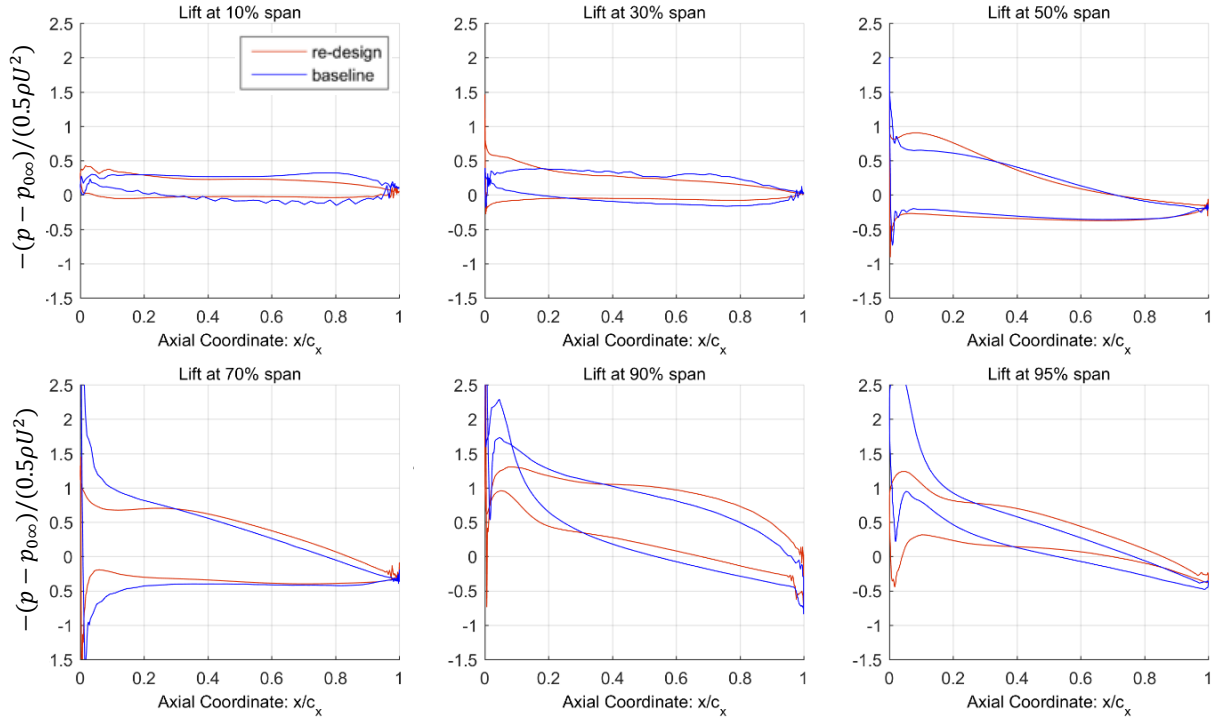


Figure 5.9 – Pressure distributions at various blade sections (CFD)

### 5.3.2 Work Input Profile and Losses

Specific work, stagnation pressure and axial velocity measured at station 4 downstream of the rotor are shown in Figure 5.10. The predicted values are shown as well. The plots confirm that the design intent was achieved and that the desired reductions in loading at the hub and the tip are satisfied.

Experimental results show that the specific work at the mid-span is approximately 15% larger than with the baseline blade, while it is 20% lower at the tip around 90% span and 10% lower at the hub, as required by the design intent. The crossing points occur at approximately 1/3 and 2/3 of the span. Peak stagnation pressure rise occurs at mid-span and is approximately 20% larger in the redesign blade. The drop of stagnation pressure rise is around 15% at the tip and 15% at the hub. The variation in pressure rise goes in line with the variation in work input, as expected. CFD accurately predicts both the pressure rise and work input, except for small differences in some regions.

The change in work input affects mass flow redistribution within the blade-row. Axial velocity reduction occurs at the tip of the redesign blade. This is balanced by an increase in flow at the mid-span. Mass flux close to the hub is similar in both cases.

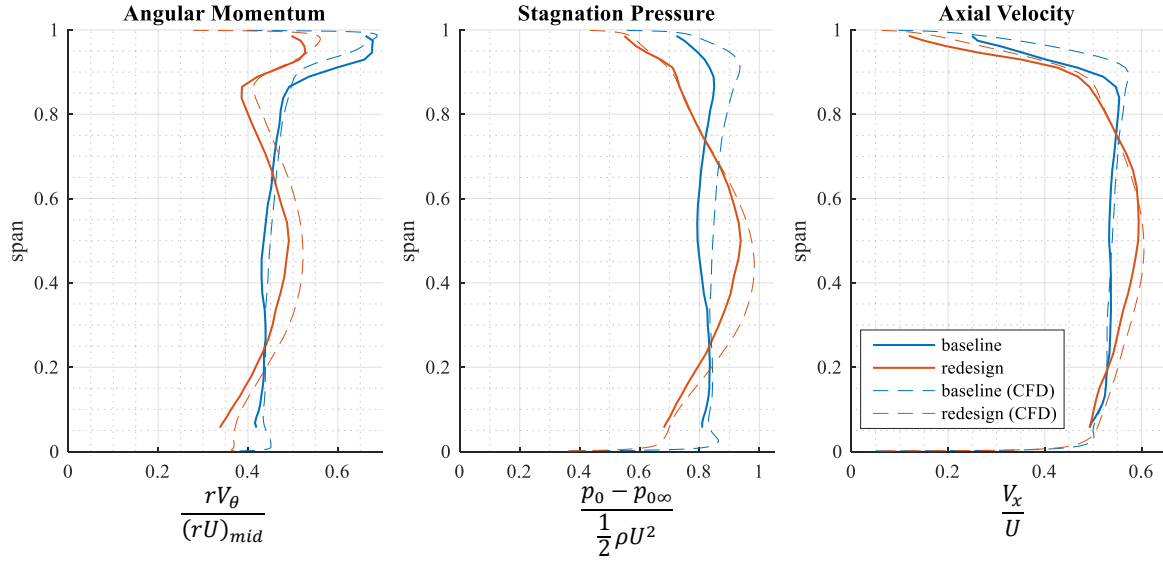


Figure 5.10 - Flow field downstream of the rotor at station 4

High work input which occurs at the mid-span leads to an increase in diffusion factor. The design intent was to increase the chord in this region to keep the diffusion factor at an acceptable level below 0.45. This was achieved successfully, as shown in Figure 5.11. The diffusion factor is calculated using the Lieblein's formula (Lieblein, et al., 1953). There is a reduction of the diffusion factor at the tip due to a reduction in loading in the tip region.

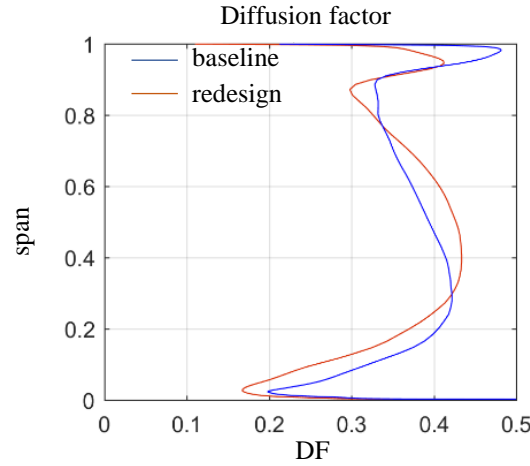


Figure 5.11 - Diffusion factor (CFD)

## 5.4 Distorted Flow Performance at Design Point

Unlike in clean flow, in distorted flow coupling between the fan and the intake pressure fields occurs over a longer length-scale, which is of the order of the fan diameter. The induced pressure field with low pressure in the low momentum region of the flow acts to drive the fluid towards the low momentum region, hence reducing the mass flow non-uniformity. As this redistribution occurs, four regions with qualitatively different upstream conditions can be

identified: i) high momentum, ii) co-swirl, iii) counter-swirl, and iv) low momentum. These are shown schematically in Figure 5.12.

The high momentum region is sometimes called the undistorted region. The flow conditions are similar to those in clean flow and there is not much swirl. However, since the flow coefficient is the same in clean and distorted flows, the high momentum region operates at a local flow coefficient which is higher than that at the design point in clean flow. Increased axial velocity means that the incidence levels are below that in clean flow at DP, as shown schematically in Figure 5.13.

The co-swirl region is the region of the flow in which the upstream flow is migrating around the spinner and in the same direction as the rotor rotation. This leads to a reduction in incidence, as shown in Figure 5.13, and a reduction in loading, making this a low work-input region. The level of diffusion is reduced too, due to low incidence and possibly even negative incidence, so the region is characterised by a low level of loss. Overall, the efficiency in this region is relatively high.

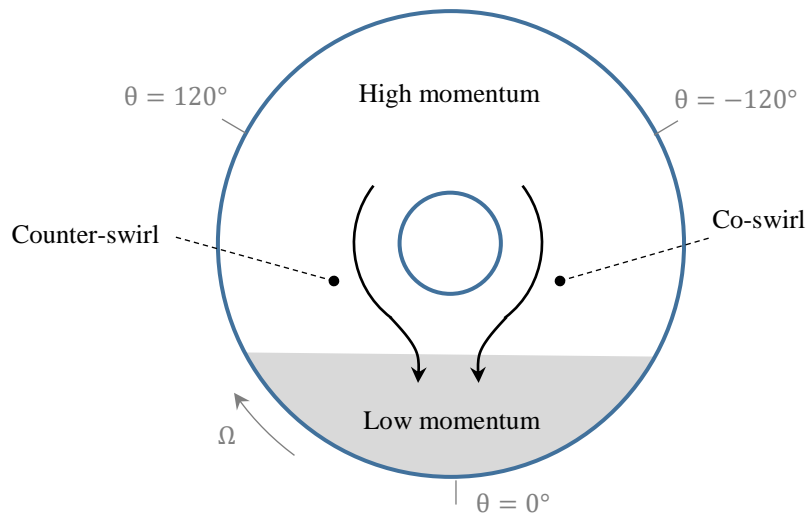


Figure 5.12 - Schematic of the main flow regions in BLI flow, station 3

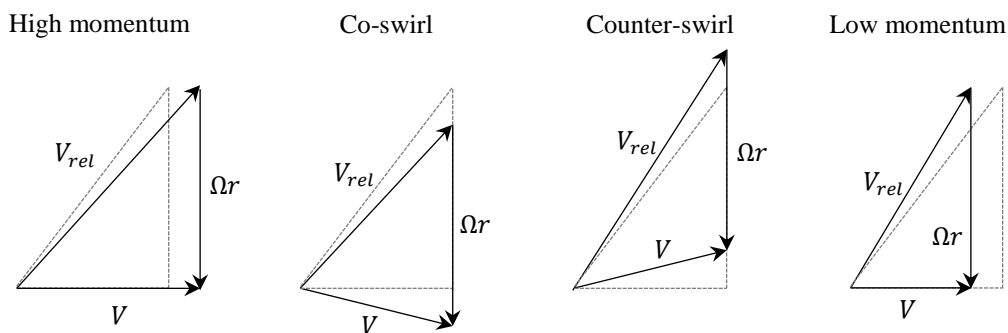


Figure 5.13 – Schematics of velocity triangles in the main flow regions at station 3

The counter-swirl region is the region of the flow in which the upstream flow is migrating towards the low momentum region and in the opposite direction to rotor rotation. The incidence is high in this region, so flow turning, work input and diffusion are high too. This is the most critical region in a distorted flow. The loss is the highest, especially at the tip where the casing boundary layer causes very high incidence levels. Stall disturbances first appear in this region during a stall inception event (see Chapter 6).

In the low momentum region, the incidence is high due to low axial velocity, as shown in Figure 5.13. However, this is not as critical as in the counter-swirl region. The main reason is a strong radial flow that occurs here. In the low momentum region, the work imparted by the blades forces the flow to redistribute and follow a similar radial mass flux distribution to that in clean flow. As a result, fluid close to the hub is moved towards the casing and this radial migration leads to a significant proportion of work input occurring due to centrifugal effects. Consequently, diffusion is low, as well as losses, so efficiency is high, which is counterintuitive since this is the distorted, low momentum region.

Performance of a fan in the BLI flow depends on the effects described. Work input, loss, diffusion, and stability depend on the upstream flow conditions and the radial flows within the blade row that determines the incidence, work input, and diffusion and loss levels. Only a brief description of the main flow features in distorted flow has been described. For a more comprehensive description and explanations, refer to (Gunn & Hall, 2014) and (Gunn, 2015). In this section, the focus is on understanding how these flow features are affected by the modifications in the rotor design, especially due to change in the work input profile.

#### **5.4.1 Impact of Work Input Profile on the Upstream Flow Redistribution**

Experimental measurements from the two cases, baseline and redesign, in BLI are shown in Figure 5.14. As flow redistribution in the intake occurs without mixing (Gunn, 2015), stagnation pressure is conserved along the streamlines and any significant changes in the flow redistribution pattern between stations 1 and 3 would be apparent in the stagnation pressure distribution at station 3. Work input profile does not have a strong impact on the upstream flow redistribution and there is little difference between the two stagnation pressure contours.

Static pressure gradient upstream of the fan is the driving force for redistribution. Measurements in Figure 5.14 show that the static pressure field at station 3 is similar in both cases. There are slight differences close to the hub and close to the casing. Where there is a difference in static pressure between the two cases, there is also a difference in velocity. The



lower static pressure at the tip in the counter-swirl region indicates that flow acceleration is slightly higher in the redesign blade. The situation is similar close to the hub, where there is also lower static pressure. Overall, the flow in the counter-swirl region accelerates more in the redesign blade. Likewise, it accelerates less in the co-swirl region close to the casing.

The slight change in the velocities reflects the fact that there is a slight difference in the detail of upstream flow redistribution. Consequently, there is a difference in swirl angle distributions

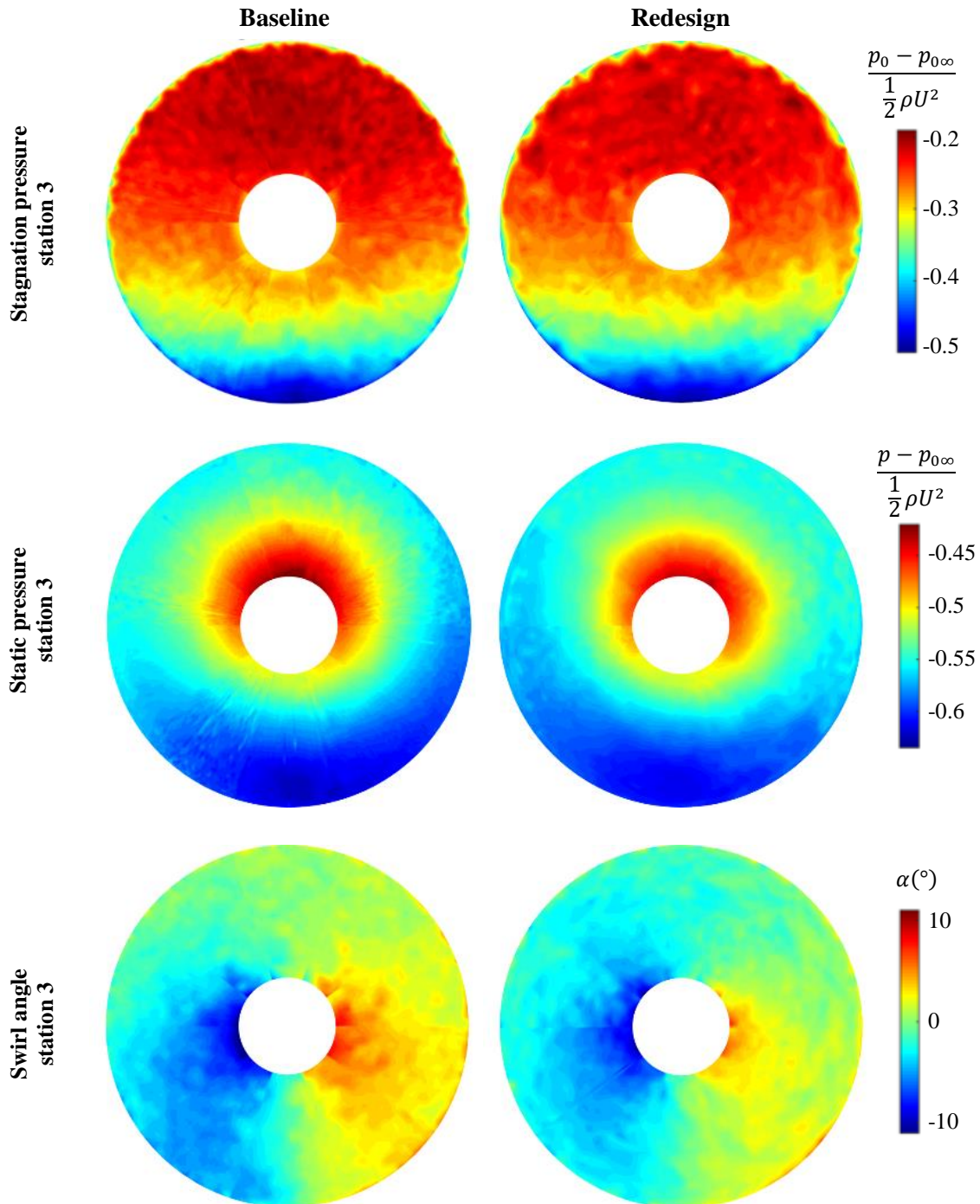


Figure 5.14 – Upstream flow conditions at station 3, stagnation and static pressures and swirl angle (exp)

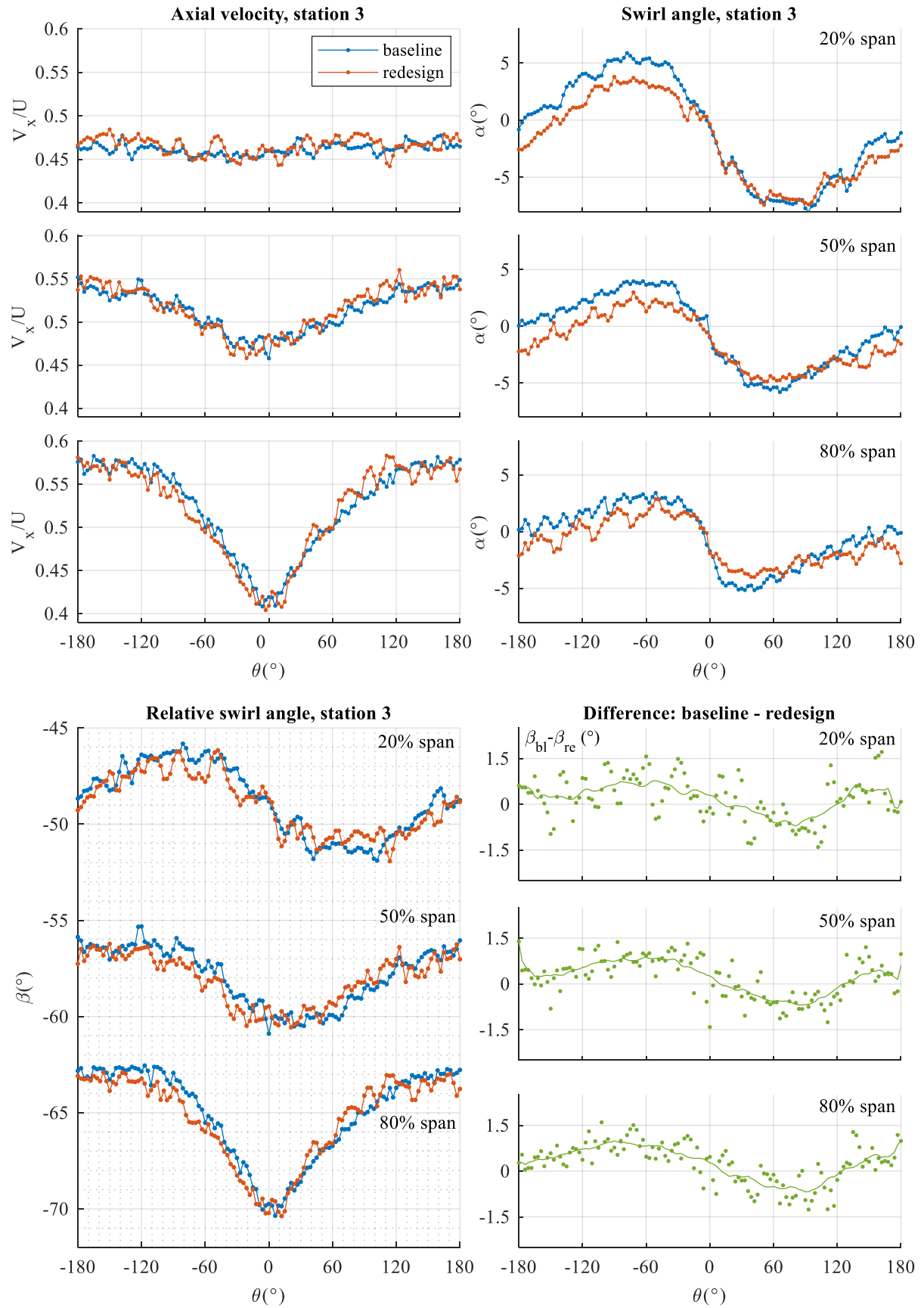


Figure 5.15 - Flow conditions at station 3, axial velocity, swirl angle and relative swirl angle (exp): baseline vs redesign

at station 3, as shown in Figure 5.14. The magnitudes of both positive and negative swirl angles are lower in the redesigned blades. This intensity of the differences is quantified in the circumferential plots in Figure 5.15.

Figure 5.15 shows unwrapped circumferential plots of axial velocity, swirl angle and relative swirl angle at station 3 at three span fractions: 20%, 50%, and 80% span. Difference between the relative swirl angles for the two cases is shown as well. The plots show that there are only slight differences between the measurements in the baseline and the redesign cases. Axial velocity plots at all three span-wise locations overlap, and there are only small differences which are of similar magnitude as the amplitudes of the wiggles caused by the distortion gauze.

Analysing closely the plot at 80% span, it can be noticed that there is a slight difference and that velocities are just slightly higher in the counter-swirl region and just slightly lower in the co-swirl region. This is expected as there is a similar variation in static pressures in those regions (see Figure 5.14). These differences in the axial velocity occurs at mid-span and tip, as shown in the radial plots in Figure 5.16.

Even though the details of flow redistribution are slightly different, the impact on incidence is minor. Variation in axial velocity is complemented by variation in swirl angle. Peak-to-peak magnitude is lower in the redesign blade at all three span fractions for which the line plots are shown. The differences are of the order of up to  $2^\circ$ . However, line plots of relative swirl angle show that there is a minor difference between the two cases. There is a sinusoidal variation with an amplitude of approximately  $1^\circ$  at all three spanwise locations, as shown in difference

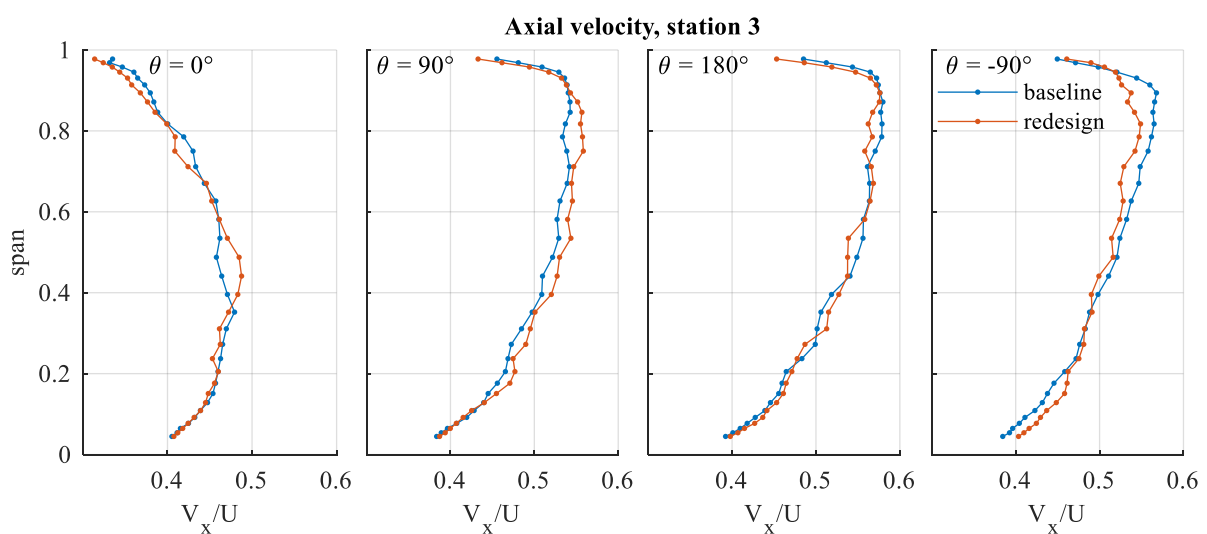


Figure 5.16 - Radial plots of axial velocity at four circumferential locations (exp)

plots. This is small compared to the design changes made which are of the order of  $5^\circ$ , so variation in incidence follows the variation in the inlet metal angles.

### 5.4.2 Rotor Flow Field

Contours of axial velocity downstream of the rotor at station 4 are shown in Figure 5.17. The plots show that there is high axial velocity at the mid-span in the redesigned blade, as expected from the clean flow performance. The contours of difference between the clean and distorted flows are shown as well. The contours show that there is little difference for both the baseline and the redesign case. In both of the cases, there is slightly higher axial velocity in the high momentum region of the flow and slightly lower axial velocity in the low momentum region of the flow. The plots indicate that distortion is mostly circumferential, with radial distortion being much less pronounced. Another major difference is the reduced size of the casing corner

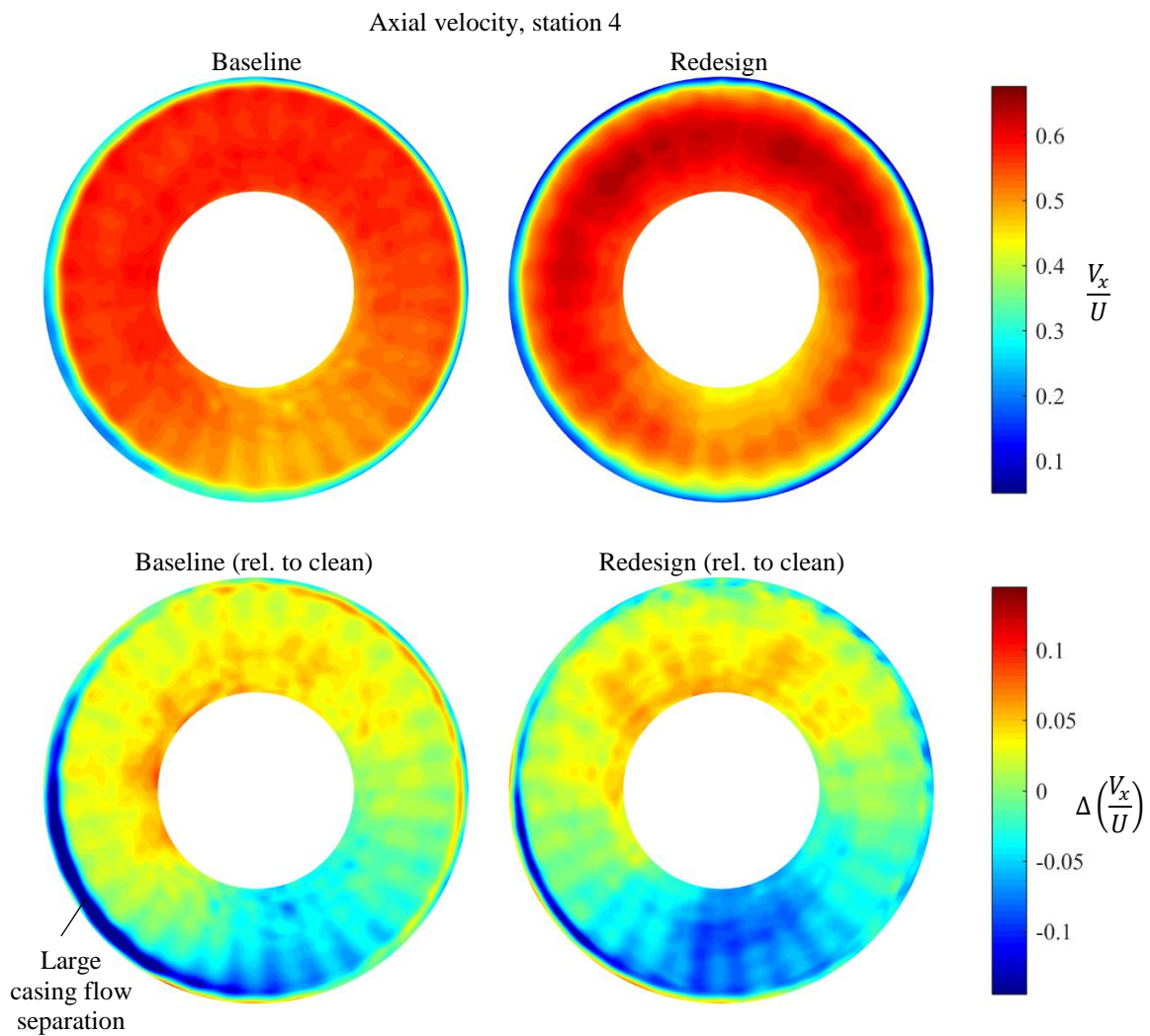


Figure 5.17 – Axial velocity at station 4 (above) and difference to clean flow (below) (exp)

separations in the counter-swirl region. This can be seen more clearly in Figure 5.18 and Figure 5.20.

Figure 5.18 shows radial profiles of axial velocity at stations 3 and 4. The line plots show that flow redistributes in such a way to have a similar spanwise distributions as in clean flow. The radial plot at  $\theta = 90^\circ$  with the baseline blade shows that there is a large casing flow separation in the counter-swirl region. One of the aims of the redesign was to reduce the size of the separation. The radial plot at  $\theta = 90^\circ$  with the redesign blade shows that this was achieved by the redesign, as is confirmed in Figure 5.19, which shows the size of the casing separation determined using the gradient based method described in (Khalid, 1995).

Comparison of radial profiles of axial velocity at various circumferential locations is shown in Figure 5.20. Unwrapped, circumferential plots at three span fractions are shown as well. The radial plots show that the size of the corner separations in the range  $\theta \in [-45^\circ, 180^\circ]$  is smaller with the redesign blade. At all circumferential locations, the radial profiles have a similar shape as the shape of the axial velocity profile in clean flow. For the redesign blade, the velocity is higher at the mid-span around the entire annulus, except in  $\theta \in [0, 45^\circ]$  where the magnitude

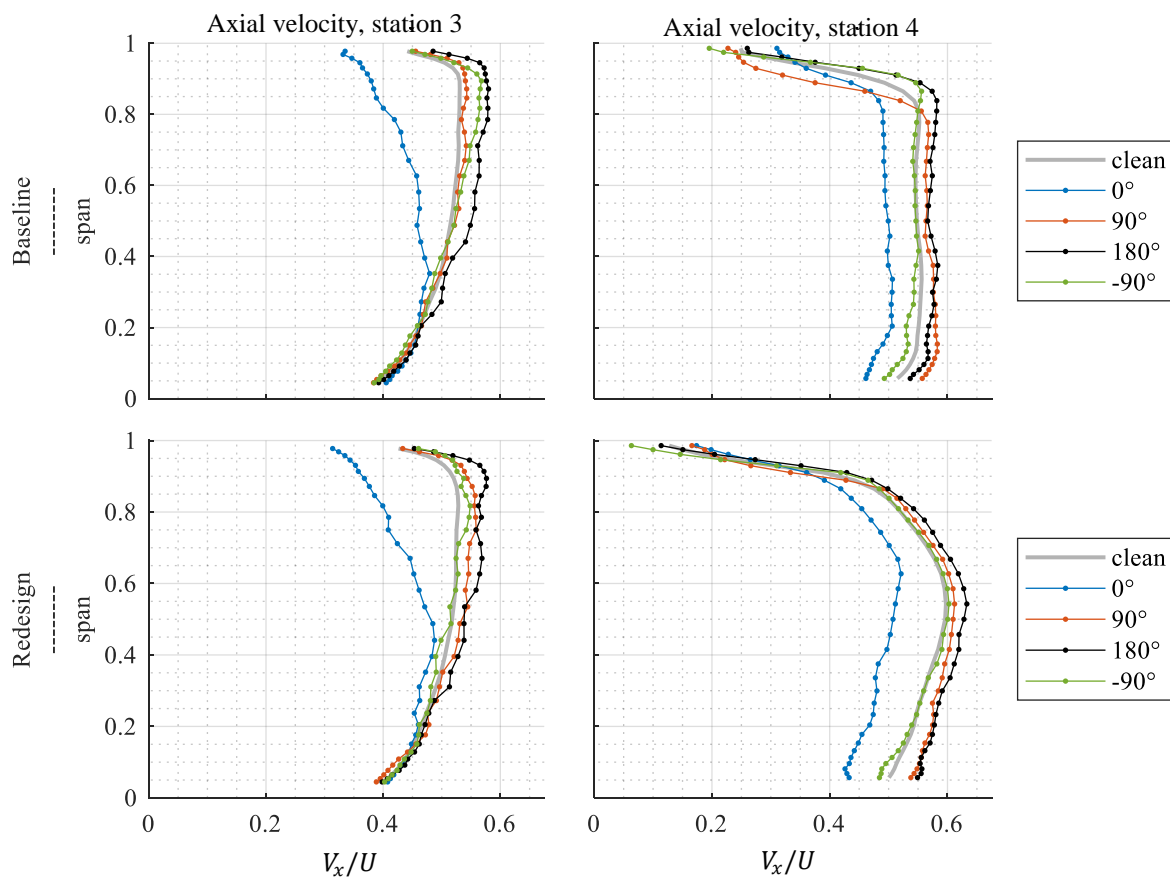


Figure 5.18 - Radial plots of axial velocity in distorted flow, stations 3 and 4 (exp)

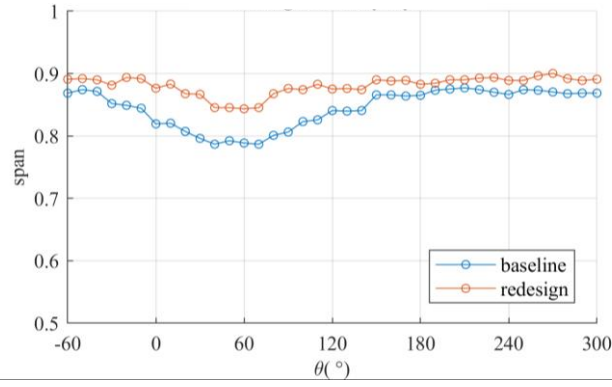


Figure 5.19 – Casing separation size at station 4 with the baseline and redesign blades. Casing separation occupies the region from the span fraction shown to 100% span.

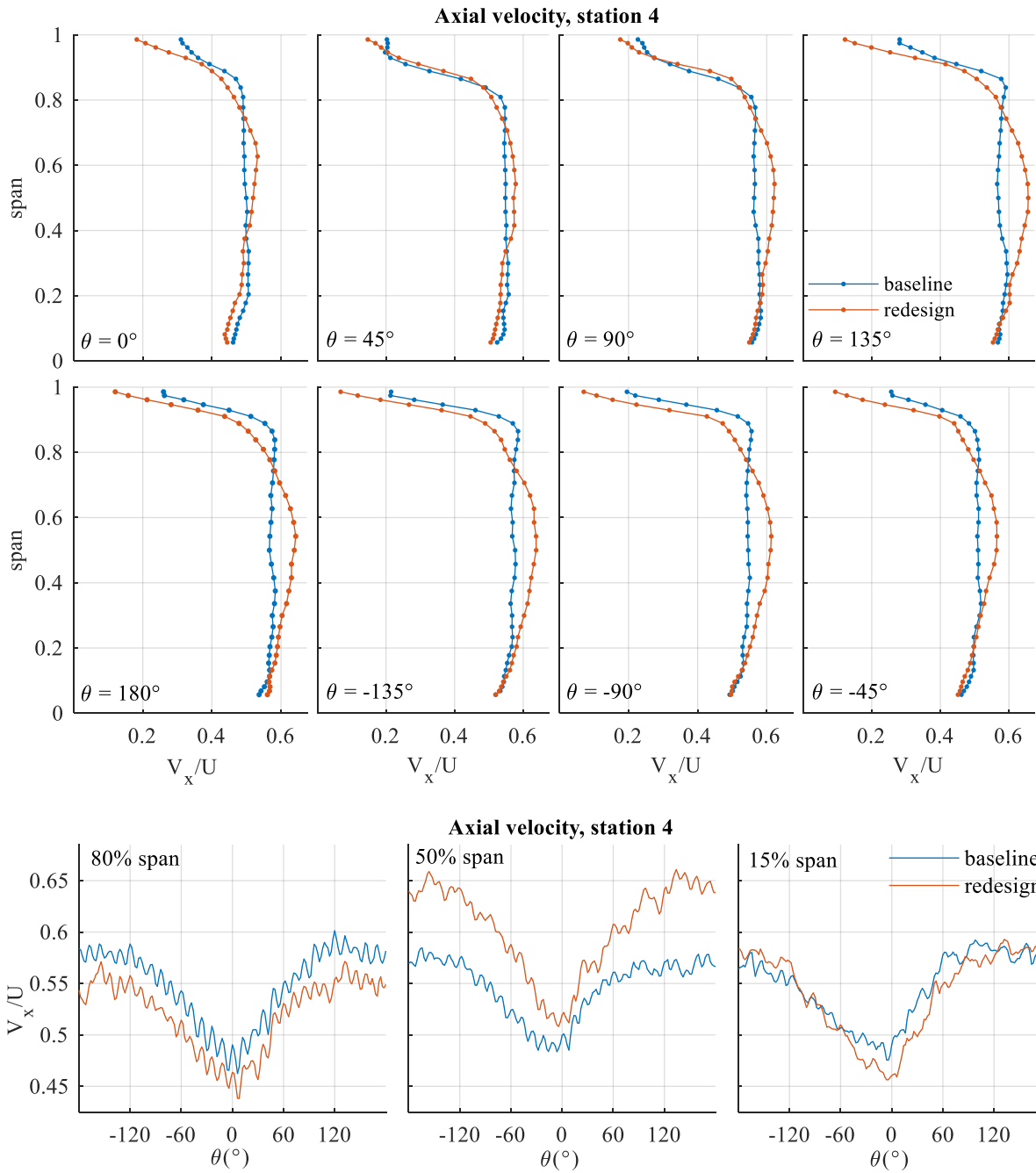


Figure 5.20 - Axial velocity at station 4, radial and circumferential plots (exp)



of axial velocity is just slightly higher than with the baseline blade. In the circumferential plot at 50% span, the velocity in the redesigned blade reduces significantly and comes close to that with the baseline blade in the low momentum region. Most of the differences in axial velocity profile occur at the mid-span and the tip region. There is little difference in the region close to the hub. The circumferential plot at 15% span confirms this and the plot at 80% span shows that the variation is similar in the two cases, except for an offset.

### 5.4.3 Loading and Pressure Rise

The two blade designs have different pressure rise distributions, as shown in Figure 5.21. The pressure rise with the redesigned blade is highest at mid-span, while there is significantly less pressure rise at the hub and the casing. This is consistent with performance in clean flow, while the effect of distortion is superimposed.

Comparison of the stagnation pressure contours is made by analysing how different they are to the respective clean flow stagnation pressure distributions. In the counter-swirl region close to the casing, labelled “A”, there is high work input, as shown later in Figure 5.23. The incidence

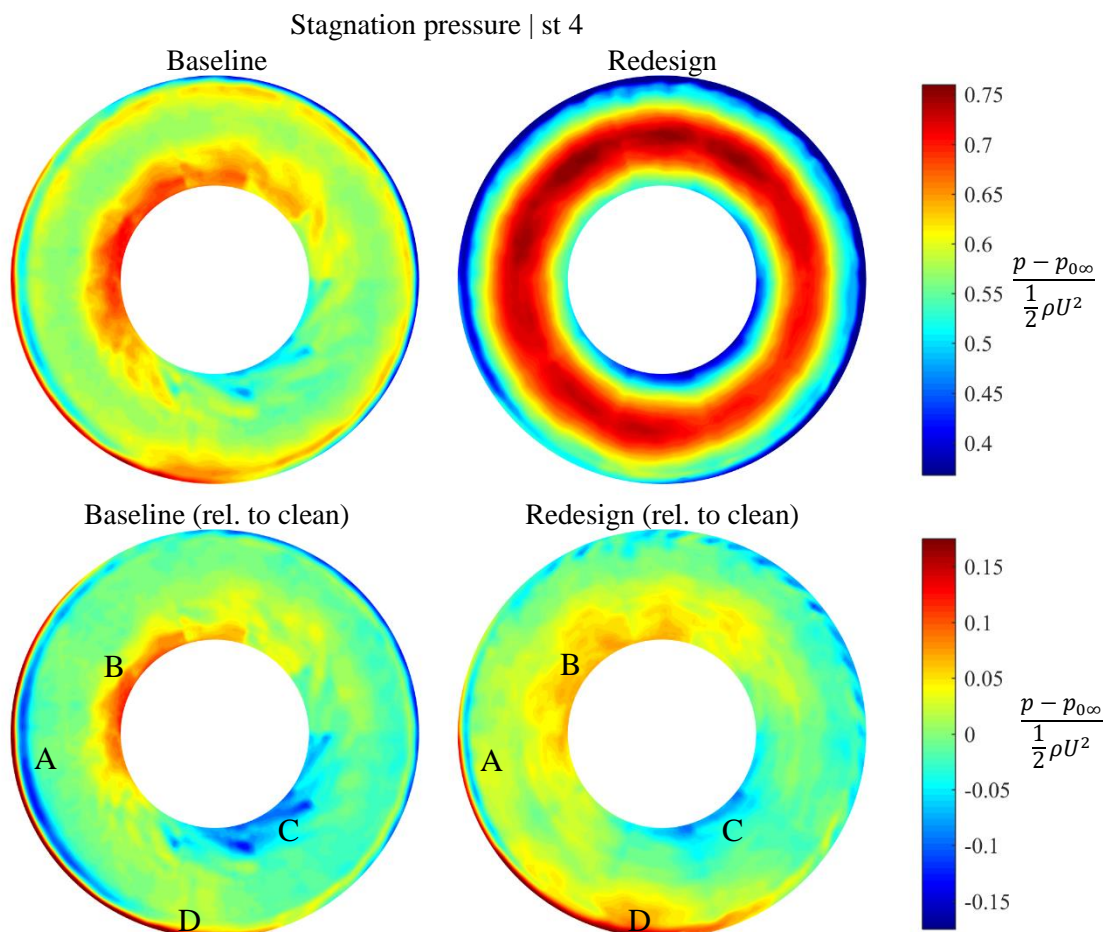


Figure 5.21 – Stagnation pressure in distorted flow, station 4 (exp)

is also very high in this region, so there is a high level of diffusion, leading to casing flow separation. In the baseline blade, most of this high work is wasted. This is improved in the redesign blade case where there is less work input and higher pressure rise is achieved, due to reduced incidence levels and reduced loading. Radial plots in Figure 5.22 corresponding to  $\theta = 90^\circ$  show the improved performance towards the tip in the redesign blade.

In the counter-swirl region close to the hub (labelled “B”), there is high pressure rise in both cases. In the baseline blade case, the high pressure rise region is concentrated mainly close to the hub, while it is more spread out in the redesigned blade. Angular momentum plots in Figure 5.23 reveal that there is not much difference in angular momentum in this region between the clean and distorted flow cases with either blade. The high pressure rise comes from the variation in the upstream flow field (cf. Figure 5.14), i.e. high incidence leads to high turning and hence high work input and pressure rise. Similar arguments explain why there is reduced pressure rise in the region labelled “C”. In the low-momentum region close to the casing (labelled “D”), there is a region of increased stagnation pressure rise in the redesigned blade case. This is due to increase in work input relative to clean flow, as shown in Figure 5.23.

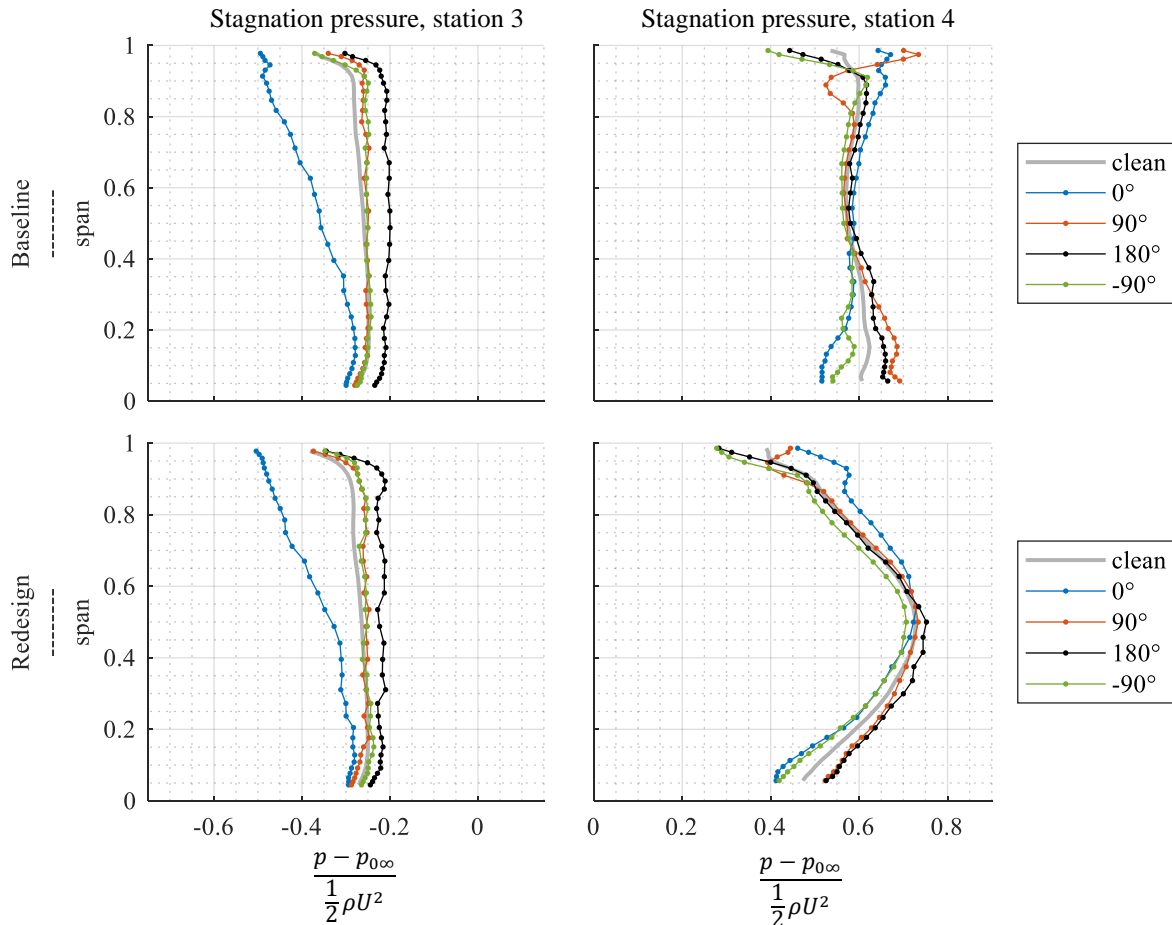


Figure 5.22 – Radial plots of stagnation pressure in distorted flow, stations 3 and 4



The contours of angular momentum in Figure 5.23 reveal that there is a region of very high work input at the tip of the baseline blade in the counter-swirl region. Since the stagnation pressure is not increased in this region, this is a region of high loss. In the redesigned blade, this loss is reduced and a band of high work input is eliminated.

As in the stagnation pressure case, radial variation of the angular momentum is shown for 4 circumferential locations,  $\theta \in \{-90^\circ, 0^\circ, 90^\circ, 180^\circ\}$  in Figure 5.24. The plots at stations 3 and 4 have the same scale so they are directly comparable. The plots at station 3 show that there is little variation radially, in both experimental cases there is a uniform variation across the span. However, there is a slight horizontal shift between the curves, showing a circumferential variation across all spans, which is of the order of 0.05, which is around 10% of the downstream average value.

Downstream of the rotor, there is significant variation in the angular momentum both radially and circumferentially. Very high work input occurs at the tip at  $\theta = 90^\circ$ . In the baseline blade, most of this work is lost. This loss is successfully reduced in the redesigned blade. In the low

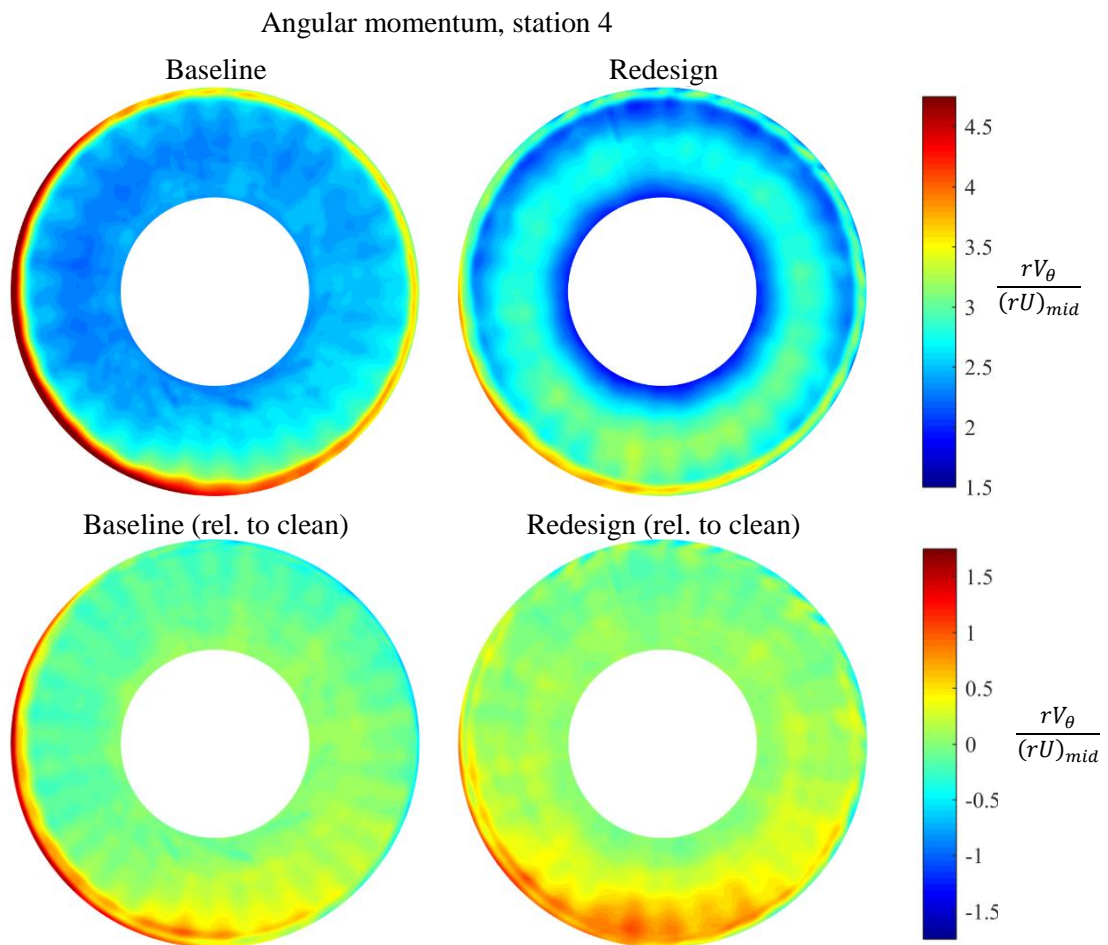


Figure 5.23 – Angular momentum in distorted flow, station 4 (exp)

momentum region at  $\theta = 0^\circ$ , there is increased work input at the mid-span and in the tip region. Most of this work is due to radial flow redistribution and is not a loss.

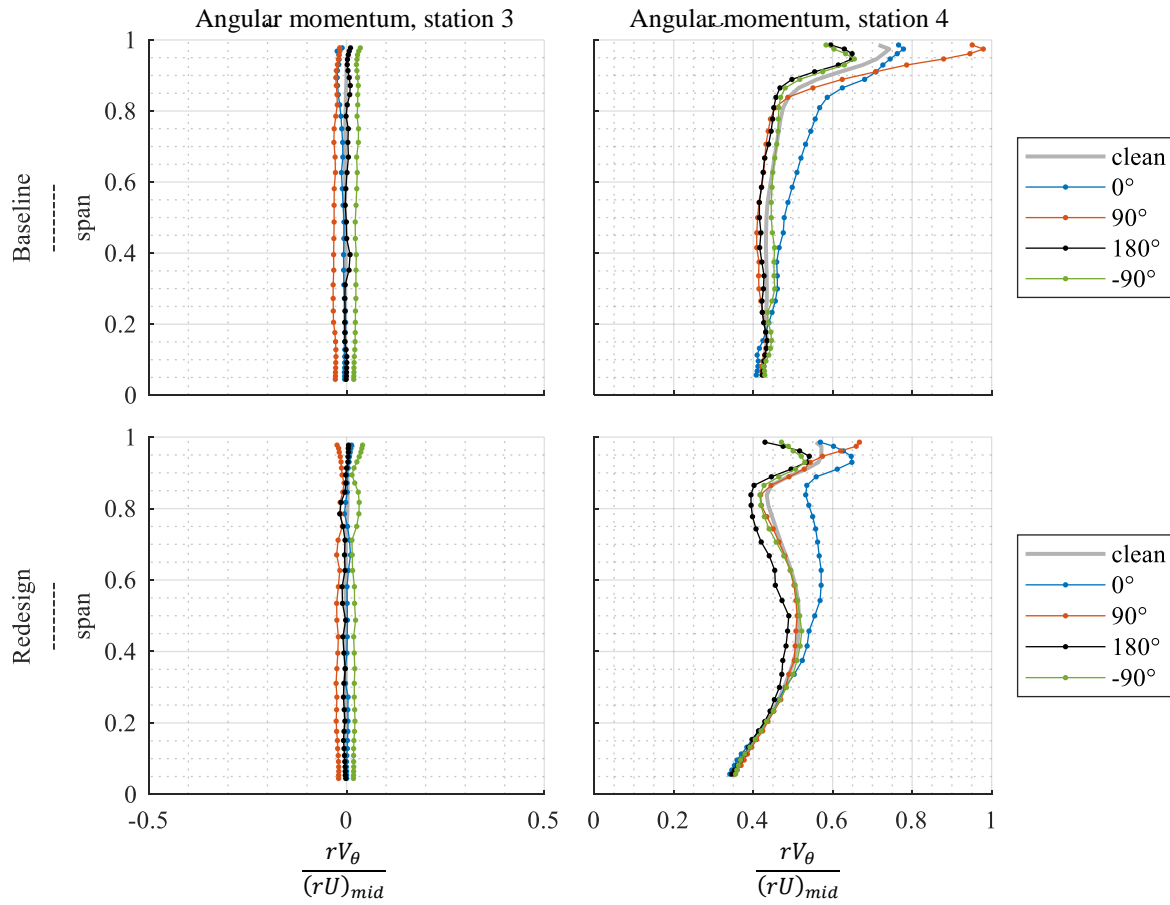


Figure 5.24 - Radial plots of angular momentum in distorted flow, stations 3 and 4 (exp)

#### 5.4.4 Stator Flow Field

The change in rotor design affects the inlet flow field to the stator. A plot of swirl angle distributions at several circumferential locations is shown in Figure 5.25. A plot of the difference between the two cases is shown as well. The plots show that there is not much difference in flow angles except very close to the casing in the region in which there is casing flow separation in the rotor. Further down the span, differences vary within the range of  $\pm 5^\circ$ . There is a difference of around  $5^\circ$  in the region close to the hub. This is due to the difference in metal angle (shown in Figure 5.3). The axial velocities in this region are the same with the two blades, see Figure 5.20, so the different relative angles lead to a difference in the absolute swirl angle seen in the plots.

The variation in flow conditions caused by the redesign is not significant. There is swirl angle variation between the two cases, but this is something that could be dealt with easily by employing non-axisymmetric stator design, as demonstrated in (Gunn & Hall, 2017).

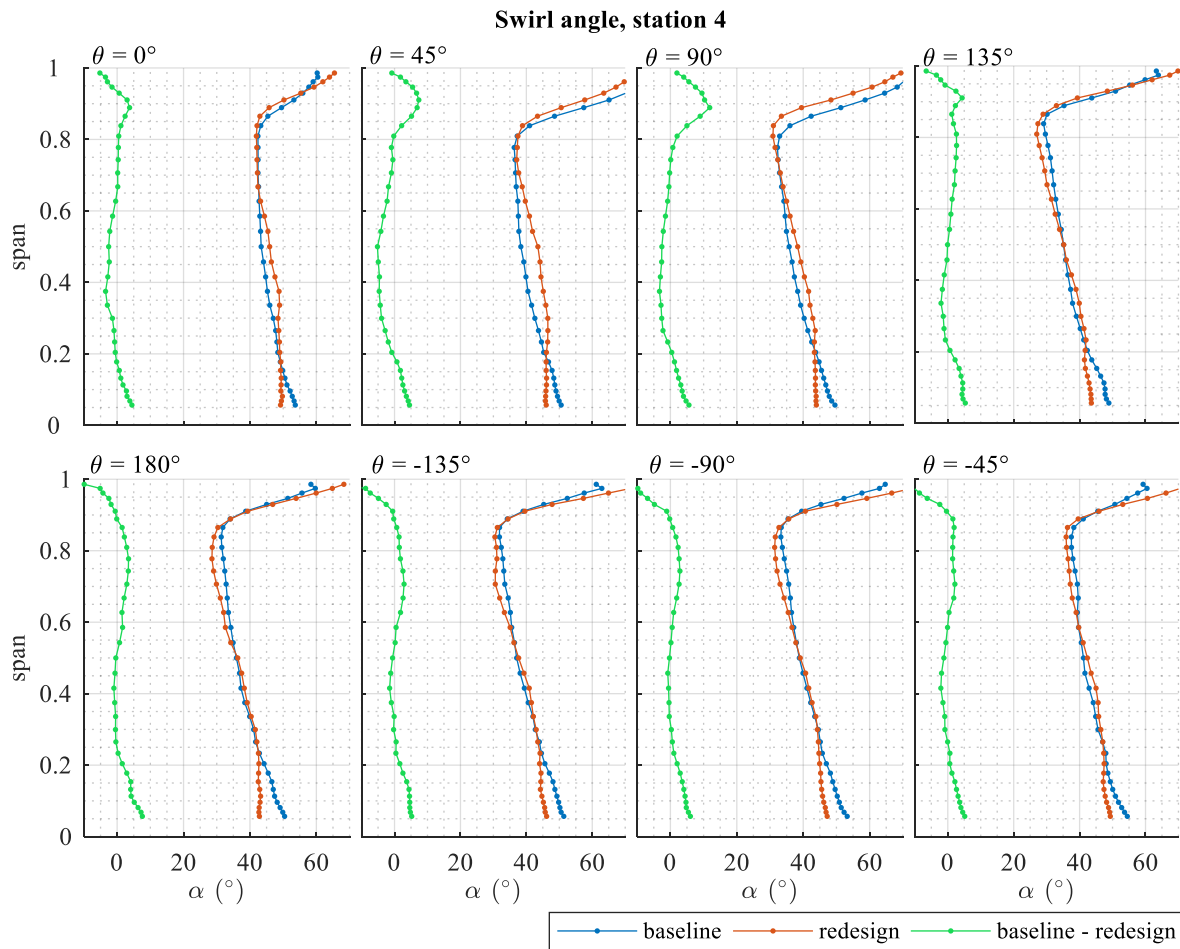


Figure 5.25 – Radial profiles of swirl angle at station 4 (exp)

### 5.4.5 Near Stall Flow Field

The redesign blade stability is improved and the stall was found to occur at a lower flow coefficient, as shown in Figure 5.5 and Table 5.2. This section shows measurements at Near Stall point. The improvement in flow range is evident from contours of axial velocity shown in Figure 5.26, in which the axial velocity upstream of the rotor is lower than in the baseline blade. Other than the velocity being lower on average, the variation is similar with both blades. Contours of swirl angle are also shown. The angles in the counter swirl region in the range  $\theta \in [0, 80^\circ]$  have very high negative value, indicating that the flow is migrating intensely in that region, which is a sign of severe flow separation and blockage in the region.

Radial profiles of axial velocity in Figure 5.27 show that there is indeed flow separation in the counter-swirl region. While the profiles at station 4 at  $\theta \in \{90^\circ, 180^\circ\}$  with the baseline blade

show that there is large casing corner separation in the counter-swirl region, the redesign blade measurements show signs of mid-span separation. This is pronounced at  $\theta = 90^\circ$ . There is a large casing corner separation as well at this location and it extends up to  $\theta = 180^\circ$  as apparent in the plot.

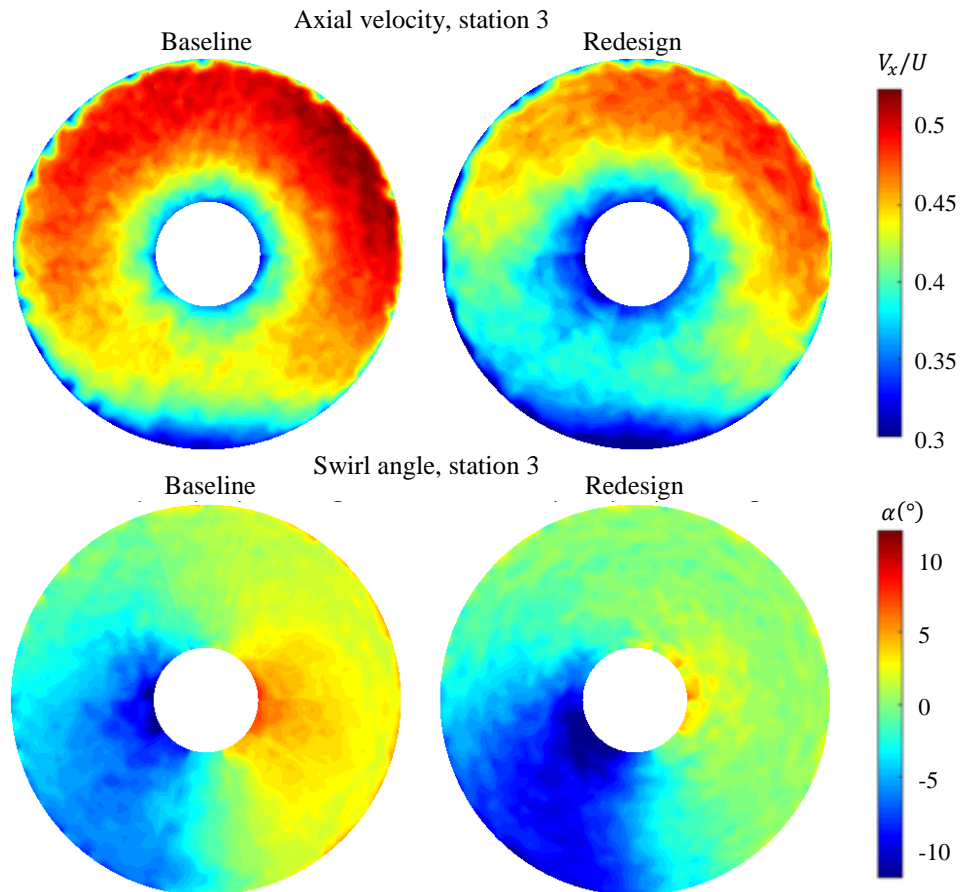


Figure 5.26 - Upstream flow conditions, axial velocity and swirl angle at near stall, station 3 (exp)

Contours of downstream of rotor stagnation pressure and axial velocity are shown in Figure 5.28. While there is a thick band of low momentum fluid close to the casing in both contours of axial velocity, there is also severe separation at the mid-span in the redesign blade in the counter-swirl region. This is consistent with the low swirl angles seen upstream of the blade row. The figure reveals that the blades are struggling to maintain stable flow close to the hub in the low momentum region,  $\theta \in [-60^\circ, 90^\circ]$ , while some part of the flow passes through the two regions of separation. This flow receives a lot of work input mainly due to very high turning. The flow does not separate, so consequently there is a high pressure rise in the region. Contour of stagnation pressure with the redesign blade shows this.

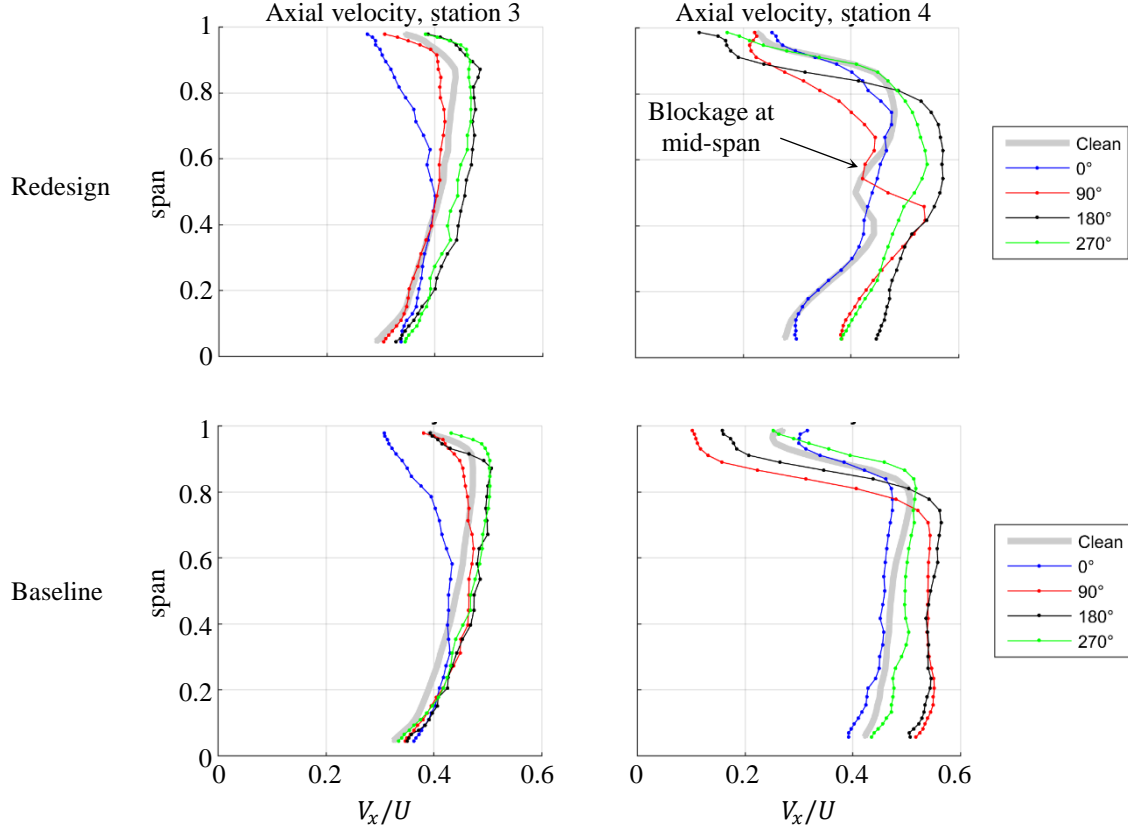


Figure 5.27 – Axial velocity radial profiles near stall, stations 3 and 4 (exp)

Circumferential plots in Figure 5.29 show the details of the flow at 50% span. The comparison is made with the flow variables at the respective design operating points. Axial velocity lines show that there is similar kind of circumferential variation with the baseline blade at  $NS_d$  point as there is at  $DP_d$ . In the redesign blade case, there is a similar variation at the two operating points except in the range  $\theta \in [50^\circ, 150^\circ]$ , where there is a drop of axial velocity. This is an indication of flow separation in this region. In the baseline blade case, the relative swirl angle is approximately constant and very close to the design point value. This is expected if the flow is attached, since it follows the metal blade angle regardless of the local velocity. In the redesign blade case, there is a clear deviation from the constant value lines at  $NS_d$  point, which confirms that the flow is disturbed and not attached in the respective region. The stagnation pressure plot shows that there is an increased pressure rise in the region preceding the separated part, where the flow work is increased. In the separated region, there is a loss of pressure rise as expected.

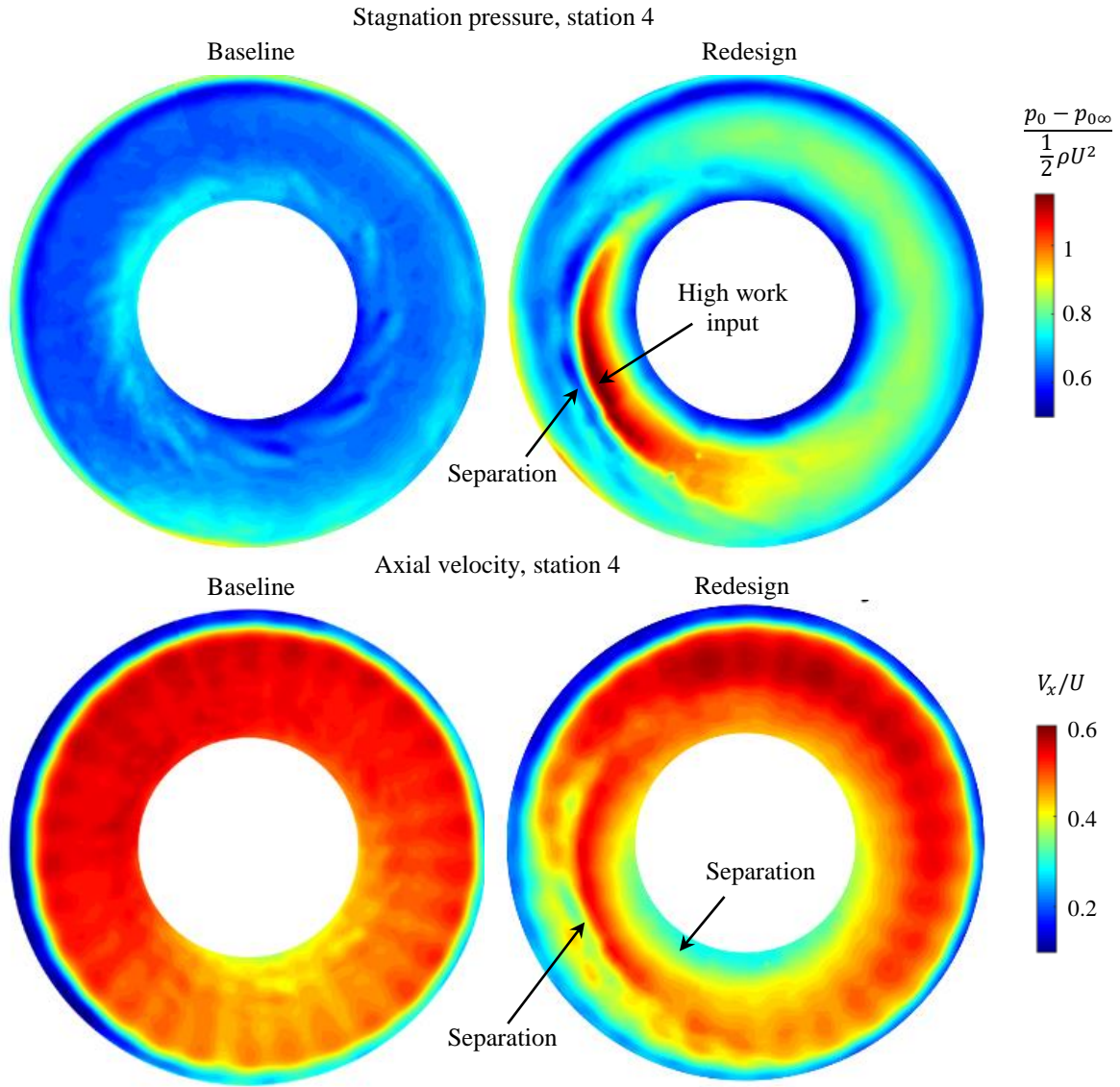


Figure 5.28 – Stagnation pressure and axial velocity at station 4

There are severe separations in the counter-swirl region of the redesigned blade at the near stall point, but the blade is operating stably nevertheless. This kind of flow separation will have a strong impact on forced response, and the severity should be investigated in the design process. It is clear that flow structures that could grow into stall cells are created when the flow separates. However, the separations are suppressed in the high momentum region of the flow, and there is no rotating stall. The stall inception process is an unsteady phenomenon and further investigation of this is presented in the next chapter.



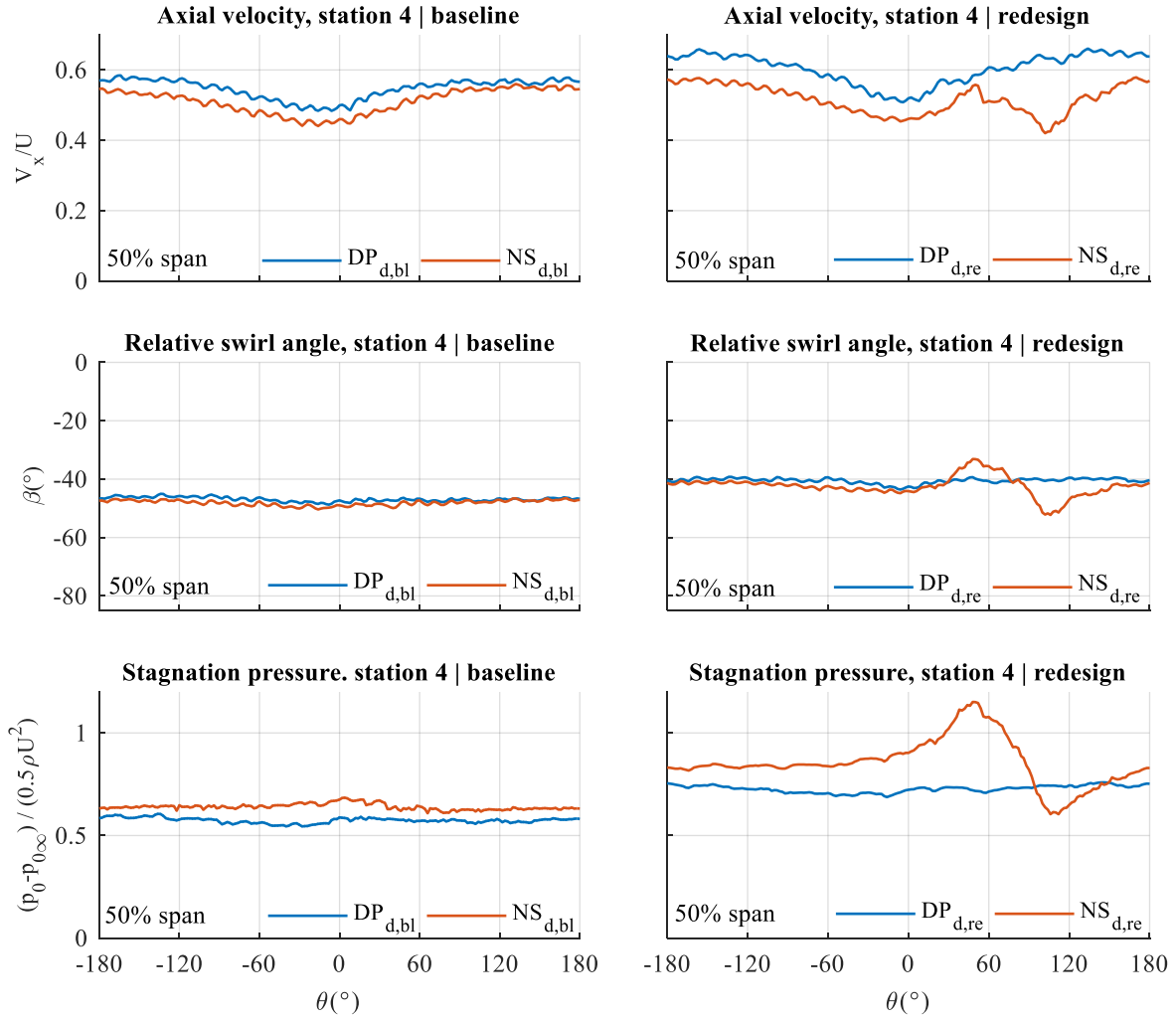


Figure 5.29 – Unwrapped circumferential plots of axial velocity, relative swirl angle and stagnation pressure, station 4 (exp)

## 5.5 Summary

The low speed BLI rig rotor blade was redesigned in order to investigate the impact of the spanwise work profile on distorted flow performance. A new set of blades was manufactured and tested in the BLI rig. Measurements confirmed that CFD can be used as a design tool, showing that the clean flow design intent was achieved.

One way to create a more distortion tolerant design would be to modify the upstream flow redistribution. However, the work input profile was found to have a weak effect on the upstream flow redistribution.

The experiments showed that improvements in the rotor efficiency when operating in distortion can be achieved by targeting the tip in the counter-swirl region, where losses are found to be the highest. Changing the work profile to give tolerance to counter-swirl was found to be

beneficial in both clean and distorted flows. Further improvements may also be possible by modifying the shape of the annulus to reduce casing diffusion.

The fan work input profile has a strong impact on flow redistribution within the blade row. In distorted flow, the flow is found to redistribute such that the radial profiles of mass flux and pressure rise at any circumferential location follow the clean flow shape. The work profile can be used to control radial flows within a blade row in order to reduce losses by utilizing centrifugal effects to add work and reduce diffusion. Importantly, design changes are found to modify radial distributions in both clean and distorted flow in the same way.

The rotor work input profile also affects the stator inlet flow field, although the differences in flow angle are small, of the order of  $5^\circ$ . It is expected that simple adjustments using a non-axisymmetric stator design could be used to mitigate any adverse effects arising due to incidence changes.

Reducing the clean flow incidence was found to improve stability margin in both clean and distorted flow. The mid-span loaded blade became critical at mid-span and heavy separations were observed in the counter-swirl region, without stall. The details of stall inception in both the baseline and the redesign rotor are explored in the next chapter.



# Chapter 6

## Stall Inception in a BLI Fan

Results in Chapter 5 and previous research indicate that the loss of stability margin for a fan operating in distorted flow is small, and that the fan maintains stable operation even when some regions locally operate beyond the clean flow stability point. The aim of this chapter is to explain the reasons for this by analysing the stall inception in the low speed BLI rig.

Unsteady casing static pressure measurements are used to track disturbances that develop in the casing region at the BLI rig rotor tip at steady operating points and during stall inception events in both clean and distorted flows. Measurements with baseline and redesign blades (see Chapter 5) are used in the analyses.

A link between incidence levels and the disturbance growth rate is identified. Incidence level in distorted flow exceeding a critical clean flow level provides a driving force for stall-type disturbances. Similarly, a drop in incidence below the critical clean flow levels dampens these disturbances. Stall is found to occur when disturbances are able to propagate around the entire annulus without being fully suppressed.

### 6.1 Baseline Blade Stall

#### 6.1.1 Clean Flow Stall

The setup used for taking casing pressure measurements is described in section 3.2.3, and the sign convention is shown in section 0. An example of a signal measured by a high frequency probe at  $DP_c$ , is depicted in Figure 6.1 (all operating points including  $DP_c$  are shown in the fan characteristics in Figure 5.5). Blade tip pressures recorded by an array of six axially placed probes are also shown in the contour plot. As the blades pass by a probe, located 10% axial chord upstream of the rotor leading edge, changes in static pressure are picked up by the probe. As a blade passes, there is a high pressure drop, due to pressure being high on the pressure side (PS) and low on the suction side (SS). The pressure then gradually increases as the next blade approaches, reaching the peak value when the blade's PS is close, and then dropping again as

the blade passes. At the clean flow design operating point  $DP_c$ , there are typically no irregularities in waveforms.

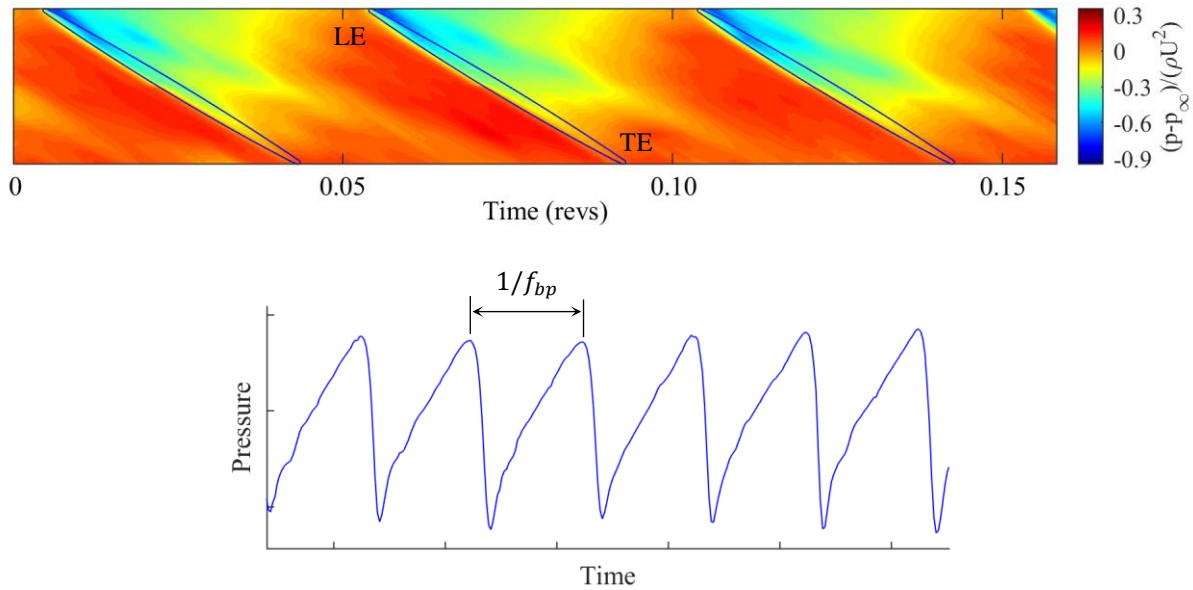


Figure 6.1 - Signals measured by high frequency probes at  $DP_c$ : tip pressure contour measured by 6 axially placed probes (above) and a waveform measured by a probe at the location just upstream of the rotor LE (below)

At the near stall point,  $NS_c$ , waveforms experience occasional irregularities. Stall inception type spikes only start appearing once the throttle setting is slightly changed to trigger stall. A stall event is shown in Figure 6.2. Prior to stall, tip flow separations lead to the creation of vortices that become visible in the waveforms as typical downwards spikes, such as “D<sub>1</sub>”-“D<sub>5</sub>”. However, these spikes do not propagate to cause stall cell formation. Eventually, a disturbance “D<sub>stall</sub>” appears and starts propagating, triggering further separations. An early stall cell forms and grows rapidly as it propagates around the annulus. The initial disturbances travel at around 58% of the blade speed and grow to occupy 160° of the annulus within less than one rotor revolution.

Another stall event, shown in Figure 6.3, presents the differences between early and fully developed stall cells. A window of  $4rev$  around the stall inception is shown. Stall occurs in the same way as in the stall event shown in Figure 6.2. An initial spike appears and quickly develops into a stall cell. Another window around  $t = 158rev$  illustrates a fully developed stall cell that moves at approximately  $\omega = 0.55\Omega$ , and occupies around a half of the circumference. The cell is composed of 3-4 sub-cells which are fully blocked, as indicated by high pressure detected ahead of the blockages. This is different to early stall cells shown in the

first window, which are characterised by the presence of spikes caused by multiple flow separations occurring during the stall inception.

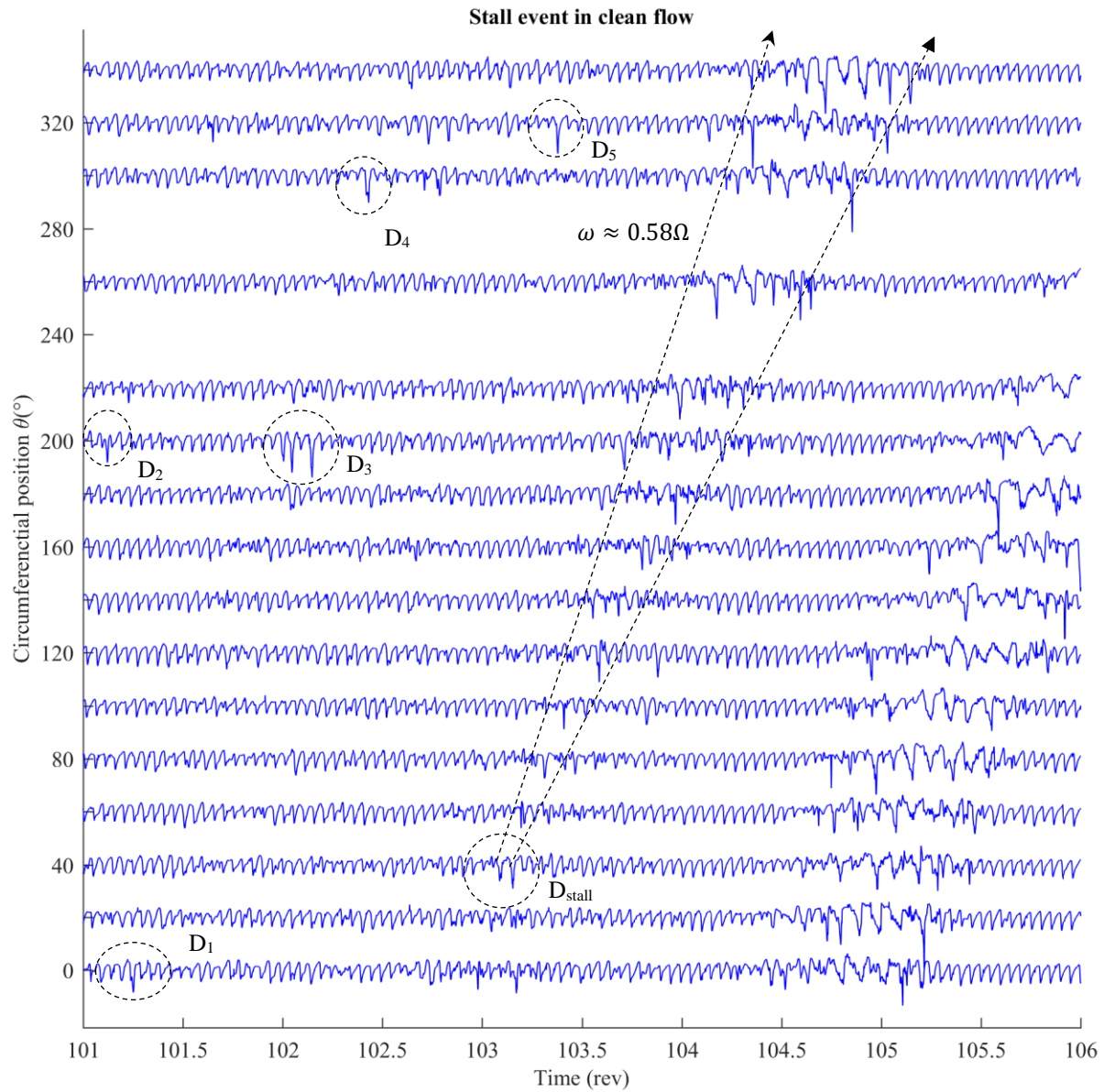


Figure 6.2 - Stall inception in clean flow

Irregularities in waveforms cause frequency content at non-harmonic frequencies. A spectrogram of a signal recorded during a stall event is shown in Figure 6.4. The signal is initially free of irregularities and the frequency content is concentrated at the blade passing frequency  $f_{bp}$  and the second harmonic. When stall occurs around  $t = 150rev$ , frequency content at a broad range of frequencies appears in the signal due to the presence of stall cells, especially at low frequencies below 50%  $f_{bp}$ .

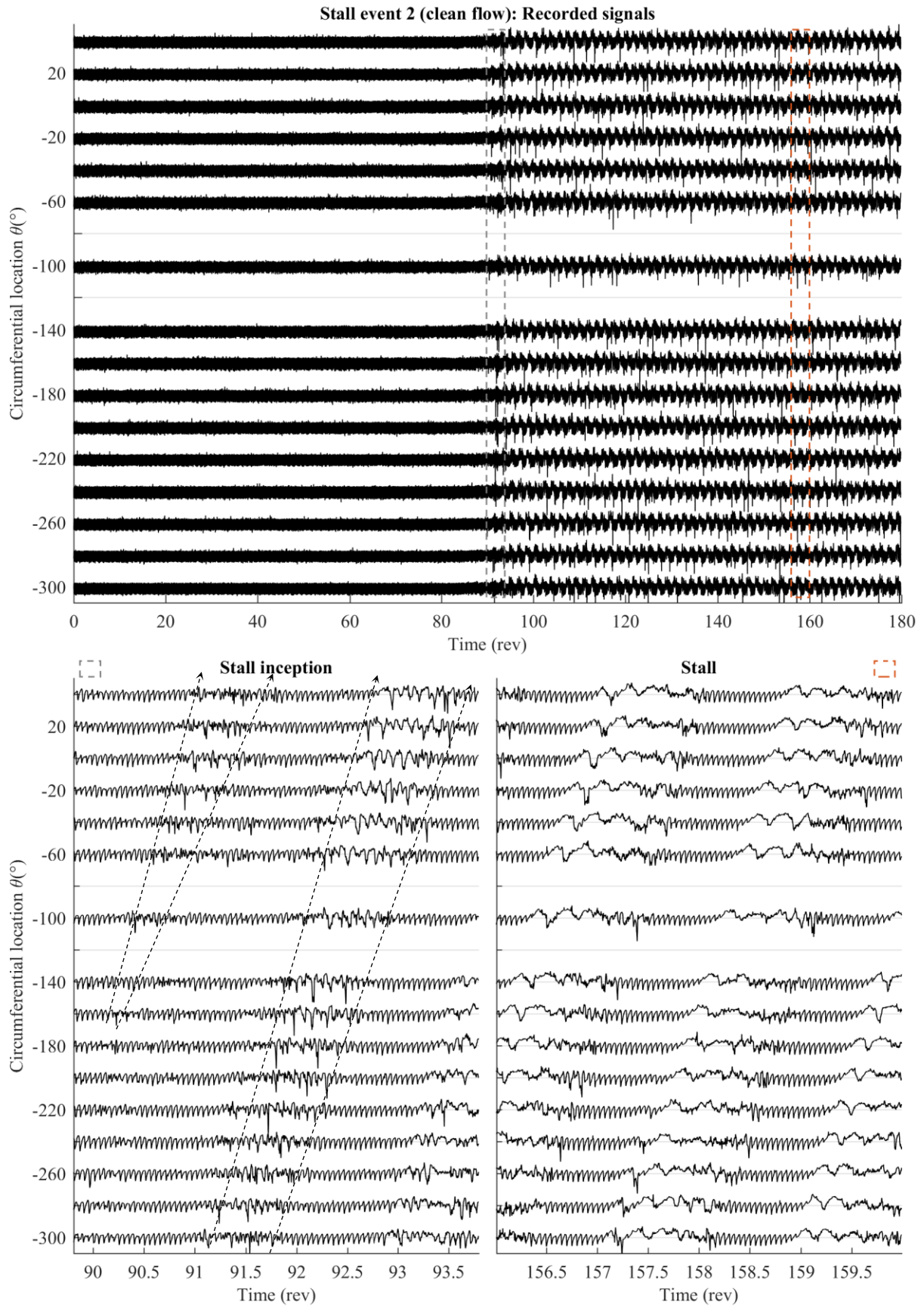


Figure 6.3 - Stall event in clean flow: signals during stall inception and after stall has occurred

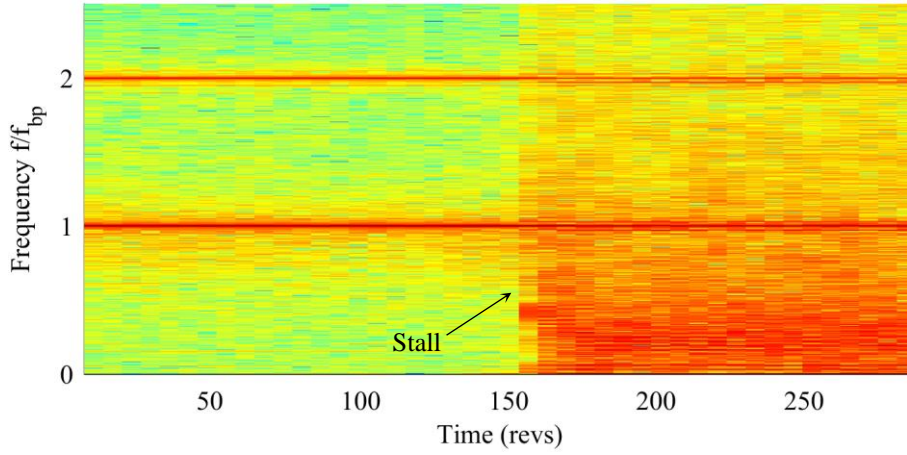


Figure 6.4 - Spectrogram of a casing static pressure signal around a stall event in clean flow

A cumulative energy plot of the signal in Figure 6.5 depicts energy contained at a range of frequencies for three time windows: when the rig is operating at  $NS_c$  before stall is triggered, around the stall inception, and after stall has occurred. The disturbance energy is calculated as described in section 3.2.3, and is non-dimensionalised by the total value at  $NS_c$ .

At  $NS_c$ , the main frequency content is at  $f_{bp}$  and  $2f_{bp}$ , as shown by step increases in the energy level at both frequencies. During stall inception, irregularities that appear give rise to content in the frequency range  $f \in [0.7f_{bp}, 1.2f_{bp}]$  due to the presence of propagating disturbances, while the main content is still at  $f_{bp}$  and  $2f_{bp}$ . The total energy of the stalled signal significantly increases, by 120%, due to stall cells being present. Approximately 50% of the total stalled signal energy is contained in the range  $f \in [0, 0.5f_{bp}]$ .

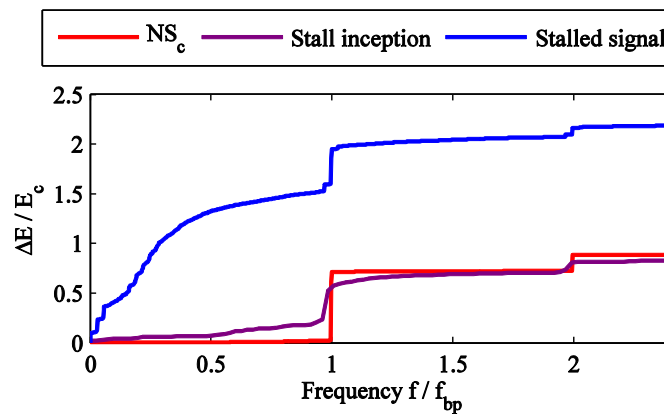


Figure 6.5 - Cumulative energy content of a casing pressure signal in the range  $[0, f]$ : before, during and after stall

Fast Fourier transforms of signals recorded at four flow conditions,  $DP_c$ ,  $NS_c$ , during stall inception and in stall, are shown in Figure 6.6. FFT of the signals confirms the previous finding that most of the content is at the fundamental frequencies in all cases. During stall inception,

content close to  $f_{bp}$  becomes pronounced. In stall, content at low frequency is present, especially below  $0.5f_{bp}$ , as shown in the figure.

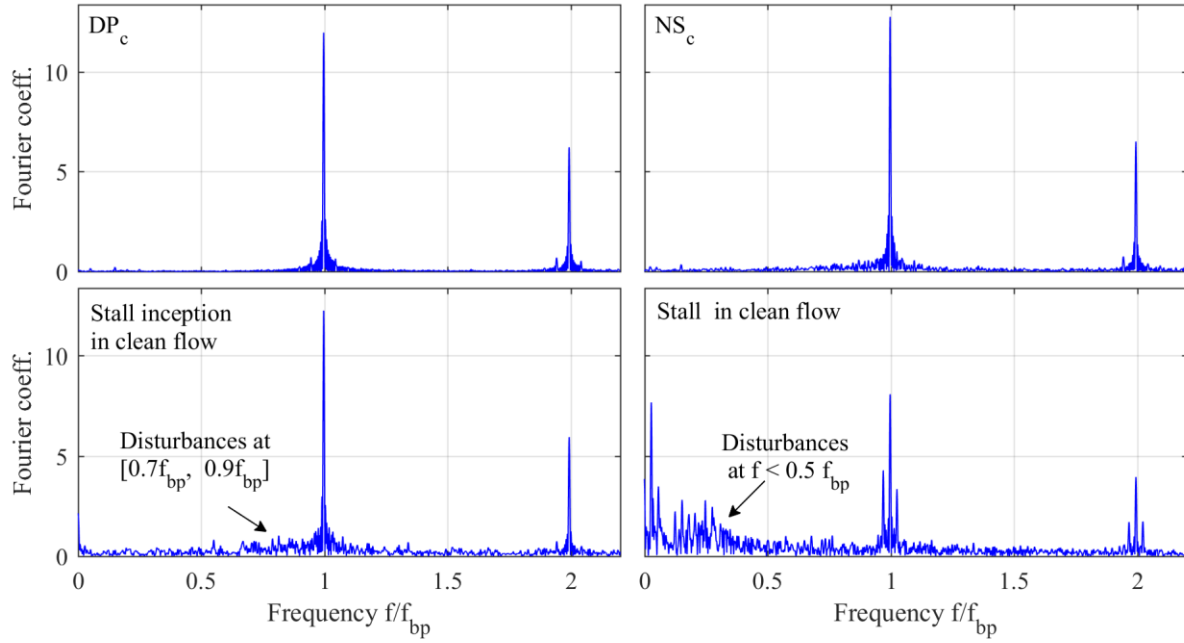


Figure 6.6 - Fourier transform of signals from a pressure transducer, recorded at/during:  $DP_c$ ,  $NS_c$ , stall inception and stall

### 6.1.2 Incidence Variation in Distorted Flow

The variation in axial velocity and swirl upstream of the rotor in distortion (see Chapter 5) leads to a variation in incidence. Axial velocity and swirl contours in Figure 6.7 show the velocity field at station 3 at the two distorted flow operating points,  $DP_d$  and  $NS_d$ . At both operating points, low axial velocities and negative swirl angle in the counter-swirl region lead to high incidence, as shown in Figure 6.7. The incidence variation is plotted relative to the critical  $NS_c$  level, i.e. *excess incidence* is defined as  $i_{excess} = i - i_{NS_c}$ . Negative *excess incidence* means that the incidence is below the critical level in clean flow, while positive *excess incidence* indicates that the incidence level exceeds the clean flow critical level. *Excess incidence* is calculated from the relative swirl angles, as shown in equation (6.1) (sign convention is as depicted in Figure 5.1).

$$i_{excess} = i - i_{NS_c} = (-\beta_3 - \chi_1) - (-\beta_{3,NS_c} - \chi_1) = -\beta_3 + \beta_{3,NS_c} \quad (6.1)$$



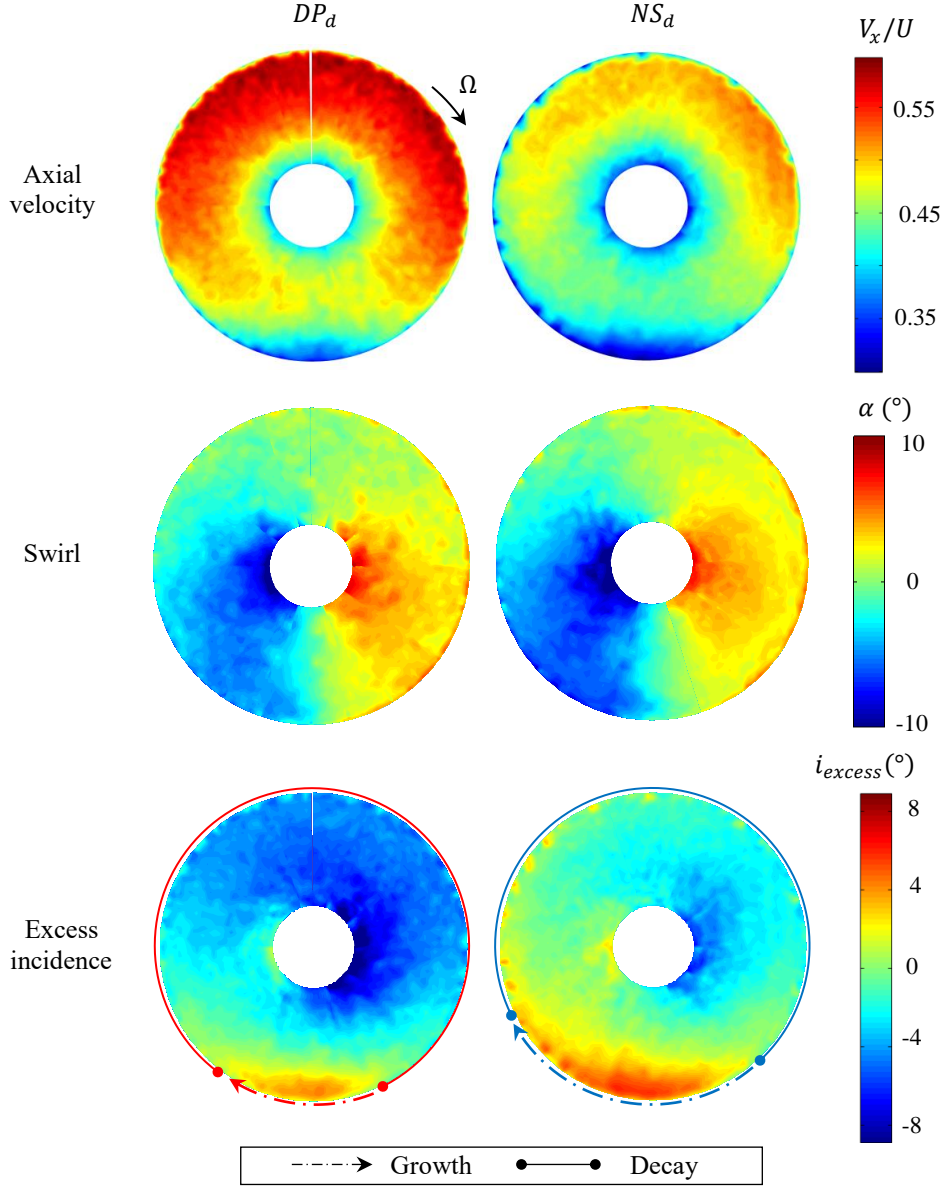


Figure 6.7 – Flow conditions at  $DP_d$  and  $NS_d$  at station 3: axial velocity, swirl and excess incidence (exp)

Flow structures responsible for stall are shown to be created in the regions where *excess incidence* is positive at the tip, even at stable operating points. Nevertheless, the fan maintains stable operation due to disturbances being suppressed in the regions of negative *excess incidence*.

### 6.1.3 Unsteady Measurements in Distorted Flow

When the fan operates in distortion, the level of irregularities in the casing pressure signal varies with the circumferential location. Figure 6.8 demonstrates probe signals at six circumferential locations around  $t = 74rev$  at  $DP_d$ . The plots show that for  $\theta \in \{30^\circ, 70^\circ\}$  the signals are disturbed, while the other four signals remain regular with virtually no disturbances.

The signal at  $\theta = -10^\circ$  remains unaffected. A comparison with the plot of *excess incidence* at this operating point depicts that the signal at  $\theta = 30^\circ$  lies within the region of positive *excess incidence*, while the signal at  $\theta = 70^\circ$  appears just after the region of positive  $i_{excess}$ . This suggests that the appearance of disturbances is linked to the *excess incidence* level. However, the signal at  $\theta = -10^\circ$  is also within the region of positive  $i_{excess}$ , but is not disturbed, which suggests that the disturbances appear and grow in the region of  $i_{excess} > 0$ , which explains the presence of disturbances at  $\theta \in \{30^\circ, 70^\circ\}$ , but their absence at  $\theta = -10^\circ$ . This hypothesis is explored further in the next section.

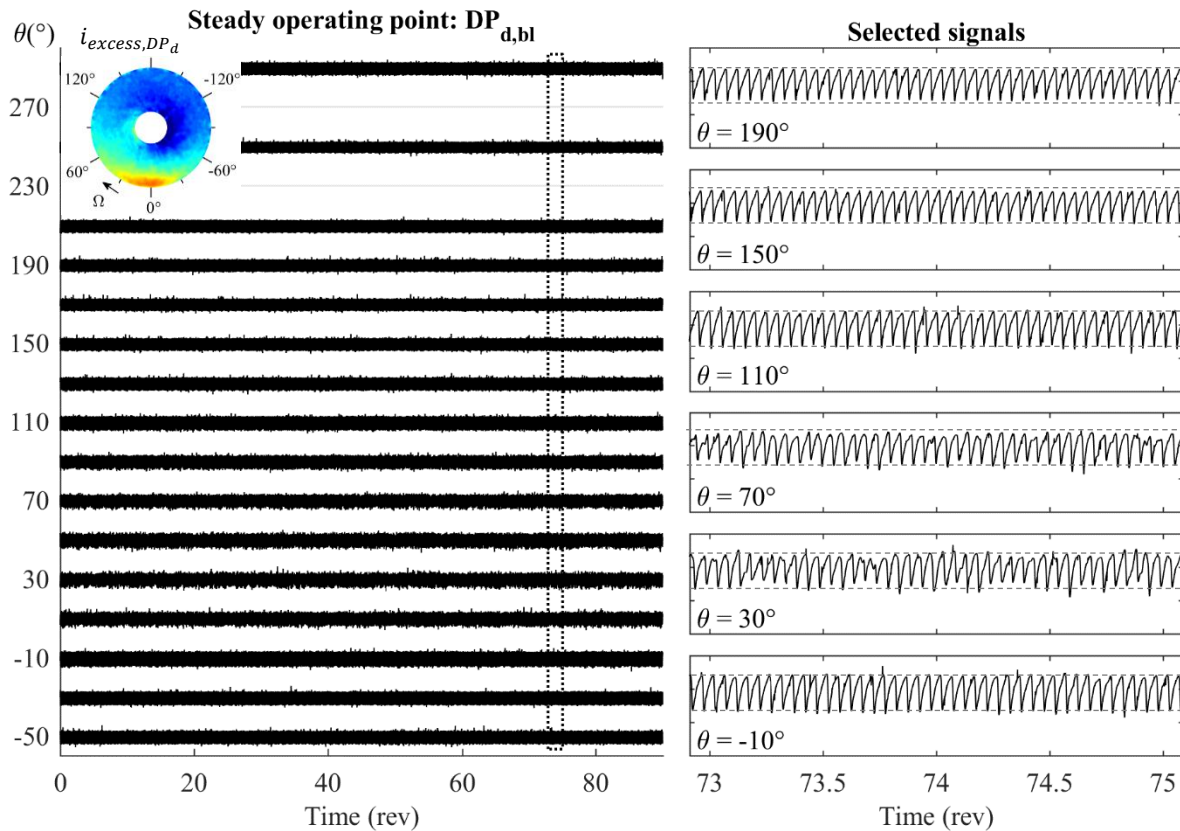


Figure 6.8 - Unsteady casing static pressure measurements at  $DP_d$

Frequency content of signals in Figure 6.8 is shown in spectrograms in Figure 6.9. Content in the range  $f \in [0.7f_{bp}, f_{bp}]$ , is seen at  $\theta \in \{30^\circ, 70^\circ\}$ , which lie the region of positive *excess incidence* in counter-swirl region, while the spectrograms of the signals at  $\theta \in \{-50^\circ, 150^\circ\}$  show that the frequency content is primarily at harmonic frequencies, as in clean flow design point operation. The frequency content that appears at  $\theta \in \{30^\circ, 70^\circ\}$  is similar to that found during stall inception events in clean flow, indicating that stall inception type disturbances are present at those locations at  $DP_d$ . However, these disturbances do not grow into a stall cell, and are cleared before  $\theta = 150^\circ$ .



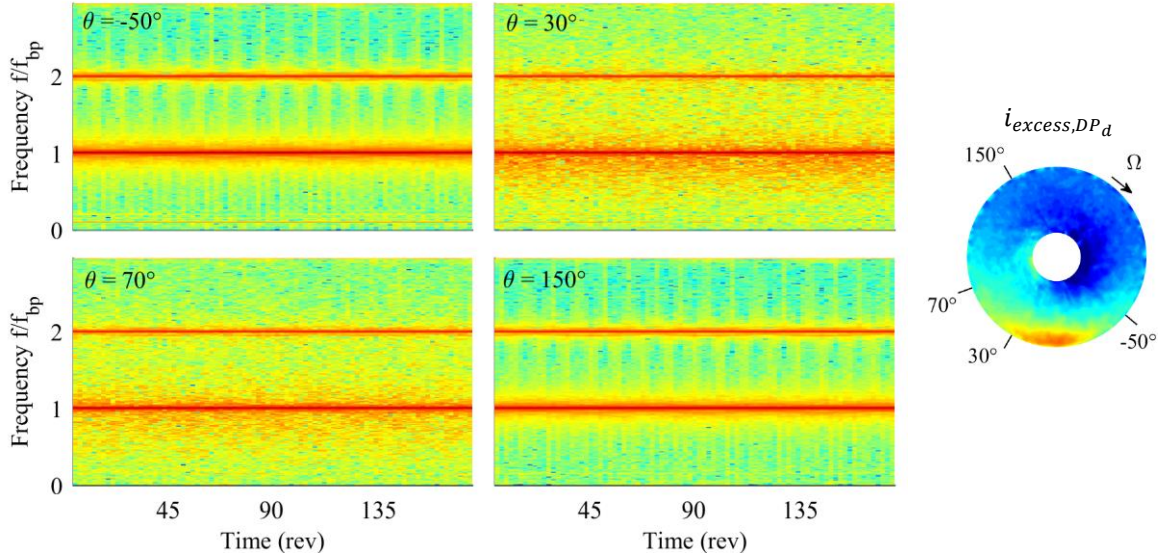


Figure 6.9 - Spectrograms of casing static pressure signals at  $DP_d$

Figure 6.10 shows signals recorded at  $NS_d$ . The signals within  $\theta \in [30^\circ, 150^\circ]$  are continuously disturbed, as demonstrated in the enlarged signals at  $\theta \in \{30^\circ, 90^\circ, 150^\circ\}$ . Spikes and occasional disturbances occur at locations just beyond this region, within  $\theta \in [150^\circ, 230^\circ]$ , such as the spike at  $\theta = 230^\circ$  at  $t = 75rev$ , labelled “ $D_1$ ”. Signals at  $\theta \in \{30^\circ, 90^\circ\}$  feature various spikes, which are indicative of the occurrences of flow separations.

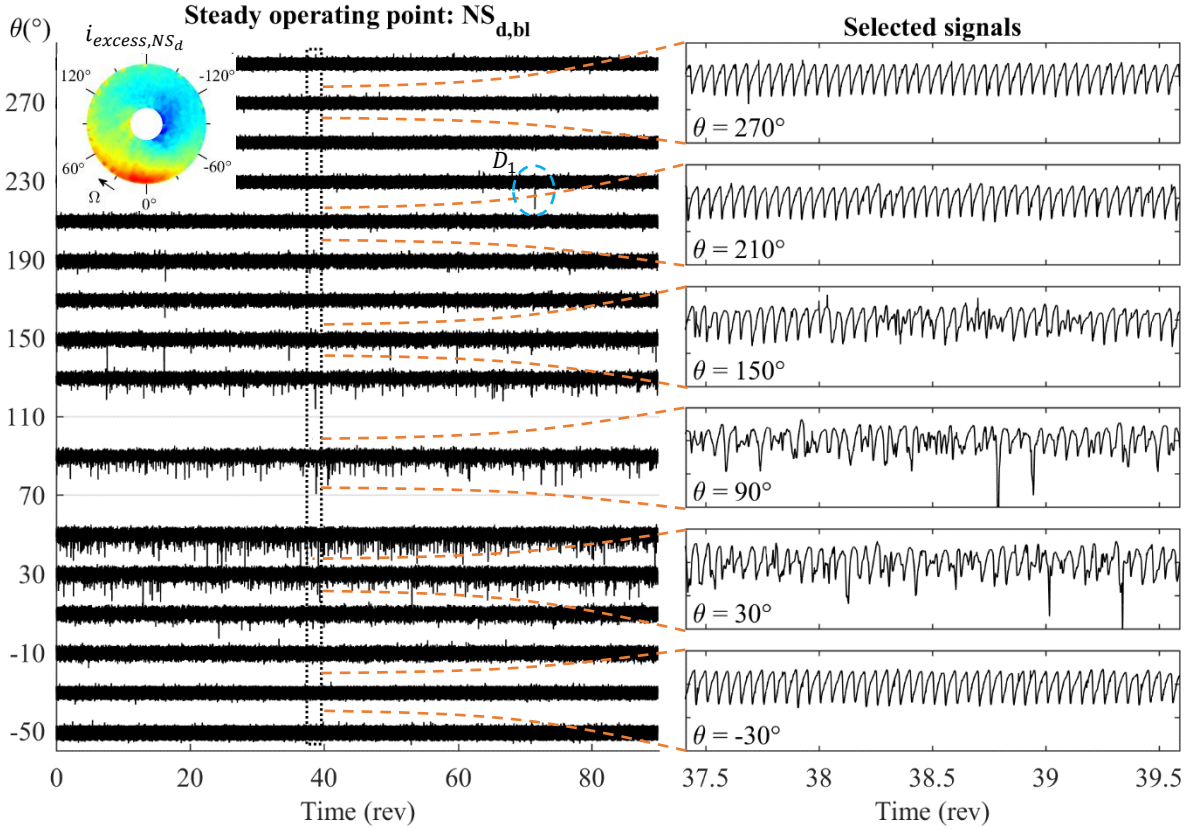


Figure 6.10 - Unsteady casing static pressure measurements at  $NS_d$

The signals are severely disturbed, with irregularities which typically rapidly grow into stall cells in clean flow (cf. Figure 6.2). Here, the disturbances propagate around the annulus but clear as they enter the region of negative *excess incidence*, as confirmed by signals at  $\theta \in \{210^\circ, 270^\circ, -30^\circ\}$  which do not experience irregularities.

#### 6.1.4 Linking to the Steady Flow Field

The disturbance energy at  $f \in [0.7f_{bp}, 0.9f_{bp}]$  is calculated for each of the signals at  $DP_c$ ,  $NS_c$ ,  $DP_d$  and  $NS_d$  and plotted against *excess incidence* at 75% span in Figure 6.11. At the design point  $DP_c$ , the energy content is negligible since the pressure signals reflect few irregularities. At  $NS_c$  the level increases, but the increase is not uniform at all circumferential locations. Significant increase occurs in half of the annulus, likely due to variations in tip gap at different circumferential locations, possibly caused by eccentricity in the rotor casing. It is shown that in eccentric compressors irregularities appear in the regions of high tip gap and disappear in the regions of low tip gap (Young, et al., 2013). The effect occurs even when the eccentricity is as small as 10% of the mean value, i.e.  $\epsilon_{max} - \epsilon_{min} = 10\%\bar{\epsilon}$ , where  $\epsilon$  is the tip gap size.

To isolate the effects of these asymmetries in the distorted flow measurements, six measurements were taken at  $DP_d$  with the distortion gauze rotated at  $60^\circ$  for each measurement, and 36 measurements were taken at  $NS_d$  with the distortion gauze rotated at  $10^\circ$  for each measurement. The results were averaged and shown as a solid line in Figure 6.11. The raw data is visible as small crosses in the plots.

From Figure 6.11, it is clear that at  $DP_d$  the energy level starts increasing over the  $NS_c$  level around  $\theta = -30^\circ$ . It peaks at  $\theta = 30^\circ$  where the value is approximately 2 times larger than the  $NS_c$  level. A comparison with the *excess incidence* contour and line plot at  $DP_d$  reveals that region  $\theta \in [-30^\circ, 30^\circ]$ , in which disturbance energy increases, is the region of positive *excess incidence* at the tip. As the blades leave this region, the disturbance energy in the signals starts decreasing.

At  $NS_d$ , the energy level lifts off at  $\theta = -40^\circ$  and peaks at  $\theta = 60^\circ$ , reaching disturbance energy approximately 7 times larger than that of  $NS_c$ . Similar to the case of  $DP_d$ , this increase in disturbance energy in the range  $\theta = [-40^\circ, 60^\circ]$  coincides with the region of positive *excess incidence* at the tip. These regions of growth at the two operating points are labelled in Figure 6.11 and in the *excess incidence* contours in Figure 6.7.

The results in Figure 6.11 indicate that positive *excess incidence* stimulates disturbance growth. The rate of increase of disturbance energy is proportional to the *excess incidence* level, i.e., the higher the *excess incidence*, the higher the disturbance growth rate. However, positive *excess incidence* is needed to maintain disturbance propagation. When the *excess incidence* becomes negative, the disturbances stabilise and start decaying. In the case of BLI, negative *excess incidence*, which is the driving force for disturbance decay, increases in magnitude as the blades leave the counter-swirl region. The disturbances originating in the region of  $i_{excess} > 0$  gradually lose energy and the disturbance energy level returns to a very low value below the  $NS_c$  level, at both operating points. This stabilising effect prevents initial stall-type disturbances from developing into stall cells.

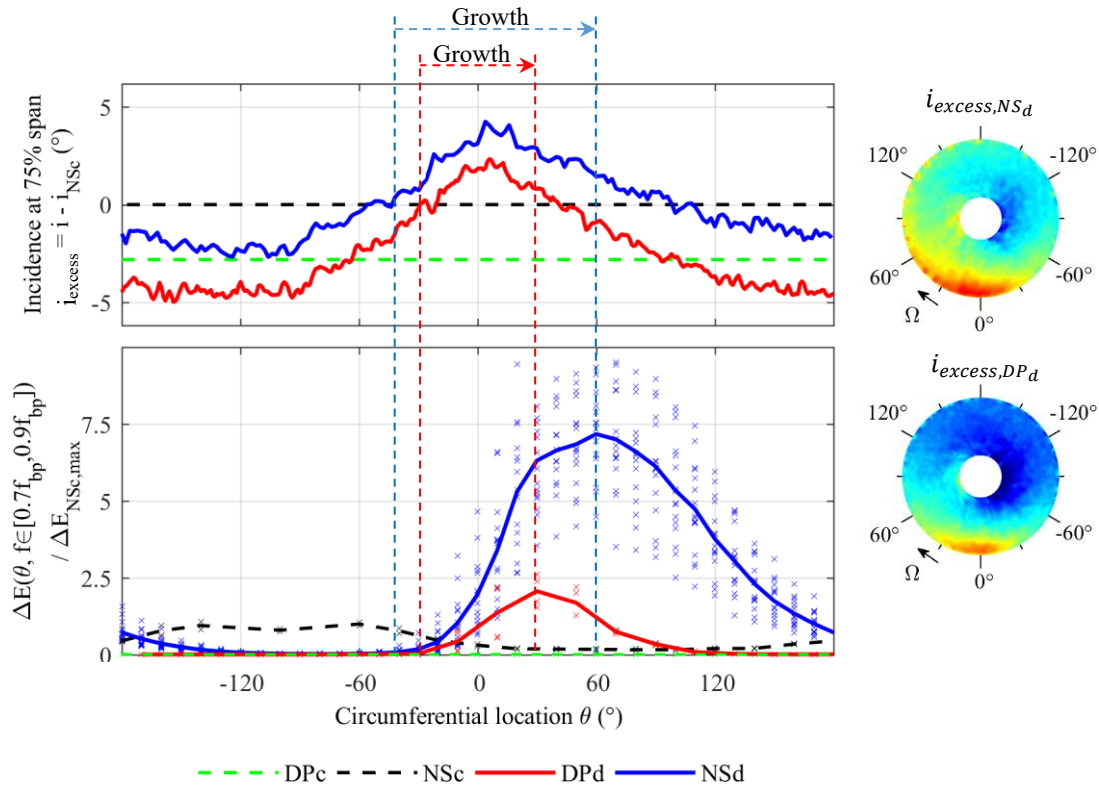


Figure 6.11 – Comparison of the incidence relative to the  $NS_c$  incidence level and disturbance energy. Crosses show data from individual measurements, averages are shown as solid and dashed lines.

### 6.1.5 Stall Inception in Distorted Flow

Spectrograms of signals recorded during a stall event are shown in Figure 6.12. At locations  $\theta \in \{-50^\circ, 210^\circ\}$ , the signals are undisturbed prior to stall, and the main content is at  $f_{bp}$  and  $2f_{bp}$ . At  $\theta \in \{30^\circ, 110^\circ\}$ , there is a high degree of irregularities in the signals, resulting in significant disturbance content at  $f \in [0.7f_{bp}, 0.9f_{bp}]$ , which is the same frequency content as

that observed during stall inception events in clean flow. In distorted flow, these disturbances are continuously present at certain circumferential locations while the rig is operating stably.

The moment of stall inception is less clear in the spectrograms compared to clean flow. Content at  $f > 0.5f_{bp}$  appears first, while content at  $f < 0.5f_{bp}$  appears several revolutions later. This is an indication that there is pre-stall activity before a stall cell forms. It is shown next that this is consistent with the behaviour seen in the waveforms during a stall inception event where disturbances undergo cycles of growth and decay before they eventually develop into a stall cell. The post stall signal is dominated by the low frequency content caused by large stall cells.

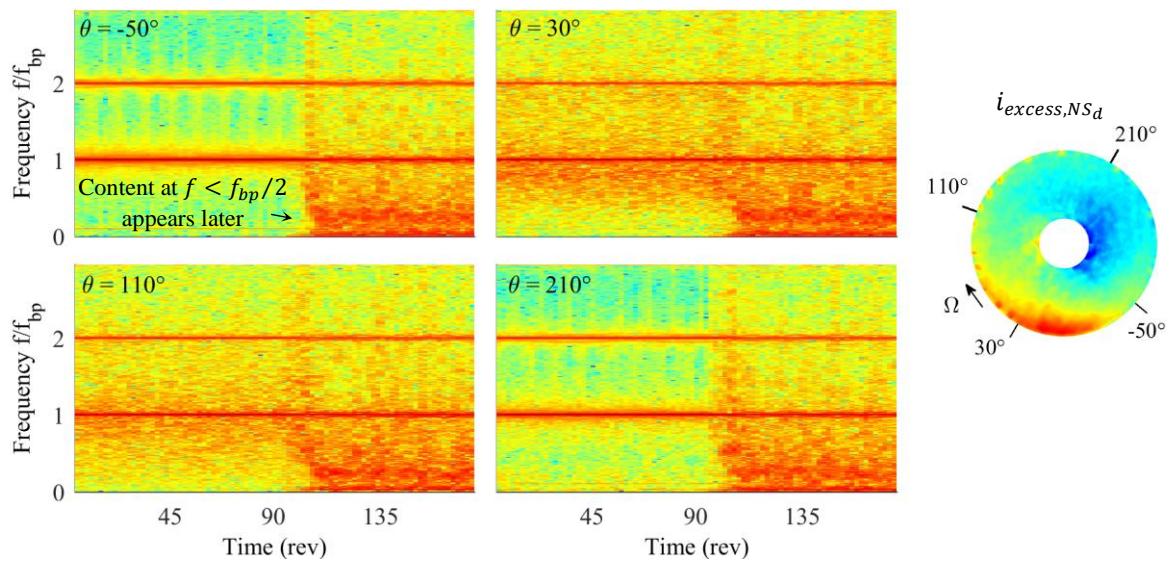


Figure 6.12 - Spectrograms of casing static pressure signals around a stall event in distorted flow

A stall inception event in distorted flow is shown in Figure 6.13. Irregularities at “D<sub>1</sub>”- “D<sub>3</sub>” are examples of disturbances that appear and propagate but are suppressed before completing a full revolution. The spike at “D<sub>1</sub>” continues to grow to  $\theta = 150^\circ$ , but then starts decaying and is cleared before  $\theta = 250^\circ$ . Similarly, spikes at “D<sub>2</sub>” and “D<sub>3</sub>” increases to  $\theta = 170^\circ$ , but then decay by  $\theta = 210^\circ$  and  $\theta = 250^\circ$  respectively. Disturbance at “D<sub>3</sub>” increases to  $\theta = 250^\circ$ , after which it starts to decay. However, this disturbance makes a full revolution without being damped out. It then continues growing and forms an early stall cell.

A major difference compared to clean flow stall inception is that a series of spikes appear at the location of initial disturbance, rather than only one spike that starts propagating. For example, when the first disturbances appear at “D<sub>3</sub>” and “D<sub>4</sub>”, they start propagating as time elapses, which is detected by consequent probes. However, the rear of the disturbance stays at the same location and is picked up by the same probe that detects the initial disturbance. In

clean flow, disturbances grow at a steady rate as they propagate, as shown in Figure 6.2, characterised by the front of the early stall cell travelling at a steady rate which is higher than the steady rate at which the rear of the cell is travelling.

Another major difference between clean and distorted flow is in the early stall cell behaviour after the initial growth. In distorted flow, the early stall cell in Figure 6.13 that initially grows rapidly starts shrinking before it makes a full revolution, which is not observed in clean flow in Figure 6.2. However, it does not decay completely and continues growing again when it reaches the region in which it was originally created, after which it grows to a fully developed stall cell.

Early stall cell propagation and growth are investigated by tracking the front and rear of the cell. The results are presented in Figure 6.14. The front and the rear of the cell were identified manually, and a plot was created to show how their location changes with time, while the data was used to calculate the temporal variation in stall cell size, which is also shown. The front is typically clearly defined, but identifying the rear requires a degree of judgement. The rear of a stall cell was defined as the last waveform that experiences “significant” irregularities.

The waveform plot shows that an initial disturbance “ $D_1$ ” starts propagating. At time  $t_1$ , the early stall cell is small in size and is located in the region of high  $i_{excess}$ , as shown in the schematic which is plotted based on the measured data. The cell keeps growing as the front moves, due to the rear of the cell lagging behind and hardly moving. The schematics at  $t_2$  and  $t_3$  show the location and size of the stall cell as it grows. After time  $t_3$ , the stall cell starts shrinking due to the speed of the front of the cell decreasing and the speed of the rear increasing, as indicated by a lower gradient between  $t_3$  and  $t_4$  in the circumferential location-time plot. At the same time, the speed of the rear increases, especially just before  $t_4$ , which is the moment when the rear leaves the region of  $i_{excess}$ . The stall cell size is reduced significantly by time  $t_4$ , as shown in the corresponding schematic. This small cell re-enters the region of  $i_{excess} > 0$ , and then starts growing again and experiences another cycle of growth and decay. With each cycle, the size of the cell shrinks less in the  $i_{excess} < 0$  region, until a fully developed stall cell forms.

The speed and size of fully developed cells in clean and distorted flow are presented in Table 6.1. Stall cells move at the same speed,  $\omega = 0.55\Omega$ , in both flow conditions. The stall cell size is approximately  $185^\circ$  in both cases, with a slight variation at different circumferential locations. In distorted flow, the stall cell is consistently larger in the counter-swirl region, and



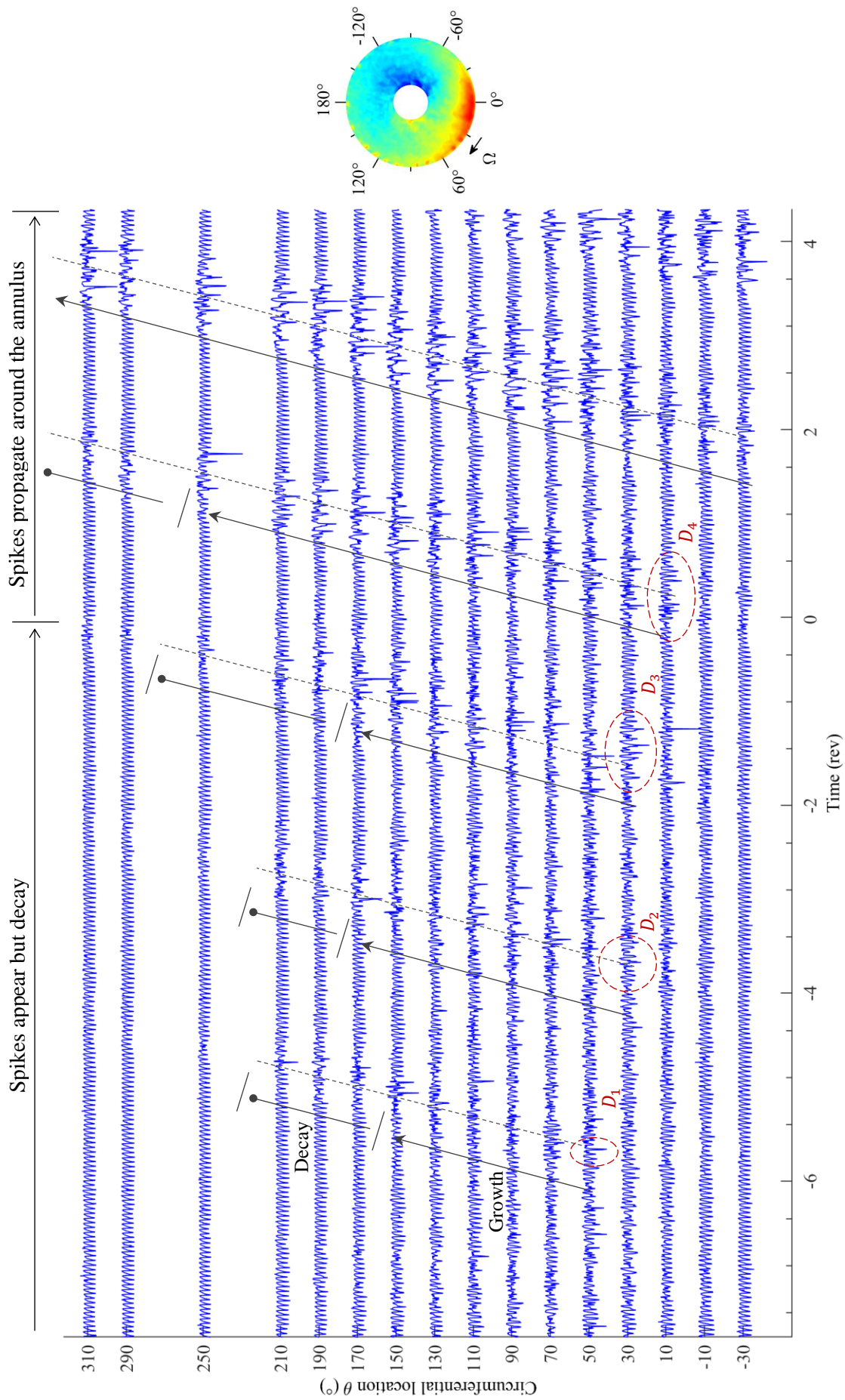


Figure 6.13— Pressure waveforms, stall inception in distorted flow. Dashed lines show propagations of spikes.

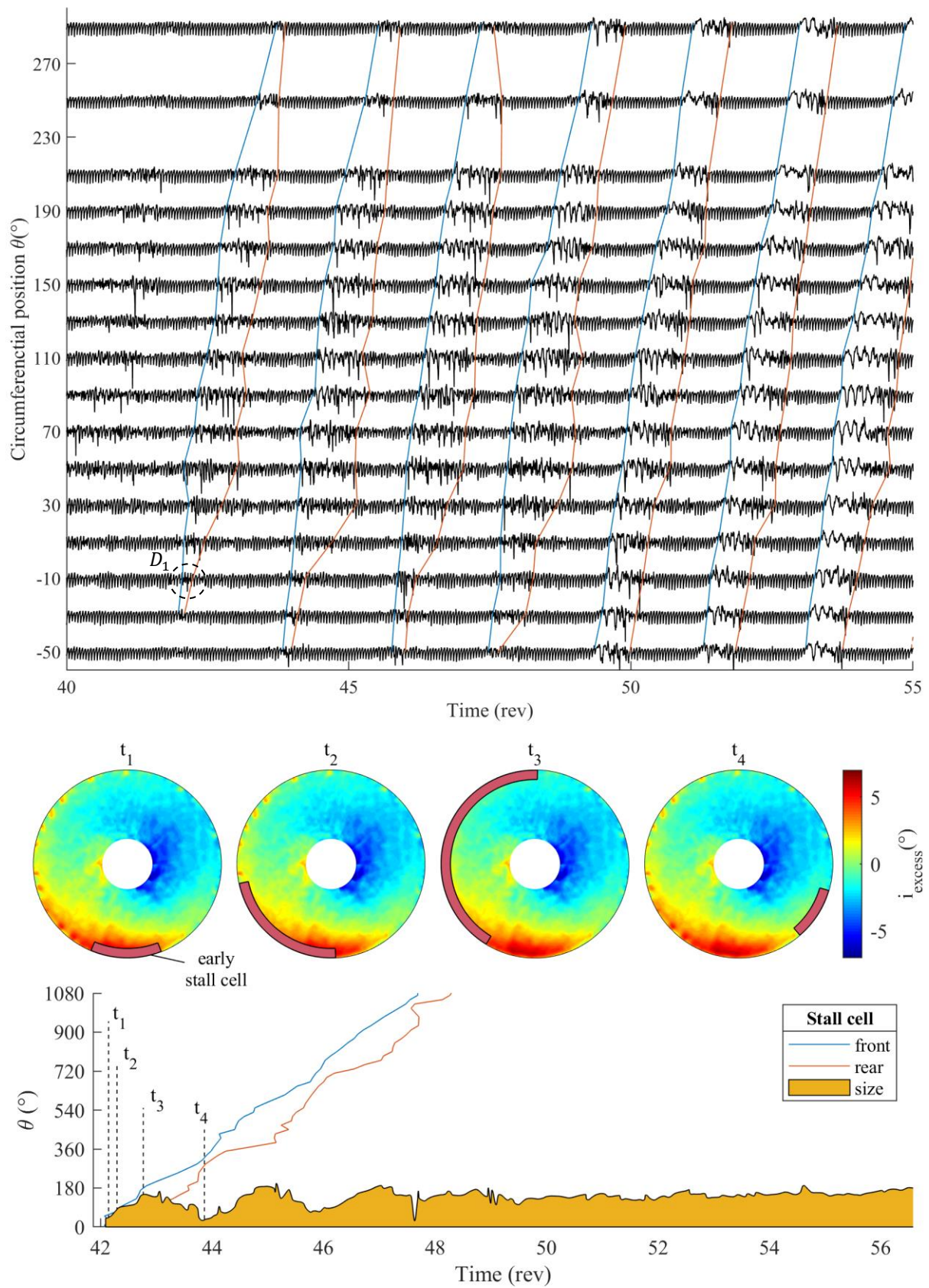


Figure 6.14 –A stall event in distorted flow with the early cell front and rear labelled (above), a schematic of the stall inception (middle) and early stall cell propagation and growth history based on the waveform data (below)

smaller in the co-swirl region. A minor change in size is also observed in clean flow stall cells. This is most likely due to sensitivity to eccentricity.

	Stall cell speed $\omega/\Omega$	Stall cell size
Clean	0.55	$185^\circ \pm 17^\circ$
BLI	0.55	$185^\circ \pm 22^\circ$

Table 6.1 - Stall cell speed and size

## 6.2 Redesign Blade Stall

The mechanism presented in the previous section shows that there is a correlation between *excess incidence* and the growth of disturbances that are responsible for stall inception. The analysis only considers the stall inception with the baseline rotor design. In this section, measurements taken with the redesign blade are investigated.

### 6.2.1 Clean Flow Stall

A stall event in clean flow with the redesign blade is shown in Figure 6.15. The main difference compared to the baseline blade measurements is a different amplitude of peak-to-peak variation, since the blade tip LE is further away from the probes, as described in section 3.2.3.

The signal prior to  $t = 140rev$  is regular, with no disturbances. Around  $t = 160rev$ , there are disturbances that propagate around the annulus. A window around that time shows how these disturbances propagate but are damped out. This is because this particular stall event is self-excited, i.e. the operating point is set just at the edge of stability limit, and stall occurs spontaneously, rather than being triggered by closing the throttle. Similar signal behaviour is seen around  $t = 228 rev$ . One of initial disturbances that appears at  $\theta = 100^\circ$  increases while it moves around the annulus, growing gradually into a stall cell. Within one revolution a stall cell is formed. It travels at  $\omega = 0.58\Omega$ , and occupies around  $155^\circ$ . The structure of this early stall cell is the same as in the baseline blade case, featuring many spikes initially. The absence of large spikes in the initial disturbance is likely to be due to increased distance between the probe and blade LEs, such that the low pressure cores of initial disturbances are not captured by the probes.



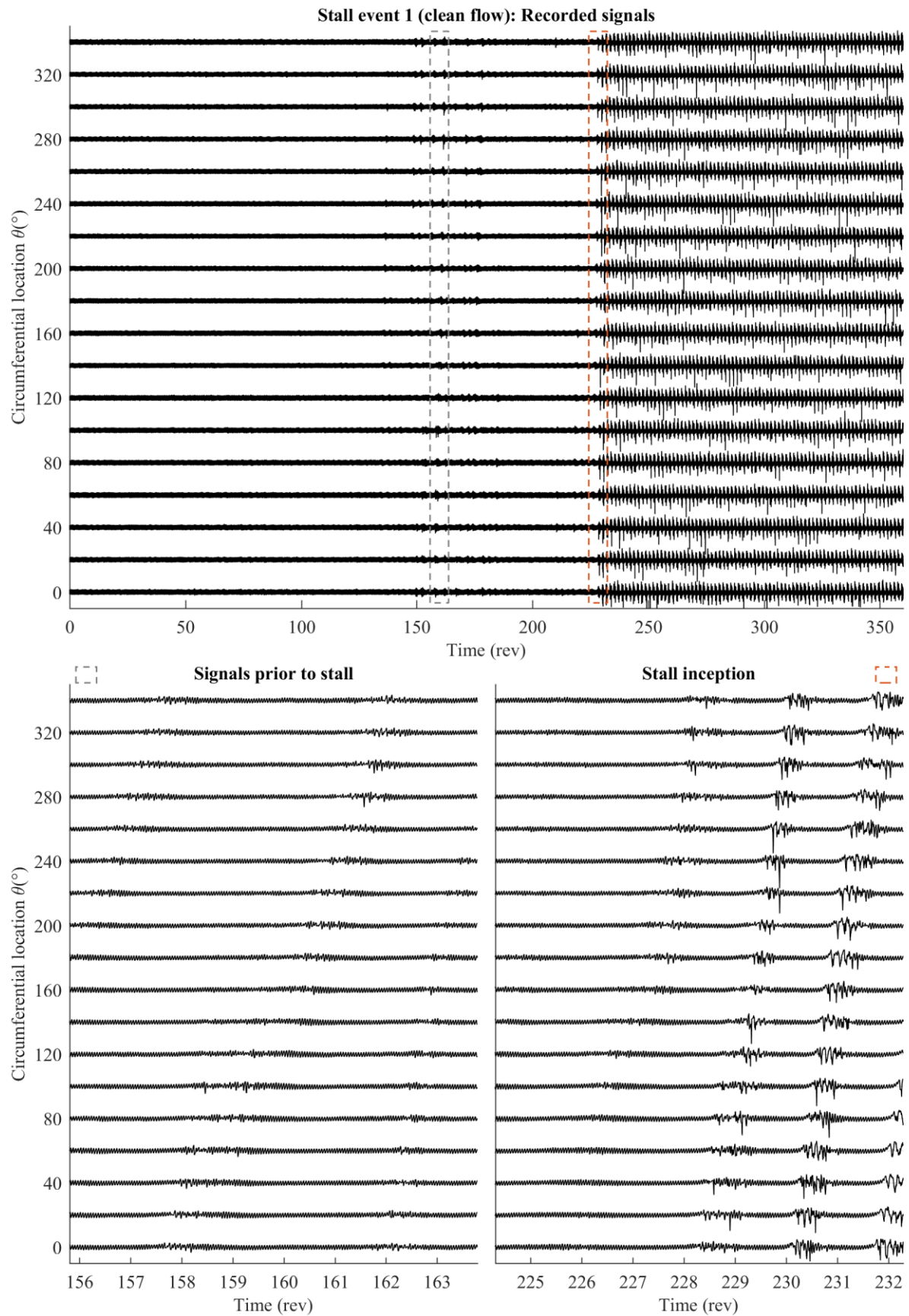


Figure 6.15 - Stall event in clean flow: signal prior to stall and during stall inception

## 6.2.2 Flow Field at Steady Operating Points in Distorted Flow

Plots of *excess incidence* for the baseline blade and redesign are shown in Figure 6.16. The plot shows that  $NS_d$  points, shown in characteristics in Figure 5.5, occur when the *excess incidence* at the tip is very similar. Regions of positive *excess incidence* occur at approximately  $\theta \in [-30^\circ, 70^\circ]$  in both cases. The region is marginally larger for the redesign blade. However, the region of negative critical incidence is also slightly more pronounced, which balances the slightly stronger driving force for disturbance growth in the positive  $i_{excess}$ .

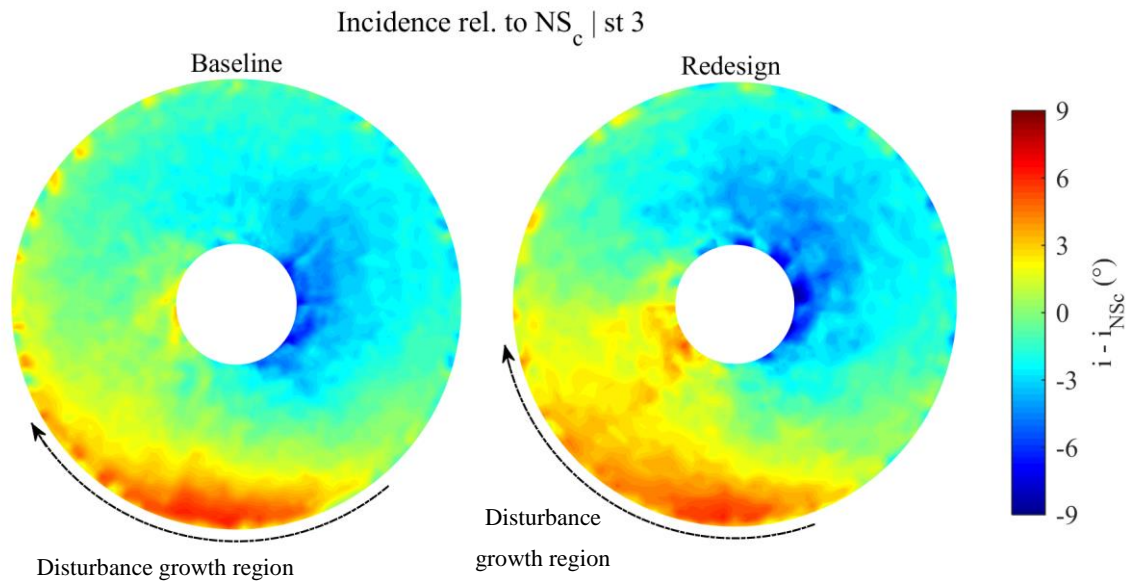


Figure 6.16 – Excess incidence at  $NS_d$ : baseline vs redesign

## 6.2.3 Unsteady Measurements

Unsteady casing pressures measured at  $DP_d$  and  $NS_d$  are shown in Figure 6.17. Waveforms at  $DP_d$  show that there are no irregularities at any of the circumferential locations, and the waveforms are undisturbed. The situation is different at  $NS_d$  and more like that in the baseline blade case at  $NS_d$ . Significant irregularities are found at  $\theta \in [40^\circ, 180^\circ]$ , while the signals in the co-swirl region are mainly undisturbed, such as the signal at  $\theta = -20^\circ$  for example, which is shown in a window around  $t = 58rev$ . Spikes are seen occasionally in the disturbed region, and they occasionally propagate deep inside the negative *excess incidence* region but are always suppressed well before the region of positive critical incidence.

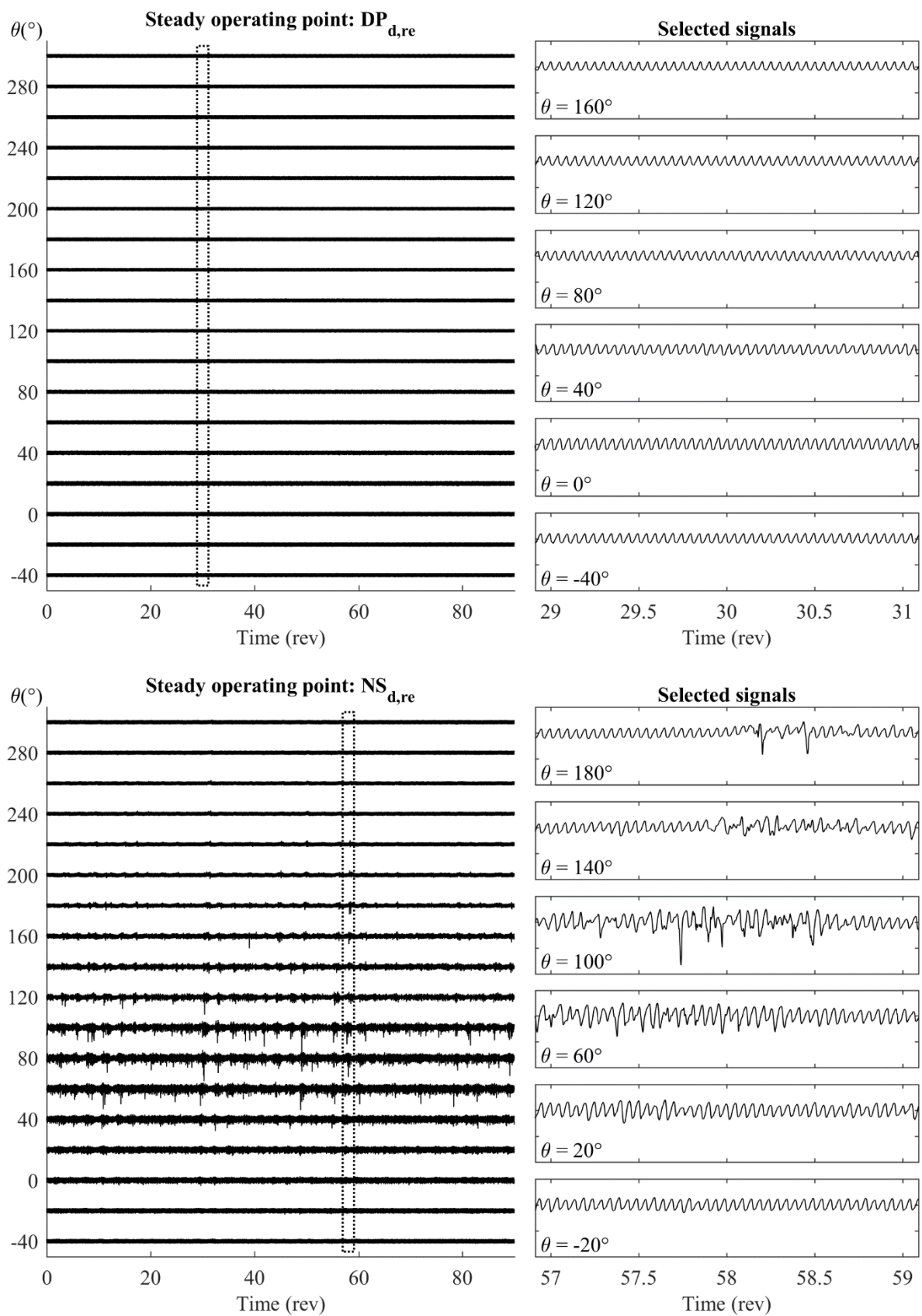


Figure 6.17 - Unsteady casing static pressure measurements at  $DP_d$  and  $NS_d$

### 6.2.4 Linking with the Steady Flow Field

Disturbance energy plots of signals at  $NS_d$  and  $DP_d$  for the baseline and redesign blades are shown in Figure 6.18. The plots show the signal disturbance energy levels in the frequency range  $f \in [0.7f_{bp}, 0.9f_{bp}]$ . All the values are non-dimensionalised by the  $NS_c$  peak level in the baseline case. Note that the absolute energy levels are significantly lower in the redesign rotor because the probes were positioned further forward from the blade LE.

The disturbance growth regions at  $NS_d$  points are labelled. As for the case of the baseline blade, the disturbance energy levels are calculated by averaging multiple measurements with the gauze rotated, in order to isolate differences arising due to any asymmetries in the rig. In the case of the redesign, 18 measurements were calculated with the gauze rotated by  $20^\circ$  each time.

The disturbance energy curves for the redesign blade are a factor of 3 lower than the level of the baseline blade. However, it is clear that the  $NS_d$  level in the redesign blade is very high and that its variation is similar to the  $NS_d$  level in the baseline blade.

*Excess incidence* levels at 75% span are plotted for comparison. Lower *excess incidence* at  $DP_d$  in the redesign indicates that this rotor is further away from stall than in the case of the baseline blade. At  $NS_d$ , the relative incidence curves overlap in both cases. There is a very slight difference in the region  $\theta \in [10^\circ, 90^\circ]$  where the incidence is higher by about  $1^\circ$  and in  $\theta \in [130^\circ, -100^\circ]$  where the incidence is smaller by approximately the same amount. The plot is representative of the critical incidence variations at the tips of the two blades.

The results confirm conclusions drawn for the baseline blade. When the *excess incidence* is positive, disturbances start growing. The growth rate is proportional to the *excess incidence* level. When the *excess incidence* drops below zero, disturbances start decaying until they are fully damped. In the redesign blade, disturbances start growing at around  $15^\circ$  later than in the baseline case, at around  $\theta \approx -25^\circ$ . The growth region is up to  $\theta \approx 60^\circ$  in relation to the baseline blade, and up to  $\theta \approx 80^\circ$  in relation to the redesigned blade, due to slightly higher *excess incidence* in the counter-swirl region. Growth regions are followed by decay regions in which the disturbance levels drop.

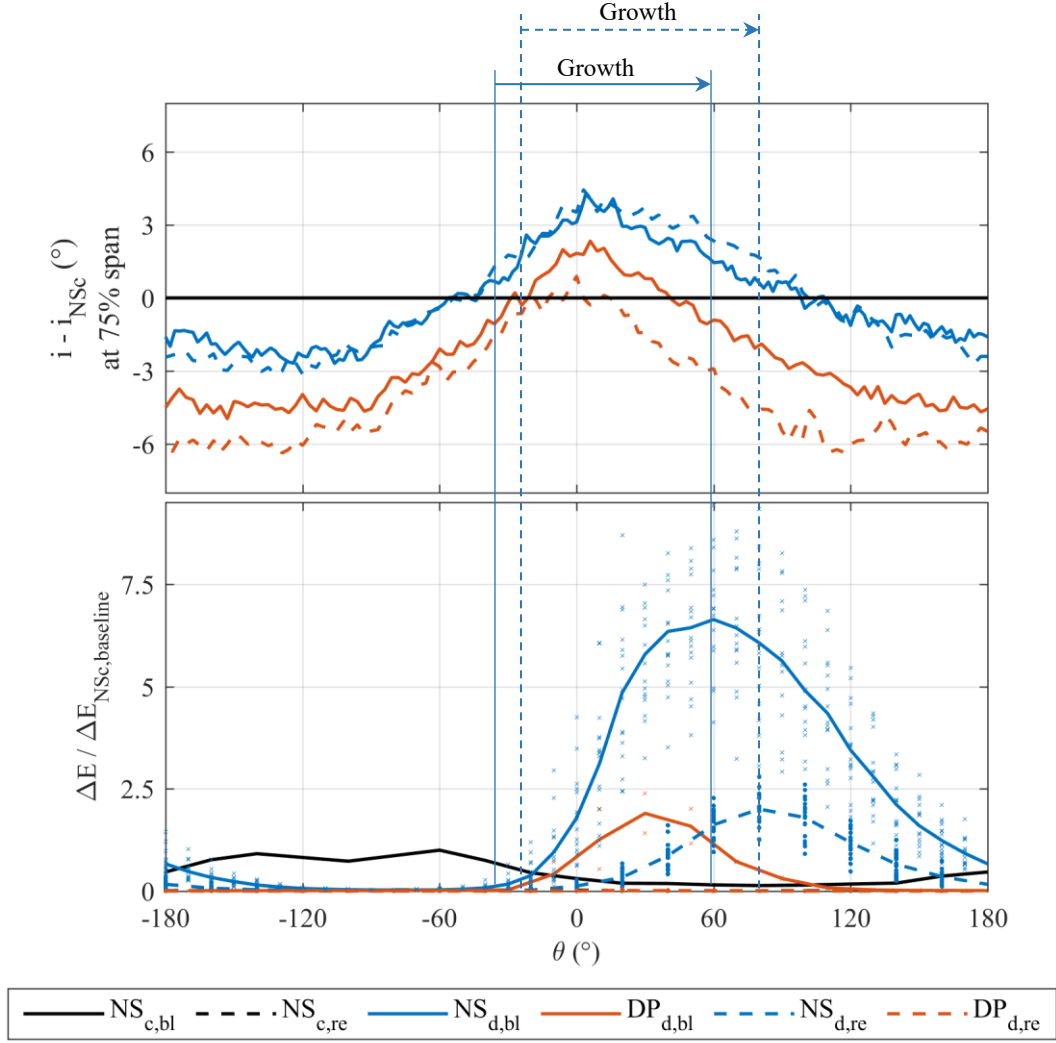


Figure 6.18 - Disturbance energy and incidence levels at the tip: baseline vs redesign

### 6.2.5 Stall Inception in Distorted Flow

A stall event in distorted flow is shown in Figure 6.19. In the plot, irregularities are seen in the region  $\theta \in [40^\circ, 160^\circ]$ . Stall-type disturbances occasionally appear around  $\theta = 40^\circ$  but are suppressed as they propagate before the region of positive excess incidence is reached. Eventually, a disturbance appears that grows into a stall cell, in the same manner as in the case of the baseline blade. An early stall cell initially grows, and then decays in the negative *excess incidence* region, eventually forming a fully developed stall cell, as shown in Figure 6.19.



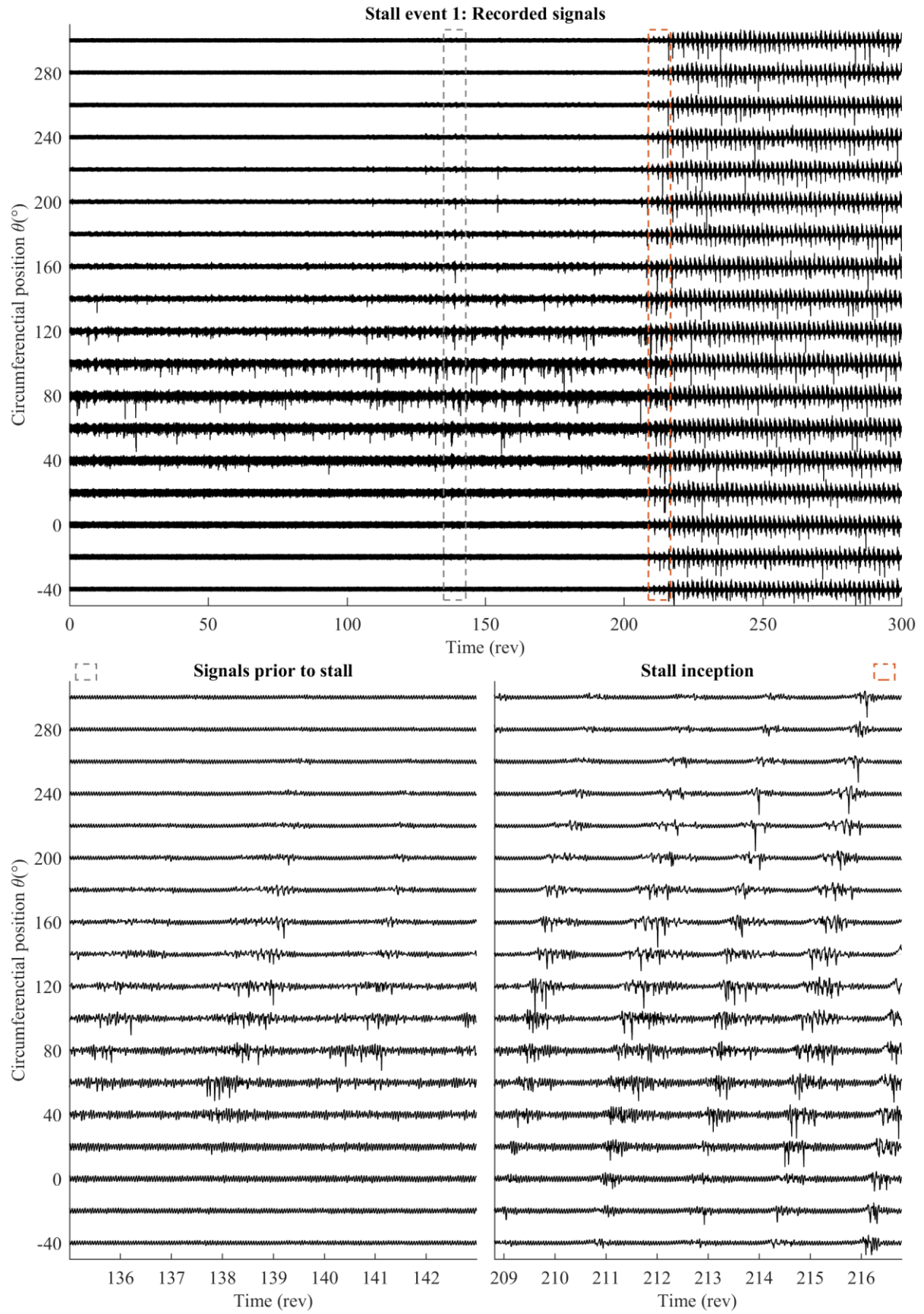


Figure 6.19 - Stall event in distorted flow: signal prior to stall and during the stall inception

A stall inception event with the redesigned blade is shown in Figure 6.20. The light grey lines follow the motion of a blade. Disturbances " $D_1$ "-" $D_4$ " appear in the region of positive *excess incidence* and initially grow, but soon start decaying as they enter the region of negative *excess incidence*. Eventually a disturbance " $D_5$ " appears and propagates around the entire annulus without being damped. It reappears at  $\theta = -20^\circ$ , inside the region of growth, after which it continues growing and develops into a stall cell. The process is the same as in the baseline blade.

The stall inception mechanism with the baseline blade described in section 6.1.5, and presented in Figure 6.14, matches that of the redesign blade, as shown in Figure 6.21. A waveform plot in which the early stall cell's front and rear are identified manually provides the data that is used to track the propagation and growth of the stall cell. An analysis of the interval  $t_2 - t_3$  which occurs during the second cycle shows that the front of the stall cell moves rapidly through the region of  $i_{excess} > 0$ , while the rear lags behind, moving at a very slow speed. Between  $t_3 - t_4$ , the cell shrinks due to the front slowing down and the rear catching up as its speed increases. Time  $t_4$  shows the moment when the front accelerates after it re-enters the positive *excess incidence* region, initiating another cycle.

The stall cell speed and size are shown in Table 6.2. Baseline blade results are shown for comparison. The stall cell size in distorted flow matches that of the baseline blade, and the same type of variation occurs with the cell is the largest in the positive critical incidence region. The speed is only marginally higher in both clean and distorted flows. The stall cell size is smaller in clean flow by approximately  $30^\circ$ .

		Stall cell speed $\omega/\Omega$	Stall cell size
Baseline	Clean	0.55	$185^\circ \pm 17^\circ$
	BLI	0.54	$185^\circ \pm 22^\circ$
Redesign	Clean	0.58	$154^\circ \pm 7^\circ$
	BLI	0.58	$183^\circ \pm 16^\circ$

Table 6.2 - Stall cell speed and size

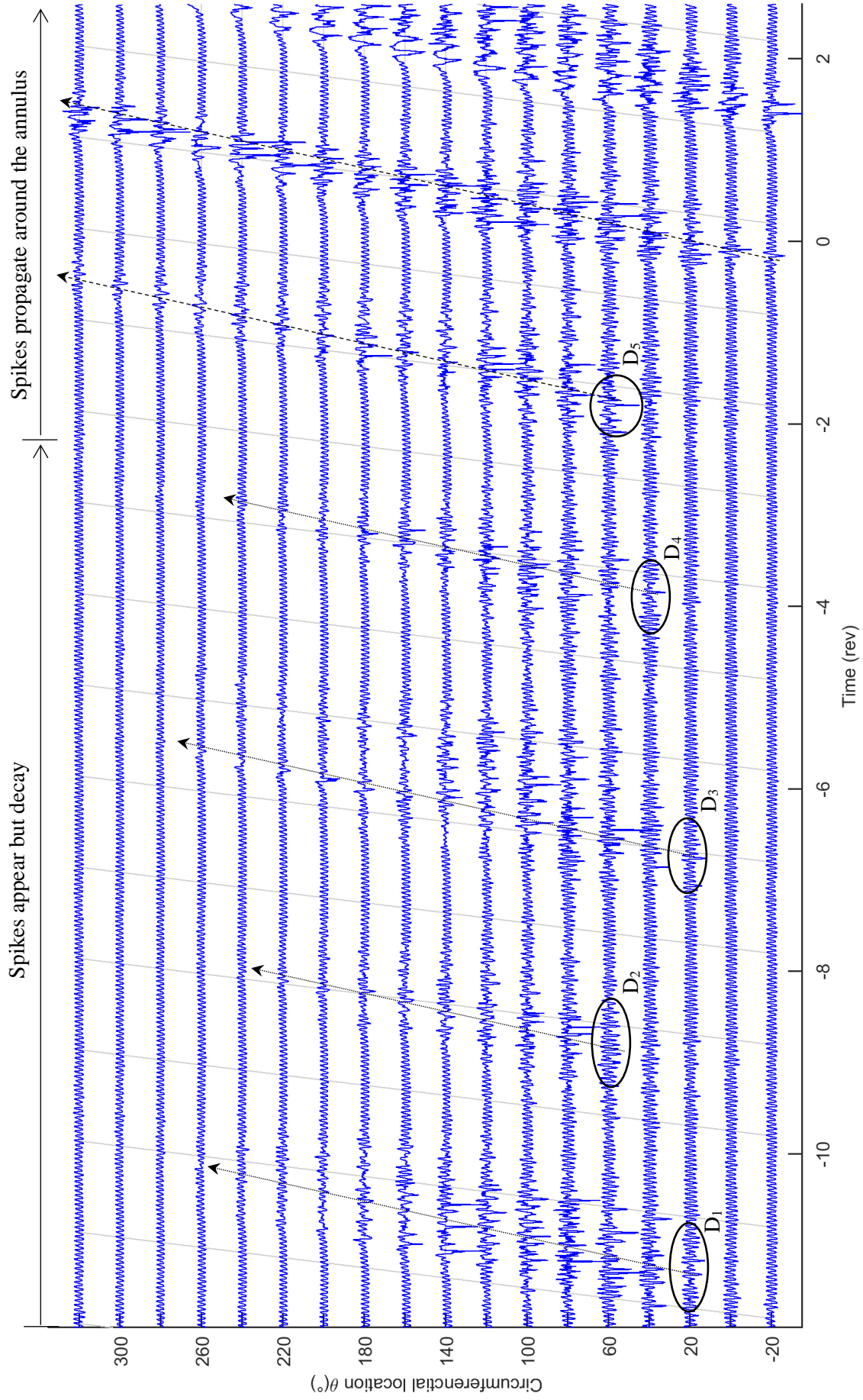


Figure 6.20 – Pressure waveforms during a stall inception event with redesign blade geometry



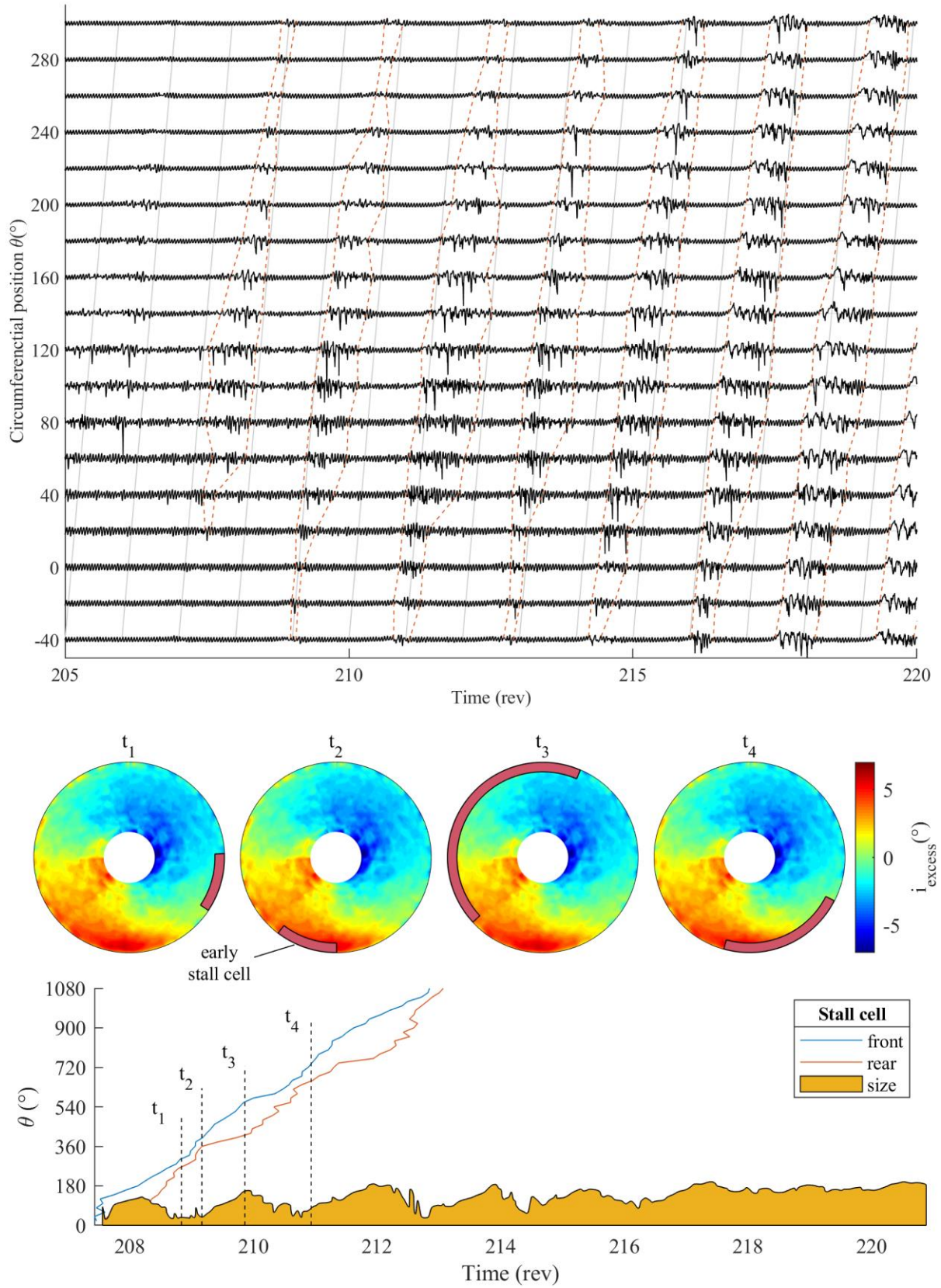


Figure 6.21 - A stall event in distorted flow with the early cell front and rear labelled (above), a schematic of the stall inception (middle) and early stall cell propagation and growth history based on the waveform data (below)

## 6.3 Summary

In this research, the drop in stability margin of the BLI rig fan due to distortion was found to be small, as shown in the steady flow measurements presented in Chapter 5. Pressure signals at a location upstream of the LE were analysed in this chapter for both the baseline and the redesign blade to provide a better understanding of the mechanism of stall inception in distorted flow.

In this Chapter, a link is identified between the incidence level above the critical  $NS_c$  level, defined as *excess incidence*, and disturbance energy at steady operating points in distorted flow. It is shown that disturbances grow when they enter the positive *excess incidence* region and decay once the *excess incidence* level drops below zero. Stall is found to occur when disturbances created in the region of positive *excess incidence* are able to propagate and enter this region again without being fully suppressed in the negative *excess incidence* region.

The mechanism is the same in both the baseline and redesign cases. Similar behaviour has been observed in tests carried out with a transonic fan operating in a BLI flow field (Cousins, et al., 2017), where blades “stall” in the region of high incidence and “unstall” as they leave the distortion region. The blade also has a substantial stability margin, but the reasons for this remain unclear (Provenza, et al., 2019). The findings in this chapter indicate that the mechanism identified by this research is likely to be the same in other compressor and transonic fans, allowing them to operate stably without the stability margin being significantly affected, even if the physical mechanisms responsible for disturbance creation and damping are not exactly the same.

# Chapter 7

## Conclusions and Recommendations for Future Work

The aim of this research was to investigate how changes to the mechanical design for aeromechanical stability in distorted flow affect the aerodynamic performance, and how changes in rotor work input profile influence the performance and stability in BLI. Design modifications were applied to two test cases, a representative transonic fan and a low speed rig fan, and the impact on the flow field investigated using experimental and computational techniques. The main findings and recommendations for future work are presented in this chapter.

### 7.1 Main Research Findings

#### 7.1.1 Blade Mechanical Design Requirements

Blades operating in distortion experience alternating forcing due to their loading changing with each revolution, as they pass through the distorted region of the flow. The forcing affects blade structural integrity, since high alternating stress on top of already very high steady stresses in rotor blades can lead to high cycle fatigue failure if the limit of allowable alternating stress amplitude is exceeded in the Goodman diagram. Design speed 1EO and 2EO vibration, and 1F/2EO and 1F/3EO resonant crossings at part speed are the main reasons for concern, as the forcing amplitude at 1EO and 2EO is very high in the BLI application, unlike in clean flow. Therefore, substantially stronger blades are needed for operation in distorted flow. Flutter free design is also required, so usual work-per-cycle calculation can be used to estimate the aerodynamic damping.

The impact of satisfying mechanical requirements on aerodynamic performance of BLI propulsors was mostly neglected in past research which often assumed around 1% loss of efficiency due to distortion in system level analyses. Work presented in this thesis is among the first to take the mechanical aspects of the design into consideration, along with the recent NASA study BLI<sup>2</sup>DTF (Arend, et al., 2017).

The approach taken in this work was to implement mechanical criteria provided by Rolls-Royce for creating a mechanically robust design that can cope with the high level of distortion in the representative inlet stagnation pressure profile used in this work. The specified criteria included requirements regarding the blade aerodynamic loading, high cycle fatigue and flutter. The aerodynamic loading requirement was not difficult to satisfy by the low pressure ratio transonic fan used in this thesis.

The main mechanical design change was required to achieve the increase of 1F-1EO frequency margin to 60% (of 1EO). The transonic VITAL fan which initially had 20% margin was used for the purposes of studying the impact of the mechanical design changes. The conventional margin in typical axial fans designed for operation in clean flow is 10%, according to Provenza (Provenza, et al., 2019). The required shift was expected to reduce 1EO vibration and strengthen the blade to reduce the steady and alternating stresses. Substantial thickening of root and hub sections was required to achieve the required frequency shift. Thickness was scaled across the blade span, with the largest increase of 50-70% of the blade thickness occurring in the region of the blade close to the root, and 25% at the mid span, while the tip thickness was not modified. The approach was successful in moving the 1F frequency to the required value. The mode two and three, 2F and 1T, frequencies were also affected by the design change. While this level of thickening was substantial, the main positive point is that there was only around 3% decrease in throat size and most of the changes took place below the supersonic tip region.

Other mechanical criteria included the separation of 1F and 1T frequencies which was satisfied with no difficulty since the separation of the two frequencies is substantially larger in typical rotor fans than required. There was also a limit on the torsional component in the 1F mode, for flutter considerations. The redesign blade had approximately the same torsional to plunge ratio in the 1F mode, resulting in a similar expected flutter margin compared to the baseline design. Implementation of the high cycle fatigue criterion which puts a limit on the AF level was subject to a combined aero/mechanical analysis and was not assessed. The thick blade was expected to have a significantly improved fatigue life, due to significant strengthening in the hub region. Next step is to plot the Goodman diagram for the design speed operation and 1F/2EO and 1F/3EO resonant crossings at part speed to check whether this improvement puts the alternating stresses well below the  $10^9$  number of cycles limit. Modelling resonant responses at part speed will be the most challenging, as an accurate estimate of the damping is needed.

### **7.1.2 Impact of Mechanical Design Changes on Aerodynamic Performance**

The work in this thesis showed that blades which are thicker in the root region are needed for operation in distorted flow, which caused approximately 3% reduction in the effective throat area. This in turn caused a reduction of the flow capacity of around 2%, which in an engine would reduce the thrust. To recover this thrust either a larger diameter fan would be needed, or the blades would need to be run at a higher speed, both of which would increase the steady stress at the root, which is undesirable from the high cycle fatigue point of view. There would also be an increase in installed mass which is undesirable.

Thickening the blades also affected the efficiency as the thicker blades were shown to experience higher profile losses at the hub and mid-span. The reduction in clean flow was the same as the efficiency and mass flow reductions in distorted flow. This indicates that impact of thickening the rotor can be assessed in clean flow and is similar in distorted flow. Some of the loss was due to an increase in incidence that arose due to lower mass flow in the hub region at the new peak efficiency point, which would not be difficult to adjust for by modifying the inlet metal angle. The encouraging fact is that thickening needs to be done in the root and hub regions of the blade, which does not affect the shock structure at the blade tip.

The overall breakdown of the efficiency and mass flow reduction is as follows: i) around 2% loss of efficiency, 0.5% due to blade thickening and 1.5% due to distortion, and ii) 3.5% reduction in mass flow, 1.5% due to thickening and 2% due to distortion. Since the mechanical design criteria was conservative, the results indicate that it is realistic to expect up to a maximum of 2-3% loss of efficiency due to distortion and mechanical design changes combined, and around 3.5-4% reduction in mass flow in BLI fans, before any distortion tolerant design features are introduced. The overall fuel burn benefit is highly sensitive to loss of efficiency; however, this level of reduction in performance is only a starting point. Findings from the low speed BLI rig tests look promising as they indicate that some of the efficiency loss is likely to be recovered by changing the work profile to offload the tip to target the regions of peak loss.

### **7.1.3 Impact of Modifying Rotor Work Input Profile**

Distortion tolerance of a fan could possibly be improved by changing the work input profile to: i) reduce peak losses and therefore improve efficiency, and ii) affect the flow redistribution. The rotor work input profile in the low speed BLI rig fan was modified for the purposes of investigating this. The redesign led to approximately 15% increased work at the mid-span and

approximately 15% decreased loading at the hub and the casing, which was achieved by changing the blade metal angles. Other design changes included extension of the chord at midspan to reduce the diffusion factor to cope with the increase in work input, and movement of the position of maximum camber and thickness forward by 10% chord.

At design point, the main impact of the design changes was the reduction in losses at the tip in the counter-swirl region, which is the critical region as this is where the incidence, diffusion and losses are the highest and in which early stall-type disturbances are initiated continuously, even at stable operating points. The design change had a powerful impact as the efficiency was significantly improved due to decrease in loss at the tip, caused by a reduction in diffusion and loading. Therefore, it was demonstrated that the tip region is the main region which should be targeted in blade redesign for operation in BLI. The flow field changes in the other regions of the flow were marginal, except for an increase in mass flow through the mid-span whose impact on the aircraft level benefit needs to be investigated further. Reduction of the work at hub did not lead to a desired reduction in flow non-uniformity in that region, which means that further design changes need to be explored in order to achieve this. Impact on the upstream flow redistribution was also weak, negligible compared to the redistribution that occurs due to overall blade loading. Alternative ways of affecting the upstream flow redistribution are needed, possibly increasing overall loading or changing the hub or casing geometries for a significantly stronger impact.

At off-design near stall conditions, the flow over the redesign blade started separating in the counter-swirl region at the heavily loaded mid span due to high incidence and diffusion. The tip was exposed to a high level of incidence in the counter-swirl region but remained stable overall. A larger operating range was achieved by relieving the loading at the tip, and some of this improvement is likely to be due to increased blockage at the separated mid-span in the low momentum and counter-swirl regions which forced more flow through the critical tip region, having a stabilising effect.

#### **7.1.4 Stall Inception Mechanism in Distorted Flow**

Measurements in the low speed BLI rig showed that loss of stability margin due to BLI was small, and that increase in range in clean flow led to an increase in range in distorted flow. In this research, the behaviour of stall cell development in the early stages of stall inception was investigated. It was shown that stall cells grow in a way which has not, to the author's knowledge, ever been previously reported in literature.

The mechanism was found to be due to front and rear of the stall cell travelling at different speeds, depending on the location of the stall cell. It was found that initial disturbances always appeared when the blades enter the region where the incidence is higher than the incidence at which stall occurs in clean flow, defined as positive *excess incidence*, which occurred in the low momentum and counter-swirl regions of the flow. During stall inception, an initial disturbance, an early stall cell, forms as a blade enters the region of positive *excess incidence*. Throughout the region, the front travels at a high speed and the rear lags behind due to new blade passages being affected as they enter the region of positive *excess incidence*. This part of the propagation cycle is characterised by high speed of the stall cell and high growth rate. Once the stall cell is large, typically occupying up to half the annulus, it stops growing. By that time, the front of the stall cell has reached the negative *excess incidence* region which causes it to slow down. The rear on the other hand keeps moving at the original speed and starts accelerating as it leaves the region of positive *excess incidence*. Now the rear is moving faster than the front, making the cell shrink. This behaviour may repeat several times until a cell reaches the region of positive *excess incidence*, without decaying completely while passing through the region of negative *excess incidence*, after which it keeps growing and gradually grows into a fully developed stall cell. This mechanism occurred in the same way with both blades tested.

This mechanism is responsible for allowing the blades to operate stably even when some regions are locally operating beyond the clean flow stability limit. Any propagating disturbances that are initiated occasionally at stable operating points in the region of positive *excess incidence*, where there is driving force for their growth, are suppressed by the mechanism. Similar behaviour was observed in recent transonic fan tests, where the blades were reported as “stalling” in the distorted region and “unstalling” in the high momentum region. This indicates that the same mechanism is likely to occur in transonic fans, even though the physics behind the stall cell behaviour would be different due to the presence of shocks.

### **7.1.5 Fan Design for BLI**

In Chapters 5 and 6 it was shown that off-loading the tip improves aerodynamic performance and the stability margin of the low speed BLI fan. Analysis of the flow field revealed that:

- The tip region in the counter-swirl and low momentum parts of the annulus is critical as this is the region of peak loss and peak diffusion in distorted flow, and the region where disturbances and early stall cells are initiated.

- Offloading the tip and loading the mid-span led to the same overall loading but reduced peak losses in BLI, which resulted in the improved overall performance.
- Offloading the tip led to improvement in the stability margin. Mid-span flow in the low momentum and the counter-swirl regions separated first, which likely contributed to improvement in the stability margin as increased blockage at the mid-span forced more flow to pass through the tip region, having a stabilising effect.
- Moderate changes in work input, i.e. around 15% reduction in tip and hub loading and around 15% increase in loading at the mid-span, did not significantly affect the upstream flow redistribution nor distortion transfer through the hub. Fine details of work distribution appeared to be of secondary importance for flow redistribution compared to the overall fan loading.

These findings can be applied to the redesign of a representative transonic fan, such as VITAL, for improved distortion tolerance. The VITAL design was optimized for clean flow and the loss of efficiency due to distortion and mechanical design changes was found to be approximately 2%. The findings from the low speed BLI rig and the analysis of the VITAL fan flow field indicate that:

- Further offloading the VITAL fan tip (it is a mid-span loaded design, see section 4.1) would be beneficial as it would reduce losses in the tip region in BLI flow in the critical, counter-swirl region. A trade-off between decreasing peak losses at the tip and increasing losses at the mid-span (due to loading the mid-span further to keep the same overall loading) will set a limit to which this can be done. Opening and closing the blade sections at the tip and mid-span to change the loading would also affect choking mass flow, so it may be necessary to impose an additional requirement of keeping the same flow capacity together with the constraint used in the low speed case of keeping the same overall loading.
- Further offloading the tip is expected to improve the stability margin. As behaviour similar to that described in Chapter 6 was observed in NASA's transonic fan tests in BLI discussed in sections 2.1.4 and 2.4.3, it is expected that relieving the tip loading will have a similar effect as in the low speed BLI rig, including the benefit of higher blockage if the flow at the mid-span separates first. Further work is needed to understand the implications on the mechanical integrity of the blade. Moreover, in



transonic fans there is a risk of flutter occurring before stall; therefore, further research is needed to investigate how the flutter margin would be affected by the design changes.

- The distortion tolerance of a fan can be improved by changing the fan design to affect the flow redistribution. Findings from the low speed rig indicate that it is not expected to achieve significant changes in the bulk flow redistribution by modifying the work input profile. Changing other fan stage parameters such as rotor-stator spacing, stator non-axisymmetric design, hub and casing geometries, and particularly the inlet duct design is expected to have a much greater impact.
- Flow analysis in Chapter 4 revealed a high level of variation of flow conditions around the annulus. Some improvement in efficiency can be expected from modifying the blade sections. Again, there would be a trade-off between changes in performance in parts of the annulus where the flow is either supersonic or subsonic, where the benefits due to adjusting a section to supersonic conditions could lead to worsened performance in the subsonic part of the circumference and vice versa. Further research is needed to investigate whether this approach could lead to meaningful improvements in efficiency.

## **7.2 Recommendations for Future Work**

### **7.2.1 Mechanical Design**

The main objective of the blade mechanical design for operation in distorted flow is to avoid aeromechanical failure due to flutter or high cycle fatigue. The work in this thesis focused on implementing mechanical design criteria specified by the industrial partner. Having design criteria is useful as it simplifies the analysis that needs to be done to assess a design. However, further work is needed to validate these criteria, as they are a conservative estimate and less stringent requirements may be needed in practice. In particular, it is of interest to understand where the optimal placement of 1F mode is relative to the 1F/2EO crossing and proximity to 1EO and 2EO lines at design speed. With more experience and further studies, the criteria will likely be modified and will gradually converge towards an accepted standard over time, similar to the clean flow mechanical design.

The assessment of flutter in BLI poses a challenge as the typical work-per-vibration cycle analysis does not converge at a single value of aerodynamic damping as in clean flow, but varies depending on which part of the flow the vibration cycle occurred in. Further work is needed to understand how flutter stability is affected if some part of the range of aerodynamic

damping becomes negative. Another issue with flutter arises when the numerical stability limit in CFD occurs before it occurred in experiment, in which case the flutter analysis cannot be carried out. While the work-per-cycle calculation may be computationally more demanding in distorted flow, indications are that there are no fundamental differences compared to usual practices currently used for flutter assessment in clean flow.

High cycle fatigue assessment is a major challenge due to difficulty modelling the resonant responses  $1F/2EO$  and  $1F/3EO$  at part speed. The reason is that the resonant response depends on the value of damping which is hard to estimate accurately. A recent NASA's experimental study found that the damping at one of those crossings was of the order of 3%, which was significantly higher than the typical 0.5-1% in clean flow, which was also the computationally predicted value. Moreover, it was noted that with 1% damping, the response would have led to breach of the Goodman diagram limit. It is important to understand whether this is an effect that is expected to repeat in distortion, or whether it was case specific. Further work is needed to understand how to improve the accuracy of modelling resonant response during these crossings at part speed, and how to analyse the impact on fatigue life.

### **7.2.2 Aerodynamic Design**

This research demonstrated that modifying the rotor work profile to reduce loading at the tip reduced the losses significantly and improved blade performance in BLI, for operation at the design speed and design operating point, and a single distortion profile. Past research has explored some of the benefits of non-axisymmetric stator design (Hall, et al., 2017) (Gunn & Hall, 2017). While these were the first steps towards studying design changes for the improvement in distortion tolerance, studying the impact of other possible design changes is needed. Changes of hub and casing geometries, or introduction of compound sweep, different blade section design, change in the overall fan loading to affect the upstream flow redistribution, may all lead to improved distortion tolerance of a fan. Further work is needed to understand their impact. With the large regions of loss eliminated, the design process could focus on using time accurate particle tracking to identify high loss regions, then tailor the design specifically to target those regions in order to maximise the efficiency.

With increase in computational power, testing of various inlet stagnation profiles or rotor and stator geometries has become possible. Future work will also need to investigate the impact of operating at off design conditions and at different speeds across the fan map. If a non-axisymmetric stator is used, there will be an impact on thrust when flight conditions change.

Flow non-uniformity in the hub region was not affected by the change in rotor work input profile and reduction of work at the hub. In architectures where there is a core downstream of the fan stage, further research is needed to investigate how the hub flow distortion can be minimised. It is not expected that the distortion will be eliminated completely, so work is needed to study the impact of distortion on the performance of the core.

### **7.2.3 Stability**

The work in this research analysed casing pressure signals to determine the stall mechanism in distortion. However, this approach did not allow investigations of the details of the unsteady flow structures that occur within the blade rows during the stall inception. A numerical approach is needed for this and is something that should be done in future research. Experimental unsteady measurements of flow field downstream of the rotor should also be carried out at near stall with the redesign BLI rig rotor blade to investigate the flow in the region where separation was found to occur at the mid-span as the blades were leaving the low momentum region and entering the counter-swirl region. Moreover, it would be interesting to test whether CFD can be used to model this behaviour, since it was observed at a stable operating point. The experiments should also include unsteady measurements of the flow field at the tip downstream of the rotor during stall inception events, especially in the low momentum and counter-swirl regions where the early stall cells first appear and grow.

Stall in transonic fans is not very well understood, even in clean flow. With the recent increase in computational power, the research is gaining momentum. It would be interesting to investigate the hypothesis that stall inception mechanism observed in the BLI rig applies to transonic machines as well. Eventually, it would be interesting to see how the unsteady flow structures develop during a stall inception event in distorted flow.

### **7.2.4 Transonic Tests**

The findings in CFD and FEA are insightful, however, transonic tests are needed to validate the computational findings. The cost of running transonic tests and traversing the flow field is very high, while installing bulky measurement rakes is undesirable as they would interfere with the flow field. Getting detailed measurements of the transonic flow field in BLI will be very challenging to achieve in practice, as experienced in NASA's BLI<sup>2</sup>DTF tests. Further work is needed in developing methods for taking detailed area traverse measurements during short run times of transonic tests.

### **7.2.5 Aircraft Level Analysis**

Computational methods and computational power now allow coupled analysis of the airframe, intake, and propulsor. A use of this should be made to further optimise intakes and fan designs and understand how the airframe flow is affected in different flight conditions. This approach is already starting to be used on more conventional rear-fuselage propulsor configurations (Tse, 2017).

Change in rotor work input affects the mass flow non-uniformity downstream of the stage. The impact of non-uniformity on the system level benefit is expected to be minor, but the impact will likely depend on the percentage of the airframe boundary layer ingested. This requires further investigation.

Findings in Chapter 4 reveal that there was a loss of flow capacity of around 3.5% that would have inevitably affected thrust. Recovering this mass flow would lead to an increase in weight. Additional increase in mass would also occur due to blade strengthening. Further work is needed to understand the impact of the added mass on the overall system level benefits.

# References

Abaqus, 2012. *Abaqus 6.12 User's Manual*, s.l.: Dassault Systèmes.

Adamczyk, J. J., Celestina, M. L. & Greitzer, E. M., 1991. *The Role of Tip Clearance in High-Speed Fan Stall*. Orlando, Florida, USA, ASME 1991 International Gas Turbine and Aeroengine Congress and Exposition, pp. V001T01A031-V001T01A031.

Agarwal, A. & Dowling, A., 2005. *The Calculation of Acoustic Shielding of Engine Noise by the Silent Aircraft Airframe*. Monterey, California, USA, 11th AIAA/CEAS Aeroacoustics Conference, p. 2996.

Arend, D. et al., 2017. *Experimental Evaluation of an Embedded Boundary Layer Ingesting Propulsor for Highly Efficient Subsonic Cruise Aircraft*. Atlanta, GA, US, 53rd AIAA/SAE/ASEE Joint Propulsion Conference, p. 5041.

Bakhle, M. A. et al., 2012. *Aeromechanics Analysis of a Boundary Layer Ingesting Fan*. Atlanta, Georgia, US, 48th AIAA/ASME/SAE/ASEE Joint Propulsion Conference & Exhibit, p. 3995.

Bakhle, M., Reddy, T. & Coroneos, R., 2014. *Forced Response Analysis of a Fan with Boundary Layer Inlet Distortion*. s.l., 50th AIAA/ASME/SAE/ASEE Joint Propulsion Conference, p. 3734.

Bakhle, M. et al., 2018. *Aeromechanics Analysis of a Distortion-Tolerant Fan with Boundary Layer Ingestion*. Kissimmee, Florida, USA, 2018 AIAA Aerospace Sciences Meeting, p. 1891.

Berrier, B., Carter, M. & Allan, B., 2005. *High Reynolds Number Investigation of a Flush-Mounted, S-Duct Inlet With Large Amounts of Boundary Layer Ingestion*, s.l.: NASA Technical Paper.

Betz, A., 1966. *Introduction to the Theory of Flow Machines*. Sec. 59, First English Edition, Pergamon, New York: s.n.

Brandvik, P. & Pullan, G., 2011. An Accelerated 3D Navier–Stokes Solver for Flows in Turbomachines. *Journal of Turbomachinery*, 133(2), p. 021025.

Brandvik, T. & Pullan, G., 2010. *SBLOCK: A Framework for Efficient Stencil-Based PDE Solvers on Multi-core Platforms*. Bradford, UK, Computer and Information Technology (CIT), 2010 IEEE 10th International Conference. IEEE, pp. 1181-1188.

- Butlin, T. & Batailly, A., 2013. *Anti-optimisation applied to the analysis of rotor/stator interaction*. San Antonio, Texas, USA, ASME Turbo Expo 2013: Turbine Technical Conference and Exposition, pp. V07AT26A001-V07AT26A001.
- Calvert, W. & Ginder, R., 1999. Transonic fan and compressor design. *Proceedings of the Institution of Mechanical Engineers, Part C: Journal of Mechanical Engineering Science*, 213(5), pp. 419-436.
- Camp, T. R. & Day, I. J., 1998. A Study of Spike and Modal Stall Phenomena in a Low-Speed Axial Compressor. *Journal of Turbomachinery*, 120(2), pp. 393-401.
- CENTRELINE, 2017. ConcEpt validation sTudy foR fusElage wake-filLIng propulsioN intEgration. [www.centreline.eu](http://www.centreline.eu).
- Cousins, W. T., Voytovych, D., Tillman, G. & Gray, E., 2017. *Design of a Distortion-Tolerant Fan for a Boundary-Layer Ingesting Embedded Engine Application*. Atlanta, GA, US, 53rd AIAA/SAE/ASEE Joint Propulsion Conference, p. 5042.
- Cumpsty, N. A. & Horlock, J. H., 2006. Averaging Nonuniform Flow for a Purpose. *Journal of Turbomachinery*, 128(1), pp. 120-129.
- Dassault Systèmes, 2012. *Abaqus 6.12 Analysis User's Manual*, s.l.: Dassault Systèmes Simulia Corp..
- Day, I. J., 1991. *Stall Inception in Axial Flow Compressors*. Orlando, Florida, US, ASME 1991 International Gas Turbine and Aeroengine Congress and Exposition, pp. V001T01A034-V001T01A034.
- Day, I. J., 2016. Stall, Surge, and 75 Years of Research. *Journal of Turbomachinery*, 138(1), p. 011001.
- de la Rosa Blanco, E., Hall, C. & Crichton, D., 2007. *Challenges in the Silent Aircraft Engine Design*. Reno, Nevada, USA, 45th AIAA Aerospace Sciences Meeting and Exhibit, p. 454.
- Defoe, J., Etemadi, M. & Hall, D., 2018. Fan Performance Scaling With Inlet Distortions. *Journal of Turbomachinery*, 140(7), p. 071009.
- Denton, J. D., 1983. An Improved Time-Marching Method for Turbomachinery Flow Calculation. *Journal of Engineering for Power*, 105(3), pp. 514-521.

- Dowling, A. & Greitzer, E., 2007. *The Silent Aircraft Initiative – Overview*. Reno, Nevada, US, AIAA Paper No. AIAA-2007-0452.
- Drela, M., 2009. Power Balance in Aerodynamic Flows. *AIAA Journal*, 47(7), pp. 1761-1771.
- El-Aini, Y., deLaneuville, R., Stoner, A. & Capece, V., 1997. *High cycle fatigue of turbomachinery components - Industry perspective*. Seattle, WA, USA, 33rd Joint Propulsion Conference and Exhibit, p. 3365.
- Felder, J., Kim, H. & Brown, G., 2009. *Turboelectric Distributed Propulsion Engine Cycle Analysis for Hybrid-Wing-Body Aircraft*. Orlando, Florida, USA, 47th AIAA Aerospace Sciences Meeting Including The New Horizons Forum and Aerospace Exposition, AIAA 2009-1132, p. 1132.
- Felder, J. L., Brown, G. V., Kim, H. D. & Chu, J., 2011. *Turboelectric Distributed Propulsion in a Hybrid Wing Body Aircraft*. Gothenburg, Sweden, 20th International Society for Airbreathing Engines (ISABE 2011).
- Ferguson, R., 2012. Boeing/NASA. [www.nasa.gov/centers/dryden/pdf/171791main\\_FS-090-DFRC.pdf](http://www.nasa.gov/centers/dryden/pdf/171791main_FS-090-DFRC.pdf).
- Florea, R. et al., 2015. Parametric Analysis and Design for Embedded Engine Inlets. *Journal of Propulsion and Power*, 31(3), pp. 843-850.
- Gonzalez-Gutierrez, G., 2015. *Aeromechanical design criteria (document)*, Derby, UK: Rolls-Royce plc.
- Gorrell, S., Yao, J. & Wadia, A., 2008. *High Fidelity URANS Analysis of Swirl Generation and Fan Response to Inlet Distortion*. s.l., AIAA Paper 2008-4985., pp. 13-20.
- Green, J. S., 2008. *Forced Response of a Large Civil Fan Assembly*. Berlin, Germany, ASME Turbo Expo 2008: Power for Land, Sea, and Air, pp. 685-692.
- Greitzer, E. et al., 2010. *N+3 Aircraft Concept Designs and Trade Studies, Final Report*, Glenn Research Center, Cleveland, Ohio: NASA/CR—2010-216794/VOL1.
- Greitzer, E. M., Mazzawy, R. S. & Fulkerson, D. A., 1978. Flow Field Coupling Between Compression System Components in Asymmetric Flow. *Journal of Engineering for Power*, 100(1), pp. 66-72.

Gunn, E., 2015. *Aerodynamics of Boundary Layer Ingesting Fans*, PhD Thesis, Cambridge, UK: University of Cambridge.

Gunn, E. J. & Hall, C. A., 2014. *Aerodynamics of Boundary Layer Ingesting Fans*. Düsseldorf, Germany, ASME Turbo Expo 2014: Turbine Technical Conference and Exposition, pp. V01AT01A024-V01AT01A024.

Gunn, E. J. & Hall, C. A., 2017. *Non-Axisymmetric Stator Design For Boundary Layer Ingesting Fans*. Charlotte, NC, USA, ASME Turbo Expo 2017: Turbomachinery Technical Conference and Exposition, pp. V001T01A003-V001T01A003.

Hah, C., Rabe, D. C., Sullivan, T. J. & Wadia, A. R., 1998. Effects of Inlet Distortion on the Flow Field in a Transonic Compressor Rotor. *Journal of Turbomachinery*, Volume 120, p. 233–246.

Hall, D. K., Greitzer, E. M. & Tan, C. S., 2017. Analysis of fan stage conceptual design attributes for boundary layer ingestion. *Journal of Turbomachinery*, 139(7), p. 071012.

Hawthorne, W., Mitchell, N. & McCune, J., 1978. Non-Axisymmetric Flow Through Annular Actuator Disks: Inlet Distortion Problem. *Journal of Engineering for Power*, 100(4), p. 604–617.

Herrick, G. P., 2011. *Effects of Inlet Distortion on Aeromechanical Stability of a Forward-Swept High-Speed Fan*. Nashville, Tennessee, US, 46th AIAA/ASME/SAE/ASEE Joint Propulsion Conference & Exhibit, p. 6711.

Hewkin-Smith, M. et al., 2017. *The Role of Tip Leakage Flow in Spike-Type Rotating Stall Inception*. s.l., ASME Turbo Expo 2017: Turbomachinery Technical Conference and Exposition, pp. V02DT46A009-V02DT46A009.

Hileman, J. I., Spakovszky, Z. S., Drela, M. & Sargeant, M. A., 2007. *Airframe Design for “Silent Aircraft”*. Reno, Nevada, US, 45th AIAA Aerospace Sciences Meeting and Exhibit.

Hoying, D. A., Tan, C. S., Vo, H. D. & Greitzer, E. M., 1999. Role of Blade Passage Flow Structures in Axial Compressor Rotating Stall Inception. *Journal of Turbomachinery*, 121(4), pp. 735-742.

IATA, 2017. IATA. [www.iata.org/pressroom/pr/Pages/2017-10-24-01.aspx](http://www.iata.org/pressroom/pr/Pages/2017-10-24-01.aspx).



Isikveren, A. T. et al., 2014. *Recent Advances in Airframe-Propulsion Concepts with Distributed Propulsion*. Saint Petersburg, Russia, 29th Congress of the International Council of the Aeronautical Sciences (ICAS 2014).

Jameson, A., 1991. *Time Dependent Calculations Using Multigrid, with Applications to Unsteady Flows Past Airfoils and Wings*. Honolulu, AIAA 91-1596, AIAA 10th Computational Fluid Dynamics Conference.

Jerez Fidalgo, V., 2012. *Fan-Distortion Interaction in Novel Aircraft Installations*. s.l., PhD Thesis. Cambridge University Engineering Department.

Jerez Fidalgo, V., Hall, C. A. & Colin, Y., 2012. A Study of Fan-Distortion Interaction Within the NASA Rotor 67 Transonic Stage. *Journal of Turbomachinery*, 134(5), p. 051011.

Katz, R., 1958. *Performance of Axial Compressors With Asymmetric Inlet Flows*, PhD Thesis, Pasadena, California: California Institute of Technology.

Kawai, R., Friedman, D. & Serrano, L., 2006. *Blended Wing Body (BWB) Boundary Layer Ingestion (BLI) Inlet Configuration and System Studies*, Hampton, Virginia, USA: NASA/CR-2006-214534, NASA Langley Research Center.

Khalid, S., 1995. *The effects of tip clearance on axial compressor pressure rise*, PhD thesis, s.l.: Massachusetts Institute of Technology.

Kim, H. & Felder, J., 2011. *Control Volume Analysis of Boundary Layer Ingesting Propulsion Systems With or Without Shock Wave Ahead of the Inlet*. Orlando, Florida, USA, 49th AIAA Aerospace Sciences Meeting including the New Horizons Forum and Aerospace Exposition, AIAA 2011-222.

Kim, S. et al., 2018. *Stall Inception in Low Pressure Ratio Fans*. Oslo, Norway, ASME Turbo Expo 2018: Turbomachinery Technical Conference and Exposition, GT2018-75153.

Korsia, J. J., 2007. *VITAL - European R&D Programme for Greener Aero-Engines*. ISABE 2009-1114, International Symposium on Air Breathing Engines.

Kulfan, B. M., 2008. Universal Parametric Geometry Representation Method. *Journal of Aircraft*, 45(1), pp. 142-158.

Kyprianidis, K. A. D., Ogaji, S. & Grönstedt, T., 2009. *Low Pressure System Component Advancements and its Impact on Future Turbofan Engine Emissions*. Montreal, Canada, ISABE-2009-1276.

LabVIEW, 2013. *Getting Started with LabVIEW*, s.l.: National Instruments.

Lane, K. A. & Marshall, D. D., 2010. *Inverse Airfoil Design Utilizing CST Parameterization*. Orlando, Florida, US, 48th AIAA Aerospace Sciences Meeting Including the New Horizons Forum and Aerospace Exposition.

Liebeck, R. H., 2004. Design of the Blended Wing Body Subsonic Transport. *Journal of Aircraft*, 41(1), pp. 10-25.

Liebeck, R. H., Page, M. A. & Rawdon, B. K., 1998. *Blended-Wing-Body Subsonic Commercial Transport*. s.l., 36th AIAA Aerospace Sciences Meeting and Exhibit, p. 438.

Lieblein, S., Schwenk, F. & Broderick, R., 1953. *Diffusion factor for estimating losses and limiting blade loadings in axial-flow-compressor blade elements*. s.l., (No. NACA-RM-E53D01), NATIONAL ADVISORY COMMITTEE FOR AERONAUTICS CLEVELAND OH LEWIS FLIGHT PROPULSION LAB.

Longley, J., 1990. *Measured and Predicted Effects of Inlet Distortion on Axial Compressors*. s.l., ASME 1990 International Gas Turbine and Aeroengine Congress and Exposition, 90-GT-214.

Longley, J. P. & Greitzer, E. M., 1992. *Steady and Transient Performance Prediction of Gas Turbine Engines*. s.l., AGARD Lecture Series, 183.

Madani, V. & Hynes, T. P., 2009. *Boundary Layer Ingesting Intakes: Design and Optimization*. Montreal, Canada, Proceedings of XIX International Symposium on Air Breathing Engines, ISABE 2009-1346.

Maffioli, A., Hall, C. A. & Melvin, S., 2015. *Aerodynamics of Low Reynolds Number Axial Compressor Sections*. Kissimmee, Florida, US, 53rd AIAA Aerospace Sciences Meeting, AIAA SciTech Forum, (AIAA 2015-1934).

Mazzawy, R., 1977. Multiple Segment Parallel Compressor Model for Circumferential Flow Distortion. *Journal of Engineering for Power*, 99(2), p. 288–296.

- McDougall, N. M., Cumpsty, N. A. & Hynes, T. P., 1990. Stall Inception in Axial Compressors. *Journal of Turbomachinery*, 112(1), pp. 116-123.
- Milli, A. & Shahpar, S., 2012. *PADRAM: Parametric design and rapid meshing system for complex turbomachinery configurations*. Copenhagen, Denmark, ASME Turbo Expo 2012: Turbine Technical Conference and Exposition, pp. 2135-2148.
- Min, J. et al., 2018. *Cyclic Symmetry Finite Element Forced Response Analysis of a Distortion-Tolerant Fan with Boundary Layer Ingestion*. s.l., 2018 AIAA Aerospace Sciences Meeting, p. 1890.
- Moore, F. K. & Greitzer, E. M., 1986. A Theory of Post-Stall Transients in Axial Compression Systems: Part I - Development of Equations. *Journal of engineering for gas turbines and power*, 108(1), pp. 68-76.
- Nickol, C., 2008. *Silent aircraft initiative concept risk assessment*, Hampton, Virginia, US: Langley Research Center, NASA/TM-2008-215112.
- Pagonis, M., 2015. *Electrical power aspects of distributed propulsion systems in turbo-electric powered aircraft, PhD Thesis*, s.l.: Cranfield University, UK.
- Plas, A. et al., 2007. *Performance of a Boundary Layer Ingesting (BLI) Propulsion System*. Reno, Nevada, 45th AIAA Aerospace Sciences Meeting and Exhibit, p. 450.
- Provenza, A., Duffy, K. & Bakhle, M., 2019. Aeromechanical Response of a Distortion-Tolerant Boundary Layer Ingesting Fan. *Journal of Engineering for Gas Turbines and Power*, 141(1), p. 011011.
- Pullan, G. et al., 2015. Origins and Structure of Spike-Type Rotating Stall. *Journal of Turbomachinery*, 137(5), p. 051007.
- Sayma, A. I., Vahdati, M., Sbardella, L. & Imregun, M., 2000. Modeling of Three-Dimensional Viscous Compressible Turbomachinery Flows Using Unstructured Hybrid Grids. *AIAA Journal*, 38(6), p. 945–954.
- Shaw, M., Hield, P. & Tucker, P., 2013. *The Effect of Inlet Guide Vanes on Inlet Flow Distortion Transfer and Transonic Fan Stability*. San Antonio, Texas, USA, Proceedings of ASME Turbo Expo 2013, GT2013-94998.

- Sisto, F., 1987. AGARD Manual on Aeroelasticity in Axial-Flow Turbomachines. Volume 1. Unsteady Turbomachinery Aerodynamics. (No. AGARD-AG-298-VOL-1), NEUILLY-SUR-SEINE (FRANCE), p. 1.
- Sloan, J. & Griffiths, B., 2012. Composites World. [www.compositesworld.com/articles/2012-farnborough-international-airshow-report](http://www.compositesworld.com/articles/2012-farnborough-international-airshow-report).
- Smith Jr., L. H., 1993. Wake Ingestion Propulsion Benefit. *Journal of Propulsion and Power*, 9(1), pp. 74-82.
- Smith, A. M. O. & Roberts, H. E., 1947. The Jet Airplane Utilizing Boundary Layer Air for Propulsion. *Journal of the Aeronautical Sciences*, 14(2), pp. 97-109.
- Spalart, P. & Allmaras, S., 1992. *A one-equation turbulence model for aerodynamic flows*. s.l., 30th aerospace sciences meeting and exhibit, p. 439.
- Srinivasan, A. V., 1997. Flutter and Resonant Vibration Characteristics of Engine Blades. *Journal of Engineering for Gas Turbines and Power*, 119(4), pp. 742-775.
- Strazisar, A. J., 1985. Investigation of Flow Phenomena in a Transonic Fan Rotor Using Laser Anemometry. *Journal of Engineering for Gas turbines and Power*, 107(2), pp. 427-435.
- Suder, K. L. & Celestina, M. L., 1994. *Experimental and Computational Investigation of the Tip Clearance Flow in a Transonic Axial Compressor Rotor*. The Hague, Netherlands, ASME 1994 International Gas Turbine and Aeroengine Congress and Exposition.
- Taylor, J., 2016. *Personal communication*, Derby, UK: Rolls-Royce plc.
- Taylor, J. & Miller, R., 2017. Competing three-dimensional mechanisms in compressor flows. *Journal of Turbomachinery*, 139(2), p. 021009.
- Tse, T., 2017. *Aft Fuselage Boundary Layer Ingesting Systems*, Master of Research in Gas Turbine Aerodynamics: University of Cambridge, Engineering Department.
- Uranga, A. et al., 2014. *Preliminary Experimental Assessment of the Boundary Layer Ingestion Benefit for the D8 Aircraft*. National Harbor, Maryland, US, 52nd Aerospace Sciences Meeting, p. 0906.
- Vahdati, M. & Cumpsty, N., 2016. Aeroelastic instability in transonic fans. *Journal of Engineering for Gas Turbines and Power*, 138(2), p. 022604.

- Vahdati, M., Sayma, A., Freeman, C. & Imregun, M., 2005. On the Use of Atmospheric Boundary Conditions for Axial-Flow Compressor Stall Simulations. *Journal of Turbomachinery*, 127(2), pp. 349-351.
- Vahdati, M., Simpson, G. & Imregun, M., 2011. Mechanisms for wide-chord fan blade flutter. *Journal of Turbomachinery*, 133(4), p. 041029.
- Vanluggene, V., 2008. *VITAL Composite Fan Blade, Design Iteration 3, Stress and Vibration analyses results*, Derby, UK: Rolls-Royce plc.
- Vo, H. D., Tan, C. S. & Greitzer, E. M., 2008. Criteria for Spike Initiated Rotating Stall. *Journal of Turbomachinery*, 130(1), p. 011023.
- Wartzek, F., Biela, C., Pixberg, C. & Schiffer, H., 2012. *Modification of a compressor test rig for measuring the influence of inlet distortions on the compressor flow*. Braunschweig, Germany, Third Symposium "Simulation of Wing and Nacelle Stall".
- Wartzek, F., Brandstetter, C., Holzinger, F. & Schiffer, H., 2015. *Response of a transonic compressor to a massive inlet distortion*. Madrid, Spain, European Turbomachinery Conference.
- Weichert, S. & Day, I. J., 2014. Detailed Measurements of Spike Formation in an Axial Compressor. *Journal of Turbomachinery*, 136(5), p. 051006.
- Welstead, J. & Felder, J., 2016. *Conceptual Design of a Single-Aisle Turboelectric Commercial Transport with Fuselage Boundary Layer Ingestion*. San Diego, California, USA, AIAA SciTech Forum, 54th AIAA Aerospace Sciences Meeting.
- Williams, T. S. & Hall, C. A., 2018. *Reverse Thrust Aerodynamics of Variable Pitch Fans*. Oslo, Norway, ASME Turbo Expo 2018: Turbomachinery Technical Conference and Exposition, pp. V02AT39A014-V02AT39A014.
- Xu, L., 2002. *Assessing Viscous Body Forces for Unsteady Calculations*. s.l., ASME Turbo Expo 2002: Power for Land, Sea, and Air, pp. 323-331.
- Xu, L., 2014. *4A11 Turbomachinery II course*, s.l.: Cambridge University Engineering Department.

Yao, J., Gorrell, S. & Wadia, A., 2007. *A Time-Accurate CFD Analysis of Inlet Distortion Induced Swirl in Multistage Fans*. s.l., 43rd AIAA/ASME/SAE/ASEE Joint Propulsion Conference & Exhibit, p. 5059.

Yao, J., Gorrell, S. & Wadia, A., 2010. High-Fidelity Numerical Analysis of Per-Rev-Type Inlet Distortion Transfer in Multistage Fans-Part II: Entire Component Simulation and Investigation. *Journal of Turbomachinery*, 132(4), p. 041015.

Young, A., Day, I. & Pullan, G., 2013. Stall Warning by Blade Pressure Signature Analysis. *Journal of Turbomachinery*, 135(1), p. 011033.